Turbulent Flow Phenomena and Boundary Layer Transition at the Circular Arc Leading Edge of an Axial Compressor Stator Blade

Samuel C. T. Perkins, B.E. (Hons)
School of Engineering

Submitted in fulfilment of the requirements
for the degree of
Doctor of Philosophy

University of Tasmania

February 2012

Turbulent Flow Phenomena and Boundary Layer Transition at the Circular Arc Leading Edge of an Axial Compressor Stator Blade

Samuel Perkins

Abstract

As fuel prices rise and environmental awareness becomes an increasingly important topic, the efficiency of engines used for power production and transport must be increased whilst decreasing exhaust gas emissions and noise levels. From results obtained during this research project, in combination with work being produced at other research facilities, it is hoped that a greater understanding of how the leading edge region of compressor blades react to changes in engine operating points in a steady and unsteady environment is gained.

This thesis investigates the boundary layer development at the leading edge of a controlled diffusion stator blade with a circular arc leading edge profile. Steady flow measurements were made inside a large scale 2D compressor cascade at Reynolds numbers of $260,000$ and $400,000$ over a range of inlet flow angles corresponding to both positive and negative incidence at a level of freestream turbulence similar to that seen in an embedded stage of industrial axial flow compressor.

The instrumented blade of a large scale 2D cascade contained a series of very high resolution static pressure tappings and an array of hot-film sensors in the first 10% of surface length from the leading edge. Detailed static pressure measurements in the leading edge region show the time-mean boundary layer development through the velocity over-speed and following region of accelerating flow on the suction surface. The formation of separation bubbles at the leading edge of the pressure and suction surfaces trigger the boundary layer to undergo an initial and rapid transition to turbulence. On the pressure surface the bubble forms at all values of incidence tested, whereas on the suction surface a bubble only forms for incidence greater than design. In all cases the bubble length was reduced significantly as Reynolds number was increased. These trends are supported by the qualitative analysis of surface flow visualisation images.

Quasi-wall shear stress measurements from hot-film sensors were interpreted using a hybrid threshold peak-valley-counting algorithm to yield time-averaged turbulent intermittency on the blade's suction surface. These results, in combination with raw quasi-wall shear stress traces show evidence of boundary layer relaminarisation on the suction surface downstream of the leading edge velocity over-speed in the favorable pressure gradient leading to peak suction. The relaminarisation process is observed to become less effective as Reynolds number and inlet flow angle are increased.

The boundary layer development is shown to have a large influence on the blade total pressure loss. Initial observations were made without unsteady wakes and at negative incidence loss was seen to increase as the Reynolds number was decreased and, in contrast, at positive incidence the opposite trend was displayed. The cascade's rotating bar mechanism was used for unsteady tests where the influence of changing reduced frequency was investigated and compared to the performance of the cascade in steady operation. Results showed that increasing the stator reduced frequency brought about an increase in total blade pressure loss. The proportion of total loss generated by the suction surface increased linearly as the reduced frequency was increased from $0.47 - 1.88$. The opposite trend was seen on the pressure surface. These differences were attributed to the influence of wake passing events on the boundary layer in the leading edge region of both surfaces.

Results from both steady and unsteady tests were compared against predictions made using the MISES solver. MISES is not capable of predicting boundary layer relaminarisation, which was shown to be clearly present on the suction surface leading to peak suction, particularly at low to moderate values of inlet flow angle and low Reynolds numbers. As a result MISES over predicts the turbulent wetted area on the blades surface when transition occurs in the leading edge region. MISES does however predict the same Reynolds number dependency of separated flow regions.

The turbulent freestream flow field in the leading edge region of the blades was investigated using 2D Particle Image Velocimetry (PIV) and a commercial Reynolds Averaged Navier Stokes (RANS) based solver. The camera focused on the leading edge region of the suction surface and computational simulations were post-processed to display the equivalent field of view. Simulations were performed using the Menter Shear Stress Transport (SST) model and the Speziale, Sarkar and Gatski (SSG) Reynolds Stress Model (RSM) implemented inside ANSYS CFX. Of particular interest was how the free-stream turbulence intensity is modeled in areas of high shear strain rate, how turbulence intensity varies as the blades leading edge is approached and the production of anisotropic turbulent fluctuations close to the edge of the boundary layer. The freestream flow field was heavily influenced by the blade row displaying an increase in turbulent intermittency and significant levels of anisotropy close to the blade's leading edge. Although the CFD did predict rises in intermittency and some anisotropy, it oversimplified the flow field and missed some of the more subtle complexities seen in the experimental results.

The importance of understanding details about transition phenomena and freestream turbulence are highlighted and new insights into how they react to changes in Reynolds number and inlet flow angle are provided which can be used by code developers and users as validation. This body of work also highlights areas that still need more investigation.

Declaration of Originality

The research presented in this dissertation was conducted at the School of Engineering in the University of Tasmania between February 2008 and February 2012. This dissertation is the work of the author alone, and includes nothing which is the outcome of work done in collaboration, except where specifically indicated to the contrary. None of the work presented in this dissertation has been submitted to any other University or Institution for any other qualification. This dissertation contains approximately 47000 words and 90 figures.

Statement of Authority of Access

This thesis is not to be made available for loan or copying for two years following the date this statement was signed. Following that time the thesis may be made available for loan and limited copying in accordance with the *Copyright Act 1968*.

Samuel Perkins
February 2012

Acknowledgements

This project was funded by Rolls Royce Plc, with significant financial and in-kind assistance from the School of Engineering at the University of Tasmania and the Whittle Laboratory at the University of Cambridge.

This project would not have been possible without the help and assistance of too many people to name individually. A special thanks must go to the University of Tasmania and Whittle Laboratory's academic, administration and workshop staff and my beloved family and friends. You know who you are, and you know how much everything you have done means to me. Without all of you, none of this would have been possible.

Thanks.

Contents

List of Figures

List of Tables

Nomenclature

Latin Symbols

a	The Speed of Sound
C	Chord (c_x = Axial Chord, $c_{x,r}$ = Axial Chord of Rotor Blade Tip)
x	Axial distance
d	Rotating bar diameter
C_p	Pressure Coefficient $\left(\frac{P_s - P_{s1}}{P_{o1} - P_{s1}}\right)$
DF_r	Diffusion Factor for Rotors $\left(1 - \frac{W_{ro}}{W_{ri}} + \frac{\Delta V_\theta}{2\sigma_r W_{ri}}\right)$
f	Frequency
$\dot{m}$	Mass Flow Rate
P	Pressure (P_s = Static Pressure, P_o = Total Pressure)
s	Pitch
T	Temperature (T_s = Static Temperature, T_o = Total Temperature)
U	Blade Speed ($\overline{U}$ = Mid-Span Blade Speed)
V	Absolute Velocity (V_x = Axial, V_r = Radial, V_t = Tangential)
W	Relative Velocity (W_t = Tangential)
$AVDR$	Average velocity density ratio $\left(AVDR = \frac{\rho V_{x1}}{\rho V_{x2}}\right)$
S^*	Non-dimensional surface length $S^* = S/S_{max}$
Tu	Turbulence intensity
$QWSS$	Quasi wall-shear stress
LE	Leading edge
TE	Trailing Edge
CD	Controlled diffusion

Greek Symbols

α	Absolute Flow Angles

β	Relative Flow Angles
η	Efficiency
λ	Wavelength
ρ	Density
σ	Solidity $\left(\frac{c}{s}\right)$
τ_q	Quasi-wall Shear Stress $\left(\frac{E^2-E_o^2}{E_0^2}\right)^3$)
ϕ	Flow Coefficient $\left(\frac{V_{x,in}}{\overline{U}}\right)$
ψ	Total to Static Pressure Rise Coefficient $\left(\frac{\Delta P_{t-s}}{\frac{1}{2}\rho\overline{U}^2}\right)$
ω	Rotational Speed
ω_s	Stator Reduced Frequency
$\overline{\omega}$	Blade Pressure Loss
Λ	integral or 'macro' turbulence scale

Subscripts

1	Inflow
2	Outflow
ref	Inlet Reference
a	Axial Direction
U	Rotational Direction Rotor/Bar
o	Stagnation Quantity
s	Static Quantity
in	Compressor Inlet
r	Rotor (ri = Rotor Inflow, rc = Rotor Casing, ro = Rotor Outflow)
S	Stator
$stall$	At the Stall Point
$design$	At the Design Point

Superscripts

$\overline{\square}$	Average quantity
$\widetilde{\square}$	Non-dimensional Quantity

Chapter 1

Introduction

In 1930 Sir Frank Whittle patented the design for a gas turbine engine intended for jet propulsion and in 1937 the first engine of its type ran successfully. Since that time the gas turbine has been developed to a large extent and is currently used in a wide range of applications; for power generation, jet propulsion and the production of rotational mechanical power on land, at sea and in the air.

Gas turbine engines today can produce anywhere from tens of kilowatts to over 500 megawatts with rated efficiencies approaching 60 percent in combined cycles. Due to their high power to weight ratio and compactness, the gas turbine engine plays an increasingly dominant roll in aircraft propulsion where the gas turbine is currently found in all but small aircraft which still use reciprocating piston engines. However for transport on land and at sea the gas turbine has had a less pronounced effect due to its high specific fuel consumption and poor off-design performance compared to its diesel engine counterpart.

Axial flow compressors are used extensively in gas turbine engines, and are particularly suited to commercial and military aircraft applications. This is due to their capability to produce larger flow rates for a given frontal area, higher overall pressure ratios and higher efficiencies compared to their centrifugal alternative, which were used in some of the first engines (Figure 1.1). This makes them ideal for the compact, low drag and light weight requirements of the aviation industry. However these advantages come at the expense of increased aerodynamic complexity and design cost [20].

The overall performance of the gas turbine engine is strongly dependent on the efficiency of the compression process prior to combustion. Axial flow compressors transfer work from a rotating blade row or a number of blade rows to the working fluid (usually air). As the working fluid passes through the rotor blade row, both pressure and kinetic energy

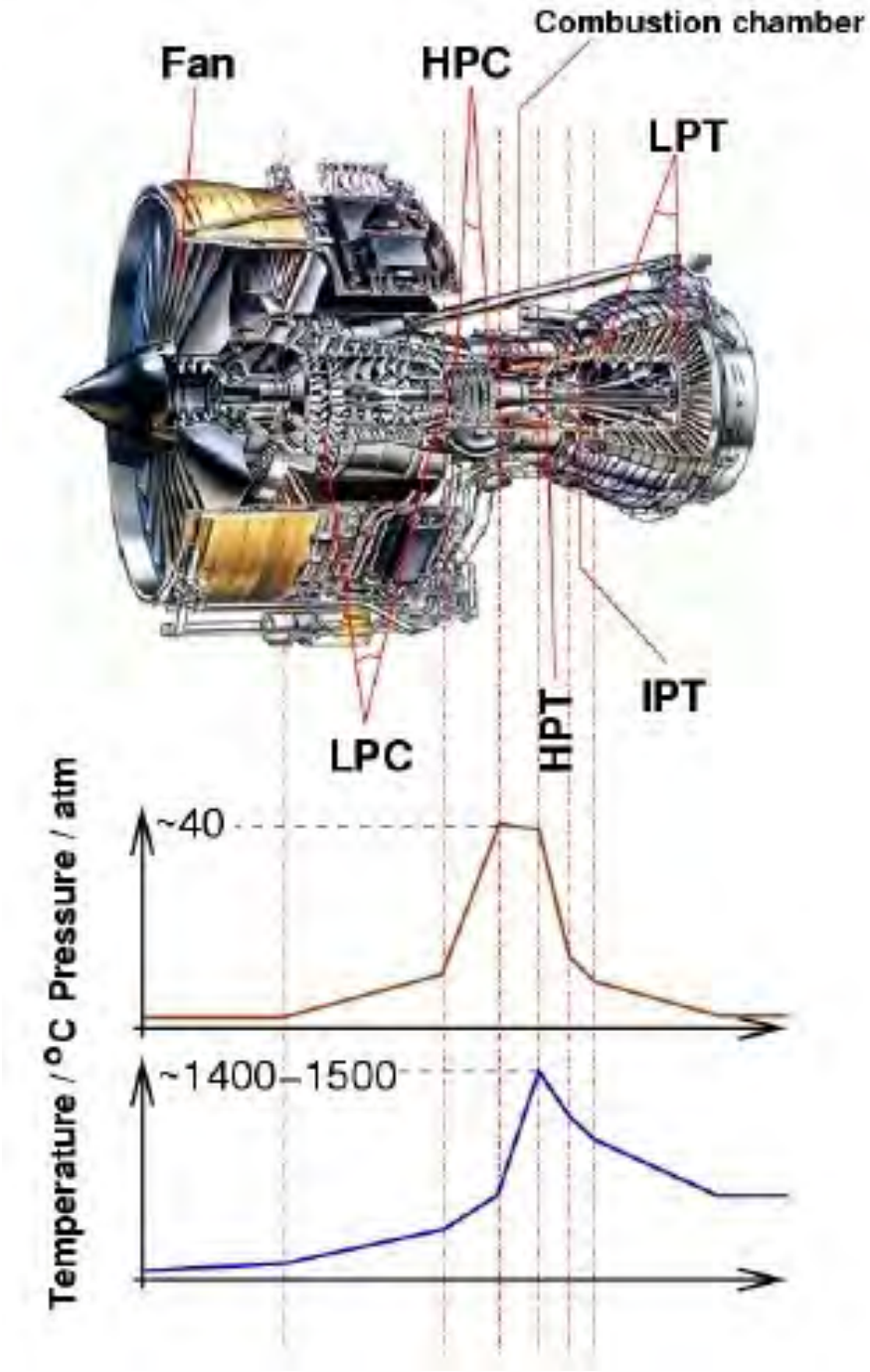

Figure 1.1: Schematic diagram of the Trent 800 showing the different stages: intermediate pressure compressor (IPC), high pressure compressor (HPC), high pressure turbine (HPT), intermediate pressure turbine (IPT), low pressure turbine (LPT) along with pressure and temperature profile through the engine. Rolls-Royce Plc.

are generally increased. Some of the kinetic energy is subsequently converted to pressure energy by diffusion in the adjacent downstream stator blade row [9].

An increase in static pressure across a single or multi-stage compressor creates an adverse pressure gradient between the inlet of the compressor and the combustion chamber of the gas turbine. This adverse pressure gradient attempts to force the flow in a direction opposed to that of the flow through the engine. The flow field is, even at design, extremely complex and is dominated by unsteady three-dimensional flow phenomena [20].

Until recently, research into axial compressor aerodynamics focussed on steady flow approximations of the flow field [29]. Steady flow methodologies have lead to modern blade designs approaching the achievable limit of aero-thermal performance and efficiency. Trends in current and future compressor designs show a push for higher blade loadings and more compact configurations. Similar design shifts have already been seen in turbine designs, with the introduction of high lift and ultra high lift blades in an attempt to reduce weight, noise and engine cost whilst maintaining efficiency and emissions requirements [78, 11, 42]. Inevitably these new design requirements will lead to intensified unsteadiness and aerodynamic complications [87].

Due to the competitive nature of the gas turbine industry, especially in commercial aviation applications, there is an increased demand for innovative design solutions and faster, more efficient, design processes. Dawes and Molinari [12] describes how a combination of past design techniques and methodologies is required to produce fast and robust methodologies capable of producing the innovative designs required to overcome the asymptote of performance in the current generation of gas turbines. For this to become reality a greater knowledge base and understanding of unsteady effects and fundamental physical processes occurring in gas turbines is required to modify and verify CFD models. This can then be utilised in the design process. This thesis aims to reduce this gap in knowledge. Until now designers have been able to design both compressor and turbine blades with impressive levels of performance, without a complete understanding of the flow phenomena in which the blades are operating [26].

It has been shown that the performance of an individual blade and the overall performance of a turbomachine can be closely related to the nature and behavior of the boundary layer flows surrounding its surface, particularly in the leading edge region. This is due to the boundary layer state having a large influence over losses resulting from skin friction drag and boundary layer separation.

Initially a laminar boundary layer forms at the leading edge of a blade and develops in a streamwise direction. A transitional region follows, resulting in a fully turbulent boundary

layer some distance downstream of the leading edge of the blade. It is common for separation, and or transition, to occur by different modes over a large range of surface positions.

Rolls Royce Pty use the MISES code as one of its key blade profile design tools, which was developed by Drela and Youngren [17] in the 1980's and is based around a 2D viscid - inviscid flow solver. It is an extremely clever program that simultaneously calculates the viscid and inviscid regions of the flow field around an aerofoil. The MISES code requires very limited computational resources by modern standards and produces results which, up to recent times, have been adequate for engineering design purposes. However the code encompasses a number of crude approximations which must be improved if the code is to assist in breaking the apparent asymptote in aero-thermal performance of the gas turbine engine.

This thesis is comprised of 8 remaining chapters describing in detail important background to the field, research methodologies and a thorough discussion of results finishing with concluding remarks and recommendations for future works.

Chapter 2 provides a review of boundary layer transition processes and how the boundary layer can affect a blade's performance along with associated computational prediction methods. It is critical to understand the works of previous researchers so that it is possible to identify research trends, past and present theories and the predictions and opinions of the leading experts in the field. This information is also pivotal in identifying gaps in the current body of research and forms the foundation of this research project.

A large scale 2D compressor cascade housed in the Whittle Laboratory at the University of Cambridge was used for the experimental component of this thesis. The cascade had the capacity to vary the inlet flow angle and Reynolds number simultaneously as well as being capable of running in both steady and unsteady operation. Chapter 3 describes this facility along with the instrumentation used during the testing program.

The search for further understanding of flow phenomena increases as does the need for faster and more accurate experimental equipment. To keep up the current state of the art technology in experimental research equipment a large number of modifications were made at the beginning of this project. Chapter 3 provides a detailed account of the experimental facilities used throughout the duration of this project. Chapter 4 then provides a detailed account of the methods used during the experimental portion of this project along with the experimental testing program.

Chapter 5 explores the effect of changing the inlet flow angle and Reynolds number on the pressure loss of a controlled diffusion stator blade under steady operation in cascade.

Of particular interest are mechanisms and trends that lead to changes in the development, transition and separation of the boundary layer in the leading edge region and how these lead to differences in the pressure loss loops at different Reynolds numbers. The study shows that both inlet flow angle and Reynolds number have significant and independent influences on a blade's loss loops and specific flow phenomena are identified and attributed to these changes in loss.

A direct comparison between MISES and the experimental results outlined in Chapter 5 is carried out in Chapter 6 outlining some of the programs shortfalls and how these could potentially lead to erroneous predictions.

A large amount of work has previously been carried out in compressor cascades with a steady flow environment however the amount of research conducted in large scale cascades with periodic unsteadiness is limited. Chapter 7 looks into the influence of changing the stator blades reduced frequency on profile loss and the flow characteristics around the blades surface. Particular focus is placed on the effect periodic unsteadiness has on boundary layer transition and separation in the leading edge region.

Chapter 8 investigates how the leading edge region of a compressor blade row influences the free stream flow field with an elevated level of freestream turbulence. The amplification and distortion of turbulence focusses on using particle image velocimetry (PIV) and CFD. Comparisons are made between two commonly used turbulence models inside ANSYS CFX and the PIV measurements.

The key findings from Chapters 5,6,7 and 8 are then brought together and summarised in the conclusion of this thesis. The summary of findings from this thesis is then used to recommended work for the future of gas turbine research based on knowledge gained during this project.

1.1 Supporting Publications

The findings from several chapters of this thesis have been published during the course of this project.

The effect of inlet flow angle and Reynolds number on the performance of a CD stator blade in cascade described in Chapters 5 and 6 was published in Perkins and Henderson [63]. The influence of period wake passing events over a range of reduced frequencies on the leading edge flow development and blade pressure loss production was also reported in [63]. This paper has been recommended for the ASME Journal of Turbomachinery.

Studies on the ability of two RANS based turbulence models ($k-\omega$ SST and RSM) to predict the amplification and distortion of turbulence in the leading edge region of a CD stator blade reported in Chapter 8 using Particle Image Velocimetry was published in Perkins *et al.* [64].

Chapter 2

Background And Literature Review

The nature of air flow inside a gas turbine engine is extremely complex, highly three dimensional and unsteady. High levels of turbulence and unsteady disturbances are primarily caused by the convection, dispersion and mixing of wakes from upstream rotor and stator blade rows. Inside the compressor of the gas turbine engine there also exists a continuous adverse pressure gradient running between the inlet of the machine and the combustion chambers, which opposes airflow through the compressor.

Boundary layer transition on the blades of the compressor and the turbine is inherently unsteady and can occur by multiple modes over a range of blade surface locations. Large portions of a blade surfaces are often covered by a boundary layer in a laminar or transitional state. The distribution of different boundary layer states can vary significantly with only slight changes in flow conditions, which must be considered if a good understanding of a blades performance is to be achieved over the operating range of a real machine.

The inherent complexities make accurate predictions of flow inside axial turbomachines extremely difficult, computationally intensive, time consuming and expensive. Use of the full unsteady Navier Stokes equations as a design tool is still a distant vision even with the computational power available today and the advent of graphics processor unit (GPU)

technology. As a result approximations are introduced to reduce calculation times, however these inherently introduce errors which must be minimised where ever possible. An increased understanding of the fundamental physical processes behind the multitude of flow phenomena is becoming increasingly important in order to improve approximations and formulate new prediction methods to minimise computational time whilst maintaining accuracy.

This chapter provides the reader with background knowledge and a review of the fundamental modes of transition, the unsteady and highly complex nature of the flow inside axial compressors and how these relate to controlled diffusion blades with circular arc leading edges. This will provide the necessary foundations for subsequent discussions on boundary layer development, transition, separation and modeling techniques in the remainder of this thesis.

2.1 The Modes Of Boundary Layer Transition

Boundary layer transition has been, and continues to be, an active research topic and is one of the few areas that contains a large number of unknowns for the turbomachinery blade designer [53, 95, 14]. Significant portions of laminar and transitional flow have been recognised on turbomachinery blading since the 1960's [93].

The transition process between laminar and turbulent boundary layers can occur under the influence of three fundamental mechanisms: natural transition, bypass transition and separated flow transition. The latter two types are commonly found in gas turbine engines however a single mechanism is rarely seen on its own and multi-mode transition is common [53, 54, 95]. Evidence has been found that up to 40% of the blade surface is governed by linear stability theory which suggests the natural transition process plays a role even when the dominating mechanism maybe be of a different type [43]. Flow conditions such as the presence of upstream wakes, Reynolds number, free-stream turbulence, blade loading and velocity and pressure gradients are determining factors as to which of the above-mentioned mechanisms dominate the transition process at a particular point in time.

Cumpsty [9] states that approximately 40% of an axial compressors loss is caused by the development of boundary layers on blade surfaces. Within a boundary layer entropy is created through viscous shearing and Denton [13] shows that this entropy production rate per unit surface area is created according to:

$$\dot{S}_a = C_d \frac{\rho U_e^3}{T} \tag{2.1}$$

where the value of C_d is $2-5$ times higher for a turbulent boundary layer compared to a laminar one (Figure 2.10). In separated flow regions there are relatively high levels of viscous shearing compared to a laminar or turbulent boundary layer. Since separated flow regions are almost always associated with the development of transitional or turbulent flow the resulting effective viscosity can be very large, (typically over 100 times that of a laminar boundary layer) and, as a result the local entropy generation rates are also relatively high [13].

The leading edge region of axial compressor blades with circular arc leading edges often contain large velocity overspeeds, which are seen as local spikes in the static pressure distribution. These are amplified when a blade is operating away from design, and produce extreme favorable and adverse pressure gradients which often lead to the formation of a boundary layer separation bubble. This combination leads to very high entropy or loss production per unit area and as a result is an area of key interest to the field. Increasing the laminar wetted area and reducing the chance of boundary layer separations will lead to a reduction in blade loss.

Orth [59] found that the unsteadiness of the a wake passing event did not affect the position of transition when compared to a steady wake impinging on a flat plate. This suggested that it was the high levels of turbulence intensity and not the periodic fluctuation in mean velocity that initiated transition. This research also demonstrated that laminar becalmed regions form upstream of, and move behind, turbulent patches. These becalmed regions allowed brief periods of laminar flow to exist downstream of the location at which an undisturbed flow becomes fully turbulent [52].

2.1.1 Natural Transition

Natural boundary layer transition typically occurs without any external forcing. Such flows must have low free-stream turbulence intensity, typically less than 1%, and pressure gradients mild enough to avoid flow separation or relaminarisation [101, 75, 51]. Natural transition occurs over a considerable streamwise length on a blade's surface and can be broken down into five main stages (Figure 2.2).

Initially a laminar boundary layer thickens to a point where small disturbances can be amplified. These disturbances are amplified as they convect downstream at a near linear

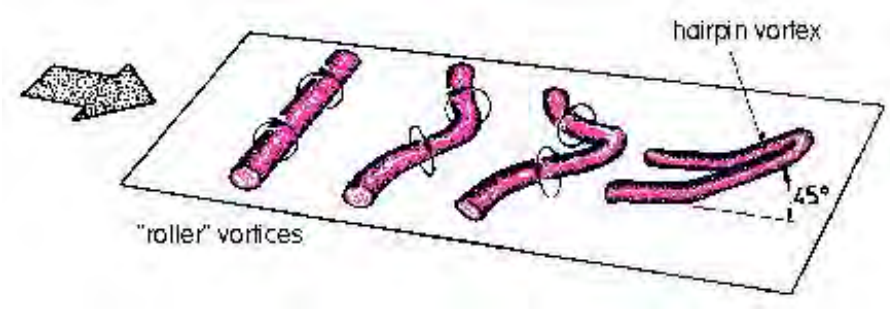

Figure 2.1: Diagram of the votex loops that form during natural transition [75]

rate. Upon amplification Tollmein-Schlichting (T-S) instability waves form which travel at approximately $0.3 - 0.35$ times the local free-stream velocity (V_{inf}) [26]. The first unstable mode is two-dimensional and occurs at a critical Reynolds number, $Re \equiv \sqrt{Ux/\nu} = 270$, or based on momentum thickness $Re_\theta = \sqrt{U\theta/\nu} = 201$.

In the second stage of natural transition the T-S waves propagate downstream and eventually begin to distort in a spanwise direction [47]. Following the initial distortions the third stage results in the formation of streamwise vorticity and the formation of an array of vortex trusses in the boundary layer (Figure 2.1). Subsequent rows of A-structures can be aligned or staggered depending on flow conditions. Aligned structures (K-type) are the result of fundamental resonance whereas the staggered arrangement (C and H-Type) are the result of subharmonic resonance.

The penultimate stage of natural transition brings about high frequency instabilities at the head of the vortex loops which are initially seen as streaklines in the flow. These streaks roll up and break down to form turbulent spots. Depending on the flow history, turbulent spots can form in a range of patterns.

The formation and propagation of turbulent spots have been studied intensely. Reports by [62] indicate they have a leading boundary velocity of approximately $0.8V$ and a trailing boundary velocity of approximately $0.5V$ and grow in a spanwise direction at an angle of approximately 22^o in zero pressure gradient conditions.

In the final stage turbulent spots propagate downstream and merge with adjacent spots forming a continuously turbulent boundary layer. Natural transition is not common as a sole mode in gas turbine engines due to the high levels of free-stream turbulence and the highly complex and unsteady flow characteristics however it has been recognised as a part of multi-modal transition.

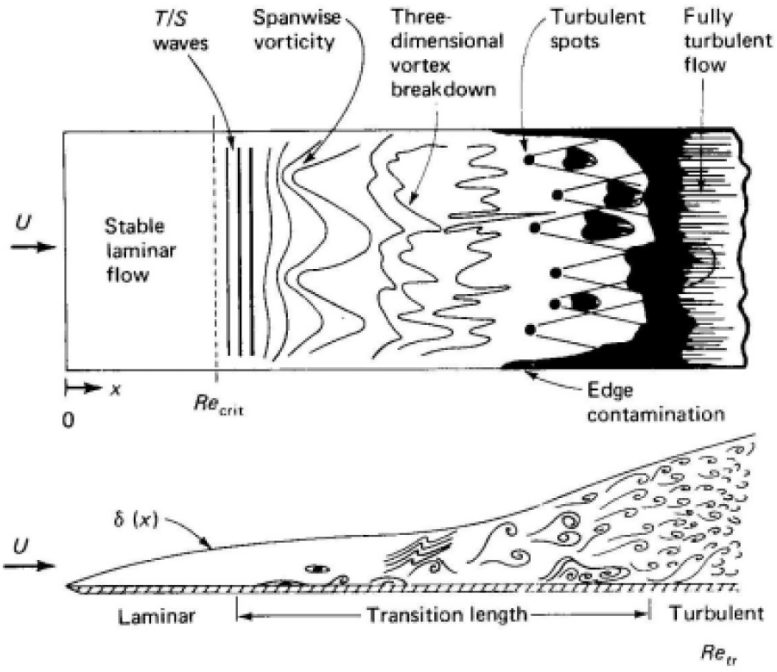

Figure 2.2: Schematic diagram of the natural transition process [101]

2.1.2 Linear Stability Theory

The linear stability theory provides a model for the natural transition process focussing on the growth of small sinusoidal instability waves in a two-dimensional parallel mean flow. The instability waves are commonly known as Tollmein-Schlichting (T-S) waves and can be represented by the following stream function:

$$\varphi(x,y,t) = \phi(y)e^{i(\alpha x-\beta)} \tag{2.2}$$

where α is real and β is complex. The wavelength of the disturbance is given by $2\pi/\alpha$. The real and imaginary parts of β give the circular frequency and the amplification factor of the disturbance respectively. From the stream function we are able to obtain the perturbation velocities and by substituting them into the Navier Stokes Equations we obtain the Orr-Somerfield equation [75]:

$$(U-c)(\phi'' - \alpha^2\phi - U''\phi) = -\frac{i}{\alpha Re} \tag{2.3}$$

If α and Re are given, then, with use of appropriate boundary conditions the Orr-Somerfeld equation yields a complex eigenvalue. The real part gives the phase velocity of the dis-

turbance and the imaginary part gives the amplification factor, which is used to determine whether a disturbance will grow, decay or remain constant. Perturbations with a negative amplification factor decay and are stable, those with a positive amplification factor grow and are inherently unstable and those with an amplification factor of zero are termed neutrally stable. The locus of such points, when plotted, in a wave number Vs Re plane produce a natural stability curve, which depicts a boundary between stable and unstable flow. Schaubauer and Klebanoff [74] carried out experimental testing in flows with turbulence intensities ranging from 0.035% to 0.014% and data collected from these experiments was the first to support linear stability theory.

For natural transition onset is usually determined using the e^n method developed by Mayle and Schulz [55] and others. e^n type methods are based on linear stability theory and involve calculation of a disturbance-amplitude ratio, or amplification ratio of disturbances using the amplification rate of the most unstable T-S wave at each streamwise position. A value of $7 - 10$ is commonly used as the critical amplification ratio, which has been determined experimentally and is related to the free stream turbulence intensity. Onset of transition is said to occur when a flow reaches an amplification ratio greater than that of the critical value [55].

2.1.3 Bypass Transition

Bypass transition is a common form of boundary layer transition in gas turbine engines [80] and was identified as far back as 1968 by [57].

It occurs in the presence of in-flow disturbances associated with high levels of free-stream (background) turbulence. A common description of Bypass transition is that transition occurs where the formation and amplification of the two-dimensional Tollmein-Schlichting instability waves is bypassed and the first sign of transition is the direct formation of turbulent spots. The modern meaning of the term also encompasses a range of transition mechanisms in highly disturbed flows. Within the Bypass class of transition variations occur depending on leading-edge geometry, mean pressure gradient and its history as well as free stream turbulence intensity level [45, 24]. Experiments carried out under geometrically similar conditions have produced different boundary layer characteristics depending on the free stream turbulence intensity.

During some hot-wire measurements Klebanoff [46] identified low frequency oscillations within a boundary layer subjected to elevated levels of free-stream turbulence. Further research showed that this effect was caused by the spanwise motion of large amplitube

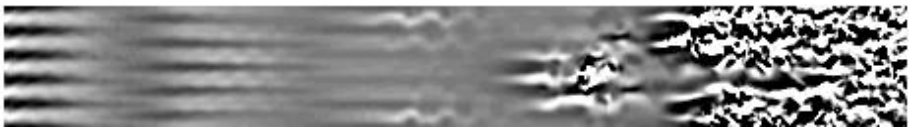

Figure 2.3: DNS results showing contours of streamwise fluctuation depicting the formation of Klebanoff modes followed by the formation of turbulent spots and the development of a fully turbulent boundary layer [105]

elongated streamwise disturbances, seen as streak or jets in the boundary layer. Such structures were named Klebanoff modes, but can also known as 'streaky structures' or 'breathing modes'.

In Bypass transition the T-S instability does not form and instead Klebanoff modes form in the perturbation field (Figure 2.1.3). Simply put, these streaky structures grow, destabilise and finally break down initialising the formation of turbulent spots which propagate and merge to create a continuous turbulent boundary layer (Figure 2.4).

Thermochromic liquid crystal flow visualisation techniques were employed by [**?** 106] to show that streaky structures form prior to transition in boundary layers subjected to high levels of freestream turbulence.

2.1.4 Separated Flow Transition

Separated flow transition occurs when a laminar boundary layer separates from a surface and undergoes complete transition to a turbulent flow regime. Separation occurs when a boundary layer experiences a sufficiently strong adverse pressure gradient ($\lambda_\theta \approx -0.082$, [91])

Laminar separations are commonly found a short distance from the leading edge of compressor blades where Reynolds numbers are inherently low. Blades with circular arc leading edges are particularly susceptible to this phenomenon as the boundary layer experiences a strong acceleration downstream of the leading edge, which is closely followed by a an extreme adverse pressure gradient due to a discontinuity in surface curvature. Upon separation the laminar boundary layer becomes highly unstable and rapid laminar-turbulent transition can occur. The separated transitional flow induces large turbulent shear stresses and increased levels of fluid entrainment into the shear layer from the free stream flow. This process energises the boundary layer fluid causing it to grow rapidly. In turn there is an increase in pressure. Turning of the separated streamline back towards the surface

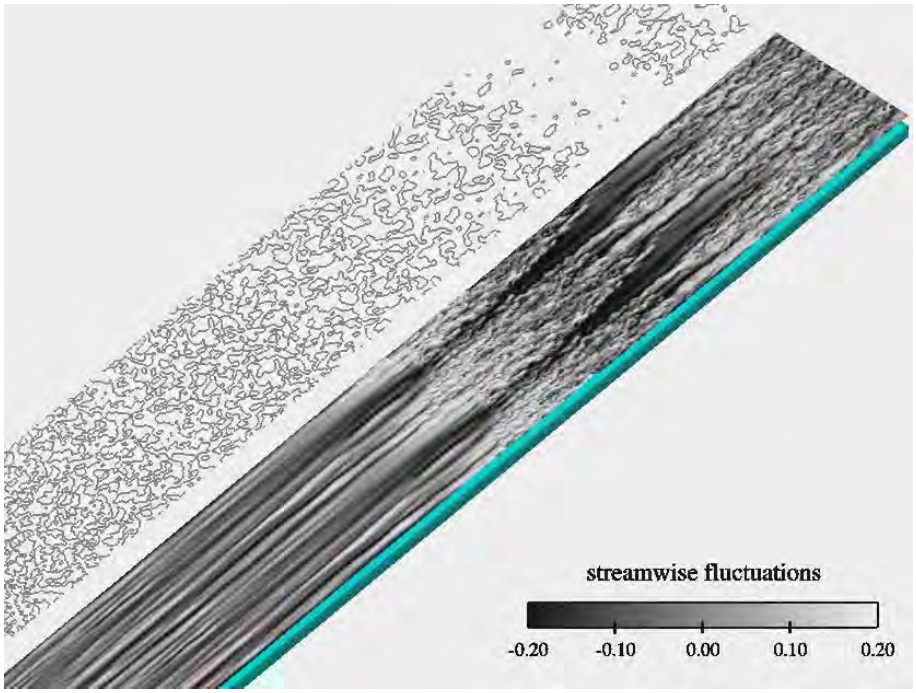

Figure 2.4: DNS Simluation of bypass transition using two wall parallel planes, one in the free stream and one in the boundary layer, showing velocity perturbations in the streamwise direction [105]

occurs when the pressure becomes equal to that of a turbulent boundary layer without a separation bubble resulting in turbulent reattachment of the boundary layer and the formation of a separation bubble [97, 2]. If, following a laminar separation, the flow encounters a sufficiently strong favorable pressure gradient it is possible for reattachment to occur before transition to turbulence is completed and in this case the pressure gradient drives the separated streamline back towards the surface.

Separation bubbles can be classified as being either "long" or "short" depending on whether the bubble has a local or global effect on the blade surface pressure distribution respectively. Tani [89] indicated that when the momentum thickness Reynolds number reached a critical value a short separation bubble could change into a long one.

If the Reynolds number is decreased or the angle of attack is increased sufficiently a separation bubble may form and burst where the laminar boundary layer separates from the surface and never reattaches. If this occurs the aerofoil is said to be in a state of stall.

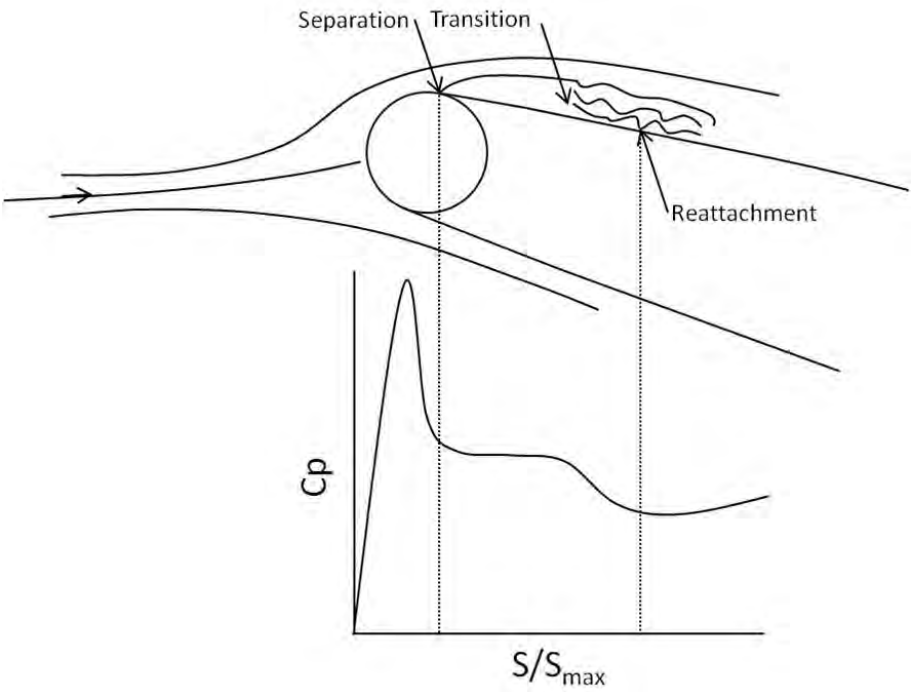

Figure 2.5: Schematic diagram of a leading edge separation bubble following a leading edge velocity overspeed at positive incidence based on Walraevens and Cumpsty [97]

2.2 Effect Of Leading Edge Shape On Boundary Layer Development

The leading edge shape of a compressor blade has a profound effect on the boundary layer development downstream of the leading edge. Walraevens and Cumpsty [97] showed that elliptical arc leading edges result in shorter separation bubbles and a reduction in the boundary layer thickness (non-dimensionalised by the leading edge thickness) when compared to their circular arc counterparts.

Pressure and velocity gradients imposed on the boundary layer have a large effect on its form and development. Large adverse pressure gradients present in the leading edge spike, often present with circular arc leading edges, can lead to laminar separation and the formation of separation bubbles. The use of elliptical leading edge profiles has been shown to reduce the occurrence of laminar separations and thus separated flow transition. This is a desirable feature as it leads to a laminar boundary layer remaining intact for longer in a streamwise direction reducing turbulent wetted area and blade pressure loss [22].

While the effect of leading edge profile is an active area of current research, it has only recently become a key area of interest. This is extremely important, as it is the leading

edge of the blade which initiates the boundary layer development over the remainder of the blade's surface.

Different leading edge compressor blade designs will react differently in steady, unsteady and highly turbulent flow conditions. It is thus vital that a given design be evaluated in a range of likely operating conditions for a real gas turbine. It has already been mentioned that large amounts of data are available for steady flow conditions. However there are significant deficiencies in knowledge of unsteady flow conditions around the leading edge of compressor blades and this is one area which could help break through the current asymptotic limit of aero-thermal performance in gas turbine engines [88, 32, 22].

2.3 Circular Arc Leading Edges

A number of considerations need to be made when selecting the leading edge shapes of axial gas turbine blading and they are often focused on a balance between machine performance and practical manufacturing tolerances [97, 88]. As the leading edge has a significant influence over the boundary development over a blade, which in turn has a large impact on its performance, the choice of leading edge shape is very important.

In modern gas turbine axial flow compressors there are two widely used leading edge shapes; circular arc and elliptical - however in recent times optimised leading edge shapes have been a focus of research in the turbomachinery field [22]. In the core of a large turbofan compressor the leading edge radii are typically $0.25 - 0.75\%$ of blade chord [88] and the chord typically ranges from approximately $100mm$ at the front of the compressor to $20mm$ at the back. The leading edge radii is therefore between approximately 0.25 and $0.15mm$. As a result the manufacturing of the leading edge region has to be extremely accurate this is not possible without time intensive and very expensive machining processes.

Due to the small sizes involved, erosion caused by the ingestion of small particles into the engine core can cause significant changes to the leading edge shape and blade performance. A blunting of the leading edge can be seen after time resulting in the possibility of an elliptical or optimised leading edge to display similar characteristics to that of a circular arc after some time in operation. Especially in areas where sand ingestion is frequent [69, 97].

As described in Section 2.2 the velocity distribution around a blade with a circular arc leading edge is complex and highly changeable. The rapid acceleration and deceleration in this region can cause the boundary layer to separate, reattach and transition within the first 2% of blade chord. This can then lead to turbulent or transitional flow over large portions of

the blade surface and is undesirable in terms of aerodynamic performance and blade row loss.

The variation of incidence changes considerably during the normal operation of gas turbine engines and is closely linked to the flow coefficient, which is a measure of the machines operating point. During a typical flight the flow coefficient will increase from a minimum value at take off to a maximum at cruise. The Reynolds number also changes significantly through the engine and inside an axial compressor at cruise altitude is seen to vary from $Re_c = 6(10)^5 - 1.2(10)^6$. Hobson and Weber [38] predicted that the Reynolds number based on chord of stator 67B could drop to values as low as $2(10)^5$ at an altitude of $15,000m$. As a result of this it is extremely important to understand the effects of changing both incidence and Reynolds number on blade performance, particularly in the leading edge region.

There have been a number of studies carried out on turbomachinery stator blades with circular arc leading edges. Sanger and Shreeve [70] studied the 67A CD stator blade profile at the Naval Postgraduate School in Monterey at at a range of Reynolds numbers from $Re_c = 4.7(10^5) - 6.9(10^5)$ and over a range of inlet flow angles from $\alpha_1 = 24.5^o - 46^o$. The 67A stator blade has a design point inlet flow angle of $\alpha_1 = 39^o$.

For inlet flow angles between $\alpha_1 = 32^o - 36^o$ transition was seen to occur inside a large separation bubble just downstream of peak suction at $x/c = 0.5 - 0.6$. At inlet flow angles values about $\alpha_1 = 36^o$ the suction surface boundary layer was seen to separate and reattach in the leading edge region due to a large velocity over-speed and subsequent rapid deceleration. When the transition location jumped to the leading edge a large increase in blade loss was expected due to the increased turbulence wetted area and momentum thickness. This was not the case and blade loss was seen to be fairly constant between $\alpha_1 = 32^o - 40^o$ and showed considerable difference from the computational prediction. Sanger and Shreeve [70] made mention that the only way this could occur would be if the boundary layer re-laminarised in the favorable pressure gradient on the blades suction surface between $x/c = 0.02 - 0.25$.

Studies were also carried out on the 67A CD stator blade by Elazar and Shreeve [18] who used LDV measurements to study the flow through a blade passage at a Reynolds number $Re_c = 7(10)^5$ over a range of inlet flow angles ($\alpha_1 = 40^o$, 43.4^o and 46^o). They found that the suction surface boundary layer remained attached until the trailing edge, except for when a laminar separation bubble formed past peak suction which moved downstream as the inlet flow angle was increased.

Hobson *et al.* [35] designed a new CD stator blade at the Naval Postgraduate School in Monterey. Cascade 67B had a design inlet flow angle of $\alpha_1 = 36^o$ and was studied at a range

of Reynolds numbers from $Re_c = 2.1(10)^5 - 6.4(10)^5$. At $Re_c = 2.1(10)^5$ a large laminar separation bubble was seen just past peak suction, this became smaller as the Reynolds number was increased to $Re_c = 3.8(10)^5$. At $Re_c = 3.8(10)^5$, if the boundary layer had undergone transition prior to previous location of separation onset, the separation was suppressed. At $Re_c = 6.4(10)^5$ no separation bubble was present and the blade experienced a trailing edge separation caused by interactions with end wall secondary flow structures.

More recent studies carried out in the Whittle Laboratory at the University of Cambridge by Wheeler *et al.* [100] and Goodhand and Miller [22] looked at the effects of changing the shape of axial compressor blade leading edges to remove leading edge spikes under design operating conditions away from the design point. Goodhand and Miller [22] looked at the leading edge spike height as a performance criteria for compressor blade profile loss. Circular arc, elliptical and idealized leading edge shapes were studied on a CD stator blade inside a 1.5 stage axial compressor. A spike height criteria was developed and its influence on blade performance was investigated. Results showed that when $\delta Cp > 0.5$ a leading edge separation bubble formed causing the time averaged transition location to jump forward on the blade causing a sharp increase in the trailing edge energy thickness, which was used as a measure of blade loss:

$$\delta_3 = \int_0^{\delta} \left(\frac{u}{u_\delta}\right)^2 \left(1 - \frac{u}{u\delta}\right) dy \tag{2.4}$$

2.4 Unsteady Flow Phenomena

There are many sources of unsteadiness within turbomachines (Figure 2.6). These different sources interact with one another to produce an extremely complex flow field with both random and periodic components.

Low pressure turbine blade rows had earlier reached an asymptote in aero-thermal performance similar to that currently being experienced in the compressor. By taking into account the periodic unsteadiness created by the passing of wakes of upstream blade rows, turbine blades have been designed to produce higher lift:loss ratios. It must be noted that the relative jet effect of passing wakes on a turbine blade is opposite to that on a compressor blade [32].

Ottavy *et al.* [60] showed that similar improvements can be made on compressor blades by suppressing separation through turbulence carried in incoming wakes and calmed regions

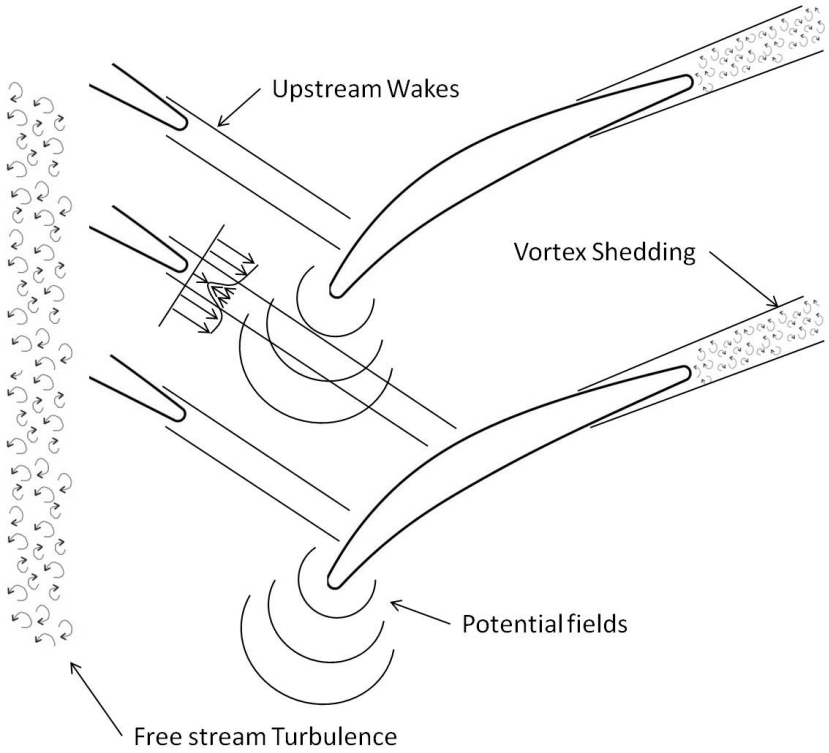

Figure 2.6: Sources of unsteadiness inside axial compressors [98]

which follow the highly turbulent wakes. Wake passing effects lead to the reduction in time-mean momentum thickness of the boundary layer on a highly loaded linear compressor cascade compared to steady inflow conditions. This suggests some potential for loss reduction through the use of unsteady wake passing events [33].

Schlichting and Das [76] also showed that turbulence generated by an oscillating turbulence grid lead to the suppression of a separation bubble that formed on the blades of a compressor cascade leading to a reduction in the amount of loss generated in the cascade. Similar findings were documented by Gibson [21] when working on a turbine cascade.

2.4.1 Periodic Unsteadiness

Periodic unsteadiness is present throughout the compressor and turbine of the gas turbine engine. The most obvious type is the relative motion between rotating and stationary blade rows which shed wakes from their trailing edges and propagate down stream. Wakes shed from upstream blade rows impinge on, and interact with, blades in downstream rows. These wakes create a relative flow of wake fluid, viewed from the free stream flow, often referred to as a negative jet. 2.7

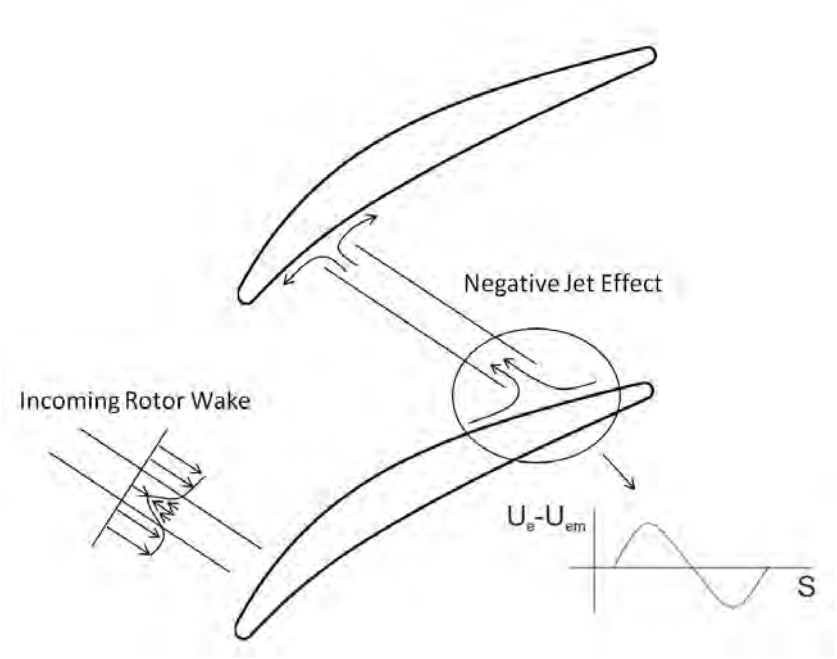

Figure 2.7: Diagram of a negative jet in a compressor blade row [98]

Negative jets cause convection of the highly turbulent fluid and, in a compressor, fluid is removed from the suction surface and introduced to the pressure surface [29]. This acts to thin the suction surface boundary layer and thickens the pressure surface boundary layer in a compressor blade row (the opposite effect to that seen in a turbine blade row). Negative jets cause fluctuations in the surface velocities and pressures and wakes also undergo significant deformation as they move past the leading edge region and into the blade row where high levels of shear are present.

Another source of periodic unsteadiness is caused by the interaction of potential flow fields which propagate upstream and downstream of both rotor and stator blade rows. This interaction creates periodic perturbations in the pressure field throughout the machine. Parker and Watson [61] showed that, for low Mach number flows, potential flow disturbances propagate approximately as;

$$f(x,y,t) = g(y,t)exp(-2\pi\sqrt{1-M^2}\frac{x}{L}) \tag{2.5}$$

This relationship shows that potential disturbances do not propagate very far upstream or downstream of a blade row and are generally seen to be a local phenomena.

The period passing of wakes over a blade's surface causes periodic unsteady transition within the boundary layer. Halstead *et al.* [26]-[27] presented detailed measurements from

surface mounted hot-films sensors placed inside a low speed multi-stage compressor and turbine facility. The unsteady nature of transition during periodic wake passing events for the base load case of an embedded compressor stator can be seen in Figure 2.8.

A patch of wake induced turbulence is initiated as the wake impacts the blades leading edge and convects over the blades surface as a wake induced turbulent strip (Figure 2.8 - area B). The turbulent strip moves slower than the free-stream flow and its growth is influenced by local flow conditions [16]. As the strips spread they eventually form a fully turbulent region of flow (Figure 2.8 - area C). Following this transitional and turbulent region was a calmed region, which showed laminar like characteristics with a value of shear stress similar to that of a turbulent boundary layer (Figure 2.8 - area D). This calmed region suppressed separations that would formed in between wakes under steady flow like situations. Transitional and turbulent flow was observed between wakes in areas E and F of Figure 2.8.

Through the removal of an upstream rotor disk Halstead *et al.* [27] showed that the influence of the calmed region was highly dependent on the rotor wake passing frequency and stator reduced frequency. The investigation showed that at a low rotor wake passing frequency the calming effect could wear off before the arrival of the next wake induced transitional strip. Surface mounted hot-films showed that after the calmed region passed between wakes, the laminar boundary layer separated and reattached in a turbulent state upstream of the location where transition was observed in calmed flow leading to a periodic shift in transition location.

Many studies have been carried out with cascade [15, 77] and flat plate [90, 104] facilities where flow conditions can be easily changed and controlled. In such facilities larger geometric scale are often used to increase measurement resolution and allow for more detailed experimental observations.

Schulte and Hodson [78] reported a decrease in profile loss of modern LP turbine blades as a result of the periodic passing of turbulent wakes interfering with the separation bubble that formed downstream of peak suction on the blade surface. Schulte and Hodson [79] later explained this effect using hot-film measurements which showed that turbulent spots forming upstream of the separation location, induced by a wake passing event, prevented the boundary layer from separating. A calmed region was also observed to follow the spots and was seen to be responsible for the suppression of separation because of an increase in shear stress and fuller "turbulent like" velocity profile.

This improved understanding of unsteady transitional phenomena lead to the steady flow design rules that limited boundary layer diffusion being challenged and a new generation

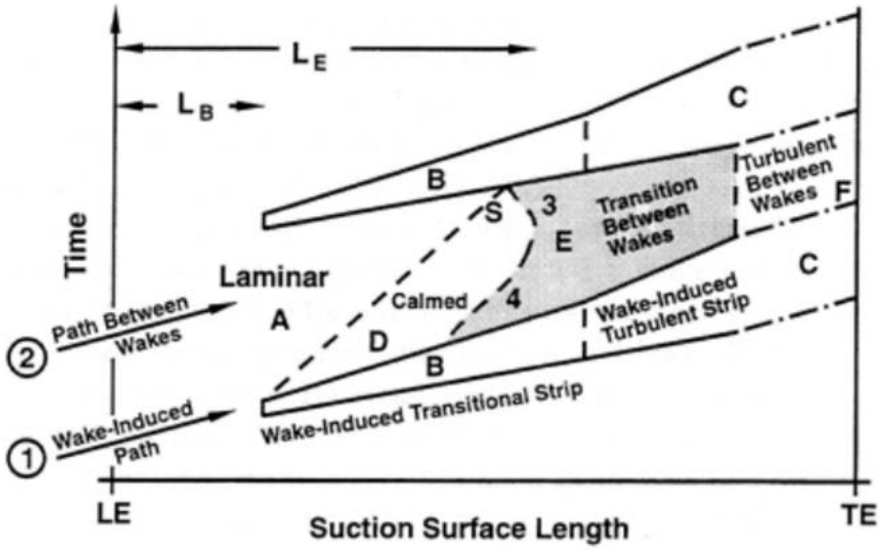

Figure 2.8: Schematic diagram displaying the nature of periodic unsteady transition on the suction surface of a compressor blade Halstead *et al.* [26]

of blade profile was created based on extensive experimental work of Curtis *et al.* [11] and Howell *et al.* [42]. These blade profiles are now known as 'high lift' and 'ultra high lift' and have allowed significant reductions in blade count by increasing individual blade loading whilst encountering minimal efficiency penalty. This huge development was only possible because of the presence of a large laminar boundary layer separation forming in the strong adverse gradient downstream of the point of peak suction which could be periodically suppressed with wake passing events. Large separation bubbles like those seen on turbine blades are not seen in compressors.

The impact of wake induced transition on compressor blade rows has received significantly less attention than that on turbines and its impact is poorly understood. Mixed results have come from a number of studies on the topic. Cumpsty *et al.* [10] did not identify a significant impact on loss but flat-plate studies carried out by Ottavy *et al.* [60] showed that unsteady wake passing events had a significant impact on blade loss, with performance improvements over the steady-flow case seen under certain operating conditions.

Abu-Ghannam and Shaw [1] suggested that transition cannot begin unless $Re_\theta < 163$ and Mayle [53] identified that the Reynolds number at the commencement of transition could be given by

$$Re_\theta tr = 400(Tu)^{-0.625} \tag{2.6}$$

These empirical correlations suggest that turbulent spots cannot form within a leading edge boundary layer where Re_θ is very small. Hughes and Walker [43] suggest that leading edge transition on compressor blades with periodic wake passing events could occur due to the amplification of Tollmein-Schlichting waves.

2.4.2 Random Unsteadiness

Otherwise known as turbulence, random unsteadiness is experienced throughout the gas turbine engine. It is random and highly complex in nature and is extremely difficult to predict. Turbulent flow consists of a mean flow velocity, which has superimposed onto it random and unsteady velocity fluctuations 2.9. Inside the gas turbine engine high levels of random unsteadiness are created when the wakes of upstream blade rows propagate downstream and merge with one another. This random unsteadiness is also referred to as free-stream or background turbulence.

Camp and Shin [6] conducted an experimental investigation into the turbulent flow field inside embedded stages of three different low-speed four stage compressors. They showed that the turbulence intensity at the inlet to stator varied from $3.6 - 7.0\%$ and the turbulence length scale location varied from $3.6 - 7.1\%$ of mean blade chord. This work clearly shows that the environment inside the axial research compressor is highly unsteady and it is expected that these levels would further increase inside real engines. A turbulence intensity of 4.0% is a widely accepted value for research purposes and has been used in numerous studies.

Place *et al.* [65] investigated how to modify low speed research facilities to better represent flow inside a multistage machine by installing upstream turbulence generating grids, fitting boundary layer trips to the hub and casing and by installing grids downstream of a stator row to replicate the potential flow field of a downstream stage. They showed that out of the previously mentioned changes elevating the free-stream turbulence by means of an upstream turbulence generating grid had the largest impact on performance leading to a 1.8% rise in stage efficiency.

Turbulence in both the boundary layer and freestream can have a marked effect on the performance of gas turbine engines and especially on the transition process. Turbulence in the free-stream flow affects boundary layer stability, transition and separation. In the boundary layer, the presence of turbulence can have both positive and negative effects. The velocity profile of a turbulent boundary layer creates a higher level of wall shear stress, leading to increased losses due to friction. However turbulent boundary layers have been

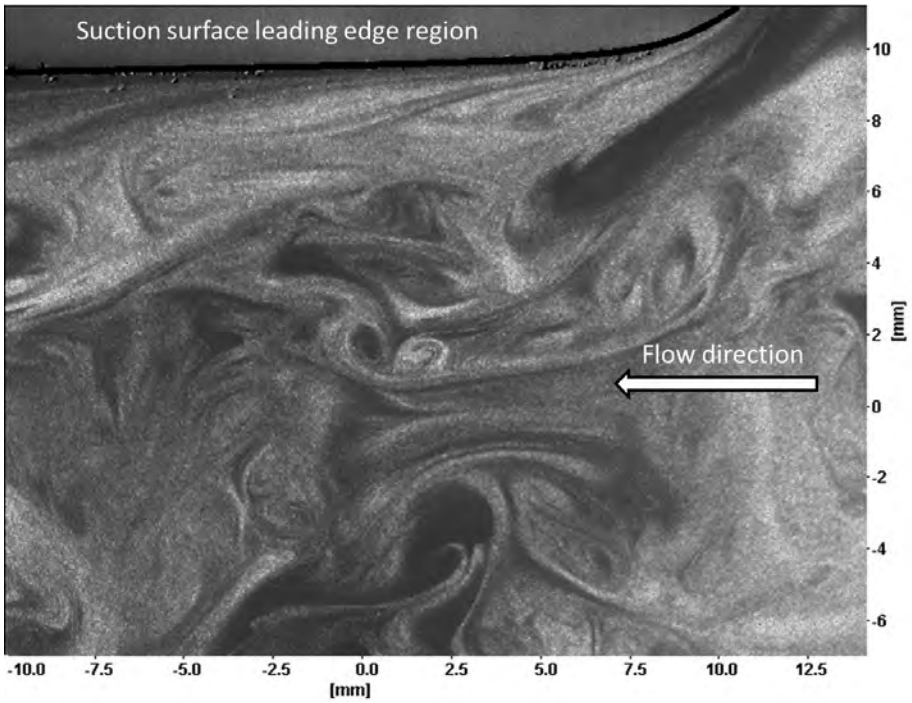

Figure 2.9: Smoke flow visualisation of freestream turbulence in the leading edge region of an axial compressor cascade [64]

shown to better resist boundary layer separation, which in turn leads to a decrease in the form losses present on a blade.

Due to its random, unsteady and complex nature turbulence cannot be easily modeled in time-mean flow calculations. Turbulence models are used to approximate the apparent turbulent shear stresses but generally these do not provide very accurate solutions for complicated flow situations such as that seen inside gas turbine engines. Denton [14] commented that free stream turbulence is one of the biggest remaining unknowns in gas turbine research.

2.5 Turbulence Amplification And Distortion Through Blade Rows

As previously mentioned, free-stream turbulence has a large impact on boundary layer development and transition on compressor blades. This is particularly true in the leading edge region where the boundary layer is extremely thin, laminar and highly receptive to free-stream disturbances, especially when a laminar separation bubble forms. It is thus critical to understand how free-stream and wake-induced turbulence behaves as it approaches and convects through blade rows if CFD turbulence models are to be designed that will lead to

the accurate prediction of transition phenomena in turbomachines without requiring large eddy simulation (LES) or direct numerical simulation (DNS). Many of the key determining factors required in computational fluid dynamics (CFD) can either be measured directly or modeled accurately and efficiently using modern computational methods, that is except for free-stream and wake turbulence, which is seldom known in many practical situations [14]. This typically leads the CFD user into making many, often crude, assumptions and the use of empirical turbulence models.

Hobson *et al.* [37], Soranna *et al.* [84] and Perkins *et al.* [64] have shown that free stream turbulence can be both amplified and distorted in regions of variable pressure gradient and/or high shear (Figure 2.9). Hobson *et al.* [37] reported that the turbulence intensity of the inlet flow to a compressor cascade, initially 1.5%, was amplified by an order of magnitude in the leading edge region and was amplified to 4.0% at the edge of the boundary layer at the trailing edge. This phenomena was seen for medium to high values of incidence and was believed to be caused by local shear, which will produce turbulence as the flow attempts to accelerate around the leading edge.

Soranna *et al.* [84] showed that free-stream turbulence became very anisotropic as it convected through a two-stage low speed research compressor. In an accelerating flow the compressed wall normal velocity fluctuations are magnified whilst the streamwise fluctuations are suppressed. The opposite was seen in adverse pressure gradient where the wall normal velocity fluctuations are suppressed and the streamwise fluctuations are enhanced. They also saw large positive production of turbulence in the immediate vicinity of the leading edge which was associated with the high levels of shear in the region. It was also shown that in an area either side of peak suction, where conditions were non-equilibrium, the wake turbulence was reduced by a rapid change in the orientation of the compressive and extensional strains. This leads to the turbulence production rate becoming negative, which in turn leads to a decrease in turbulent kinetic energy.

Sarkar and Voke [71] indicated that the surface normal fluctuations are more effective than the streamwise fluctuations in initiating transition and it is clear that if the performance of a blade is to be predicted accurately the above mentioned phenomena must be modeled correctly. A number of turbulence models currently used in turbomachinery design processes assume isotropic and homogeneous (frozen) turbulence, which cannot possibly lead to physically correct results.

Compressor blades with circular arc leading edges, such as that utilised in this research project are used throughout modern gas turbine engines and are susceptible to extremely high levels of shear in the leading edge region at values of incidence where a leading edge spike exists.

More experimental information is required to gain a deeper understanding of the flow around compressor blade leading edges and particle image velocimetry (PIV) would be an ideal measurement system to look at both boundary layer phenomena and how free-stream disturbances behave in regions of high shear.

2.6 Predicting Boundary Layer Development And Free-Stream Turbulence

Modeling the boundary layer transition process and boundary layer characteristics is critical for loss and performance predictions of a given aerofoil. The boundary layer transition process is strongly dependent on the free stream turbulence flow field and both of these phenomena should be modeled accurately early in the blade design process.

In the leading edge region of a compressor blade the boundary layer is extremely thin, laminar and highly receptive to free-stream turbulence, especially when laminar separation bubbles form. A number of detailed studies have shown the importance of the leading edge region and how sensitive it is to small changes in geometry and flow parameters [31, 23].

Changes in levels of free-stream turbulence intensity have a significant impact on boundary layer development particularly when separation or transition is possible. This results in it having a large influence on blade performance, which in turn can have a significant impact on engine performance [53, 95, 24, 88]. Free-stream turbulence also has a large effect on the mixing out of non-uniformities in enthalpy, entropy and temperature.

Researchers have been studying the transition process for decades and have developed a wide and detailed understanding about the modes of transition. However accurate prediction methods for the onset of transition and transition length are still highly sought after today. Many different numerical flow solvers may be used to determine the onset and development of the boundary layer transition process using a number of techniques. A review carried out by Savill [72, 73] examines the the ability of a variety of numerical methods and models to predict transitional flow phenomena.

In general there are three approaches to modelling of transitional flow. The first superimposes components of a laminar and turbulent boundary layer, using empirical data to specify the transition onset location as well as the boundary layers progression to a fully turbulent state. The second approach models transition implicitly using the diffusion of turbulent energy into the boundary layer from the free-stream. This method is implemented

along with a turbulence model such as the common $k = \omega$ or $k - \epsilon$ models. The third approach includes an equation for the transport of intermittency in addition to the governing flow equations [56].

The ability of the full set of the Navier Stokes equations to describe the motion of air at temperatures and pressures near atmospheric conditions is not in doubt [4]. However to evaluate numerical solutions of the full time-dependent equations for turbulent flow is only possible using large super computers and even then the computation time is often months for geometrically simple problems at low Reynolds numbers. As a result engineers have turned to the time-averaged form of the Navier Stokes equations, commonly known as the Reynolds Averaged Navier Stokes equations (RANS), however doing this relies on a number of assumptions being made. Using these has implications such as in the application of the Reynolds decomposition assumption, which allows for the varying chaotic velocity fluctuations to be separated from the mean velocity. Once broken apart, turbulence models are introduced to represent the chaotic velocity fluctuations.

Averaging the full equations does have implications, eliminating some terms from the full set of equations. To overcome this problem apparent mean stress terms are introduced (Reynolds stresses), but in doing so the number of unknowns become greater than than number of equations. As a result Reynolds-stress transport equations are used to express the conservation of each Reynolds stress. An infinite number of these equations would be needed to restore all the information lost by time-averaging, which is not possible and thus a finite number of equations is used and any missing information is supplied from experimental data and correlations. The result of this is that the finer details of the turbulent flow field is often missed and blade performance and flow characteristics are often poorly predicted.

Even with the rapid advances in computer technology the RANS equations are still not at the stage where they can be used as a blade design tool. It is unlikely this will change in the near future although the advent of GPU technology may accelerate this process. To overcome this issue, a large number of flow solvers have been developed to be used in the design and optimisation of gas turbine blades. Many of the codes use different computational methods to evaluate flow properties and rely on a multitude of experimental correlations, approximations and assumptions. The Abu-Ghannam and Shaw method [1] is a very well known correlation and relates various flow properties such as turbulence intensity in the free-stream to the momentum thickness Reynolds number Re_θ to predict transition onset.

With the computational power available today these simple models take very little time to solve and thus it is assumed that this is not an important factor, making them ideal for the

use in optimisation routines. However models based on experimental correlations have a number of inherent problems as they are typically only accurate for a narrow band of flow conditions and within this band only predict certain flow characteristics well. The laminar-turbulent transitional region is one area which is poorly predicted over a wide range of flow conditions and geometries by such methods.

The inadequacy's within these models bring about a number of interesting and challenging problems for the engineer. To improve their accuracy new and innovative correlations and prediction techniques must be formulated and applied to existing models. In the past this has been done by combining more than one correlation or modifying existing ones.

A number of flow solvers have been developed over time based on different numerical techniques. One code of particular importance to this thesis is the MISES code of Drella and Youngren [17]. MISES is a $2D$ viscid-inviscid solver which breaks the flow around an aerofoil into two parts, the viscid boundary layer and the inviscid free stream flow. Two sets of calculations are solved simultaneously. Firstly the viscid region of the flow is determined and, depending on its profile, a stream line is displaced from the blades surface to represent the new apparent shape of the aerofoil. At the same time the new pressure distribution around the displaced surface is evaluated. This process repeats until convergence is achieved.

2.7 Loss Generation In Turbomachinery

It is important to understand different loss generation mechanisms that occur in turbomachinery blade rows and how these can be used to provide a measure of blade profile loss. Denton [13] provides a comprehensive summary of the various loss prediction mechanisms that occur in turbomachinery and his derivation for entropy creation within a boundary layer is seen below.

$$\dot{S} = \int_0^{\delta} \left(\frac{1}{T} \tau_x y \right) dV_z \tag{2.7}$$

where $\dot{S}$ is the rate of entropy production per unit surface area and

$$\dot{S} = \frac{1}{T} \tau \frac{dV}{dy} \tag{2.8}$$

is the entropy production rate per unit volume of a boundary layer and can be interpreted as viscous shear work which, can be converted in to a dissipation coefficient.

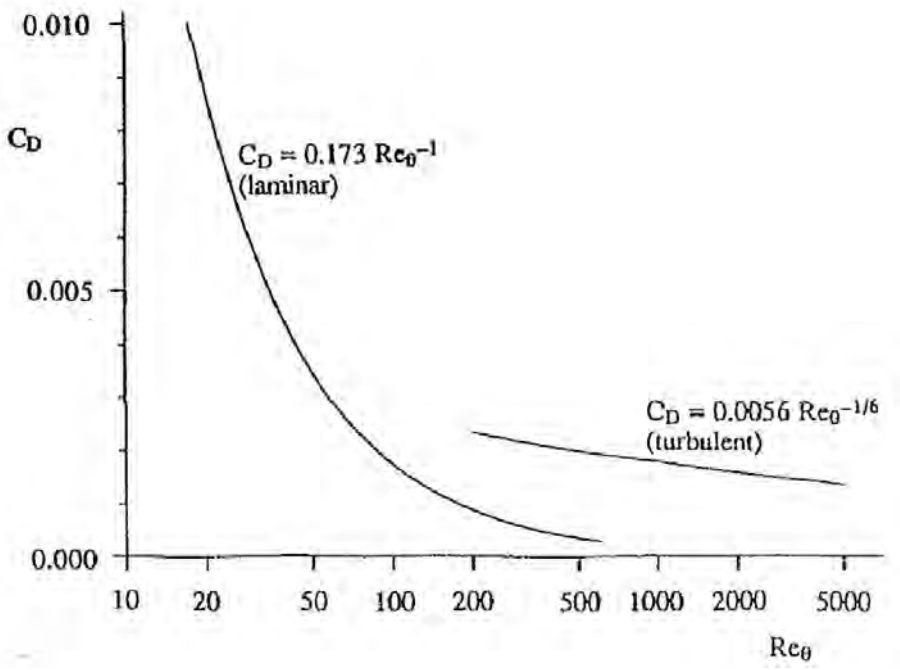

Figure 2.10: The variation of dissipation coefficient for laminar and turbulent boundary layers

$$C_d = \frac{T\dot{S}_a}{\rho V_\delta^3} \tag{2.9}$$

The value of C_d can be plotted for both laminar and turbulent boundary layers as seen in Figure 2.10

It is then possible to calculate the rate of entropy production over a blades surface.

$$\dot{S} = \int_{LeadingEdge}^{TrailingEdge} \frac{\rho V_\delta^3 C_d}{T_\delta} dx \tag{2.10}$$

Due to the constantly changing state of a boundary layer on a blade in unsteady operation is it difficult to obtain accurate values of C_d for the laminar, turbulent, transitional, calmed and separated regions of flow. The loss breakdown within a boundary layer can be seen in Figure 2.1.

The profile loss of a turbomachinery blade can also be seen as a function of the trailing edge momentum thickness (θ) which grows with the boundary layer over a blade's surface. This development is also dependent on the initial value, θ_0, at the leading edge. Keeping the

Table 2.1: The breakdown of loss generation within a boundary layer

Region	Fraction of total loss produced
Sublayer	50%
Logarithmic	40%
Outer	10%

initial value of the momentum thickness low is important and its effect can be seen in the following breakdown of the boundary layer momentum integral equation.

$$\frac{d\theta}{dx} + (H+2)\frac{\theta}{u}\frac{du}{dx} = \frac{C_f}{2} \tag{2.11}$$

In regions of flow with a strong adverse pressure gradient, such as that seen in the leading edge velocity spike, the value of skin friction becomes small and as a result it is neglected from the right hand side of the equation such that when

$$\frac{du}{dx} \Rightarrow 0; \frac{dp}{dx} \Rightarrow 0; \frac{C_f}{2} \approx 0 \tag{2.12}$$

$$\frac{d\theta}{dx} \approx -(H+2)\frac{\theta}{u}\frac{du}{dx} \tag{2.13}$$

which can be written as

$$\frac{d\theta}{\theta} \approx -(H+2)\frac{du}{u} \tag{2.14}$$

integrating wrt x gives

$$\int_0^x \frac{d\theta}{\theta} \approx \int_0^x -(H+2)\frac{du}{u} \tag{2.15}$$

$$ln\left(\frac{\theta}{\theta_0}\right) \approx -(H+2)\left(\frac{u}{u_0}\right) \tag{2.16}$$

this can then be written to produce

$$\theta(x) = \theta_0\left(\frac{u}{u_0}\right)^{-(H+2)} \tag{2.17}$$

This result shows that the momentum thickness at the trailing edge is proportional to its value at the leading edge. Small variations in θ_0 can be amplified in the presence of a separation and lead to a large variation in the trailing edge momentum thickness and resulting profile loss. The formation of a separation bubble will lead to an increase in the local value of θ. This will potentially lead to a large increase in the trailing edge momentum thickness as well as increased levels of local entropy generation.

2.8 Conclusions

Current gas turbine engine design practice is typically based on improvements of previously successful designs. Dawes and Molinari [12] suggest that, to overcome the apparent asymptote of aero-thermal performance, a new and innovative approach to design should be adopted with 3D CFD introduced early in the design process rather than for analysis once the initial design has been created.

This chapter has reviewed the fundamental modes of boundary layer transition as well as the sources and impacts of unsteadiness within the gas turbine engine. These are two key areas that CFD solvers are currently poor at predicting accurately in the design process and as a result are two areas that require significant attention.

Improvements and advances in computational power are constantly reducing the time required to solve CFD solutions. However realistic solutions to the unsteady Navier-Stokes equations are still not available as a design tool. Large Eddy Simulation (LES) CFD solutions are available, but they require a large amount of time and computational resources, which makes them an unreasonable design tool. However LES simulations still give vital insight into detailed flow characteristics, thus making them a key tool in modern CFD research.

A number of gaps exist in the the body of knowledge concerning flow characteristics in gas turbine compressors. The majority of these gaps involve understanding specific and highly complex flow phenomena in both steady and unsteady environments. Such information is of key importance to the blade and CFD code designer. This is a vital step if CFD codes are to achieve an increasingly large usage in the initial stage of an innovative design process.

This draws our attention to the flow at small distances downstream of the leading edge and concentrates research into the nature of the boundary layer under varying flow conditions in both a steady and unsteady environment.

Chapter 3

Experimental Facilities and Intrumentation

3.1 Experimental Facilities

The experimental investigations carried out throughout this project used a controlled diffusion compressor blade with a circular arc leading edge profile. The blade profile was tested inside a large-scale 2D cascade wind tunnel located in the Whittle Laboratory at the University of Cambridge, UK. The blades were many times the size of blades used in actual engines allowing for elevated Reynolds numbers and very high resolution measurements to be taken in the leading edge region.

Blades inside the two dimensional cascade had a chord, C, of 285mm and a leading edge circle of diameter 10.6mm allowing for previously unseen measurement resolution in the leading edge region of the blades. Measurements in the blade to blade plane could be taken in either a steady or unsteady flow environment with the use of rotating bar mechanism. A range of Reynolds numbers and inlet flow angles could also be covered. As a result the blade profile could be examined under a large variety of flow conditions and the resulting

data and observations could be used to compare how the blade performance alters with changing flow characteristics.

3.2 2D Cascade Description

A linear compressor cascade was used to simulate the flow through an annular compressor stator blade row. The large scale 2D cascade used in this project was situated and built in the Whittle Laboratory at the University of Cambridge and was designed with five passages using four whole blades and two half blades to complete the top and bottom passages. Each of the blades has a chord of 285mm and a pitchwise spacing of 280mm giving the cascade a solidity of 0.99. The design inlet flow angle was 45^o and the maximum achievable Reynolds number under steady operation was $Re_c = 400,000$ and under unsteady operation was $Re_c = 300,000$. Ideally seven or more blade passages are used in a compressor cascade to aid flow periodicity, but this was not possible due to size restrictions of the available wind tunnel exits.

The cascade was placed at the left hand exit (when facing upstream) of the Rhoden tunnel at the Whittle Laboratory - a large open circuit wind tunnel down stream of a centrifugal fan. Before entering the cascade the flow was controlled using a number of screens and honeycomb sections to improve uniformity before being accelerated through a 3 : 1 area contraction. Downstream of the contraction the flow passed through a turbulence grid designed to produce a turbulence intensity of 4.0% at the leading edge plain of the instrumented blade, which, as mentioned previously, is a widely accepted value for a embedded stage of a multistage machine [65, 6].

Bleed slots were positioned at the turbulence grid and upstream of the cascade inlet plain to remove high loss boundary layer flow from the tunnel walls prior to the flow entering the cascade. End wall tip gaps were present between the blades and the cascade end walls to help control end wall flows and minimise any three dimensional flow from occurring in the adverse pressure region on the suction surface of the blades. These were shown to be highly effective using flow visualisation techniques.

Static pressure tappings were placed in the middle of each blade passage on both side walls 0.5C downstream of the trailing edge and in the leading edge plane and a pitot tube was used to provide a reference pressure downstream of the in-tunnel rotating bars in line with the blades leading edges.

An exit traverse slot was positioned 1C downstream of the blade trailing edges and a three

axis traverse mechanism was used to perform exit area traverses of the cascade using a 3HP. Due to spatial restrictions it was not possible to place an automated traverse mechanism at the cascades inlet however an accurate, custom made, manual traverse system was devised to traverse the inlet plain through a slot milled out of the inlet section upstream of the rotating bar mechanism.

Originally the cascade was designed to be used at a fixed inlet flow angle of $\alpha_1 = 45^o$. Modifications were made to the inlet section downstream of the turbulence grid and supporting frames were added to allow for a $\pm 5^o$ variation of inlet flow angle away from the blade's design operating point. The front of the cascade was supported on stub axles inside two thrust bearings mounted on an outrigger support system, which were aligned with the instrumented blade's leading edge to maintain a constant distance between it and the turbulence grid. The rear of the cascade could be be raised (increase positive incidence) or lowered (increase negative incidence) using three screw jacks attached to one of the lateral supporting members at the rear of the cascade. This system, in combination with a digital inclinometer, could set the cascade to within $\pm 0.1^o$.

As incidence was increased or decreased the inlet flow area to the cascade must decrease or increase respectively. Two movable false floors were placed inside the inlet section to ensure the inlet area and flow angle remained consistent as the incidence of the cascade was varied. The floors were combined with an additional bell-mouth styled inlet located upstream of the turbulence grid to ensure the flow was parallel and as uniform as possible when passing through the turbulence grid. Initially due to a poorly designed inlet streamline curvature was present through the turbulence generating grid and, as a result, there was an uneven generation of loss across the grid, which seriously affected the inlet velocity distribution to the cascade. The bell-mouth inlet also had to be adjusted with any change in incidence to maintain alignment with the false floors inside the inlet. Figure 3.1(a) shows a schematic of the complete cascade and inlet mechanism, which is explained in detail in Section 3.2.2.

3.2.1 CD Stator Blade Row

The CD stator blade row was designed for a 1.5 stage research compressor at the University of Tasmania by Hughes and Walker [43] in collaboration with Roll-Royce plc in Derby UK. The blade row was designed to incorporate features typical of modern controlled diffusion (CD) blading whilst maintaining the same outlet flow as the C4 blades previously used in the research compressor. Controlled diffusion blade profiles are designed around a pre-described surface velocity distribution, a method which is seen to provide significant aerodynamic benefits. A constant chord of 152.4mm was used, which is exactly double the

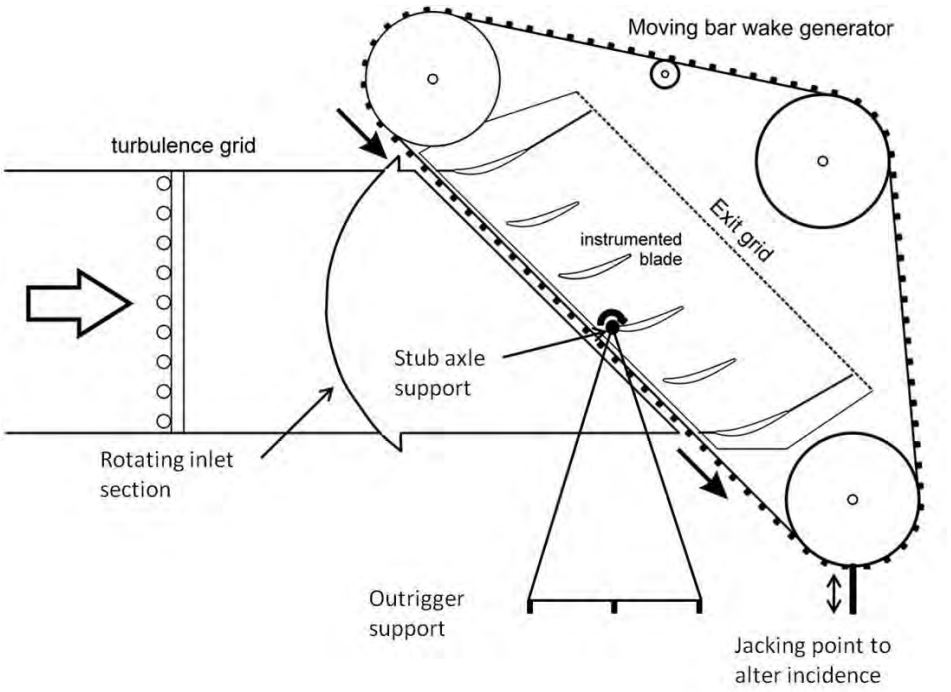

(a) Schematic diagram of the 2D compressor cascade used in this research project

(b) Photograph of the 2D compressor used in this research project

Figure 3.1: Photo and schematic diagram of the compressor cascade research facility

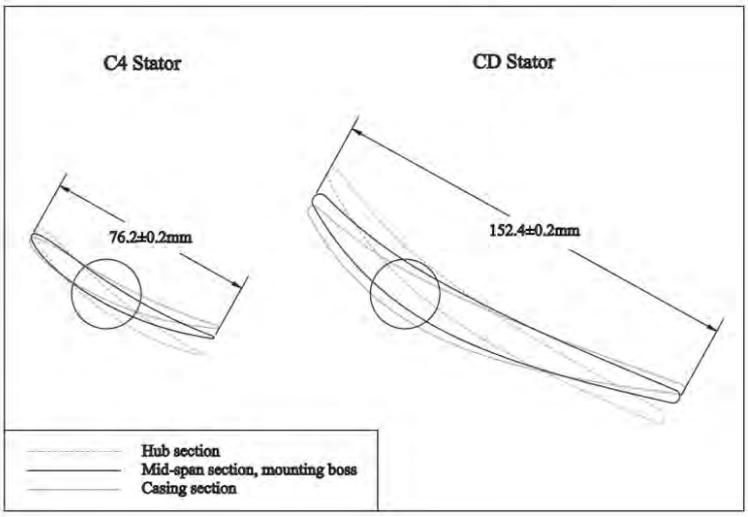

Figure 3.2: Hub section, mid-span section and casing section profiles of the C4 and Cd stator blade profiles

chord of the previous C4 blade. A schematic of the *C*4 and CD blade profiles at hub, mid span and tip can be seen in Figure 3.2. The CD blade count was reduced from 38 to 19 during the blade row modifications. By reducing the blade count by half each of the stator blades still experienced the same pitchwise flow field for a given clocking arrangement given the inlet guide vanes and rotor blades were not altered.

The stator blades were manufactured by Complete Fabrication, Whittlesford, UK from a 3D CAD model. A master blade was CNC machined from Prolab 65 modeling compound. The master blade was then measured using a DEA global coordinate measuring system and displayed an accuracy of $1.5\mu m$. The maximum deviation from the design at mid-span was less than $\pm 0.2mm$ at the leading edge and less than $\pm 0.3mm$ over the whole blade profile.

The blade design used in the large scale cascade was taken from the mid-span profile of the CD stator blade row. Five out of the six blades in the cascade were manufactured out of modeling board with the sixth, being the instrumented blade, was manufactured on a Stereo Lythograph printer. The instrumented blade was split into three $200mm$ spanwise lengths due to manufacturing constraints. One section of the blade was instrumented with 54 hot-film sensors, one was left untouched for PIV measurements and one was instrumented with 194 surface static pressure tappings (Figure 3.4). Figure 3.3 shows a CAD image of the instrumented blade. The Stereo Lythograph printer with the chosen blade alignment has a documented tolerance of $32\mu m$ which equates to a maximum potential deviation of 0.01% chord.

The blade's 194 static tappings were concentrated in the leading edge region on the pressure

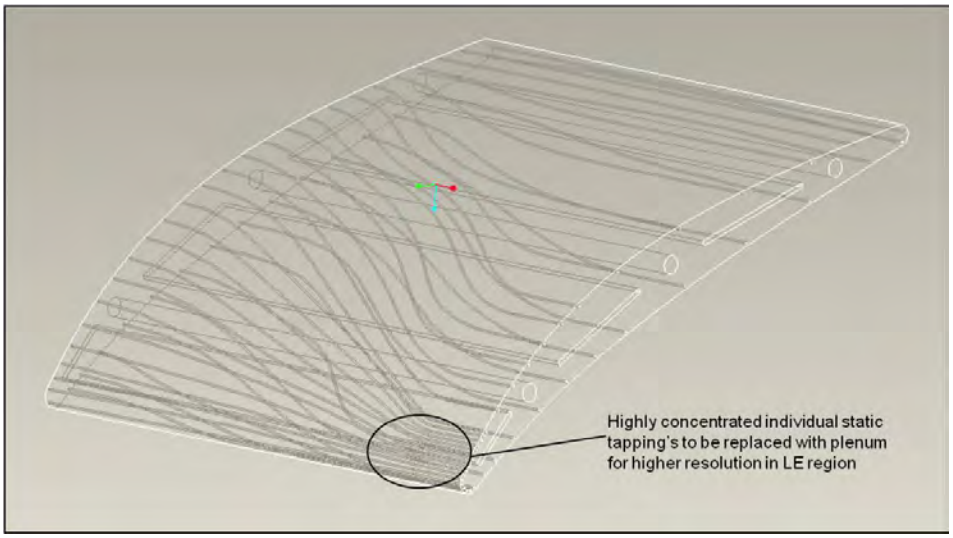

Figure 3.3: 3D CAD drawing of the static pressure tapping section of the instrumented blade

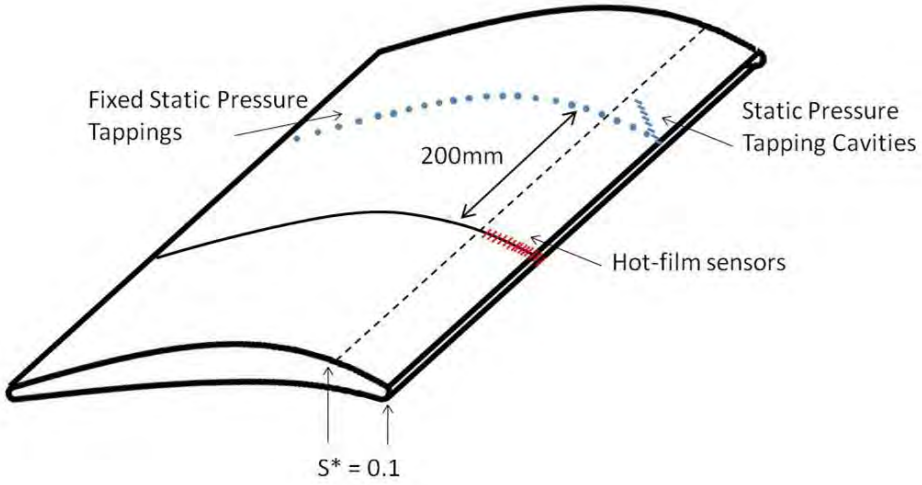

Figure 3.4: Schematic drawing of the instrumented blade showing locations of hot-film sensors and static pressure tappings

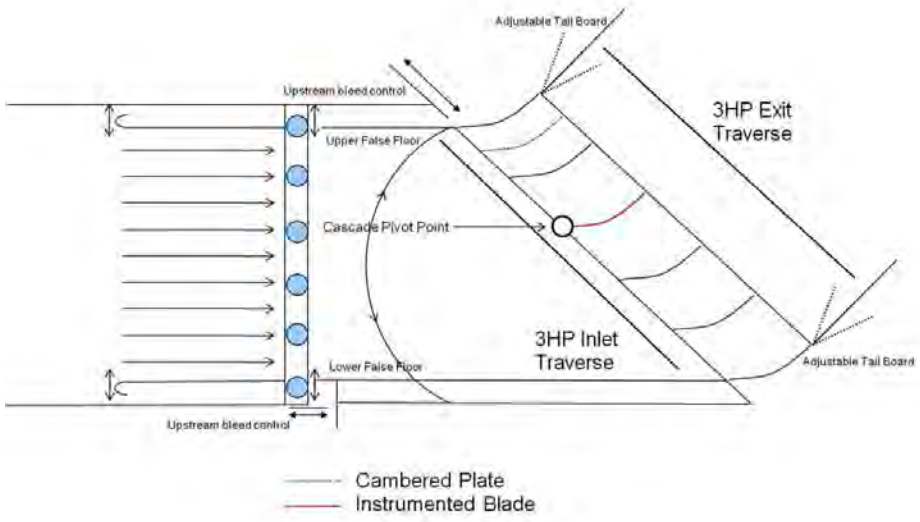

Figure 3.5: Schematic diagram of the variable incidence inlet mechanism used with the 2D compressor cascade

and suction surfaces. 157 of the tappings were within the first 15% of surface length. To fit such a large number of tapping on to the blade nine hollow cavities were created under the blade's surface. Each of the cavities had up to 15 holes drilled into it and each cavity had a single pressure line leading to a Scanivalve stepping valve and PSI pressure transducers (Section 3.5.4). The sole downfall of this technique was only one tapping could be measured in each cavity at a time and so obtaining pressure from all the cavities was time consuming.

Placing the PIV, hot-film sensors and blade static tappings on the same blade ensures that each section of the blade experiences the same inlet flow conditions and periodicity, as long as two-dimensionality is maintained in the inlet, even if the periodicity is poor (Section 3.4)

3.2.2 Variable Incidence Inlet

To allow for variations of inlet flow angle the entire cascade was rotated relative to a fixed inlet flow from the wind tunnel. A number of modification were made to the cascade itself and a new variable incidence inlet section was made (Figure 3.5 and 3.6).

As incidence is varied the effective inlet flow area changes and the inlet had to be modified to accommodate this. A system was implemented to allow the upper and lower floors of

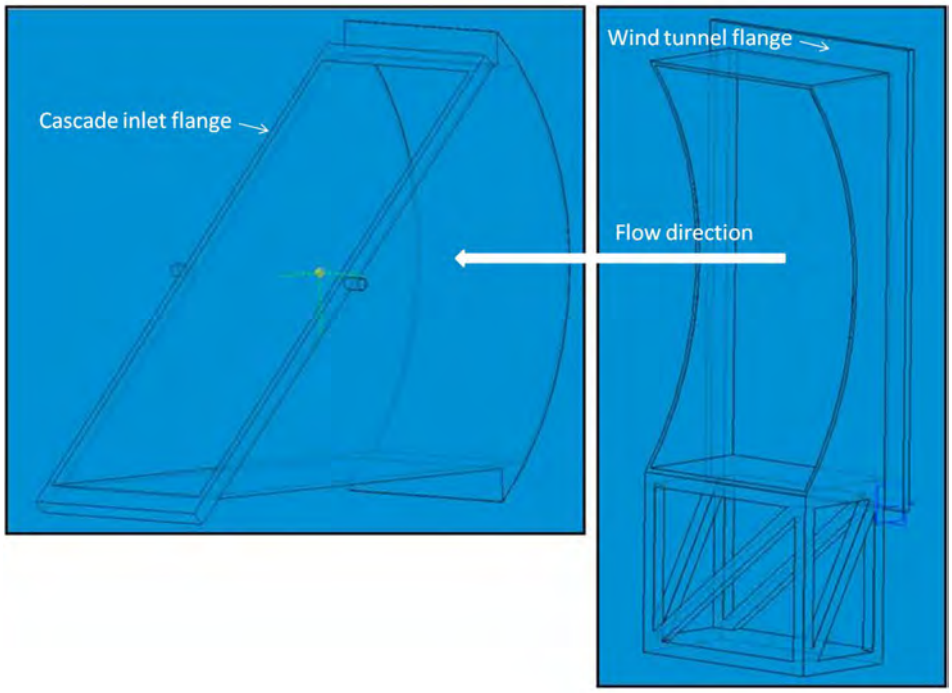

Figure 3.6: 3D CAD drawing of the variable incidence inlet mechanism used with the 2D compressor cascade

the inlet section to be controlled and to ensure the correct inlet area was maintained and that the floors remained parallel with the upstream walls of the tunnel and inlet flow.

With an increase in incidence angle the top of the cascade moves in an upstream and downward direction, whilst the bottom moves in a downstream and upward direction. The false floors had to have the capacity to extend and contract to accommodate for the streamwise movement at the top and bottom of the cascade as well a be able to move vertically. The bell mouth style inlet sections upstream of the turbulence grid remained at a fixed streamwise location but had to remain aligned with the downstream inlet section and had to move vertically as the inlet flow angle changed.

Once finalised the system allowed for quick and accurate set-up times.

3.2.3 Rotating Bar Mechanism

Unsteady flow measurements were possible using a rotating bar mechanism (Figure 3.7)which consisted of two large belts holding carbon fibre bars in a spanwise orientation which shed wakes upstream of and produced periodic unsteadiness in the stator blade row. The belts traveled through a slot in the inlet of the cascade just upstream of the blade leading edges

Figure 3.7: Photograph of the rotating bars in the cascade inlet section upstream of the compressor cascade

using a series of pulleys and an electric drive motor. The bars entered through the top of the cascade and traveled parallel to the leading edge plain. An ABS electronic variable speed drive (VSD) was used to control the frequency of the drive motor to within $0.1Hz$. Motor frequency could be easily converted to bar passing frequency. A trigger box and optical sensor were used to check the bar passing frequency and to trigger unsteady data acquisition routines. The blade passing frequency was easily altered and fixed by increasing or decreasing the motor speed using the VSD.

A derivation of stator reduced frequency is contained in Section 4.2.6 along with an description of the carbon fibre bar choice and spacing options.

3.2.4 Turbulence Generating Grid

A 2D turbulence grid (Figure 3.8) was designed and placed at the exit of the wind tunnel contraction upstream of the cascade to achieve a nominal turbulence intensity of 4.0% and $\frac{\Lambda_x}{Chord} = 0.1$ at the inlet plane of the cascade. Roache [68] shows equations 3.1, 3.2 and 3.3 can be used to determine the bar diameter and streamwise distance required to produce a designated turbulence intensity and mixing length as follows.

Figure 3.8: Photograph of the turbulence generating grid upstream of the compressor cascade

$$Tu = C\frac{x}{d}^{-\frac{5}{7}} \tag{3.1}$$

$$\frac{\Lambda_x}{d} = 0.2\frac{x}{d}^{\frac{1}{2}} \tag{3.2}$$

Equating equations 3.1 and 3.2 gives

$$\frac{\Lambda}{Chord}\frac{C}{d} = 0.2\frac{x}{d}^{\frac{1}{2}} \tag{3.3}$$

Solving for x and d gives

$$d = 0.017m$$

$$x = 1.14m$$

The nearest commercially available bar was of $d = 0.019m$ was used and thus x was corrected to $x = 1.26m$. The resulting mixing length was $\Lambda_x = 31mm$ which corresponded to $\frac{\Lambda_x}{Chord} = 0.11$ and was considered to be acceptable.

3.3 Compressor Cascade Setup

A number of specific techniques were developed during use of the 2D cascade to ensure accurate and repeatable measurements could be made throughout the experimental program. Two key parameters required attention when setting up the cascade: flow periodicity about the instrumented blade and the two-dimensionality of the flow over the blade - particularly in the adverse pressure gradient of the suction surface. During the initial stages of using the cascade a number of factors adversely effected the cascade's characteristics. As a result mechanisms were developed to control the flow through the cascade, some of which were more effective than others as will be outlined in the following section.

To obtain acceptable flow periodicity through a compressor cascade, the inlet flow leading to the cascade must have a uniform distribution of flow angle, total pressure and velocity. Once this has been achieved, obtaining good flow periodicity can still be difficult in large scale cascades with a small number of blades, given the small number of blade passages between the upper half-blade and the instrumented blade.

A number of techniques and modifications were built in to the original design of the cascade such as: trailing edge tail boards, circumferential inlet boundary layer bleeds and a perforated grid were placed over the exit of the cascade to increase the static pressure throughout the blade row to above atmospheric, however they did not provide adequate periodicity or two-dimensionality in the eyes of the author.

Problem areas inside the inlet section of the cascade were initially identified using a range of simple experimental techniques such as; surface oil die flow visualisation and wool tufts to identify regions of separated and non two-dimensional flow as well as pitot probes, traversed manually, to highlight areas of low total pressure.

As a result a number of additional modifications were made which will be outlined in the following sections.

3.3.1 Control Of Bulk Inlet Flow

Initially a forward facing step was placed at the leading edge of the false floor sections just downstream of the turbulence grid. A combination of blockage effects from the turbulence grid and a stagnation region that formed upstream of the forward facing step, which acted as a natural contraction, caused streamline curvature as the flow approached the false floor leading edges (Figure 3.9(a)). This imposed incidence onto the floors and caused significant

separations to form at the sharp leading edges which eventually re-attached to the surface of the false floors but were seen as a large loss concentration at the entrance to the cascade blade row. The streamline curvature also created a velocity profile across the grid generating a non-uniform distribution of loss which created additional non-uniformities in the inlet total pressure distribution.

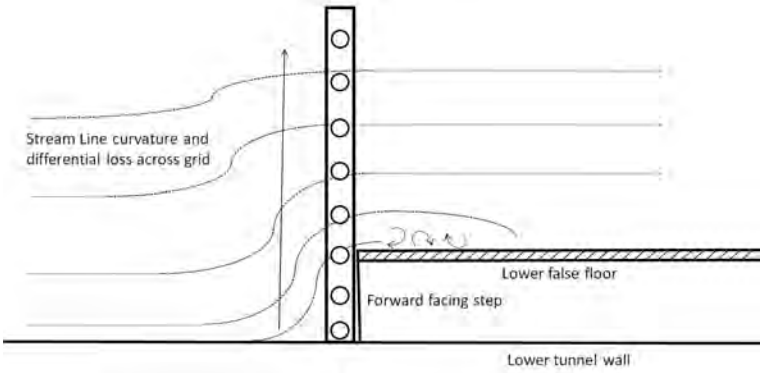

(a) Schematic diagram of the inlet to the turbulence grid with a forward facing step was present at the leading edge of the false floors in the cascade inlet.

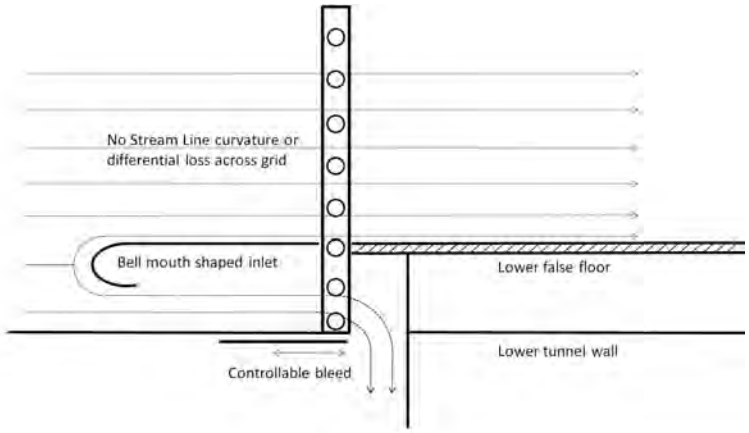

(b) Schematic diagram of the bell mouth inlet upstream of the turbulence generating grid in the cascade wind tunnel.

Figure 3.9: Schematic diagrams of inlet modifications implemented upstream of the turbulence generating grid.

A new bell-mouthed inlet section was designed to sit upstream of the false floors and turbulence grid (Figure 3.9(b)). Its purpose was to ensure parallel flow passed through the turbulence grid with an even velocity distribution onto the false floors inside the inlet and reduce the chance of a boundary layer separation forming at the leading edge of the false floors.

In the initial design a similar problem was encountered in that streamline curvature imposed incidence onto the leading edges of the new bell mouth shaped leading edges. A stagnation region formed upstream of the bell-mouth inlet as flow on the tunnel side of the inlet had nowhere to bleed off. To rectify this and move the stagnation point of the flow to the centre of the leading edge a controllable bleed slot was created between the outside surface of the floating floor and the tunnel. This would allow previously stagnant flow to escape from the tunnel and prevent a natural contraction forming upstream of the new inlet. Controlling the bleed flow rate at the top and bottom of the cascade was also used to re-distribute the inlet flow to the cascade. This proved to be a very effective control mechanism as long as separation bubbles did not form on the false floors of the inlet section. The only issue created was a reduction in the maximum mass flow rate through the cascade slightly reducing the maximum achievable Reynolds number.

Controlling the inlet flow to the cascade was most effective when using a combination of adjustable false floors, a bell-mouth inlet upstream of the turbulent grid and large bleed slots located at the top and bottom of the inlet section. By opening and closing bleed slots and aligning false floor sections the bulk inlet flow could be controlled and re-distributed to provide periodic inlet and exit flow conditions about the instrumented blade.

3.3.2 Trailing Edge Tail Boards

Two tail boards were positioned downstream of the upper and lower half-blade trailing edges. These were designed to assist with the local control of exit flow angle and static pressure at the exit of the cascade. By changing the angle of a tail board the flow at the top and bottom of the cascade is forced to follow the direction of the board in the absence of flow separation and as a result the flow in that region is also re-distributed.

The lower tail board was seen to be effective in controlling the local exit flow angle and static pressure at the bottom of the cascade, however the top tail board was not. Changing the exit flow angle alters not only streamline curvature but also the effective exit area of the cascade both of which alter the cascades exit static pressure.

Ultimately the tail boards were most effective in fine tuning the cascade rather than for large changes to the bulk flow through the cascade.

3.3.3 Top Blade Passage Loading

The suction surface of the half blade at the top of the cascade became overloaded at positive incidence and a trailing edge boundary layer separation formed. The separated flow region formed a blockage in the top blade passage which caused the bulk flow entering the top of the cascade to be re-distributed through the remaining passages and in doing so caused it to 'dive' towards the bottom of the cascade. This increased the inlet flow angle of the lower blades in the cascade, increasing their loading, and creating a pitchwise non-uniformity in inlet flow angle. This issue is seen in many, if not every, compressor cascade however it was a particularly large problem in this one as the instrumented blade was located only two passages below the top of the rig and was highly sensitive to issues in neighboring passages.

To alleviate this problem a cambered aluminium plate was inserted into the top passage to help remove loading from the top blade. This dramatically improved the periodicity of the cascade by unloading the upper half-blade and freeing up the flow in the top blade passage by suppressing the formation of a trailing edge separation.

The boundary layer on the top tail board was also separating, adding additional blockage in the top passage downstream of the blade's trailing edge. To resolve this problem holes were drilled just downstream of the tail boards leading edge. This created a series of boundary layer bleed holes in the leading edge region of the tail board significantly altering the flow over the board by removing the separated flow region. This was confirmed using flow visualisation using a cotton streamer placed near the boards surface.

Both of these techniques were seen to improve the distribution of inlet and exit flow angle in the cascade which, in turn improved the distribution of velocity in the cascade by reducing streamline curvature.

3.3.4 Circumferential Boundary Layer Bleed And Blade Tip Gaps

One issue often faced in cascades with low aspect ratios is the formation of secondary flow separations where the adverse pressure gradient of the suction surface meets the boundary layer of a cascade's side wall. In the cascade used throughout this project the blades had an aspect ratio of 2.1 however measures were still taken to try and maintain an average velocity density ratio (AVDR) of unity.

When secondary flows occur they lead to a blockage effect in the blade passage that causes a stream tube contraction of the free stream flow and a channeling of high loss boundary

layer flow towards the mid-span region of the blade. Mid-span stream tube contraction increases the free-stream flow velocity over the rear portion of the blade reducing the magnitude of the adverse pressure gradient which decreases the likelihood of a trailing edge separation forming. This can lead to a unrealistically low measurement of blade pressure loss. However, as well as contracting the freestream flow, high loss boundary layer fluid is channeled towards the mid-span of the blade and can lead to a thickening of the boundary layer and a corresponding increase in wake thickness and loss.

A circumferential boundary layer bleed was placed just upstream of the leading edge plane of the blade row and was designed to remove the thick turbulent boundary layer that forms in the wind tunnel and inlet section walls of the cascade. If this boundary layer is not removed it can lead to enhanced secondary flow separation in the end wall region of the suction surface's adverse pressure gradient. Tip gaps were also placed between the cascade end walls and the blades to allow for tip-leakage flow from the pressure surface to the suction surface which is known to significantly reduce the formation of secondary flows. The gap between the end wall and the blade measured 5mm nominally (Figure 3.7).

3.3.5 Wind Tunnel Total Pressure Distribution

The Rhoden wind tunnel at the Whittle Laboratory was used for the cascade testing as it provided the largest mass flow available (Figure 3.10). It is a duplex type tunnel, meaning two exits supplied by a single fan. A Y-junction section with a large sealing gate is located upstream of each exit contraction which acts to divert flow into one of two exits and seals the other as only one exit can be used at a time. This is excellent for space saving in a crowded laboratory but it creates some aerodynamic complications and less than ideal flow characteristics.

Firstly as the flow is forced around a bend in the tunnel streamline curvature occurs which imposes a velocity gradient across the tunnel. Directly downstream of the Y-junction was a series of honeycomb sections and meshes designed to straighten the flow and even out non-uniformities. This creates issues, similar to that experienced with the turbulence grid, when a flow with a non-uniform velocity profile passes through any grid or screen as non-uniform loss of total pressure occurs, which can result in a worsening of the total pressure distribution.

As well as creating a differential pressure drop across the honeycomb and screens the pressure gradient imposed by the surface curvature drives high loss boundary layer fluid on the top and bottom walls of the tunnel towards the inside of the bend where the static pressure

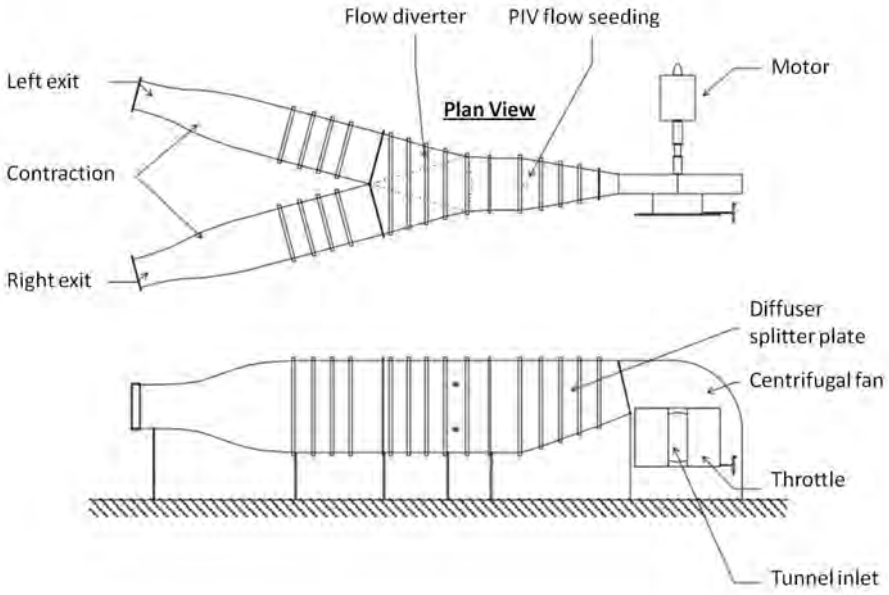

Figure 3.10: Schematic of the Rhoden duplex open circuit wind tunnel used in this research project

is low. This transport of low velocity boundary layer fluid can migrate onto the side wall of the tunnel creating a concentration of high loss fluid, which can then migrate through the contraction before entering the cascade.

The contraction then has an influence as streamline curvature once again imposes a pressure gradient on the flow. This initially drives the flow and in particular the boundary layer fluid towards the centre of the contraction. An opposing pressure gradient follows as the flow is straightened at the contraction exit. During this reversal an overturning of the boundary layer can occur and the high loss boundary layer fluid can be forced away from the surface of the tunnel forming a local concentration of high loss fluid. Figure 3.11 shows the total pressure distribution for both side of the Y-junction clearly showing symmetry between the two sides where pressure gradients are reversed in the Y-junction.

3.4 Final Flow Periodicity And Two-Dimensionality

Figures 3.12(a), 4.3(a), 3.12(c) and 3.12(e) show a high level of flow periodicity about the instrumented blade over the range of inlet flow angles tested. Each of the upstream and downstream traverse plots are normalised to the leading or trailing edges of the instrumented blade respectively and extend to half a pitch above and below this centre point.

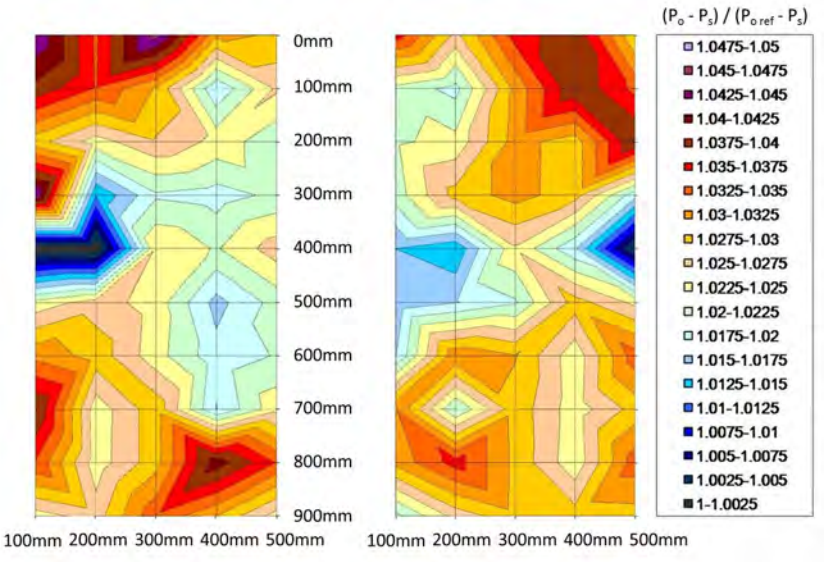

Figure 3.11: Total pressure distribution for the left hand (left) and right hand (right) exit of the Rhoden wind tunnel

This was used as initial test data to ensure that the cascade was going to be able to perform adequately.

Figure 3.12 shows that previously mentioned techniques appear to work well as initial exit traverses showed that the cascade displayed high levels of two-dimensionality.

Given the constraints imposed by the low blade count and large scale of the compressor cascade the above findings were deemed to be adequate for the experimental test program of this project.

3.5 Instrumentation

Basic flow conditions were measured using a series of pressure tappings and pneumatic probes. Three-hole cobra probe (3HP) traverses were used to perform upstream and downstream traverses of blade row to obtain loss, periodicity and flow angle data. The location of laminar-turbulent transition zone and the development of quasi wall sheer stress on the instrumented blade surface was measured using surface mounted hot-film sensors. Particle image velocimetry (PIV) was used to study how the free stream turbulent flow field was amplified and distorted in the leading edge region of the compressor blade. Hot-wire probes were also used briefly to obtain a measure of the turbulent intensity and turbulent length scale at the inlet of the cascade. A series of high resolution blade surface static tappings

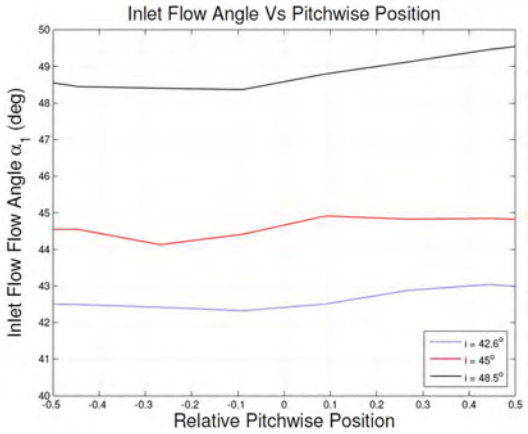

(a) Inlet flow angle distribution of the compressor cascade

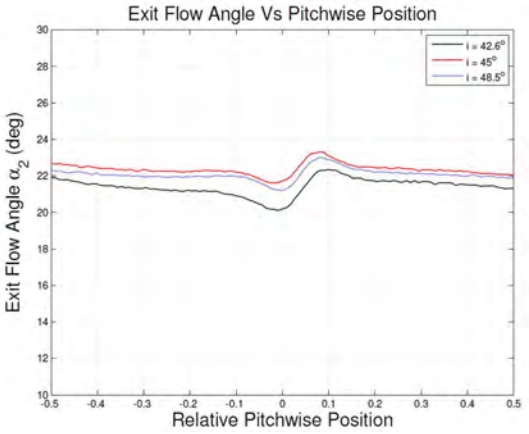

(b) Exit flow angle distribution of the compressor cascade

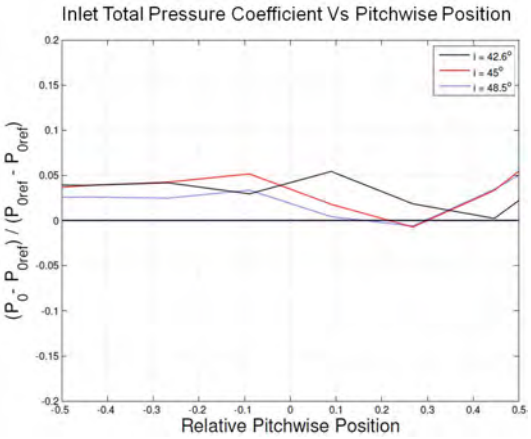

(c) Inlet total pressure distribution of the compressor cascade

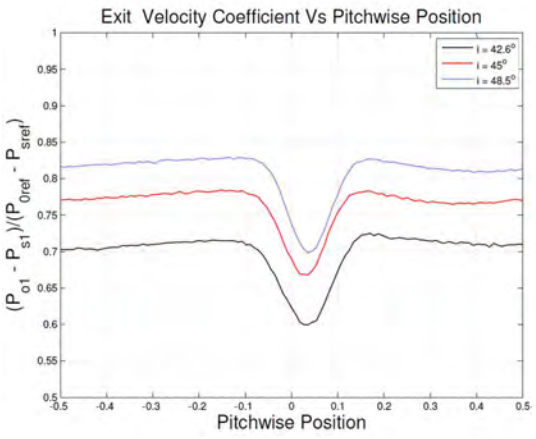

(d) Exit flow angle distribution at the inlet of the compressor cascade

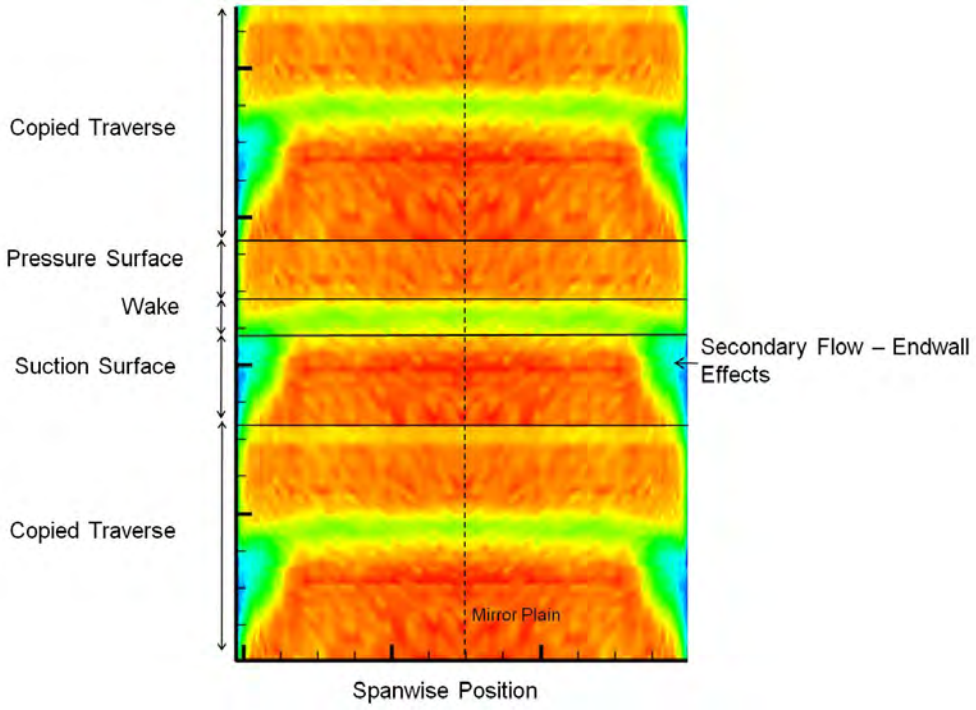

(e) Repeated and mirrored exit area traverse of velocity showing showing high levels of two-dimensionality at the exit of the instrumented blade at design incidence

Figure 3.12: Inlet and exit flow periodicity of the cascade

were used to measure the blades static pressure (Cp) and velocity distributions.

The following sections outline the specific equipment used throughout this project.

3.5.1 Thermometer

The air temperature in the aerodynamics laboratory was measured at the inlet to the compressor working section using a TempScan platinum resistance thermometer, which has a manufacturer specified accuracy of $\pm 0.01^{o}$C. The temperature probe was placed between the turbulence grid and the inlet plain of the cascade and recorded the temperature at every measurement point.

3.5.2 Multimeter

An Analogic DP100 5 (1/2) digital multimeter was used to measure the AC bridge voltages of the anemometers during hot-wire and hot-film measurements. The manufacturer specification states an accuracy of 0.45% of full scale output for AC voltages when using the $200mV$ range. The multimeter was linked and controlled using an RS-323 interface by the data acquisition and control computer.

3.5.3 Constant Temperature Anemometers (CTA)

At the Whittle Laboratory hot-film measurements were taken using a 15 channel StreamLine Research CTS system which allowed data from 15 films to be acquired simultaneously. The 15 channels were housed in three separate cabinets. Each channel passed its signal through a signal conditioner which contained high and low-pass filters, DC-offset and gain functions. The CTA's and signal conditioners were all controlled using Dantec StreamLine application software, which constitutes a full experimental platform including calibration capabilities where required and temperature compensation.

3.5.4 Pressure Transducer

All pressure measurements were obtained using a 16 port PSI NetScanner 9116 coupled with a Scanivalve 2000. The PSI allows 16 ports to be measured simultaneously at a rate of 100Hz relative to atmospheric conditions or an in tunnel reference pressure. The PSI pressure transducer acquired data at a sampling frequency of 100Hz, a sampling period of 15 s

and a settling time of 10 s was used for all measurements. Lengthy settling and acquisition times were chosen as the result of a sensitivity analysis carried out on the equipment. The PSI was coupled to a 48 port sequential Scanivalve stepping valve. Pressure values were obtained by a PC running LabView software via an ethernet connection. The Scanivalve 2000 allowed an additional 48 ports to be measured sequentially relative to a single reference pressure, which was connected in parallel with the PSI's reference pressure. The Scanivalve was also computer controlled via an RS323 connection using home and step commands built into the above mentioned LabView program. The acquisition period and settling time could be controlled for each traverse location or Scanivalve port.

The reference dynamic pressure was seen to vary by $\pm 1.5Pa$ corresponding to an accuracy of $\pm 1.4\%$ at $Re_c = 260,000$.

3.5.5 Hot-Wire Probes

During experimental testing in the 2D cascade at the Whittle Laboratory single-element hot-wire probes were used to take fast-response steady and unsteady velocity measurements. Initially hot-wires were to be used for boundary layer traverses but, due to time restraints on the project, a single probe was only used to determine the turbulence intensity at the inlet to the compressor cascade using an auto correlation technique.

The research of [7] showed that the Nusselt number could be accurately related to the Reynolds number in low Reynolds number flows $(ie. Re = 0.01 - 140)$. A functional relationship was produced to explain their experimental findings.

However, two problems were identified. One occurred at very low Reynolds numbers where natural convection can start to significantly effect the total amount of heat transfer from a wire. The second was at a Reynolds number of 44 where a discontinuity in the experimental data was identified. The discontinuity was attributed to eddy shedding and the formation of a Karman vortex street.

The original relationship formed by Collis and Williams was later improved by [94] with experimental calibration data. The modification was achieved by introducing a quadratic term and Walkers correlations can be seen below.

$$Nu \left(\frac{T_m}{T_a} \right)^{-0.17} = a \left(Re_d^{0.45} \right)^2 + b \left(Re_d^{0.45} \right) + c \tag{3.4}$$

Where T_m is the mean temperature between the wire (T_w) and the free-stream air (T_a), Re_d

is the Reynolds number based on the wire diameter d and the three constants a, b and c are determined experimentally during calibration.

The Nussult number may also be expressed as;

$$Nu = \frac{Q}{\pi L \left(T_m - T_a\right) K_a} \tag{3.5}$$

$$Nu = \frac{E^2 R_p}{\pi L \left(T_m - T_a\right) K_a \left(R_t\right)^2} \tag{3.6}$$

Where Q is the heat transfer rate from the wire to the fluid, E is the constant temperature anemometer bridge voltage, R_p is the probe operating resistance, L is the length of the wire, k_a is the thermal conductivity of air and R_t is the combined resistances of the probe forks, cables and resistors used in the anemometer bridge. All fluid properties were evaluated at the mean temperature T_m.

T_w is controlled by selecting an appropriate probe operating resistance with the anemometer.

$$R_{opp} = R_{lead} + \left(1 + OHR\right) R_{cold} \tag{3.7}$$

Where R_{lead} is the resistance of the probe leads, R_{cold} is the resistance of the wire and the probe leads in atmospheric conditions and $(1 + OHR)$ is the ratio of operating resistance to cold resistance and will be kept equal to 1.8 for all tests to achieve a $T_w \approx 180^o$.

3.5.6 Hot-Film Sensors

In all hot-film measurements TAO System Senflex Multi-Element Surface Hot-Film Sensors were used which provide a largely non-intrusive device for measuring blade surface velocity fluctuations. The substrate is made from 0.002″ thick Upilex S Polyimide film. The leads placed onto the sheet have a standard thickness of 0.0005″ and a width of 0.03″. The sensor element connected to the leads are approximately 0.004″ wide and 0.057″ long with a thickness of $0.2\mu m$.

In measurements taken in the 2D cascade at the Whittle Laboratory, 30 sensors were used, which were located between the stagnation point and just downstream of peak suction on the suction surface of the blade. These sensors gave a maximum resolution of 0.84% of surface length.

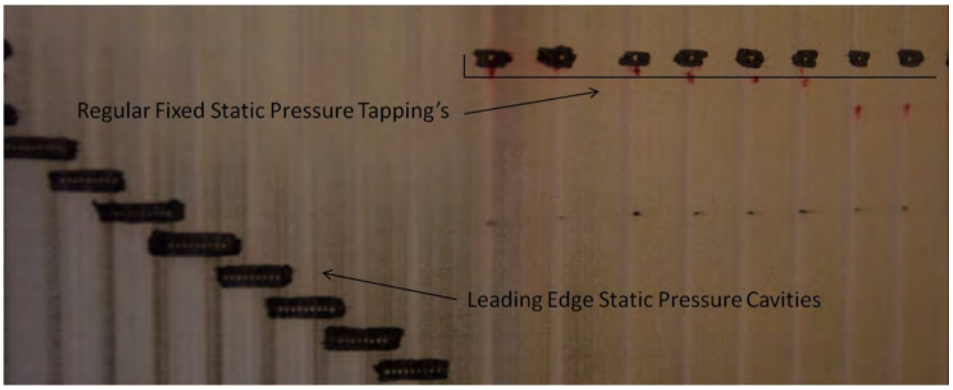

Figure 3.13: Photograph of the instrumented blades static pressure tappings in the leading edge region

3.5.7 Blade Surface Static Pressure Measurements

Surface pressure tappings were placed around the blade to measure the blade's overall static pressure distribution. Static tappings were concentrated in the leading edge where a micro tapping technique was used similar to that by [3]. 9 cavities were placed in the leading edge region, each cavity having 9 tapping holes leading to the blade's surface and one delivery tube leading to the scani-valve. Each tapping in this region had a diameter of $0.3mm$ and a centre to centre spacing of $0.6mm$ (3.13).

The method involved placing a very thin clear adhesive tape over the cavity/cavities of interest to seal all the holes (the thickness of the tape was not available). One hole was then pierced and so continuity was formed between that tapping and the scani-valve. The tape was punctured with a fine needle by eye, which proved to be a very repeatable and successful method. This procedure could then be repeated by replacing the tape and creating a new hole in a different location in the same cavity (3.14).

During a single run, 1 tapping from each of the 9 cavities could be measured and in the next run a different tapping in each cavity could be measured leading to very high resolution surface pressure distributions.

To ensure the tape had negligible influence over the blade's static pressure distribution a number of tests were repeated using the fixed tapping points both with and without tape and the values of static pressure and static pressure were extremely precise.

The step change response of each tapping was tested to ensure that a steady state pressure had been reached before the data acquisition process commenced. The waiting period was found to be a maximum of 12 seconds and to err on the side of caution 15 seconds was

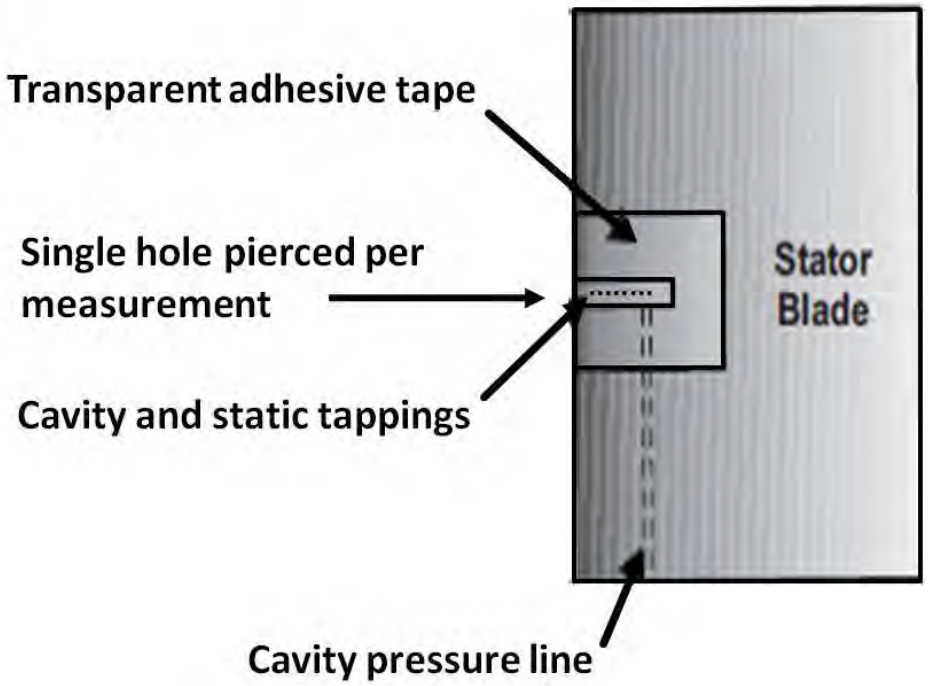

Figure 3.14: Experimental set-up for leading edge static pressure measurements

used.

3.5.8 3-Hole Cobra Probe

Two custom made three hole cobra type probes (Figure 3.15) were used at the Whittle Laboratory to measure flow angle, total pressure and dynamic pressure at a given location in a flow. Identical experimental and calibration procedures were used for both probes. The calibration technique was developed on a functional basis by considering ideal flow around a cylinder. Three functions were defined in terms of flow angle (α), probe geometry and Reynolds Number and are as follows:

$$f_1(\alpha, geometry, Re) = \frac{P_{top} - P_{bottom}}{P_{centre} - 0.5(P_{top} + P_{bottom})} \tag{3.8}$$

$$f_2(\alpha, geometry, Re) = \frac{P_o - P_{centre}}{P_{centre} - 0.5(P_{top} + P_{bottom})} \tag{3.9}$$

$$f_3(\alpha, geometry, Re) = \frac{P_{centre} - P_{bottom}}{(P_o - P_s)} \tag{3.10}$$

Figure 3.15: Picture of a 3 hole cobra probe

Given that each probe is of a fixed geometry and the probe was calibrated over a range of flow angles and Reynolds numbers the flow angle can be directly obtained from f_1 and with this coefficients of dynamic and total pressure may be determined from

$$0.5\rho U^2 = \frac{(P_{centre} - P_{bottom})}{f_3} \tag{3.11}$$

$$P_{total} = \frac{f_2 + P_{centre}}{P_{centre} - 0.5(P_{top} + P_{bottom})} \tag{3.12}$$

The probe calibration at the Whittle Laboratory was carried out in an open circuit calibration wind tunnel. Figures 3.16 - 3.18 display the calibration curves obtained from these tests. A range of flow speeds were tested around those expected during the experimental program to ensure there were no significant Reynolds number effects. The results showed very little dependance on flow speed and with stable atmospheric conditions no Reynolds number correction was required.

During the calibration process the probe was placed in a rotary traverse head identical to that used in the experimental rig. The probe was geometrically nulled to place the probe head within $\pm 0.1^\circ$ of horizontal. A reference block and a digital inclinometer were used to null all the probes.

Each of the calibration procedures were repeated numerous times to ensure good repeatability and as a result each probe is deemed to measure flow angle to within $\pm 0.3^o$ and static pressure to within 0.1% of the actual value as measured using the static tappings of a Neptune 3HP.

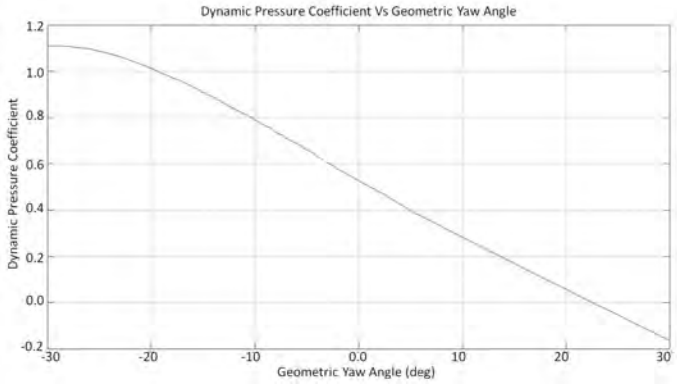

Figure 3.16: 3HP dynamic pressure calibration plot

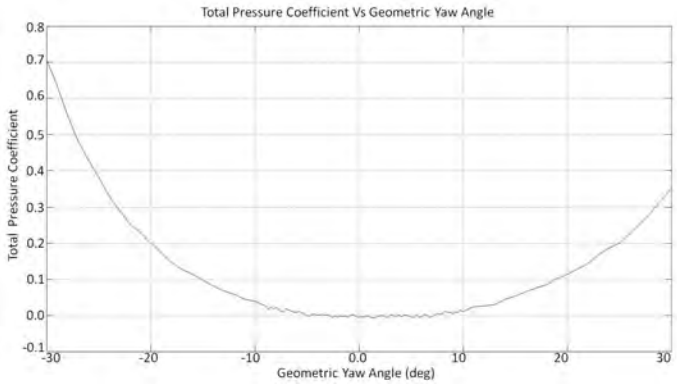

Figure 3.17: 3HP total pressure calibration plot

3.5.9 Particle Image Velocimetry (PIV)

At the Whittle Laboratory a LaVision FlowMaster PIV system was used to view the time averaged flow field in the leading edge region of the compressor cascade and provide qualitative flow visualisation images. The set-up consisted of a frequency-doubled double-pulse $120mJ$ Nd-YAG laser and a double frame 12 bit CCD camera $(1280x1024))$ array. Optical access for the camera was good for the region of interest however a laser guiding arm was used with a light sheet optical lens to deliver a sheet of laser light onto the leading edge region on suction surface side of the blade at mid-span. The laser was fired through a glass window in the base of the cascade inlet section to keep the laser and guiding arm outside

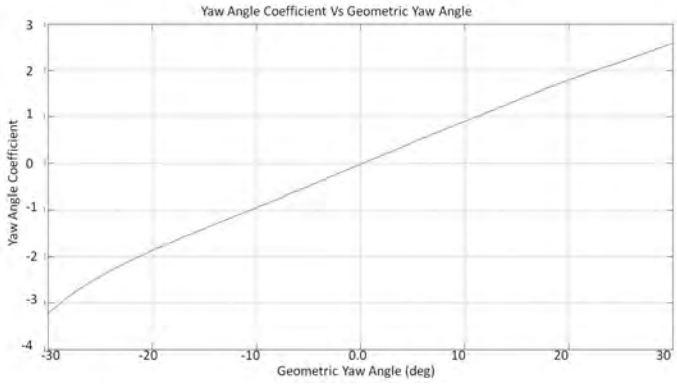

Figure 3.18: 3HP yaw angle calibration plot

the tunnel thus avoiding obstruction (Figure 3.19)

PIV was used in the suction surface leading edge region of the cascade's instrumented blade. The laser sheet was fired in the blade-blade plane at 50% span, whilst the camera was aimed, through an optical window, along the blade in a spanwise direction. The PIV interrogation window measured $52 \times 36.25mm$ and covered the first 7.5% of blade chord.

The PIV results produced both instantaneous and time averaged information about the velocity flow field as well as key properties such as $2D$ turbulence intensity and Reynolds stresses.

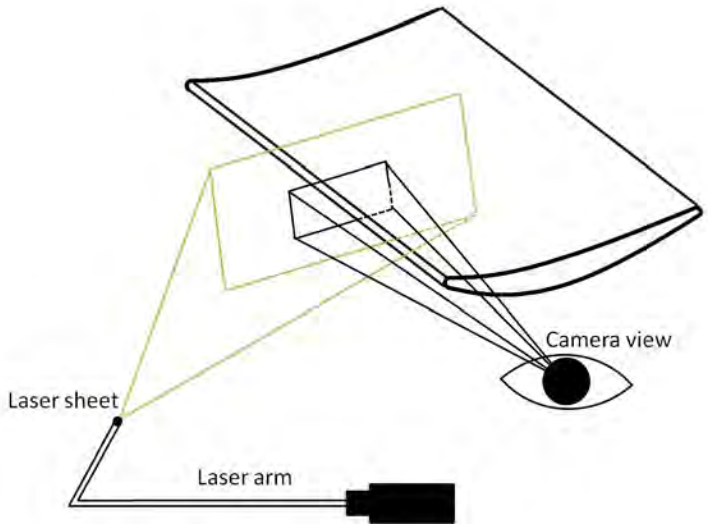

Figure 3.19: Schematic of the PIV laser and camera setup and orientation

Chapter 4

Experimental Approach

4.1 Introduction

For decades, low-speed testing has had a large impact on the direct design of the gas turbine engine. In more recent times such experimental facilities are being used as a validation tool for CFD codes and design methodologies, which has become a dominant tool in the turbomachinery design process.

It is well known that the environment created inside low-speed test facilities differ from those found inside real high speed and high temperature turbomachines, however many types of flow phenomena remain very similar in nature. Wisler [102], Wisler *et al.* [103] provide numerous examples of how low speed testing can provide detailed information on a wide range of complex flow phenomena that have been seen in real compressors and turbines. Wisler *et al.* [103] also discusses some of the limitations that are inherent in low speed testing, such as phenomena due to compressible flow effects, which cannot be accounted for. However flow in the low-pressure turbine and the intermediate and high-pressure stages in compressors is generally seen to be subsonic, where phenomena such as shock waves and associated interactions are insignificant.

4.2 Flow Environment Inside High and Low Speed Machines

In both high and low speed machines, the flow is highly complex and three dimensional, especially near the hub and the casing of the blades where secondary flow effects become more prevalent.

Secondary flows are seen as undesirable flow features and are brought about by viscous effects. Near the blade end walls, where the suction surface boundary layers often undergo a local separation upon interaction with the end wall boundary layers, the flow becomes highly three-dimensional. The separated flow regions are know as corner separations as they typically start in the corner between the hub, casing and the blade. They often propagate away from the corner towards the mid-span of the blade's trailing edge. This migration causes a variation in the amount of flow deviation in a spanwise direction with overturning occurring close to the end walls. It also creates a contraction of streamtubes in the midspan region of the blade leading to an increase in the average velocity density ratio (AVDR) [23].

A different type of secondary flow occurs in the tip gap region, between the rotor tip and the casing wall, of the rotor blades. This tip gap flow develops into a tip leakage vortex which trails the blade from the trailing edge and significantly enhances downstream mixing processes in the casing region. The tip leakage flow significantly effects corner separations and stall patterns.

There is currently a great deal of research attention in this area as both tip leakage flows and corner separations are seen to make considerable contributions to the overall loss in total pressure for a blade row. Detailed measurements by Oliver in the UTAS research compressor showed that the spanwise distribution of total pressure became increasingly non-uniform at high compressor loading and this effect was amplified near the end walls. As corner separations grow with incidence, the primary streamtube is contracted by the high loss fluid migrating towards the mid-span point of the blade. This results in a decrease in the level of diffusion across the stator blade row increasing the exit velocity at the mid-span location. A decrease in diffusion also reduces the likelihood of the flow to experience a trailing edge separation, which is to be expected at high values of incidence.

All measurements taken in this thesis were concentrated in the mid-span plan of the blade where the flow is typically free from most end wall effects (Section 3.4).

4.2.1 Differences Between Real Machines and Simplified Research Facilities

As a result of differences between low-speed research facilities and commercial multi-stage compressors and the need to best reproduce the true nature of the flow environment modifications are made to research facilities. Place *et al.* [65] looked at how the flow inside a single stage axial compressor could be made more akin to that inside real multi-stage machines. It was shown that a number of modifications could be made to the single-stage machine to improve its similarity with real machines; rows of metal teeth were attached to the hub and the casing walls to thicken the wall boundary layers, turbulence grids were added upstream of the compressor stage to raise the inlet turbulence level and pressure losses associated with downstream blade rows were reproduced with the use of a screen placed downstream of the stator blade row. A number of the modifications made were concerned with changing the behavior of the end wall flow patterns.

During the testing program in this thesis all the measurements were made at a mid-span location where flow phenomena are mostly influenced by the freestream turbulence level and the periodic passing of wakes from upstream blade rows: as a result end wall effects and corner separations are of secondary importance.

4.2.2 Inlet Free Stream Turbulence

In the large scale compressor cascade used in this thesis a turbulence generating grid was installed upstream of the blade row and was designed using correlations by Roache [68] to produce an isotropic free-stream turbulence intensity of 4.0% at the leading edge plane. The free-stream turbulence level was based on measurements taken by Camp and Shin [6] and are seen to represent the freestream turbulence level of an embedded stage of a multi-stage axial compressor.

The freestream turbulence level was confirmed to be $Tu = 4.0\%$ at the leading edge of the instrumented blade using a single element hot-wire probe and through time averaged PIV. The PIV measurements also showed that, away from the blade's surface, the turbulence was essentially isotropic in the blade to blade plane as designed [8].

4.2.3 Compressor Loading

Commercial gas turbine engines must have the ability to operate safely over a wide range of operating conditions. Cumpsty [9] identifies one of the major difficulties in compressor

aerodynamics is achieving high efficiencies at design conditions whilst maintaining satisfactory performance under off-design conditions such as at take off.

Flow incidence onto a blade row is controlled by the flow coefficient in the UTAS research compressor and this has a dramatic impact on machine performance. In the 2D cascade flow incidence was controlled by changing the geometric orientation of the blades relative to the fixed inlet flow of the wind tunnel, neglecting potential flow effects.

During the unsteady testing in the compressor cascade the flow coefficient and inlet flow angle were matched to that tested by Henderson [30] in the research compressor at UTAS.

4.2.4 Reynolds Number

Reynolds number has a large impact on the aerodynamic performance of a blade row particularly when boundary layer separation and transition are present. As a result it is important to generate Reynolds numbers as engine representative as possible in low-speed testing. The typical variation of Reynolds number inside a turbofan engine at cruise altitude can be seen in Figure 4.1, where the characteristic length is blade chord. The Reynolds number in the compressor ranges from $0.6x10^6 - 1.2x10^6$ (Figure 4.1). This is much higher than can be achieved in many low-speed research facilities. In the compressor cascade the maximum Reynolds number that can be reached is $0.4x10^6$, which brings with it criticism from some portions of the research community and, as a result, the implications of testing at low Reynolds numbers must be well understood.

Cumpsty [9] explains that all compressors rely on a turbulent boundary layer in the adverse pressure gradient of the blades suction surface to allow the flow to decelerate without the formation of a major two-dimensional separation. It is common, particularly at low Reynolds numbers, for a laminar boundary layer near the leading edge or just downstream of peak suction to separate and form a separation bubble, which is a separated region that re-attaches to the surface. Cumpsty goes on to summarise work carried out by Rhoden [67] on a cascade of C4 compressor blades at near design incidence using a range of Reynolds numbers.

It was shown that at a Reynolds number of $Re = 0.3x10^5$ a massive separation bubble is present on the suction surface with no re-attachment resulting in a large loss in blade force. By doubling the Reynolds number to $Re = 0.6x10^5$ the flow still separated past the point of peak suction, but it re-attached forming a large separation bubble. Further increasing the Reynolds number reduced the size of the separation bubble, however it was still present until a value of $Re = 4.8X10^5$ was reached, where the separation bubble was

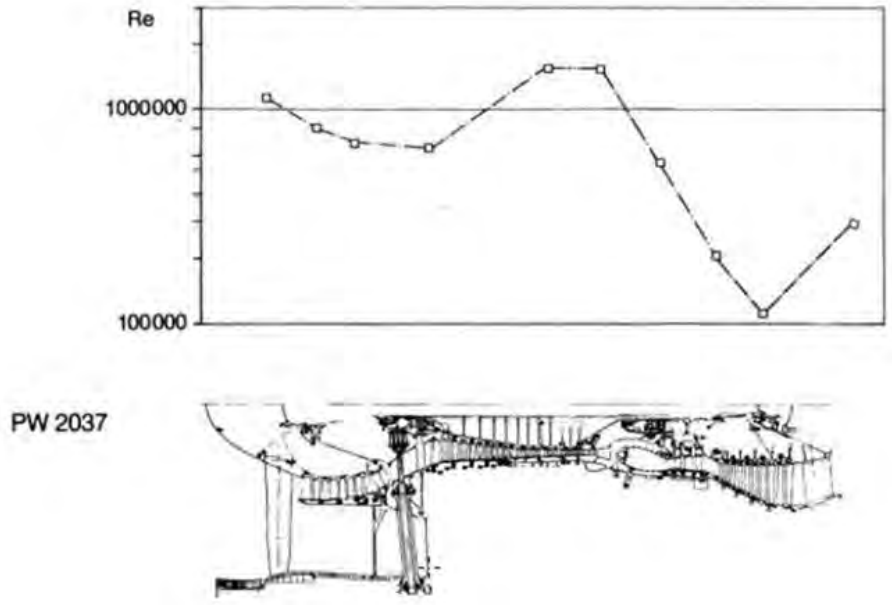

Figure 4.1: Diagram showing how the Reynolds number varies through a commercial gas turbine engine

no longer visible from static pressure distribution measurements. The Reynolds number corresponding to a significant step change in performance due to the presence of a large separation is known as the critical Reynolds number and in the study by Rhoden was seen to occur between $0.3x10^5 - 0.6x10^5$. This study showed that the effect of Reynolds number on performance decreases with an increase in Reynolds number. Hobson *et al.* [34] explained that the design point Reynolds number, based on chord, for stator $67B$ was almost $1,000,000$ but was estimated to decrease to $200,000$ at an altitude of $15,000m$. They carried out low speed testing at Reynolds number between $210,000$ and $640,000$ to look at the effect of this on the presence of separation bubbles.

If Reynolds number was further increased, the laminar-turbulent transition location moved further upstream and the turbulent wetted area over the blades surface increased. At some point the blade's loss on the suction surface also began to increase. This occurred when the benefit of having a turbulent boundary layer past peak suction is out-weighed by the increased loss inherent in a turbulent boundary layer compared to a laminar one due to increases in shear stress at the surface.

Halstead *et al.* [26] recommended that low speed testing should be carried out for stage averaged Reynolds numbers greater than $3x10^5$ and that, if this were adhered to, similar

flow phenomena would be seen in the low speed case as in the high speed case to a certain extent.

In this thesis efforts are concentrated on studying flow patterns in the near leading edge region of a blade row. When looking in this region it is common to look at the Reynolds number based on a characteristic length to the the leading edge radius. In doing this many low-speed test rigs have engine representative Reynolds numbers in this area, when the leading edge geometry is used. This was found to be the case in the research compressor at UTAS and in the cascade at the Whittle Laboratory.

4.2.5 Flow Coefficient

During unsteady operation the flow coefficient of the compressor cascade was set by varying the speed of the rotating bar mechanism for a given Reynolds number. The unsteady tests were designed to be compared with tests carried out by Henderson [30] in the UTAS research compressor and as a result the Reynolds number based on chord and flow coefficient both needed to be matched. Close to design incidence was chosen for the unsteady tests and a flow coefficient $\phi = \frac{V_{axial}}{U} = 0.675$ was required at $Re_c = 230,000$. This then remained unchanged for all unsteady tests. The reduced frequency was altered by the removal or addition of bars at different spacings to alter the bar passing frequency seen by the instrumented stator blade.

The speed of the rotating bar mechanism was controlled by an electronic VSD and checked using a trigger box, which displayed the bar passing frequency.

4.2.6 Machine Reduced Frequency

Speidel [85] was the first person to investigate the effects of periodic wake passing events on the performance of an aerofoil. The parameter called reduced frequency was developed, which correlated the profile loss of an aerofoil with frequency of wake passing without knowledge of the state of the boundary layer. The reduced frequency was defined as: a measure of the number of wake segments in a blade passage at any one time. It is thus related to the relative spacing of rotor and stator blades, the blade chord as well as the operating point of the machine and is proportional to the blade passing frequency.

For a given operating condition in the compressor cascade the values of ϕ, Re_c and α_1 are kept constant and as a result the reduced frequency can be changed only by adjusting the pitchwise spacing of the rotor and stator blade rows. The pitch of the stator blades in the

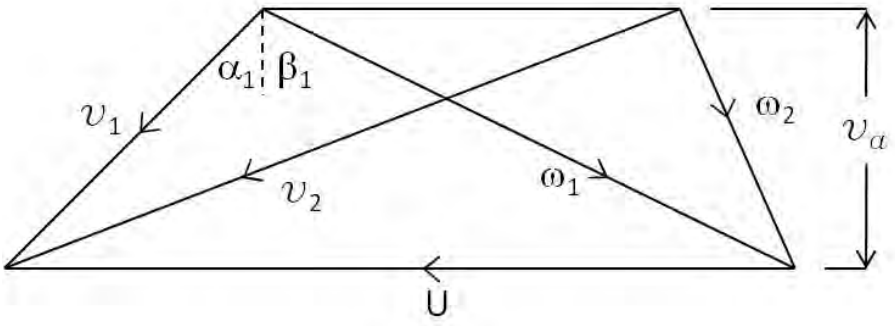

Figure 4.2: Velocity triangle for an axial compressor stage

cascade were fixed, but the spacing of the rotating bars could be changed easily and as a result this was the mechanism used to adjust the reduced frequency.

Information obtained from Rolls-Royce Plc showed that the reduced frequency of the first stator blade row of a large three spool axial gas turbine is $\omega_s = 0.84$ and that a typical target reduced frequency for an embedded stage is $\omega_s = 1$.

The unsteady portion of this project's experimental program aimed to test reduced frequencies of $\omega_s = 0.5$, 1.0 and 2. This was somewhat constrained by the available spacing of the rotating bars and the design flow coefficient chosen of $\phi = 0.675$. As a result reduced frequencies of $\omega_s = 0.47$, 0.94 and 1.88 were achieved at $Re_c = 230,000$, $\alpha_1 = 45.5^o$ and a flow coefficient of $\phi = 0.675$ which matched the conditions used by Henderson [30] inside the UTAS research compressor.

From this variation the impact of reduced frequency on the flow through a large scale compressor cascade could be examined.

The derivation of a simple expression for a stator blade's reduced frequency can be seen below.

$$\omega_S = \frac{f_r C_S}{v_1} \tag{4.1}$$

$$f_r = \frac{1}{T_r} = \frac{u}{S_r} \tag{4.2}$$

$$\omega_S = \frac{u C_S}{S_r v_1} = \frac{c_S}{s_r}\frac{u}{v_1} \tag{4.3}$$

$$\omega_S = \frac{c_S}{s_S}\frac{s_S}{s_r}\frac{u}{v_a}\frac{v_a}{v_1} \tag{4.4}$$

$$\omega_S = \sigma_S \frac{s_S}{s_r}\frac{1}{\phi}\cos(\alpha_1) \tag{4.5}$$

$$\omega_S = \left(\frac{\sigma_s \cos(\alpha_1)}{\phi}\right)\left(\frac{s_S}{s_r}\right) \tag{4.6}$$

$$\omega_S = \left(\frac{\sigma_s \cos(\alpha_1)}{\phi}\right)\left(\frac{s_S}{s_r}\right) \tag{4.7}$$

The appropriate bar diameter and spacing can then be selected to achieve the desired flow condition. Where the wake $TU = 7.0\%$ with a corresponding velovity deficit $= \frac{0.255}{V_1}$

$S_{bar} = 0.158m$ or multiples of $0.079m$, $d_{bar} = 0.055m$, $Y_{Pbar} = 0.38$, $U_{bar} = 30.9ms^{-1}$, $\phi = 0.685$

Experimental tests could then be matched to reduced frequencies typically found inside real machines.

4.3 Experimental Measurements

The following sections describe processing and data reduction techniques used through the results chapters of this thesis and create an important link between raw data obtained during the testing program and the result displayed in this document.

4.3.1 Total Pressure and Flow Angle

The magnitude and distribution of total pressure (P_o) and flow angle (α_1) provide information about the performance of axial turbomachines. Throughout the experimental program in this thesis measurements were taken using two custom made three-hole cobra type probes similar to that shown in Figure 3.15. Traverses were made at the mid-span of the cascade upstream and downstream of the stator blade row. Details of the probe can be found in Chapter 3 along with calibration information. These measurements provided information about the time averaged total pressure, velocity and flow angle distributions.

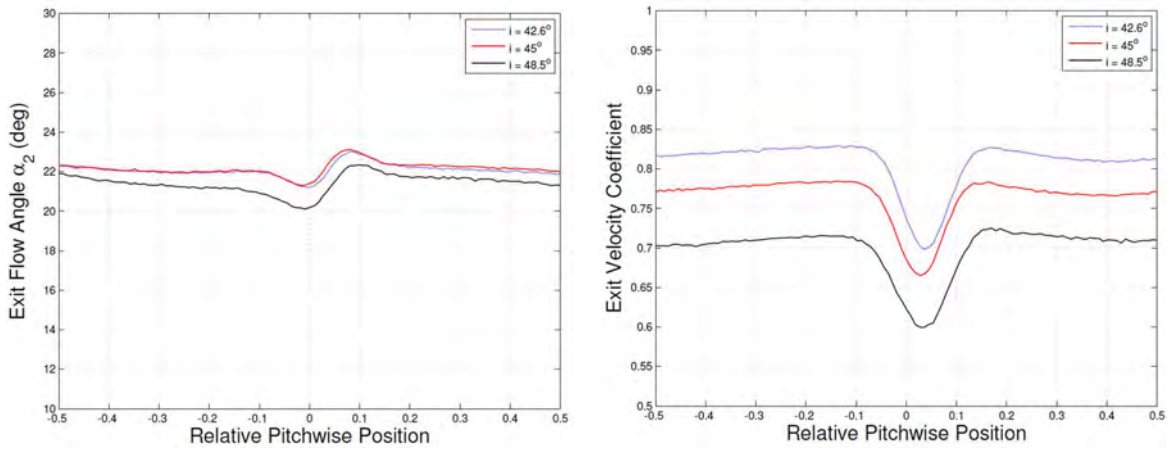

(a) Variation of exit flow angle over a single pitch normalised to the trailing edge of the instrumented blade at Re = 260,000

(b) Variation of exit velocity coefficient over a single pitch normalised to the trailing edge of the instrumented blade at Re = 260,000

Figure 4.3: 3HP traverses displaying the distribution of velocity coefficient and exit flow angle at the exit of the cascade

In the compressor cascade these measurement are particularly important as a check for periodicity. Inlet and exit traverses were carried out to ensure that flow conditions were periodic about the instrumented blade. Essentially a cascade is a simplification of an annular blade row where perfect periodicity is enforced and as a result the periodicity inside a cascade must be maintained within reasonable limits. Figures 4.3(a) and 4.3(b) show that good periodicity was achieved in both exit flow angle and exit velocity coefficient over a pitch centered about the instrumented blade and over a single pitch the exit flow angle is seen to vary by less than 0.25^o and the exit velocity coefficient by less than 2%.

Figure 4.3(b) shows that as incidence is increased the blade becomes more heavily loaded leading to an increase in the static pressure rise across the blade row. This is seen as a decrease in the exit velocity coefficient. Figure 4.3(a) shows how the exit flow angle changes with pitchwise position and changes in angle due to the velocity deficit as the wake is crossed by the probe. At $\alpha_1 = 48.5^o$ a trailing edge separation is present decreasing the exit flow angle.

All measurements were taken relative to an in-tunnel static reference pressure using a Scanivalve pneumatic switching valve. The step change response time was measured for all the ports and an appropriate settling time was chosen to ensure no transient pressures influenced the pressure readings.

4.4 Blade Surface Pressure Measurements

Time averaged surface pressure tappings are one of the most frequently used methods of determining information about the time averaged flow around a blades surface. Tappings are often used to look at general trends over the entire blade surface and are rarely used to identify specific and detailed characteristics of the flow. In this study a very large number of static pressure tappings, concentrated in the leading edge region, were used to obtain a detailed look at the static pressure distribution, which before now has not been done successfully because of spatial restraints.

Due to the large size of the blades used in the compressor cascade and the technique described in Section 3.5.7 over 25 static pressure tappings were placed in the first 7% of the suction surface, which would typically be covered by only a few tappings.

The data acquisition sampling rate was fixed at $100Hz$ over a period of 10 seconds after a settling time of 15 seconds.

At each tapping location a local static pressure coefficient was evaluated using

$$C_p\,(i) = \frac{P_{o1}(i) - P_s(i)}{P_{o1}(i) - P_{s1}(i)} = \frac{P_{o1}(i) - P_{s1}(i)}{\frac{1}{2}\rho V_1(i)^2} \tag{4.8}$$

where the subscript 1 indicates conditions at the inlet of the compressor cascade measured using sidewall static pressure tappings and the fixed pitot probe. $C_p(i)$ can then be plotted against the location of the surface tapping to provide an indication of the static pressure distribution over the blade's surface.

4.5 Time-Averaged Stator Blade Pressure Loss

The pressure loss coefficient, $\bar{\omega}$, is often used to express pressure losses found in cascades and turbomachinery stages. Pressure losses are commonly determined by evaluating the total pressure and velocity fields upstream and downstream of a blade row. A range of instrumentation can be used for this task, the most common being: hot-wire, three-hole or Kiel probes.

The approach used in this study was to measure the mid-span wake momentum thickness using a three hole cobra probe and from this a correlation could be used to determine the stator blade pressure loss. This technique was also used by Henderson [30]

Cumpsty [9] explains an empirical relation initially developed by Lieblein [49] in the 1960's. This relates the wake momentum thickness, inlet and outlet flow angles to mass averaged stagnation pressure loss for an 'unstalled' blade row and can be written as

$$\bar{\omega} = \frac{P_{o1} - P_{o2}}{P_{o1} - P_{s1}} = \frac{\theta}{S} \frac{1}{\cos(\alpha_2)} \left[\frac{\cos(\alpha_1)}{\cos(\alpha_2)} \right] \tag{4.9}$$

Equation 4.5 ignores mixing losses that occur over a considerable distance downstream of the blades trailing edge. As a result of this measurements made closer to the trailing edge of a blade may under-estimate the wake momentum thickness and as a consequence the pressure loss coefficient. The wake shape factor decreases with distance downstream of the trailing edge and will approach a value of unity as the wake completely mixes out.

Lieblein and Roudebush [50] developed a correlation for the mixed out stagnation pressure loss for an 'unstalled' blade row which are based on measurements made at an arbitrary distance downstream of a blade's trailing edge. This may be written as

$$\bar{\omega} = \frac{2\hat{\theta}_2 \cos^2(\alpha_1)}{\left(1 - \hat{\theta}_2 H_2\right)^2 \cos^2(\alpha_2)} \left[1 + \frac{\hat{\theta}_2}{2} \left[H_2^2 - \sin^2(\alpha_2) \left(H_2 - \frac{1}{1 - \hat{\theta}_2 H_2} \right)^2 \right] \right] \tag{4.10}$$

where the momentum thickness of the wake is defined as

$$\hat{\theta}_2 = \frac{1}{\cos(\alpha_2)} \left(\frac{\theta}{S} \right)_2 \tag{4.11}$$

There are a number of different ways to determine the momentum thickness of the wake. In the most basic case, where there is no wake curvature and a uniform free-stream velocity profile, the velocity deficit is simply equal to the difference between the velocity outside the wake U, which equals the inviscid flow velocity U_inv, and the velocity inside the wake u. However flows with wake curvature require a discontinuity in the inviscid velocity profile due to different free-stream velocity on either side of the wake centreline. As a result of this an assumption is made about the shape of the inviscid velocity profile using a method proposed by Walker *et al.* [96] who proposed fitting a curve to the free-stream profile on each side of the wake. These two curves were extrapolated inwards towards the wake centreline creating a separate function for U_inv. This technique was used in the current study and can be seen in Figure 4.4(a).

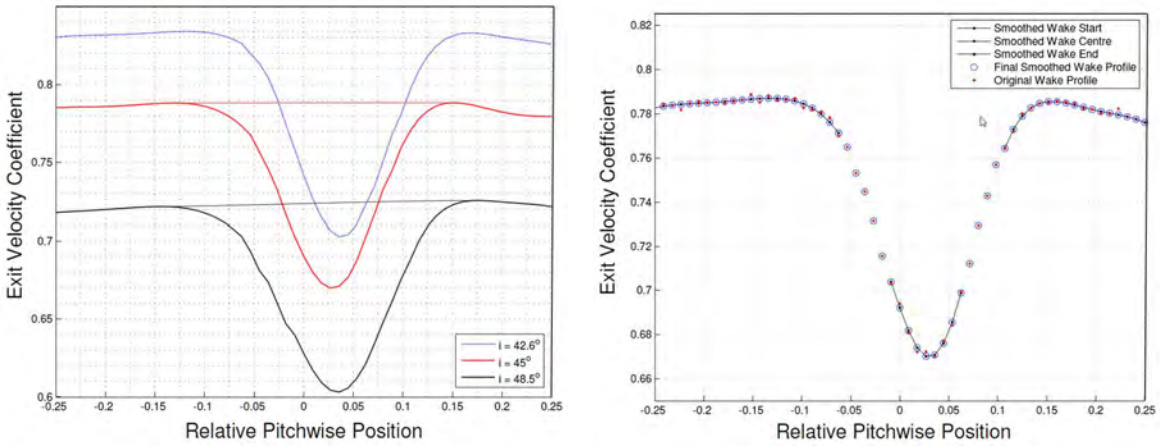

(a) Plots of the exit velocity coefficient of the wake profile and extrapolated inviscid profile at $Re_c = 260,000$

(b) Plots of the original and smoothed exit velocity coefficient of the wake profile at $Re_c = 260,000$ and $\alpha_1 = 45.8^o$

Figure 4.4: Plots showing the distribution of exit velocity coefficient used in blade pressure loss calculations

The centre line of the wake was defined as the point of minimum velocity and the extremities of the wake were defined by the point of maximum velocity on either side of the centre line as this produced the most consistent results. Some slight smoothing of the raw velocity distribution was implemented to remove spurious points that were leading to inconsistencies in the prediction of the start and finish of the wake. A typical example of the original and modified wake profiles can be seen in Figure 4.4(b).

The wake momentum thickness was evaluated using the following integration

$$\frac{\bar{\theta}}{S} = \int_0^1 \frac{\bar{u}/\bar{u}_s}{\bar{U}_i nv/\bar{u}_s}\left[1 - \frac{\bar{u}/\bar{u}_s}{\bar{U}_i nv/\bar{u}_s}\right]\cos(\alpha_2)ds \tag{4.12}$$

which is performed across a complete stator pitch at a constant axial distance downstream of the stator trailing edge. The fact that the traverse plane is not perpendicular to the wake centreline is corrected by the $\cos(\alpha_2)$ term.

Repeated measurements of blade pressure loss at various points in the loss loop presented an accuracy of $\pm 2.5\%$ when the average velocity density ratio (AVDR) for the two measurements was consistent. If the AVDR varied between two cases at a given inlet flow angle the test was repeated until a consistent value was obtained.

4.6 Presentation of Hot-film Measurements

Hodson *et al.* [39] developed a method for interpreting hot-film signal obtained without calibration by evaluating the quasi wall shear stress (τ_q), which is seen to be proportional to the actual wall shear stress (τ_w). The quasi wall shear stress is derived from the raw anemometer bridge voltage in zero flow (E_o) and under experimental conditions (E) by

$$\tau_q = \left(\frac{E^2 - E_o^2}{E_0^2} \right)^3 \alpha \tau_w = \mu \frac{du}{dy}|_y = 0 \tag{4.13}$$

The quasi wall shear stress trace can be interpreted to identify separated flow regions as well as laminar-turbulent transitional flow behavior. Solomon and Walker [82] looked into several different methods to process hot-film data on a compressor stator blade at the University of Tasmania. Of the methods tested the TERA method for determining turbulent intermittency was found to give the clearest differentiation between the laminar, turbulent and transitional flow regimes, but it required manual adjustment of the detector function threshold for each sensor in the array, which proved to be time consuming and inefficient.

Solomon and Walker [83] developed a new method for determining turbulent intermittency without the need for manual adjustment of the detector function threshold for each sensor. The method combined the probability density function (PDF) method of Hazaeika and Hirsch [28] and the peak-valley counting (PVC) method of Zohar and Ho [107]. The hybrid PDF/PVC was used in this present study to look at transitional behavior in the linear cascade over a range of incidence and Reynolds numbers. The method is summerised in the following passages [30].

Initially the quasi wall shear stress trace is classified into laminar or turbulent parts depending on the signals characteristics. A detector function is defined as the derivative of the quasi wall shear stress with respect to time $\left(D = \delta\tau_q/\delta t\right)$. The intermittency distribution is set to zero and an initial threshold for the detector function is set to $0.7\,(D)_R\,MS$. The trace is then separated into parts: where the detector function exceeds this threshold and where it does not. The parts that exceed the threshold are examined for occurrences of peaks and valleys, which are characteristic of high frequency turbulence fluctuations. Regions where peaks and valleys exist within a designated window are assigned an intermittency value of 1 and regions that lie within the threshold are assigned an intermittency value of 0. This provides an initial estimate of the intermittency distribution. Selection of the window size must take into account the sampling frequency used in data acquisition

and also the characteristic frequency of the turbulent fluctuations. A detailed discussion of window selection is given by [81].

Once an initial estimate of the intermittency distribution is known, an iterative approach is used to optimise the detector function threshold. The first stage is to calculate the PDF for the respective laminar and turbulent parts, assuming Gaussian distributions. This updated value is used to re-evaluate the intermittency distribution. The process is repeated until the threshold has converged to an acceptable level providing stable results. A relaxation factor is used to update the threshold, which aids in damping oscillations in the solution process.

The calmed flow following the passage of a turbulent spot is characterised by a higher shear stress than laminar flows. As the calming effect wears off, the shear stress reduces asymptotically to that of a laminar boundary layer. In addition to the laminar-turbulent identification, relaxing flow is assumed to occur following positive identification of turbulent flow while the shear stress is continuously decreasing. Detection of relaxing flow is terminated by the first increase in τ_q.

4.7 Blade Surface Trajectories

It is common to show time-varying quantities around a blade surface in the form of a time-distance plot. Using this approach particles or disturbances in the flow can be tracked as they convect over the blades surface. In this thesis blade surface trajectories are used to assist with the identification of temporal variations of ensemble averaged intermittency.

Time-distance blade trajectory plots of particles travelling at different fractions of the freestream velocity assist in identifying various characteristic events such as wake induced turbulent strips and turbulent spots.

The time taken for a particle to travel between two surface locations s_1^* and s_2^2, on a blades surface may be determined by integration of the surface velocity distribution. This may be expressed as

$$t = C \int \frac{1}{U} ds^*$$

and can be used to interpret the leading and trailing edge celerities of characteristic events such as the formation and convection of turbulent spots and turbulent bursts over the surface.

For this study 4 different celeritiy plots were used corresponding to $0.5xV_{\text{inf}}$, $0.7cV_{\text{inf}}$, $0.88xV_{\text{inf}}$ and $1xV_{inf}$.

4.8 Surface Oil Dye Flow Visualisation

Diesel oil was mixed with a florescent dye to create a bright paint-like liquid, which could be painted on to surfaces where flow pattern identification was required. Once painted on to a surface the oil follows the streamlines of any flow over that surface carrying the bright dye pigment with it. After being exposed to a flow the oil begins to evaporate, leaving behind the dye as a dry surface coating highlighting the streamlines and surface trajectory of the flow over the surface. UV lights can be used to bring out the dye and photographs can be taken of the surface flow patterns.

This technique is highly effective at identifying separated flow regions, however the surface must be flat as otherwise gravity can influence the distribution of dye significantly. As a result surface flow visualisation was only used in the leaving edge region of the instrumented blade where the blade's surface was kept within $\pm 5^o$ of horizontal. It could not be used at the trailing edge of the blade as the significant incline restricted the flow of dye and depicted the early and non-realistic prediction of a trailing edge separation.

4.9 Presentation of Particle Image Velocimetry (PIV) Results

1000 instantaneous image pairs were obtained for each data set to create a time average picture of the turbulent flow field in the leading edge. The raw vector fields underwent minimal pre-processing within the LaVision Flowmaster software to ensure results were not smoothed out or created by artificial extrapolation. The pre-processed image pairs were then imported into MATLAB as 1000 2D vector arrays and were initially averaged to give a single time averaged vector array of velocities across the PIV cameras field of view. In this study measurements were concentrated in the leading edge region of the suction surface and upstream there of.

The following flow field properties were evaluated:

Instantaneous velocity fluctuations - $u' = u - \bar{u}$ and $v' = v - \bar{v}$

Time averaged magnitudes of velocity fluctuation - $\overline{|u'|}$

Speed of the flow (scalar) - $U = \sqrt{\overline{u}^2 + \overline{u}^2}$

Turbulence intensity - $Tu = \frac{\sqrt{\left(\overline{u'^2} + \overline{u'^2}\right)} \times 0.5}{Speed}$

Shear strain - $\omega = \frac{1}{2}\left(\frac{dv}{dx} - \frac{du}{dy}\right)$

Turbulent kinetic energy - $TKE = frac12 \left(\overline{u'}^2 + \overline{v'}^2\right)$

Anisotropy of turbulence - $\frac{\overline{|u'|}}{\overline{|v'|}}$

Using these instantaneous and time averaged flow properties it is possible to identify how the leading edge of a compressor blade influences the freestream flow field. To accompany the processed results the PIV setup was also used to take instantaneous smoke flow visualistation images of the turbulent flow field in the leading edge region. Large concentrations of smoke were injected into the flow which was illuminated by the laser sheet allowing a photo to be taken by the PIV camera.

Chapter 5

Effect of Changing Incidence and Reynolds Number on CD Stator Blade Flow Characteristics in Steady Flow

5.1 Introduction

This chapter explores the influence of varying the chord based Reynolds number and inlet flow angle on the performance of a controlled diffusion (CD) compressor stator blade with a circular arc leading edge inside a large scale, low speed, 2D cascade. Details of the CD stator blade and the compressor cascade used in this study are outlined in Chapter 3.

The investigation aims to answer a number of questions concerning how detailed flow phenomena, that occur in the leading edge region of the blade, change with the above mentioned variations in flow conditions and influence the production of blade pressure loss.

Of particular interest is how the leading edge spike effects boundary layer transition and

separation processes and, in turn, how these lead to variations in blade pressure loss. It will be seen that these two critical parameters have a significant influence over the performance of gas turbine stator blade rows.

The effects of leading edge shape on boundary layer development has been widely investigated, however a number of questions still remain as to exactly what happens in the leading edge region of a blade where large, rapidly changing, pressure gradients are present. This chapter addresses some of these questions and shows how changing both incidence and Reynolds number affects the development of boundary layers in the leading edge region of a CD stator blade with a circular arc leading edge.

The development of blade pressure loss is also investigated and linked to flow phenomena on the pressure and suction surface of the blade.

5.2 Scope Of Investigation

In this investigation two Reynolds numbers were tested $Re_c = 260,000$ and $Re_c = 400,000$, corresponding to the maximum speed of the wind tunnel and a Reynolds number chosen, based on discussions with Rolls Royce, that was previously tested by Henderson [30] in the axial flow research compressor at the University of Tasmania (UTAS).

Although the range of inlet flow angles were limited due to constraints imposed by the experimental facilities they were able to cover the normal operating range of an embedded stator blade inside a real engine. Inlet flow angles of $\alpha_1 = 42.6^o, 43.6^o, 44.4^o, 45^o, 45.8^o, 46.2^o, 47.4^o, 47.75^o$ and 48.5^o were tested at both Reynolds numbers. The range of angles tested are not equispaced as when setting the inlet flow angle the cascade a one degree increase in the cascades geometric orientation did not correspond to a one degree increase in inlet flow angle and a series of repeat tests we conducted where inlet flow angles could not be matched perfectly.

At the highest inlet flow angle the blades experienced a trailing edge separation, which indicates the blade is close to the point of stalling and would no longer be in a safe point of operation in a real engine. The design inlet flow angle for the CD stator blade is $\alpha_1 = 45^o$.

The point $S^* = 0$ corresponds to the centre of the leading edge circle with the suction surface denoted by positive values of S^* and the pressure surface by negative values.

In the leading edge region of the blades suction surface between $S^* = 0 - 0.07$, twenty five static pressure tappings with a spacing of $S^* = 0.002$ were used to give a very high resolution plot of the static pressure coefficient (Cp) distribution. On the remainder of

the suction surface static pressure tappings were spaced with $S^* \leq 0.02$ upstream of peak suction and $S^* \leq 0.09$ between peak suction and the trailing edge. The maximum static pressure tapping spacing on the pressure surface was $S^* \leq 0.12$.

Fifteen hot-film sensors were also mounted in the leading edge region of the instrumented blade with the first film located $S^* = -0.0214$ past the stagnation point on the pressure surface and the final film located at $S^* = 0.0959$ on the suction surface. All of the films had a consistent spacing of 2.54mm corresponding to $S^* = 0.008$.

Data from all 15 films were acquired simultaneously by 15 constant temperature anemometers at a rate of 60kHz and low pass filtered at 30KHz. Processing of the hot-film data produced a range of results such as time average turbulence intermittency (γ), time averaged quasi wall shear stress and time resolved raw traces of quasi wall shear stress, which can be used to track events convecting along the blades surface. $\gamma = 1$ corresponds to a fully turbulent boundary layer and $\gamma = 0$ indicates a laminar boundary layer.

The following sections will use the previously mentioned experimental techniques to explain how performance characteristics of a CD stator blade with a circular arc leading edge profile change with Reynolds number and incidence as well as comparing the experimental findings with predicted results from the well known CFD solver used in current industrial turbomachinery design processes - MISES.

5.3 General Trends In The Static Pressure Coefficient Distribution.

The current body of knowledge in the turbomachinery field has lead us to a good understanding of how a blade, with circular arc leading edges, should react to changes in inlet flow angle and Reynolds number. These typical changes and trends will be used, initially, to demonstrate a high level of confidence in the results obtained during this experimental program and will provide a detailed picture of how such a blade reacts to test conditions outlined in Section 5.2.

The CD stator experiences an incidence dependent leading edge velocity over-speed on both suction and pressure surfaces. At low inlet flow angles, considered to be those below the design operating point and identified as negative incidence, a large velocity spike is seen on the pressure surface of the blade and at high inlet flow angles, considered to be those higher than the design operating point and identified as positive incidence, an over-speed is seen on the suction surface.

When the inlet flow angle is increased from negative to positive incidence both Reynolds

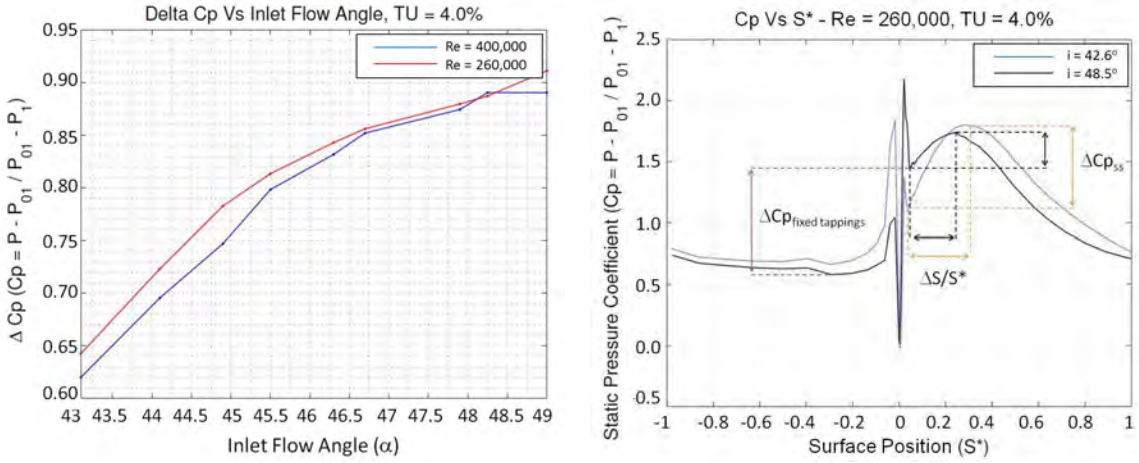

(a) (b)

Figure 5.1: Influence of inlet flow angle on a change in Cp measured from two fixed static pressure tappings located on either side of the blade's leading edge $(left)$. Cp distribution at the minimum and maximum inlet flow angles tested $(right)$.

numbers tested produced a gradual change in spike height, with the pressure surface spike decreasing in size as the suction surface spike increases (Figure 5.2).

Increasing the inlet flow angle results in peak suction moving upstream, shortening the length over which the favorable pressure gradient can influence and potentially stabilise the boundary layer. This is coupled with a decrease in the value of Cp at peak suction. The point of minimum Cp, or trough, directly following the leading edge velocity spike increases in magnitude with incidence further reducing the slope of the favorable pressure gradient leading to peak suction (Figure 5.1(b)). Reducing the inlet flow angle has an overall effect of elongating the surface length leading to peak suction and increases the favorable pressure gradient. The effect of this trend on boundary layer development will be discussed further in Section 5.5.2.

A corresponding trend can also be shown using differences between the value of Cp at two fixed tappings located either side of the leading edge stagnation point. The blade can then be used in a similar fashion to a wedge type pressure probe. The fixed locations are shown in Figure 5.1(b) and were chosen to lie in locations where Cp is least sensitive to small changes in surface location. Figure 5.1(a) displays how the magnitude of ΔCp varies with inlet flow angle. Values of ΔCp can be calibrated against $3HP$ inlet traverses and the blade can then be used to measure, or verify, the inlet flow angle to the cascade in future tests. During this body of work this technique was not used.

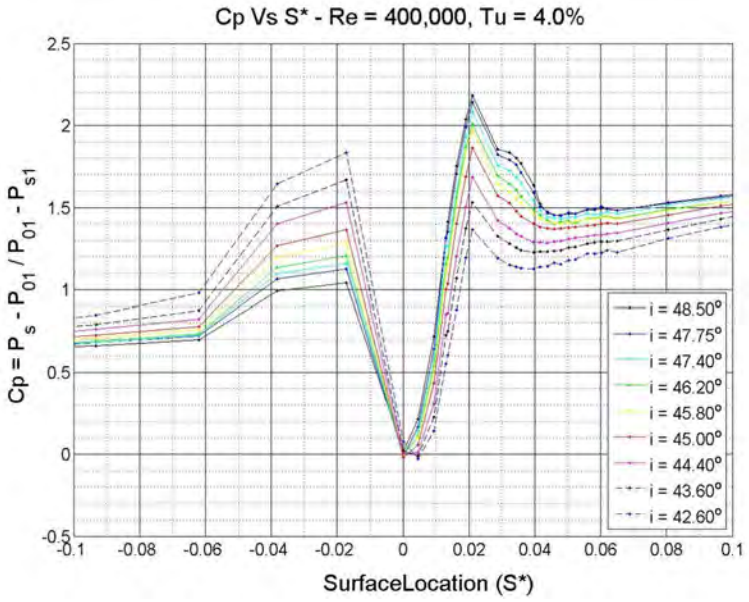

Figure 5.2: Static pressure coefficient (Cp) distributions at $Re_c = 400,000$ over a wide range of inlet flow angles

5.4 The Leading Edge Velocity Spike

Figures 5.2 and 6.8(b) indicate considerable differences in the shape of the Cp distribution with incidence and also with Reynolds number respectively. This is especially evident at high inlet flow angles but can also be seen at moderate values of positive incidence. Of particular interest to this study is how the shape of the leading edge spike changes as the flow decelerates rapidly beyond its peak value and the boundary layer becomes highly susceptible to separation and rapid transition. Downstream of this region the pressure gradient shifts from having an extreme adverse gradient, to a substantial favorable one, over a very short surface length $(S^* = 0.04 - 0.05)$. A separated boundary layer re-attaches to the surface in this region, by means of turbulent entrainment, or due to forcing by changes in the pressure gradient.

At values of inlet flow angle between $\alpha_1 = 42.6^o$ and the design point $\alpha_1 = 45^o$ the static pressure distributions are essentially independent of Reynolds number. The only apparent difference is a small change in spike height, which is believed to be caused by slight changes in the flow distribution of inlet flow upstream of the blade row (Section 3.2). Increasing the inlet flow angle past $\alpha_1 = 45^o$ to the maximum achievable value of $\alpha_1 = 48.5^o$, makes trends in the leading edge region of the suction surface become increasingly more sensitive to changes in Reynolds number. This Reynolds number dependency is mostly due to the formation of a leading edge separation bubble.

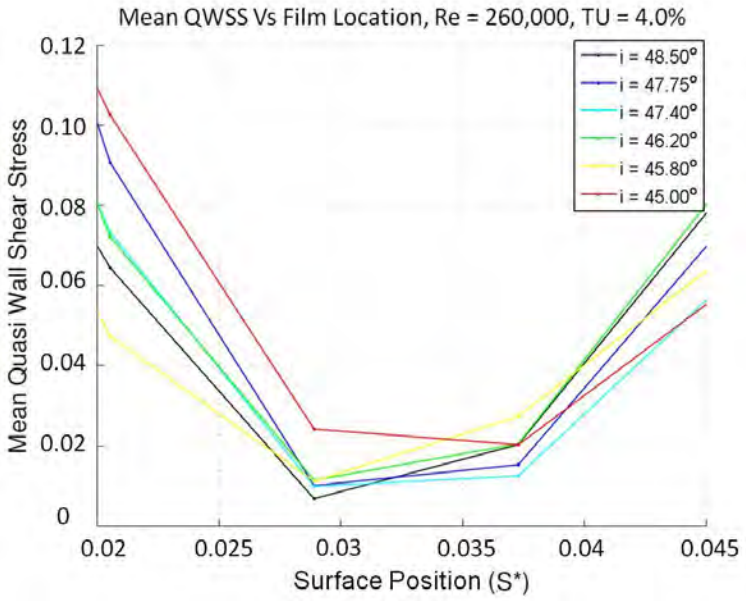

Figure 5.3: Time averaged quasi-wall shear stress in region where leading edge separation bubbles are seen to form at $Re_c = 400,000$

Figure 5.3 shows that as the inlet flow angle is increased past $\alpha_1 = 45^o$ there is a significant decrease and subsequent asymptote in the minimum value of quasi-wall shear stress, indicating that the boundary layer has separated from the surface. It must be noted that, in all cases, the rapid deceleration in the leading edge over-speed will cause a sharp decrease in quasi-wall shear stress, which could be mistaken for a separated boundary layer. It is thus critical to identify a sharp decrease in the minimum value of quasi-wall shear stress that does not change with an increase in incidence. Evidence of the boundary layer separation is also supported by Figure 5.6(a), which show that the quasi wall shear stress (τ_q) approaches zero at $S^* \approx 0.029$. From Figure 5.5 it is also clear that, at both Reynolds numbers following $S^* = 0.029$ the static pressure plateaus, indicating that the boundary layer has separated from the surface.

Goodhand and Miller [22] developed a criterion to determine whether the boundary layer separates in the leading edge region, drawing the initial point of transition upstream of peak suction. It is based on the change in Cp during the deceleration of the velocity over-speed. A value of $\triangle Cp$ was obtained between the peak value at the top of the velocity over-speed and the minimum value in the leading edge region downstream of the spike. They showed that if $\triangle Cp \geq 0.5$ the boundary layer was seen to separate and subsequently undergo transition. Results from the present study found that all cases where a separated boundary is evident have a $\triangle Cp \geq 0.5$ and when $\triangle Cp \leq 0.5$ the boundary layers appears to remain attached to the surface. This is not a hard and fast rule but merely an additional

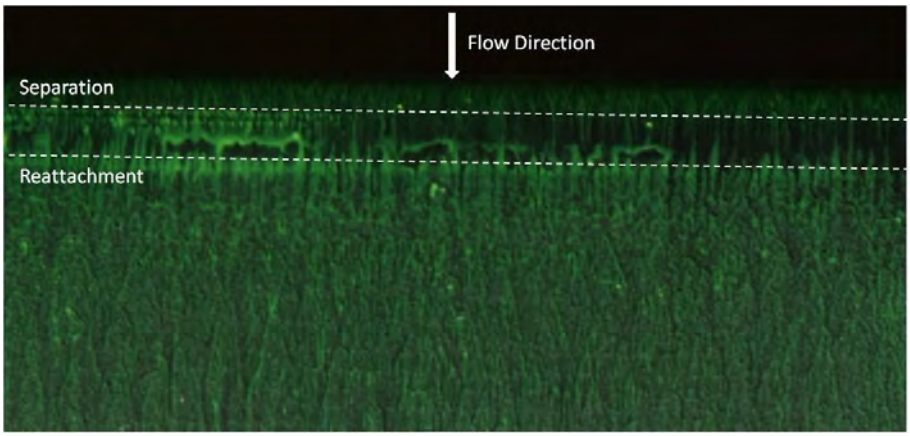

Figure 5.4: Suction surface flow visualisation showing a leading edge separation bubble at positive incidence and $Re_c = 260,000$

guide to aid the interpretation of results. Direct evidence of a separation bubble can be seen in Figure 5.4.

Downstream of the separation location $(S^* \simeq 0.029 - 0.06)$, the Cp, intermittency and τ_q distributions are clearly dependent on both Reynolds number and inlet flow angle and differ considerably from one another (Figures 5.5, 5.6(a) and 5.6(b)). Figure 6.8(b) shows the length of the leading edge separation bubble is clearly shorter at $Re_c = 260,000$. The separation location of the bubble is taken from just upstream of the point where the static pressure distribution begins to plateau and the reattachment location from where the pressure gradient begins to resume its strong adverse gradient. Although the point of separation does not alter significantly with a change in Reynolds number, the re-attachment point does. This is understandable as at a higher Reynolds number the boundary layer is going to lead to a more rapid transition process. More turbulent entrainment will occur at the edge of the separated shear layer forcing the bubble back towards the surface over a shorter distance than in the lower Reynolds case.

The accuracy of this technique is limited by the resolution of the static pressure tappings on the suction surface, however results agree closely with predictions of MISES that will be discussed in Section 6.2.3.

This region covers the extent of the separation bubble at high values of positive incidence and has been the subject of much discussion over the years. Denton [13] has also indicated leading edge separation bubbles are responsible for the highest amount of loss per unit area on a blades surface, which makes understanding any differences and their consequences very important.

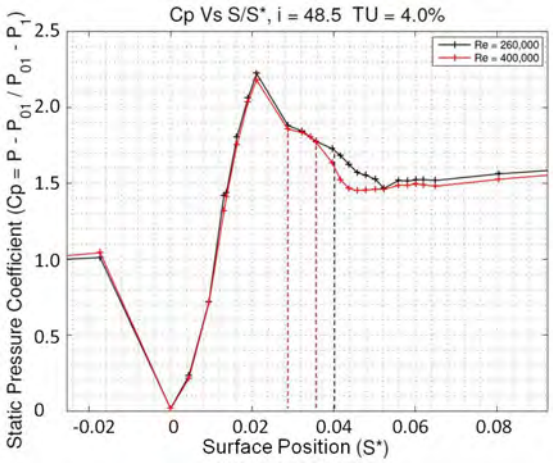

Figure 5.5: Time averaged leading edge static pressure coefficient (Cp) distribution with the separation, transition and reattachment locations

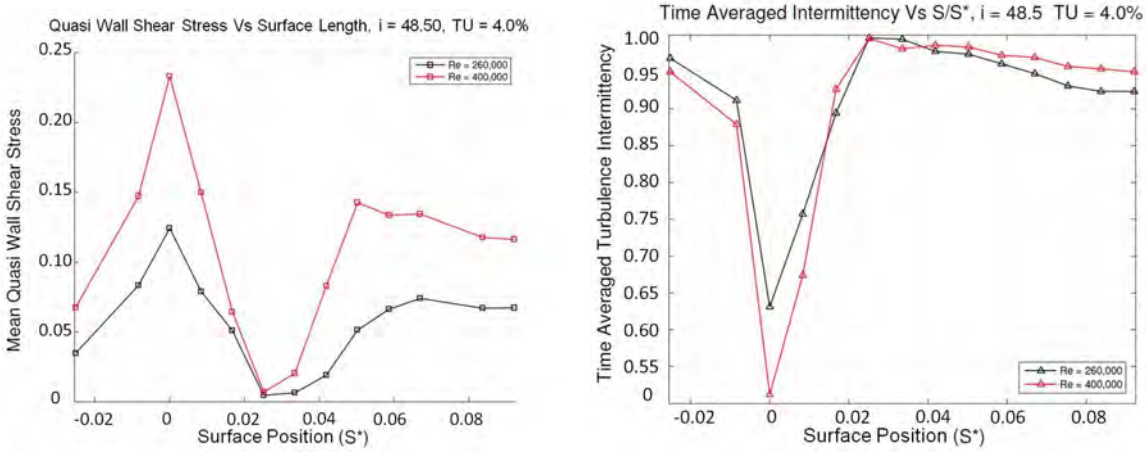

(a) $\alpha_1 = 47.75^o$ (b) $\alpha_1 = 48.5^o$

Figure 5.6: Leading edge distribution of time averaged quasi-wall shear stress (a.) and turbulent intermittency (b.)

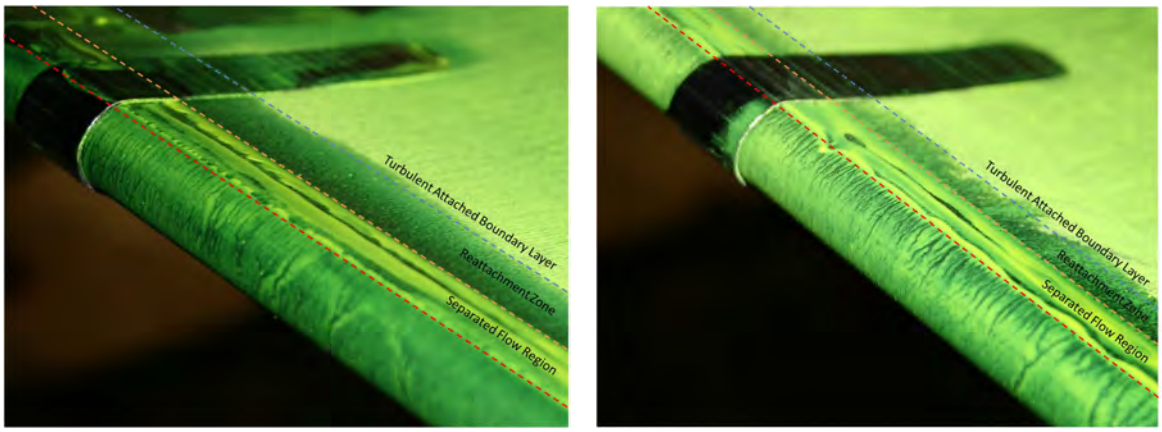

(a) $Re_c = 260,000$ and negative incidence

(b) $Re_c = 400,000$ and positive incidence

Figure 5.7: Surface flow visualisation images of a pressure surface leading edge separation bubble

The spacing of static pressure tappings, particularly on the pressure surface, does not fully resolve the leading edge velocity spike. As a result it is expected that the peak value of the velocity over-speed is severely underestimated and at high values of negative incidence a plateau in the Cp distribution is likely to occur in the decelerating region of the spike indicative of the formation of a separation bubble.

On the pressure surface of the blade, a leading edge separation bubble forms at all values of incidence tested and is highly Reynolds number dependent, especially at negative incidence. Direct evidence of a pressure surface separation bubble can be seen from surface oil flow visualisation shown in Figures 5.7. The images were taken with the cascade set at negative incidence as this is where the largest pressure surface separation bubble will occur. Comparing the image taken at $Re_c = 260,000$ and that taken at $Re_c = 400,000$ clearly demonstrates the effect that Reynolds number has on leading edge separation bubbles. A clear reduction in the length of the separated flow region can be seen.

It is well known, from previous studies, that the boundary layer on the pressure surface of a circular arc CD stator blade transitions to a fully turbulent state in the presence of a separation bubble near the leading edge [30, 31, 22]. Once turbulent, the boundary layer remains in this state along the entire length of the pressure surface as there is no favorable pressure gradient to relaminarise it or cause it to separate at the trailing edge. As a result of this, the leading edge spike region and the separation bubble are likely to be determining factors when looking at the effect of the pressure surface boundary layer on a CD stator blade's performance at negative incidence.

At large values of negative incidence the suction surface spike is small but there is the

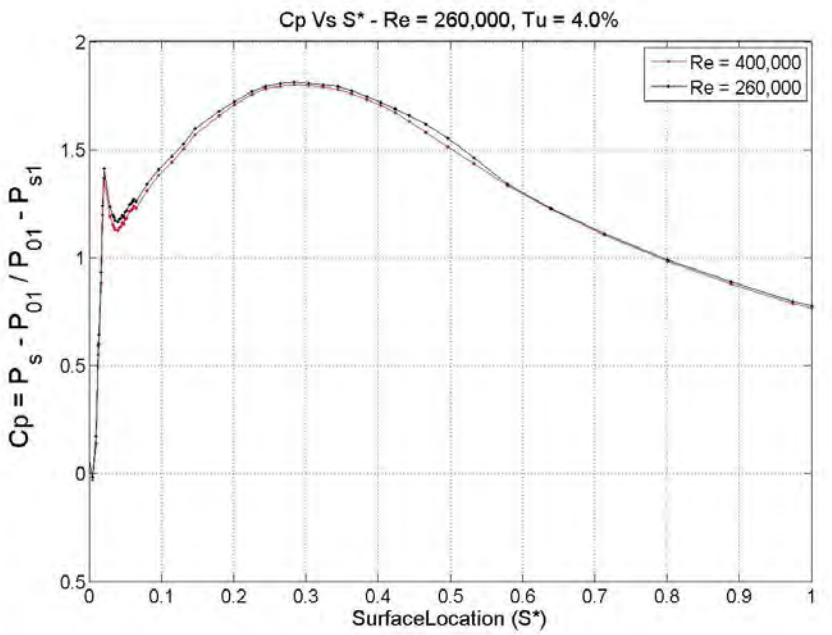

Figure 5.8: Suction surface Cp distribution at negative incidence indicating the formation of a separation bubble at $Re_c = 260,000$ downstream of peak suction

strongest acceleration leading to peak suction. This results in a laminar boundary layer existing from the leading edge to peak suction. Previous studies have shown that as this laminar boundary layer meets the adverse pressure gradient following the point of peak suction it is unable to remain attached to the surface and forms a separation bubble inside which, the boundary layer becomes highly unstable and undergoes rapid transition. It is through vigorous entrainment of turbulent flow, inside the separated flow region, during the transition process that the boundary layer is driven back towards the surface forming a separation bubble.

This type of transition process has been seen on low pressure turbine blades many times before [39]. Evidence of such a separation bubble can be seen for the $\alpha_1 = 42.6^o$ and $Re_c = 260,000$ case, by means of a perturbation in the static pressure distribution down stream of peak suction (Figure 5.8). The difference between this case and that a the high Reynolds number is clearly visible as the latter does not show signs of a separation bubble.

5.5 Distribution of Turbulent Intermittency and Boundary Layer Development

Solomon and Walker [83] developed a new method for determining turbulent intermittency without the need for manual adjustment of the detector function threshold for each sensor. The method combined the probability density function (PDF) method of Hazaeika and Hirsch [28] and the peak-valley counting (PVC) method of Zohar and Ho [107]. The hybrid PDF/PVC was used in this present study to look at transitional behavior in the linear cascade over a range of incidence and Reynolds numbers (Section 4.6). The code bases its calculation on raw traces of quasi-wall shear stress ($\tau_q = \left(\frac{E^2 - E_o^2}{E_0^2}\right)^3$). The traces are also useful in providing confidence in the code and identifying turbulent events that convect over the blades surface (Figure 5.15).

At negative incidence, upstream of the pressure surface velocity spike which will be large, elevated levels of intermittency can be seen in the stagnation region (Figure 5.11(a)). The minimum inlet flow angle obtainable is not extreme, however a large velocity over-speed is created, leading to very high and rapidly changing levels of shear strain. The leading edge region of compressor blades can contribute to the amplification and distortion of background turbulence generated by the turbulence generating grid (Section 2.5). As the flow accelerates rapidly, from stagnation through the velocity over-speed, the boundary layers intermittency level decreases from $\gamma \simeq 0.6$ to 0.

When the plot of time average intermittency is compared with that of Cp, it appears that the final film, on the pressure surface, is located in the decelerating portion of the velocity spike, which is not, in fact, the case. This is due to the lack of static pressure tapping resolution in this region as explained in Section 5.4.

Increasing the inlet flow angle to $\alpha_1 = 45.0^o$ results in the level of intermittency at the leading edge of the pressure surface gradually decreasing until the boundary layer is almost completely laminar between the stagnation point and the last film located at $S^* = -0.0214$. The velocity over-speed and corresponding levels of shear strain are significantly smaller at design than they are at high values of negative incidence and this plays a key role in the identified changes in intermittency.

Further increases in incidence past design bring about an increase in intermittency but the increase is first seen at a location downstream of the leading edge velocity spikes peak value. For $\alpha_1 = 46.2^o$ to $\alpha_1 = 48.5^o$ elevated levels of intermittency begin to move upstream towards the stagnation point, through the favorable pressure gradient of the pressure surface velocity spike (Figures 5.11(g) and 5.11(i)). At $\alpha_1 = 48.5^o$ the boundary layer is seen to

have an intermittency value of $\gamma = 0.9$ with in $S^* = 0.005$ of the blades stagnation point and reaches a value of 1 a short distance downstream this location.

At positive incidence the pressure surface velocity spike is small. As a result the strong favorable pressure gradient, in the first portion of the spike, acts over a very short surface length and has little effect on stabilising the boundary layer. These trends can be seen in Figures 5.10 and 5.11.

Elevated levels of intermittency in rapidly accelerating and extremely thin boundary layers close to a blade's leading edge is currently a key research topic in the turbomachinery field [14, 36, 37]. Previously literature has lead to the belief that between the stagnation point and the peak value of the velocity over-speed ($S^* \simeq 0 - 0.02$) the boundary is laminar and separates, as such, shortly after the rapid deceleration of the velocity spike commences.

Figures 6.8(b) and 5.6(b) display a trend contrary to this popular belief. At high incidence the level of turbulent intermittency is seen to rise rapidly as the flow accelerates through the velocity over-speed, which has previously been seen to help maintain a laminar boundary layer. As the peak in velocity is reached, the calculated value of turbulent intermittency approaches unity. The flow then encounters the extreme adverse pressure gradient where the boundary layer reaches an intermittency value of $\gamma = 1$, separates from the surface and forms a separation bubble.

By increasing α_1 from 47.75^o to 48.5^o there is a significant increase in high frequency disturbances in the raw quasi-wall shear stress traces at the blades leading edge (Figure 5.9). Such disturbances could well be caused by free-stream, surface normal or streamwise velocity perturbations impinging into the extremely thin laminar boundary layer in the stagnation region. It is unlikely that a turbulent boundary layer could be sustained in such a region due to its strong favorable pressure gradient and extremely small value of Re_θ [1, 53]. As a result the boundary layer may indeed appear to be turbulent, but could well be a thin laminar boundary layer experiencing a large number of external influences from the free-stream.

High levels of instability in a separated shear layer are known to promote a rapid transition process. Significant amounts of turbulent entrainment following the transition process drives the boundary layer towards the surface closing the bubble. In the current situation it is possible that, if the boundary layer is in a turbulent state before the deceleration of the spike, turbulent entrainment might not be the only driving force behind the re-attachment process, particularly at very high values of incidence and low Reynolds numbers. Turbulent entrainment will be occurring in the separated shear layer, however the re-attachment process may be assisted by changes in the pressure gradient from extremely adverse to

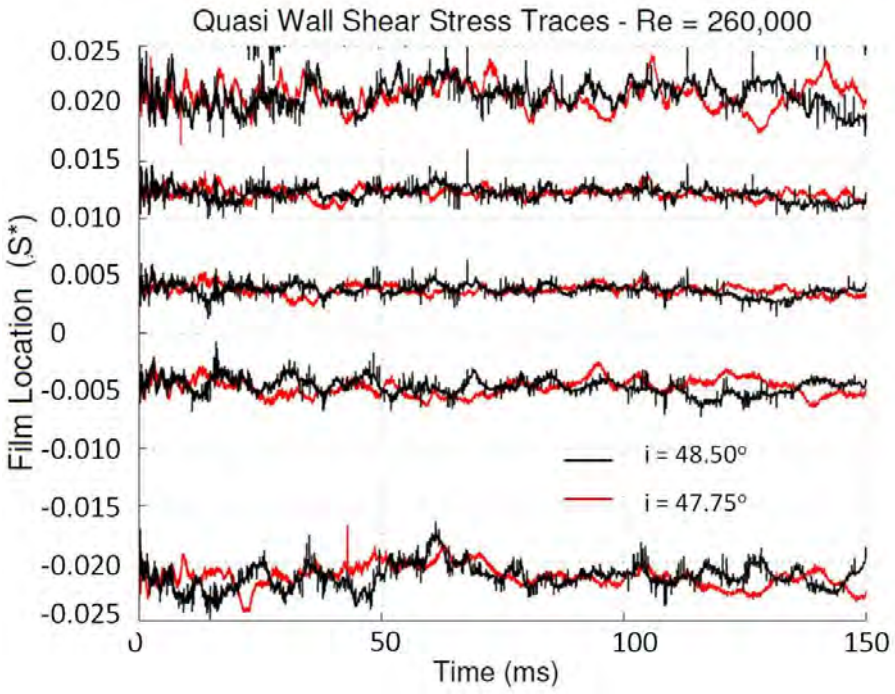

Figure 5.9: Raw traces of τ_w in the leading edge region at high incidence

favorable at the end of the spike.

Changes in the shape of the Cp distributions discussed in Section 5.4 is connected predominantly with the length and shape of the separation bubble in the leading edge region which, in itself is a direct result of separation and reattachment processes.

Unlike trends identified on the pressure surface, the boundary layer on the suction surface shows an increase in intermittency with incidence across the leading edge region.

All cases show that between $S^* = 0 - 0.06$ the point of maximum intermittency and correspondingly minimum quasi wall shear stress were obtained from either of the hot-film sensors located between $S^* \simeq 0.0289$ - 0.0373. Both of these films lie in the strong adverse pressure gradient of the leading edge velocity spike.

A gradual increase in turbulent intermittency is seen over the early portion of the suction surface between $\alpha = 42.6^o$ and $\alpha_1 = 45^o$ with the $Re_c = 400,00$ case showing consistently elevated levels compared to the case with $Re_c = 260,000$. Higher Reynolds numbers lead to an increase in boundary layer instability and are associated with the early onset of transition.

When increasing the inlet flow angle past $\alpha_1 = 45^o$ the boundary layer transitions rapidly to a turbulent state just down stream of the leading edge $(S^* = 0.0289)$. This corresponds

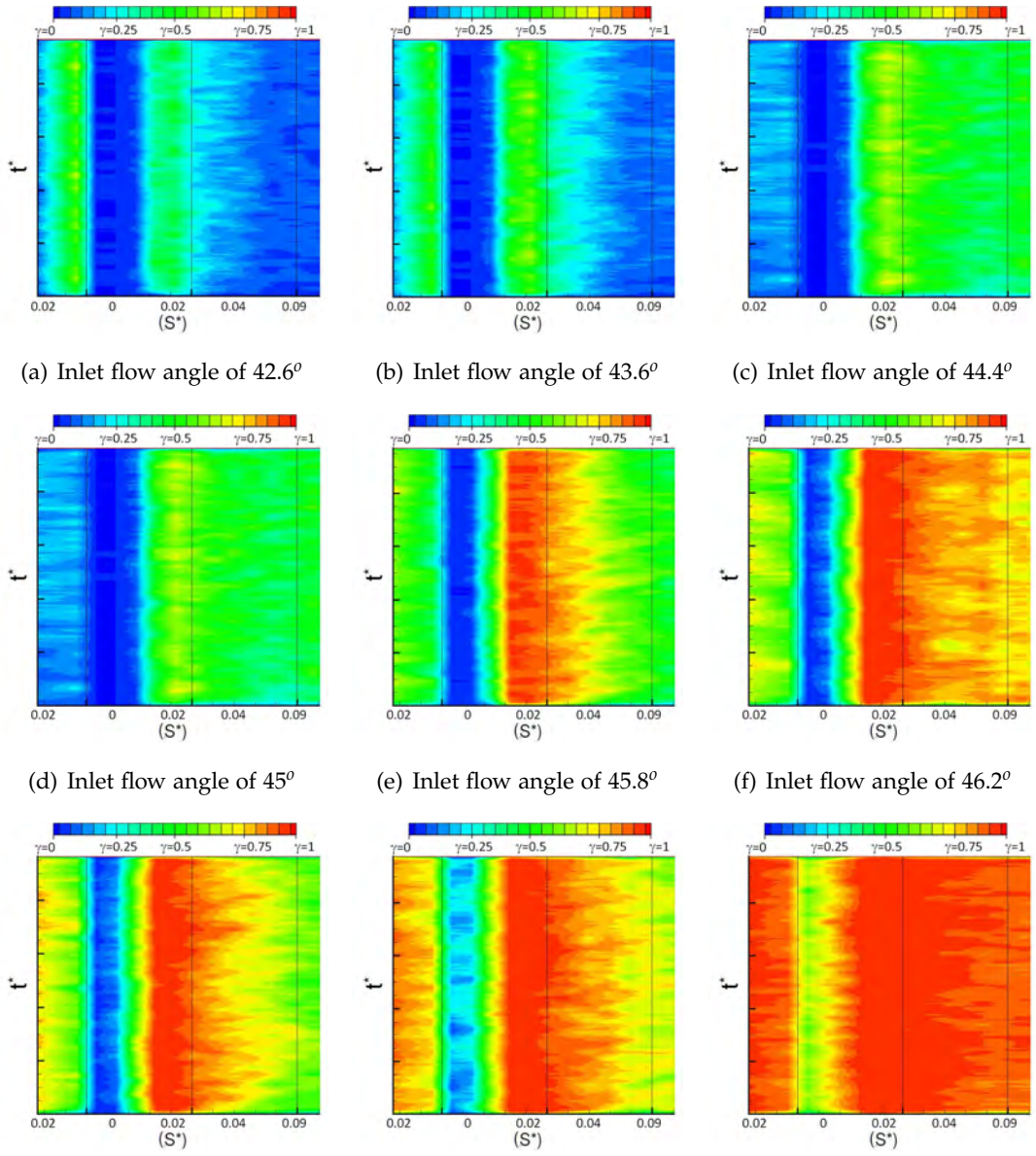

(a) Inlet flow angle of 42.6^o (b) Inlet flow angle of 43.6^o (c) Inlet flow angle of 44.4^o

(d) Inlet flow angle of 45^o (e) Inlet flow angle of 45.8^o (f) Inlet flow angle of 46.2^o

(g) Inlet flow angle of 47.4^o (h) Inlet flow angle of 47.75^o (i) Inlet flow angle of 48.5^o

Figure 5.10: Comparison of inlet flow angle effects on the time averaged intermittency distribution at $Re_c = 260,000$.

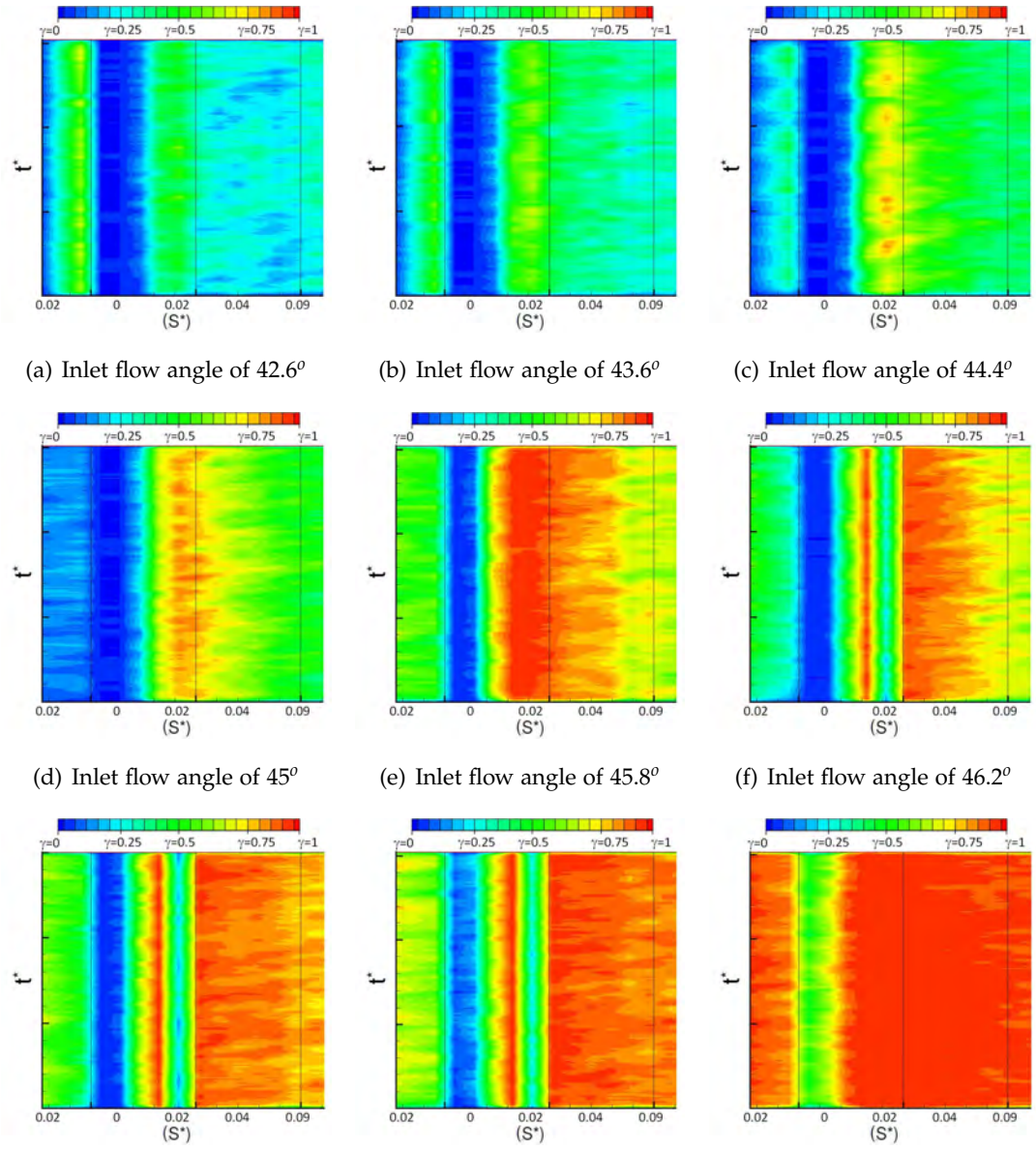

(a) Inlet flow angle of 42.6^o (b) Inlet flow angle of 43.6^o (c) Inlet flow angle of 44.4^o

(d) Inlet flow angle of 45^o (e) Inlet flow angle of 45.8^o (f) Inlet flow angle of 46.2^o

(g) Inlet flow angle of 47.4^o (h) Inlet flow angle of 47.75^o (i) Inlet flow angle of 48.5^o

Figure 5.11: Comparison of inlet flow angle effects on the time averaged intermittency distribution at $Re_c = 400,000$.

to evidence of a leading edge separation bubble forming in the extreme adverse pressure gradient in the downstream section of the velocity over speed. Previous research has shown that separated shear layers are extremely unstable and undergo rapid transition which ties in closely with this observation.

After the separation bubble reattaches to the surface the flow accelerates along the suction surface towards peak suction. The turbulent intermittency is seen to reduce significantly over this portion of the blade's surface at negative incidence and moderate values of positive incidence. At $\alpha_1 = 45.8^o$ and $Re_c = 260,000$ the boundary layer changes from having a turbulent intermittency of $\gamma = 1$ to $\gamma = 0.4$ between $S^* \simeq 0.0293$ and $S^* = 0.1$. This is discussed in more detail in the following Section 5.5.2.

As the inlet flow angle is further increased the extent of the fully turbulent region at the leading edge increases gradually with final transition, to a fully turbulent boundary layer, occurring in the region of peak suction where the favorable pressure gradient begins to relax before becoming adverse. At $Re_c = 400,000$ and $\alpha_1 = 47.4^0$ or $\alpha_1 = 47.75^o$ the level of turbulence intermittency drops only slightly from $\gamma = 1$ to $\gamma \approx 0.85$ in the region of accelerating flow where as at $Re_c = 260,000$ the level of intermittency is seen to drop to a value of approximately 0.65. Once $\alpha_1 = 48.5^o$ the boundary layer is seen to remain in a fully turbulent state from just downstream of the stagnation point to the trailing edge.

5.5.1 Trends in Quasi Wall Shear Stress Downstream of the Leading Edge Spike

As the hot-film sensors were not calibrated prior to use they cannot be used to give a quantitative value of wall shear stress. Trends in quasi wall shear stress can, however, be used to identify how a boundary layer develops under certain conditions, which can help explain how a boundary layer may be developing. These trends can then be compared between different runs under various flow conditions.

Figures 5.12 and 5.13 show that, at $Re_c = 260,000$, downstream of the reattachment point $(S* \geq 0.06)$ that τ_q remains almost constant. τ_q is proportional to $\frac{du}{dy}$ which, for a constant boundary layer thickness (δ), should increase in a favorable pressure gradient. A constant value of τ_q, in an accelerating flow, must then be linked with a moderate increase in δ. At $Re_c = 400,000$ the value τ_q decreases significantly following the completion of the re-attachment process (S^*). This shows that the boundary layer in the higher Reynolds number case must be thickening at a greater rate compared to the $Re_c = 260,000$ case as the flow accelerates up the suction surface.

During the relaminarisation process, seen to be occurring downstream of the leading edge

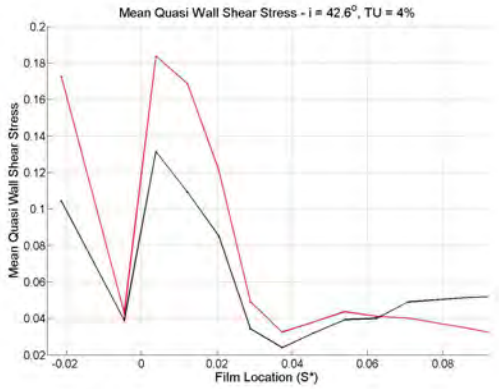

(a) $\alpha_1 = 42.6^o$

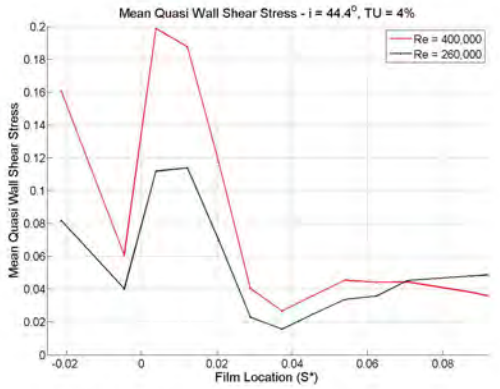

(b) $\alpha_1 = 44.4^o$

Figure 5.12: Time averaged leading edge distribution of τ_q at negative incidence

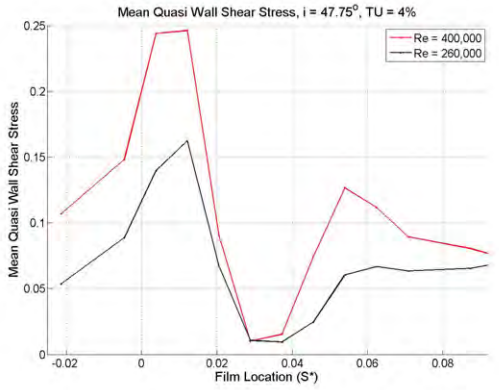

(a) $\alpha_1 = 47.75^o$

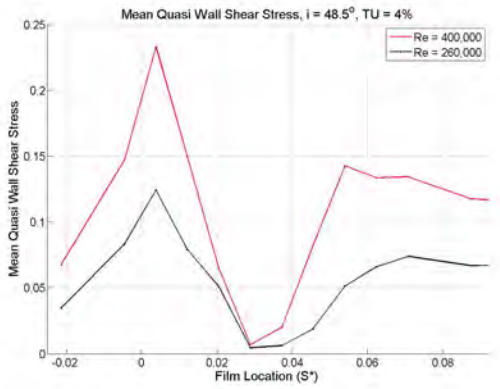

(b) $\alpha_1 = 48.5^o$

Figure 5.13: Time averaged leading edge distribution of τ_q at positive incidence

spike, the boundary layer velocity profile should become more laminar like and as a result, ignoring other effects, this should correspond to a decrease in quasi wall shear stress. As the flow is accelerated towards peak suction there is potential for δ to reduce and thus increase $\frac{du}{dy}$. It is possible for these two processes to occur simultaneously, which could lead to a plateau in the τ_q down stream of the leading edge spike. This is seen at $Re_c = 260,000$ with positive incidence and can be seen in Figure 5.13(a). A rapid rise in quasi wall shear stress is seen followed by a plateau and a slight increase. The rapid increase in shear stress can be partially attributed to the reattachment process of the separation bubble and the increase following the plateau could well be attributed to a thinning of δ^* in the favorable pressure gradient.

For the case of $Re_c = 400,000$ a significant decrease in τ_q can be seen to occur after a similar rapid rise as was previously mentioned in the $Re_c = 260,000$ case following the leading

edge spike in the favorable pressure gradient leading to peak suction. This would suggest that the boundary layer is growing with increasing δ^* as it accelerates towards peak suction. This could possibly be due to large levels of turbulent entrainment from the free stream and the boundary layer becoming unstable at a far higher rate than in the $Re_c = 260,000$. As a result of this it is expected that the boundary layer will transition to turbulence more rapidly at a higher Reynolds number, which is seen in this study.

A similar effect of Reynolds number can be seen between the τ_q plots at lower values of incidence and a gradual change can be seen with increasing incidence. Figures 5.12(a) and 5.12(b)

There were no hot-film sensors downstream of peak suction on the suction surface, however the static pressure distributions can be used to give a good indication of how the flow, over the blade's surface, behaves as it is typically more predictable than in the leading edge region and has been investigated extensively in the past. From the point of peak suction to the trailing edge there is little change in the general trend in Cp with incidence. That is other than, at very high values of incidence, where the Cp distribution plateaus near the trailing edge, indicative of a trailing edge separation forming, and that the blade is approaching the point of stall.

5.5.2 Boundary Layer Relaminarisation

The concept of boundary layer relaminarisation is poorly understood and documented in the literature. In this study it is defined as a process where a boundary layer moves toward a more laminar state associated with a decrease in turbulent intermittency, as the decay of turbulence outweighs its production [19]. Figures 5.10 and 5.11 show this trend very clearly. For a boundary layer to fully relaminarise, it would be require to move from a fully turbulent state to a laminar one ($\gamma = 1 \rightarrow 0$). This is a dramatic change and requires a very strong favorable pressure gradient over significant surface lengths. This can be found on turbine blades with circular arc leading edges but not in axial compressors.

A number of criteria proposed to identify the potential for relaminarisation in highly accelerated boundary layers are listed by Narasimha and Shreenivasan [58], where the concept of relaminarisation is investigated in great detail. One of the most commonly used criteria, and the one adopted in this study, is the acceleration parameter $K = \nu \frac{U'}{U_\infty^2}$. This criterion suggests that relaminarisation would be possible for a value of $K \geq 2 \times 10^{-6}$ over a distance of at least 20δ. Figures 5.14(a) and 5.14(b) show how the acceleration parameter changes when the flow moves up the suction surface towards peak suction. The threshold value of

$K = 2 \times 10^{-6}$ outlined by Narasimha and Shreenivasan is shown. Based on the Blassius solution for a laminar boundary layer 20δ corresponds to $S^* \simeq 0.035$.

Two trends are instantly visible when comparing these plots: a general increase in the magnitude of the acceleration parameter with decreasing incidence and also an increase in the length of the surface over which it could act to stabilise a boundary layer. It is also clear that for a given value of incidence, the low Reynolds number case shows a higher value of K.

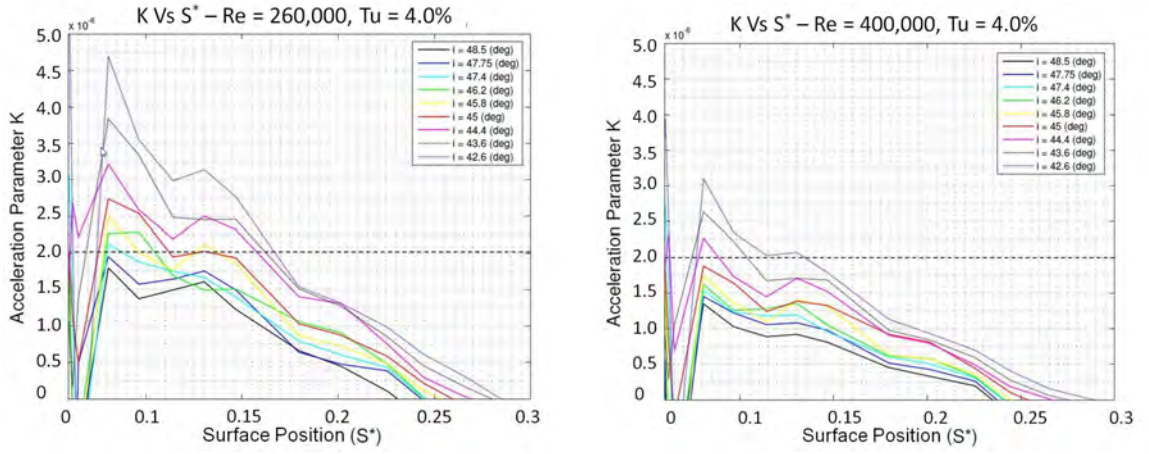

(a) $Re_c = 260,000$ (b) $Re_c = 400,000$

Figure 5.14: Change in acceleration parameter (K) in the favorable pressure gradient of the suction surface leading to peak suction

As a result full or partial relaminarisation is more likely to occur at low inlet flow angles and lower Reynolds numbers. Also a decrease in inlet flow angle and Reynolds number will also help prevent transition from occurring in the leading edge region.

Figures 5.15(a) and 5.15(b) support that, not only is the boundary layer undergoing relaminarisation but there is a distinct difference between the appearance of the raw traces with an increase in Reynolds number. The highlighted areas on both plots identify key turbulent events that grow rapidly in the adverse pressure gradient of the velocity over-speed and following this significantly reduce in magnitude as they move through the favorable pressure gradient of the suction surface. This clearly demonstrates that the favorable pressure gradient is damping turbulent fluctuations which can then be associated with a decrease in the time-averaged turbulent intermittency.

Increasing the Reynolds number raises the percentage of high frequency fluctuations present in the traces and with this is a increase in the overall level of turbulence intermittency. Large perturbations are more easily identified at a lower Reynolds number.

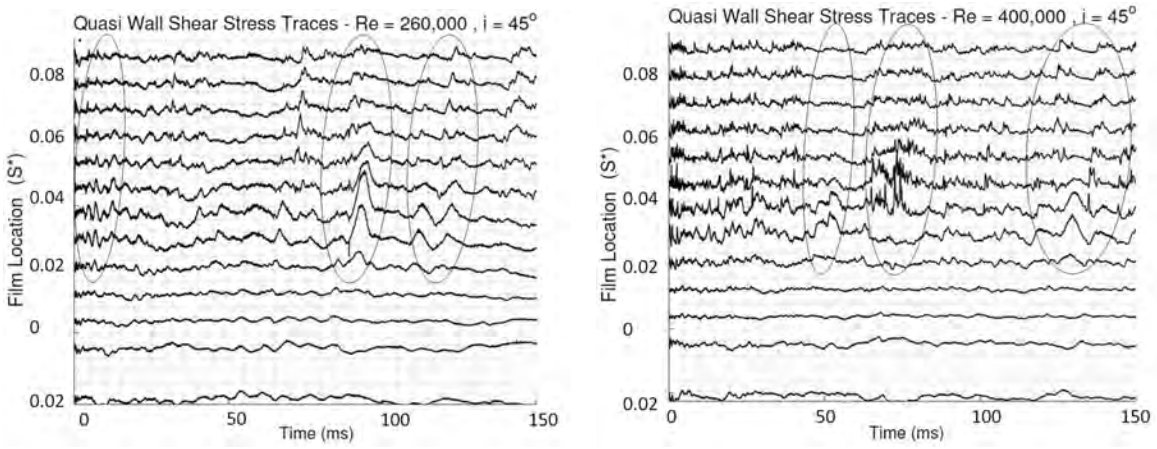

(a) $Re_c = 260,000$ (b) $Re_c = 400,000$

Figure 5.15: Raw traces of QWSS showing the damping of turbulent events initiated in the leading edge region leading to a reduction in the time averaged intermittency at two Reynolds numbers.

5.6 Boundary Layer History And Its Effect On Reynolds Number Dependency In The Leading Edge Region

It is important to consider the history of a boundary layer when trying to explain subtle differences in flow characteristics in highly complex flow regimes. Prior to the point where there are clearly Reynolds number dependencies the development of quasi-wall shear stress, Cp and turbulent intermittency appear to posses very similar characteristics.

At high values of inlet flow angle, prior to $S^* = 0.02$, the shape of the leading edge spike does not change with Reynolds number and the point of maximum Cp is almost identical when the two cases are compared. The same can be said from $S^* = 0.02$ to 0.0293 where the flow commences its rapid deceleration following the point of maximum velocity.

After the boundary layer separates from the surface a change in Reynolds number from $Re_c = 260,000$ to $Re_c = 400,000$ leads to a significant change in the shape of the Cp distributions. Between the leading edge stagnation point and the point of separation the boundary layers at the two tested Reynolds number show almost identical trends in intermittency. Figures 5.16(a) and 5.16(b) show that at lower values of incidence, near the design point, the higher Reynolds number case clearly shows higher levels of turbulence intermittency over the measured portion of the blades surface.

Looking at the relative state of $\tau_q = \left(\frac{E^2 - E_0^2}{E_0^2}\right)^3$ at different Reynolds numbers (Figures 5.13 and 5.12) in the region of interest leading up to the point where the boundary layer separates

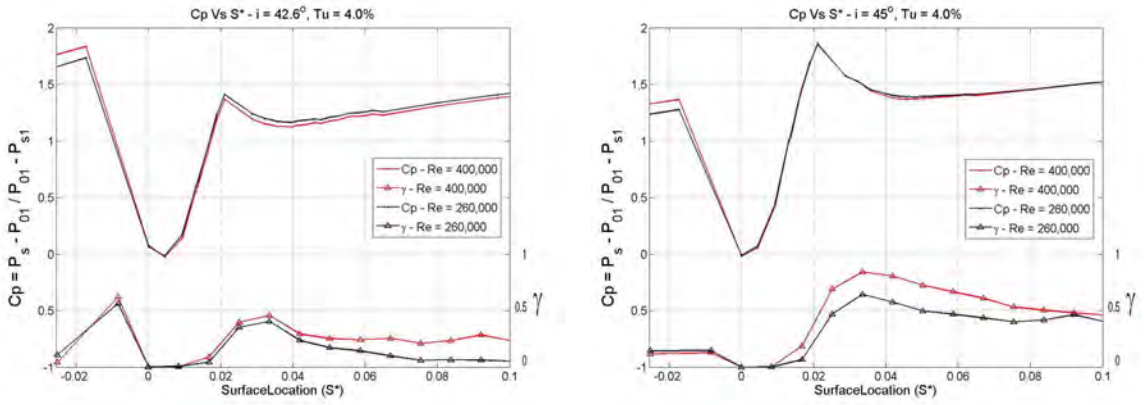

(a) $\alpha_1 = 42.6^o$ (b) $\alpha_1 = 45^o$

Figure 5.16: Leading edge Cp and intermittency distribution near design incidence

from the surface the $Re_c = 400,000$ case shows significantly higher levels of quasi wall shear stress, which could be considered indicative of a thinner and more stable boundary layer. The same difference is consistent in the reattachment zone.

At $Re_c = 400,000$ the boundary layer experiences a far more extreme pressure gradient in the re-attachment region of the separation bubble and as a result the re-attachment process is completed over a shorter surface length resulting in a shorter separation bubble. For the $Re_c = 260,000$ case the pressure gradient imposed on the flow during re-attachment is more gradual leading to a longer bubble.

It is generally understood that at a higher Reynolds number, upon separation, turbulent entrainment is likely to occur more vigorously leading to a more aggressive transition and/or reattachment process. This would be valid if, prior to separation, the boundary layer was laminar, however the time averaged intermittency plots show that at the point of separation the boundary layer is already turbulent with $\gamma = 1$. This is, of course, unless the boundary layer is laminar prior to separation and the intermittency and high frequency turbulent velocity perturbations impinging on the boundary layer are leading to a false prediction of turbulence as discussed in Section 5.5.

5.7 Influence of Reynolds Number And Inlet Flow Angle On Blade Pressure Loss

The previous sections have outlined how changing the inlet flow angle and Reynolds number of a compressor cascade can have a significant impact on the flow distribution and

development over a CD stator blade's surface. This information is now used to provide sufficient evidence in order to explain trends in the loss loop plots shown in Figure 5.17.

It is apparent from these results that the differences between the two loss loops are centered about a point very close to the design inlet flow angle where the two curves converge on the same value ($\omega = 0.022$). At negative incidence testing at $Re_c = 400,000$ shows a significantly lower level of loss compared to the $Re_c = 260,000$ case and the reverse can be seen at moderate to high, positive, incidence. To explain these differences flow observations made in the earlier parts of this paper must be re-visited.

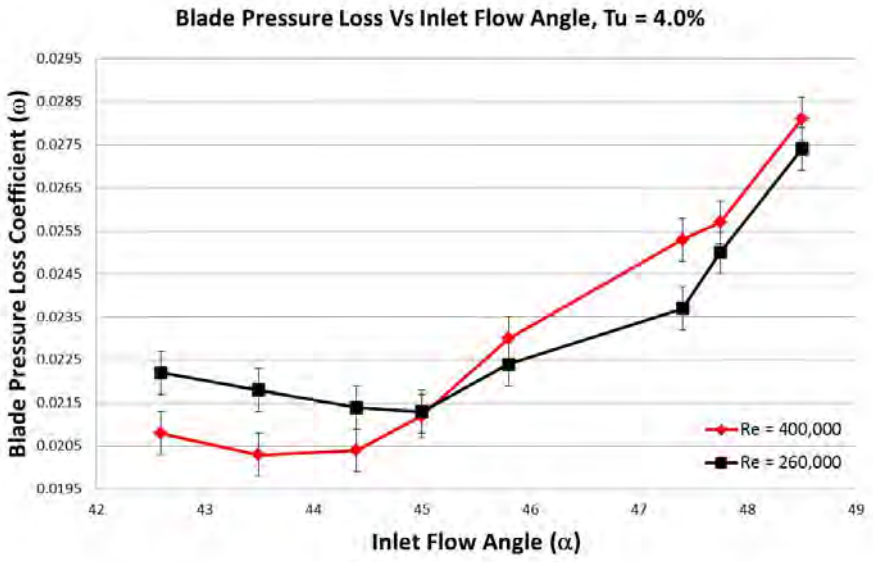

Figure 5.17: Loss loop plot showing the change in blade pressure loss with increasing inlet flow angle

At negative incidence two key factors determine the differences in loss seen between the $Re_c = 260,000$ and $Re_c = 400,000$ cases: the separation bubbles seen to form downstream of peak suction on the suction surface at $Re_c = 260,000$ and also in the leading edge velocity spike on the pressure surface.

The boundary layer on the pressure surface separates from the surface in the decelerating region of the velocity spike before undergoing rapid transition. A turbulent boundary layer is then maintained over the entire surface. This has to be the case as the pressure gradient downstream of the leading edge region on the pressure surface is close to zero with only a slight acceleration towards the trailing edge of the blade leaving no potential for the boundary layer to relaminarise. As a result the turbulent wetted area at both Reynolds numbers will be almost identical, varying only with changes in bubble length.

The size of the leading edge separation bubble does change significantly with Reynolds number which, as has been mentioned previously, creates the largest amount of loss per unit length on a low speed blade's surface [13]. Figures 6.4(a) and 6.4(b) show the bubble is seen to decrease in length from being approximately 18mm to 12mm from the point of separation to the point of reattachment with an increase in Reynolds number from $Re_c = 260,000 - 400,000$. The length was measured using a scale fitted around the leading edge of the blade. An increase in bubble length of 6mm or $S^* = 0.02$ is observed which is significant compared to the leading edge circular arc which has a radius of 5.3mm.

On the suction surface, the boundary layer development at both Reynolds numbers show very similar trends other than evidence of a separation bubble forming downstream of peak suction on the suction surface at $Re_c = 260,000$. At $Re_c = 400,000$ there is a slightly elevated level of intermittency over the surface and transition is expected to occur slightly closer to the leading edge. It is expected that these differences will have a very small influence on the differences in profile loss between Reynolds numbers at negative incidence.

As the inlet flow angle is increased to $\alpha_1 = 45^o$ the pressure surface velocity spike height decreases, reducing the size of the pressure surface separation bubble and as a result the component of loss from the pressure surface also decreases. A bubble is seen to form at both Reynolds numbers but the same Reynolds number dependency is still present with the $Re_c = 400,000$ case forming a shorter bubble. On the suction surface, the leading edge spike height increases and although there will be little difference in the final transition locations between the two Reynolds number cases, the boundary layer shows an elevated level of intermittency at $Re_c = 400,000$ leading to peak suction.

At design incidence $\alpha_1 = 45^o$ both cases show very similar trends in intermittency, Cp and quasi-wall shear stress and as a result show very similar trends in loss, which is to be expected. This also shows that the blade is most stable to changes in Reynolds number at its design point indicative of a well designed profile.

Between design incidence and $\alpha_1 = 45.8^o$, a separation bubble is seen to form at the leading edge of the suction surface. This results in the loss at both Reynolds numbers increasing rapidly. The higher Reynolds number case begins to show slightly higher values of blade pressure loss, which can be connected to an increase in intermittency and wall shear stress.

As the inlet flow angle is further increased to $\alpha_1 = 47.75^o$ the blade has significantly higher blade pressure loss values at $Re_c = 400,000$. This is the opposite trend to that seen at negative incidence. Higher levels of turbulent intermittency are seen over a greater area on the suction surface and the final point of transition occurs slightly earlier.

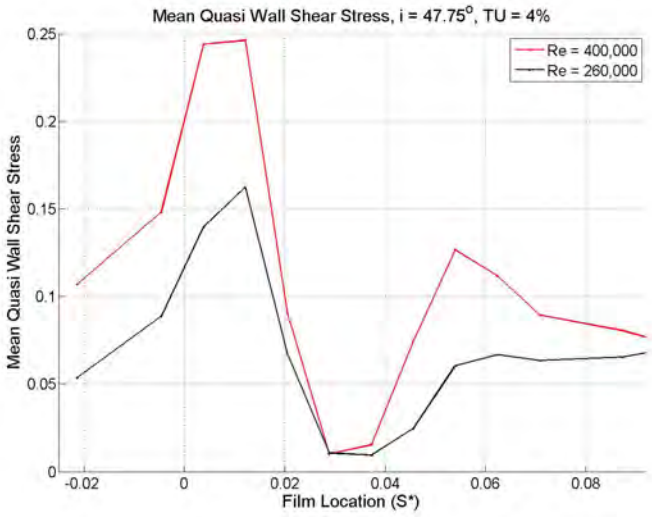

Figure 5.18: Leading distribution of time averaged quasi-wall shear stress

Figure 5.18 shows that at $Re_c = 400,000$ there is a rapid decrease in quasi-wall shear stress in the lead up to peak suction, which indicates significant thickening of the boundary layer that is not seen in the $Re_c = 260,000$ case and will lead to an increase in the momentum thickness at the trailing edge and thus an increase in loss. The pressure surface separation bubble is small at positive incidence and the boundary layer is turbulent over almost the entire surface. As a result changes in its size and associated loss generation will not change significantly with Reynolds number.

When maximum incidence is approached, blade profile loss for both Reynolds number cases converges. Transition occurs at the leading edge and a separation bubble is present. A fully turbulent boundary layer exists over both surfaces downstream of the leading edge which separates in the adverse pressure gradient close to the trailing edge. Prior to this point, both loss loops display a rapid increase in loss. This starts at $\alpha_1 = 47.4^o$ for $Re_c = 260,000$ and at $\alpha_1 = 47.75^o$ for $Re_c = 400,000$ and can be accounted for by the formation of a trailing edge boundary layer separation.

5.8 Conclusions

This chapter has examined, in detail, the flow around a CD compressor stator blade with a circular arc leading edge in cascade. Changing the inlet flow angle and Reynolds number in the cascade brought about significant changes in blade pressure loss. At negative incidence, loss was seen to increase as the Reynolds number was decreased - changes in incidence also

brought about moderate changes in loss. In contrast, at positive incidence, the opposite trend was displayed, with blade pressure loss increasing with Reynolds number and was more heavily influenced by changes in the inlet flow angle, which became more apparent at high inlet flow angles.

A separation bubble formed, at the leading edge of the pressure surface, under all test conditions. The bubble length was dependent on Reynolds number and incidence. A gradual decrease in bubble length was observed as incidence was increased. The same trend was observed when increasing Reynolds number from $Re_c = 260,000$ to $Re_c = 400,000$. The Reynolds number dependency was more evident at negative incidence as the bubble was larger and a visible change in bubble length was observed using flow visualisation. The suction surface separation bubble formed at values of positive incidence ($\alpha_1 > 45^o$) and displayed the same Reynolds number dependency as that seen on the pressure surface although the differences were smaller due to an overall decrease in bubble length compared to that seen on the pressure surface. Reynolds number effects are thus more prevalent at off design operating points where the possibility of large separated flow regions is increased. This is particularly important when leading edge separation bubbles are possible as subsequent transition and increases in momentum thickness have significant influences over blade performance and loss generation.

When a laminar separation bubble forms at the blade's leading edge it leads to rapid transition and the formation of a boundary layer upon reattachment. On the pressure surface this boundary layer is maintained along the blade's surface to the trailing edge. On the suction surface, the favorable pressure gradient downstream of the leading edge, leading to peak suction, has a relaminarising effect on newly developed, fully turbulent, boundary layer. The potential for relaminarisation is highest at negative incidence, where the boundary layer is least susceptible to transition at the leading edge, and decreases as incidence and blade loading increases.

Elevated levels of high frequency perturbations are seen in the raw quasi wall shear stress traces of films located between the stagnation point and the peak of the velocity over-speed. The turbulent intermittency routine identifies these fluctuation with a turbulent boundary layer, which would be impossible to sustain in such a strong favorable pressure gradient and with such small values of Re_θ [66]. This could be misleading if insufficient attention is paid to looking at the raw traces on which the intermittency routine bases its decisions. These findings tie in with those of Chapter 7 which reveal how freestream turbulence is amplified and distorted in the leading edge region of the blade row and demonstrates how such turbulence is penetrating though the thin laminar boundary layer onto the blades surface.

At negative incidence the blade has a lower level of pressure loss with an increased Reynolds number where as at positive incidence the opposite trend is observed. A sharp rise in loss is seen as the inlet flow angle of the cascade is increased past the blade's design point ($\alpha_1 = 45^0$) and transition shifts forwards to the leading edge separation bubble. The point where the initial point of transition jumps to the blade's leading edge could be called a critical value of incidence for this blade profile at a particular Reynolds number and freestream turbulence intensity. When the inlet flow angle is increased to a point nearing blade stall, the loss at both Reynolds numbers begin to converge. At this point a fully turbulent boundary layer is present over the entire surface of the blade.

These findings confirm that boundary layer relaminarisation is possible with a sufficiently strong favorable pressure gradient over a significant surface length and is most likely to occur at a low Reynolds number and negative incidence. Separation bubbles form at the leading edge of both surfaces, this initiates rapid transition, increasing the turbulent wetted area on the blade and local loss generated inside the bubble. The bubble also leads to an increase in the momentum thickness at the leading edge and, as the momentum thickness at the trailing edge is proportional to that at the leading edge, this can have a large impact on blade pressure loss (Section 2.7).

Chapter 6

Comparison Between MISES and Experimental Predictions of Cascade Performance

6.1 Introduction

How well the MISES flow solver, developed by Mark Drela and Harold Youngren [17] at MIT in the 1980's, and other preliminary design codes predict the performance of compressor blades in cascade is of key importance to the turbomachinery industry today. Especially with the increased reliance on "blind" optimisation routines during early stages of the design process.

MISES is a collection of programs used for the analysis and design of cascade blade rows. It is a 2D/quasi-3D coupled viscous/inviscid Euler method, which solves the viscous boundary layer and inviscid freestream flow regimes simultaneously. A block diagram of the MISES system and all its components is shown in Figure 6.1, which is a modified version of the MSES code that utilises a modified Abu-Ghannam and Shaw criterion for the pre-

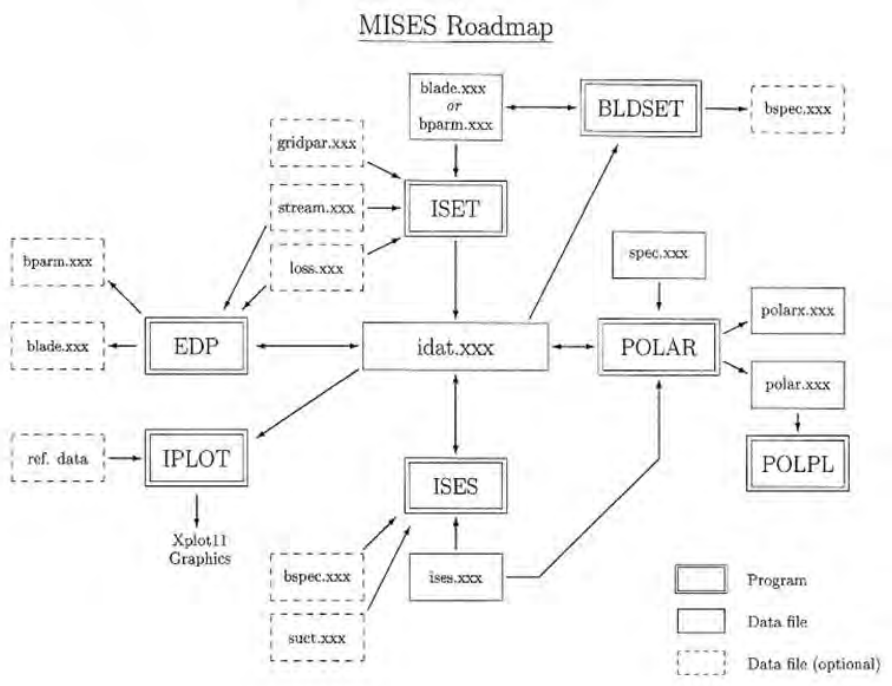

Figure 6.1: Block diagram of the MISES system [**?**]

diction of transition onset and includes both linear-stability (natural) and bypass transition correlations. A user defined inlet turbulence level is thus required [1].

An investigation was carried out using MISES at all the conditions tested experimentally (Section 5.2), allowing for a direct comparison to be be made between the two sets of results.

Inlet and exit pitchwise three-hole probe traverses were carried out to determine the inflow and outflow conditions of the compressor cascade, which were used in MISES' input files. Of particular importance were the inlet and outlet flow angles and the pressure loss coefficient of the stator blade. The time-mean static pressure distribution and velocity distribution of the stator blade were made using a series of static pressure tappings and hot-film data was interpreted to determine the location of boundary layer separation and transition locations.

This chapter explores the differences between predicted and experimental loss loops. Measurements obtained in Chapter 5 are compared against post-processed results from output files produced in MISES. These comparisons are then used to identify how well MISES predicts flow patterns around a CD stator blade with a circular arc leading edge in cascade and what leads to its inaccuracies.

6.2 Comparison Between Experimental Results and MISES

It is evident that the MISES predicted and experimental loss loops, are both Reynolds number and incidence dependent. Figure 6.2 clearly indicates the Reynolds number dependency predicated by MISES differs significantly from that found experimentally at positive incidence, but not at negative incidence. The following section will explain the mechanisms behind the similarities and differences between the two loss loops.

Three main areas of the loss loops will be discussed: negative incidence, design incidence and positive incidence at two Reynolds number: $Re_c = 260,000$ and $Re_c = 400,000$. The general trends will also be compared with unsteady data published by Henderson [30] measured inside the 1.5 stage low-speed axial compressor at the University of Tasmania, which has a stator blade row with an identical mid-span blade profile to the blade tested during this project.

Figure 6.3 compares predicted and experimental static pressure distributions at a range of inlet flow angles for both tested Reynolds numbers. It is clear that the overall static pressure distribution and thus blade loading, including that in the leading edge region, is well predicted by MISES. Differences in the leading edge spike height could be accounted for by a lack of static pressure tapping resolution

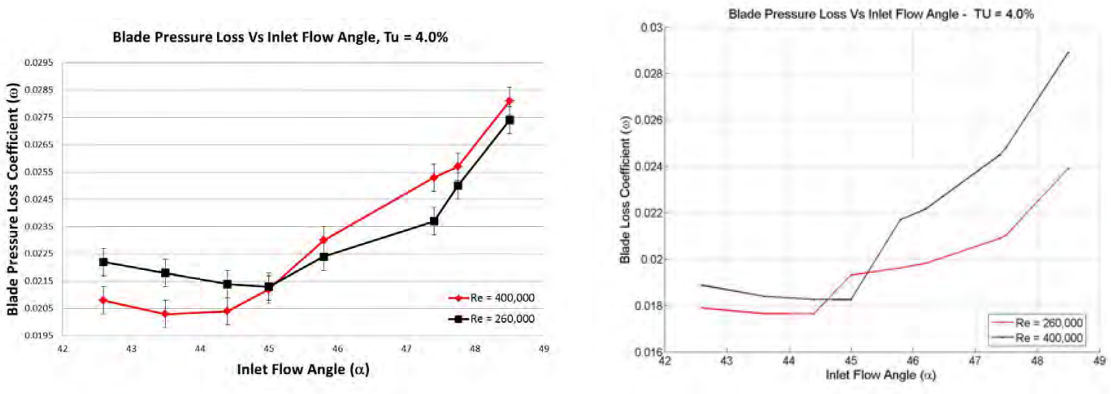

(a) Experiment

(b) MISES

Figure 6.2: Loss loop plots showing the change in blade pressure loss with increasing inlet flow angle

6.2.1 Negative Incidence $\alpha_1 = 42.6^o - 45^o$

At large values of negative incidence and low Reynolds numbers, the suction surface boundary layer of a compressor blade is expected to remain laminar until downstream of peak

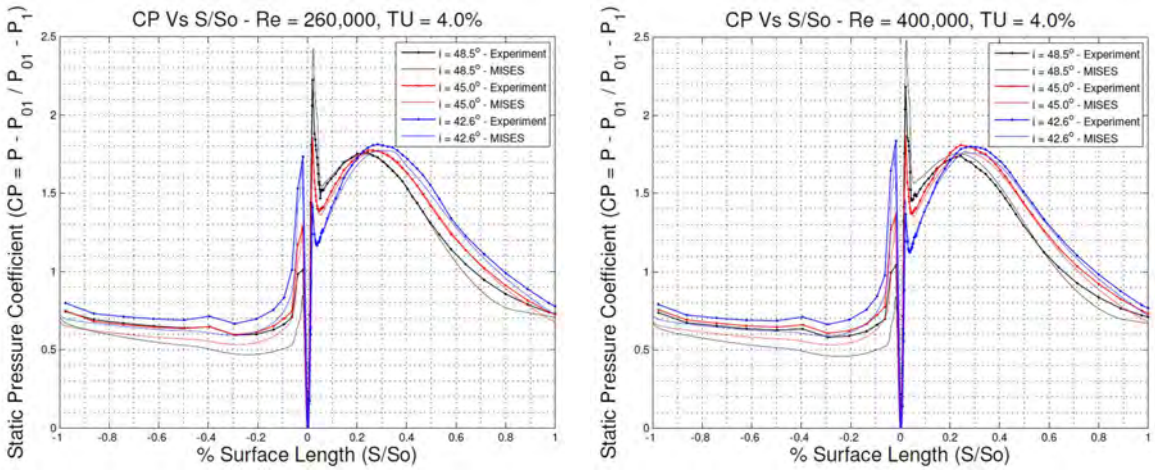

(a) $Re_c = 260,000$ (b) $Re_c = 400,000$

Figure 6.3: Comparison of Cp distributions between MISES and experimental results over a range of inlet flow angles

suction where transition then occurres inside a separation bubble that forms in the adverse pressure gradient on the blades surface. As either the value of incidence or Reynolds number is increased, the likelihood of the boundary layer undergoing separated flow transition downstream of peak suction reduces and transition becomes more likely to occur close to peak suction by a natural or bypass mechanism ([97], [34]).

At negative incidence the experimental loss loops and those predicted by MISES show an increase in loss with Reynolds number. On the suction surface, MISES predicts that transition occurs in the adverse pressure gradient downstream of peak suction or just upstream of this location where the favorable pressure gradient begins to relax. MISES does not predict the formation of a separation bubble on either the suction or pressure surface downstream of the leading edge region under any of the test conditions at negative incidence. It does however predict a perturbation in the Cp distribution directly downstream of the point of transition onset. This could easily be confused with the formation of a separation bubble, as in the adverse pressure gradient it appears to depict a plateau in static pressure, which is a well known characteristic of a separated flow region but the wall shear stress does not reach zero - MISES' condition for separation onset.

Downstream of the point of separation the wall shear stress (τ_w) will be greater than zero in the re-circulating flow region of the bubble. It is thus apparent that the perturbation represents a change in the shape of the boundary layer as a result of transition. At $Re_c = 400,000$ the perturbation in Cp moved upstream of peak suction into the favorable pressure gradient, where boundary layer separation is not possible - confirming the previous explanation.

Experimental Cp distributions also show a perturbation in Cp downstream of peak suction at $Re_c = 260,000$ at the lowest value of incidence. This perturbation occurs a significant distance downstream of peak suction between $S^* = 0.45 - 0.55$ which could be the formation of a small laminar separation bubble, however this evidence is not conclusive. If this were the case it would lead to an increase in pressure loss at lower Reynolds numbers due to high entropy production rate associated with separated flow regions.

Intermittency distributions are interpreted to obtain transition locations on the suction surface which are expected to be very similar between experiment and MISES at both Reynolds numbers. The main exception being at $Re_c = 400,000$, which showed an elevated level of intermittency before the boundary layer finally transitions to a fully turbulent state near peak suction. The final transition location is not expected to differ significantly at negative incidence with Reynolds number. This should cause little change in the turbulent wetted area seen on the blades suction surface. As a result similar levels of loss will be attributed to the suction surface with varying Reynolds numbers (Figure 6.5(a))

Predictions from MISES (Figure 6.7) and experimental flow visualisation (Figures 6.4) shows that a separation bubble forms in the leading edge region of the pressure surface over the entire range of inlet flow angles and Reynolds numbers tested. The size of the bubble is strongly Reynolds number dependent, decreasing in length with increasing Re_c - a well documented trend previously discussed in Chapter 5.

Experimental and computational predictions of the flow development on the pressure surface at low inlet flow angles are very similar at both tested Reynolds numbers. The only significant difference comes from the extent of the separated flow region at the leading edge which, as previously mentioned, produces the greatest amount of loss per unit length out of commonly encountered boundary layer flow characteristics [13].

From the above mentioned trends the majority of the elevated level of loss seen at $Re_c = 260,000$ compared to $Re_c = 400,000$ at negative incidence is attributed to an increase in size of the separation bubble at the leading edge combined with the increased potential of a separation bubble forming downstream of peak suction at low Reynolds numbers. This is confirmed when individual surface loss plots are generated (Figure 6.5) which show a relatively large increase in loss with a decrease in Reynolds number on the blades pressure surface compared to the suction surface.

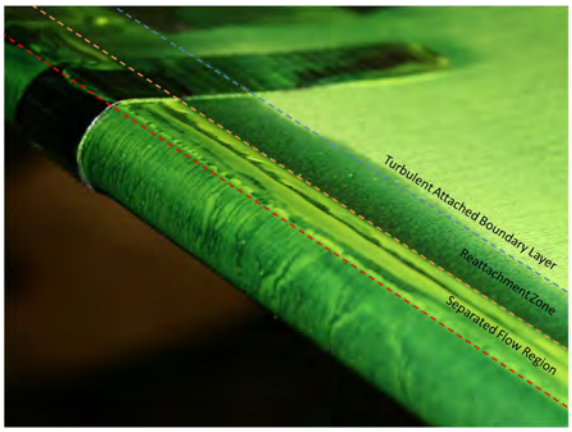

(a) $Re_c = 260,000$ and $\alpha_1 \approx 42.6^o$

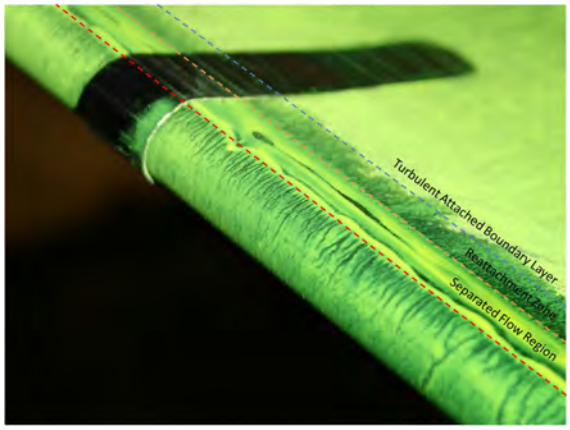

(b) $Re_c = 400,000$ and $\alpha_1 \approx 42.6^o$

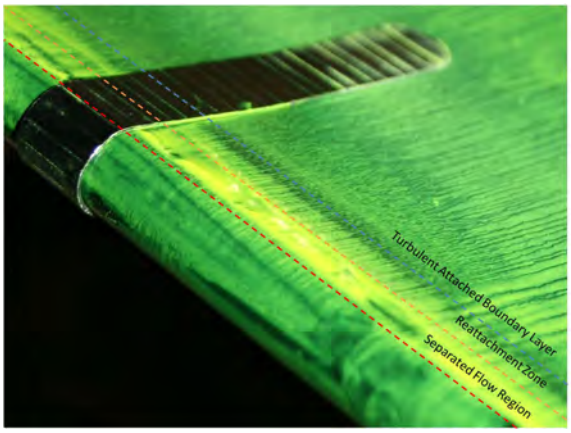

(c) $Re_c = 260,000$ and $\alpha_1 \approx 48.5^o$

Figure 6.4: Surface flow visualisation images of a pressure surface leading edge separation bubble

6.2.2 Design Incidence $\alpha_1 = 45^o$

At and around the CD stators design operating point, both experimental and computational results show that the overall blade pressure loss curves become independent of Reynolds number. Figures 6.5 and 6.6 both show that loss generated on the pressure and suction surfaces are also independent of Reynolds number. This is not unexpected as at design incidence, blade performance, stability and efficiency should be least sensitive to changes in flow conditions.

Increases in loss attributed to the increase in size of the pressure surface separation bubble at low Reynolds numbers are balanced by the an increase in the overall intermittency levels on the suction surface leading to peak suction at $Re_c = 400,000$. There is no evidence of separated flow on the suction surface at design incidence and the turbulent wetted areas on

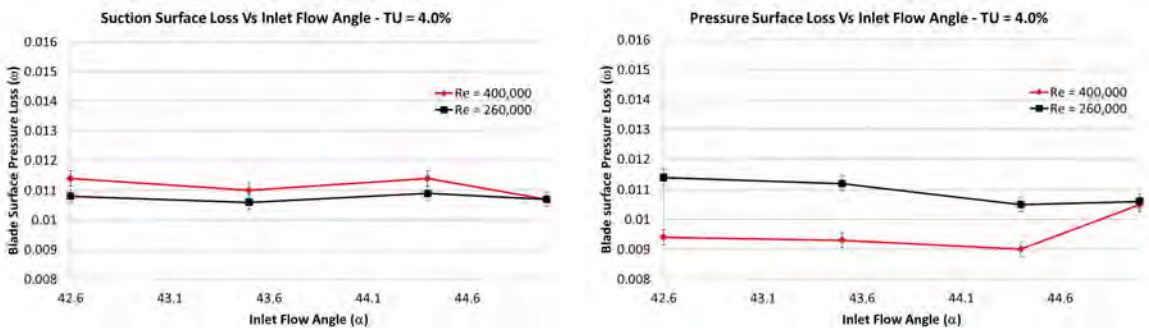

(a) Change in suction surface loss with Reynolds number at negative incidence

(b) Change in pressure surface loss with Reynolds number at negative incidence

Figure 6.5: Plots showing the distribution of loss generated by the pressure and suction surfaces at $Re_c = 260,000$ and $Re_c = 400,000$ for values of negative incidence

the pressure surface is almost identical at both Reynolds numbers.

This is the region where both Reynolds number cases show that the pressure loss is most sensitive to changes in inlet flow angle. The increased sensitivity is caused by the formation of a leading edge separation bubble, which results in the location of transition jumping to the leading edge of the blade - increasing the turbulent wetted area and enhancing the importance of boundary layer relaminarisation. When a separation bubble forms and transition jumps to the leading edge, MISES predicts a discrete discontinuity in the loss loop as the code is incapable of calculating relaminarisation and a step increase in turbulent wetted area is predicted.

6.2.3 Positive Incidence $\alpha_1 = 45 - 48.5^o$

At positive incidence significant differences are observed when comparing the loss loops predicted by MISES and that shown from experimental findings. MISES' predictions show the low Reynolds number case of $Re_c = 260,000$ has significantly higher levels of loss (Figure 6.2(b)). Additional MISES simulations show this trend continues as the Reynolds number continues to decrease below $Re_c = 260,000$. The opposite trend is seen in the experimental loss loops (Figure 6.2(a)), which shows an increase in blade pressure loss with Reynolds number.

Figure 6.6 indicated that on the suction surface an increase in Reynolds number corresponds to an increase in loss generated for inlet flow angles between $\alpha_1 = 45^o$ and 47.75. The increase in loss is linked with an increase in turbulent intermittency over the early portion of

the suction surface. Under these conditions transition occurs inside the leading edge separation bubble followed by relaminarisation of the boundary layer as it accelerated towards peak suction. Chapter 5 showed that boundary layer relaminarisation was more effective at lower Reynolds numbers, leading to a decrease in the production of loss in favorable pressure gradient on the suction surface.

At inlet flow angles greater than $\alpha_1 = 47.4^o$ a trailing edge separation forms at both tested Reynolds number. The separated flow region is slightly more prominent at $Re_c = 260,000$, which should lead to a increase in blade loss generated at the lower Reynolds number. However this is not the case as a result of a difference in turbulent wetted area over the front portion of the blade due to the increased amount of relaminarisation at low Reynolds number (Section 5.5.2).

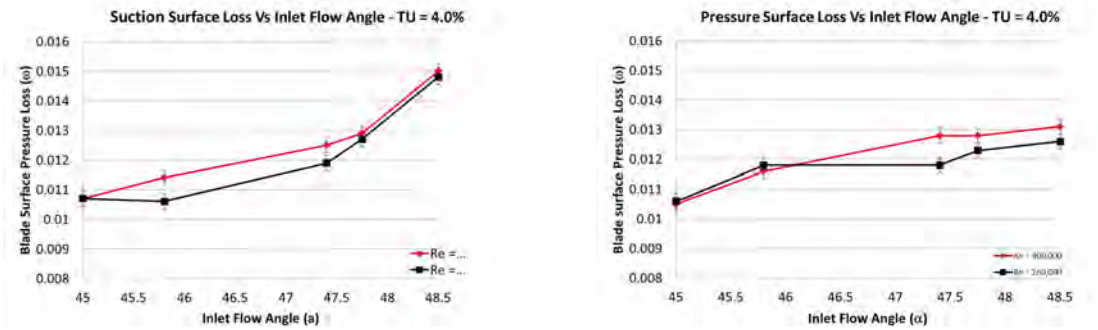

(a) Change in suction surface loss with Reynolds number at positive incidence

(b) Change in pressure surface loss with Reynolds number at negative incidence

Figure 6.6: Plots showing the distribution of loss generated by the pressure and suction surfaces at $Re_c = 260,000$ and $Re_c = 400,000$ for values of positive incidence

Both data sets predict a separation bubble forming in the decelerating portion of the suction surface leading edge spike at both Reynolds numbers tested for the incidence range of $\alpha_1 = 45.8^o$ - 48.5^o. Evidence also points to the bubble length being Reynolds number dependent - decreasing in size with increasing Reynolds number as was seen at negative incidence on the pressure surface (Figure 6.8).

A leading edge separation bubble is also seen on the pressure surface at positive incidence for both $Re_c = 260,000$ and $Re_c = 400,000$ in both sets of results. As a result transition occurs at the leading edge and the turbulent wetted area on the pressure surface will be essentially independent of Reynolds number and will vary only as the separation bubble changes length.

As incidence is increased, the length of the separation bubble on the pressure surface decreases as the velocity overspeed peak value reduces in size (Figure 6.4(c) and 6.4(a)). As

a result of this global reduction in bubble size, differences in bubble length as a result of changes in Reynolds number, and associated losses, will reduce and should play a less dominant role in the differences between loss loops at high incidence. This trend is not supported by Figure 6.6 which shows a greater difference in loss on the pressure surface at positive incidence as previously mentioned, however the difference in loss increases with Reynolds number - supporting the differences identified in the overall loss loops.

MISES predicts that the pressure surface separation bubble has an almost constant length with an increase in inlet flow angle and the Reynolds number dependency of the bubble length also remains almost constant as a result. These differences will lead to MISES over predicting the amount of loss generated on the pressure surface at positive incidence and will indicate a larger component of loss from the pressure surface at a lower Reynolds numbers - both of which lead to MISES predicting a larger value of loss at $Re_c = 260,000$ compared to $Re_c = 400,000$ at positive incidence.

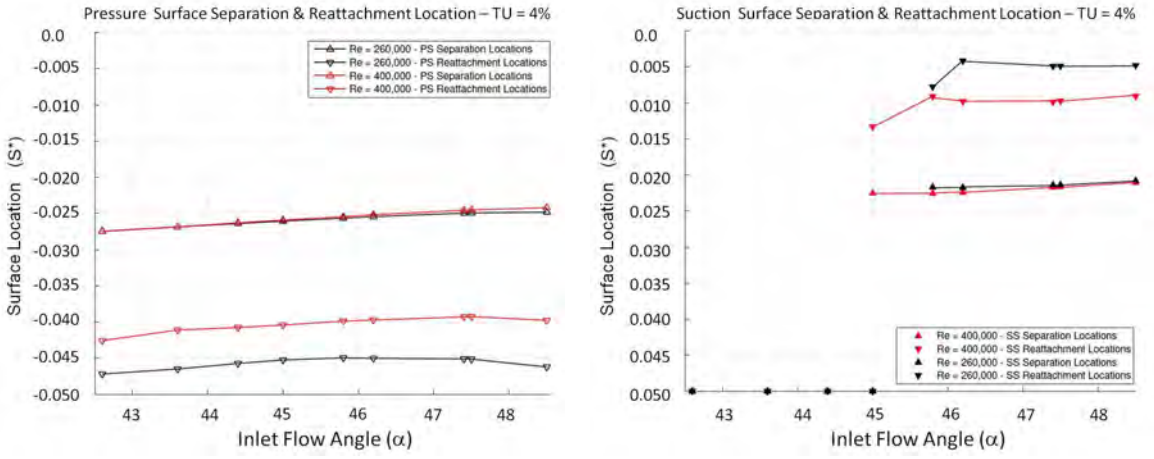

(a) Suction surface

(b) Pressure Surface

Figure 6.7: Suction and pressure surface separation and reattachment locations predicted by MISES.

One key difference between the experimental findings and MISES predictions at positive incidence is the location of the point of final transition.

MISES predicts that once a separation bubble forms at the blades leading edge, transition is triggered within the bubble, and a fully turbulent boundary layer then exists over the entire remainder of the blades surface. The formation of a separation bubble and subsequent jump forward in transition location from near peak suction to $S^* \simeq 0.05$ is seen to occur at $\alpha_1 = 45^o$ for $Re_c = 400,000$ and at $\alpha_1 = 45.8^o$ for $Re_c = 260,000$. This dramatic shift in transition location corresponds to the discontinuity in the blade pressure loss seen in Figure 6.2(b).

The experimental results show that although a separation bubble is seen to form first at $\alpha_1 = 45.8^o$ for both Reynolds numbers causing the boundary layer to undergo rapid transition. Following this the boundary layer is seen to relaminarise as it accelerates towards peak suction before finally undergoing transition in the relaxed or adverse pressure gradient (Section 5.5.2). From this point a fully turbulent boundary layer is sustained to the trailing edge of the blade.

For inlet flow angles of 45.8^o and $Re_c = 260,000$ the level of turbulent intermittency reduces to a value of approximately 0.5 within the first 10% of surface length following the leading edge separation where the value of turbulent intermittency approaches unity. The prediction of such a relaminarisation phenomena is not possible within MISES. As a result, the presence of a leading edge separation bubble will lead to the prediction of a fully turbulent boundary layer over the entire surface downstream of the leading edge velocity overspeed. A significant difference in turbulent wetted area between the two data sets is the result with MISES displaying a greater coverage of fully turbulent flow that will inevitably lead to an increased predicted loss production on the suction surface.

Due to the spacing of the hot-film sensors it is not possible to obtain a very accurate measurement of the length of the separation bubble that forms in the leading edge of the suction surface from quasi-wall shear stress measurements. Figure 6.9 shows that there is a clear step down in τ_q when moving from $\alpha_1 = 45^o$ to $\alpha_1 = 45.8^o$. It also shows that the separation bubble is seen to form in the same region as that predicted by MISES (Figure 6.7(b)). MISES predicts the point of separation to occur very close to $S^* = 0.0275$, which lines up almost exactly with a hot-film sensor and the lowest value of τ_q seen on the surface. Comparing plots of C_f from MISES and τ_q from the experimental results, strong similarities are observed in the trends predicted around the separated flow region.

Unfortunately the reattachment location at both Reynolds numbers is predicted to lie between the two sensors located at $S^* = 0.0373$ and $S^* = 0.0456$. To support results from the hot-film sensors the Cp distributions can also be used to determine the location where the boundary layer separates and reattaches to the surface (Figures 6.8 and 6.7. This clearly shows that both MISES and experiment show that bubble length is Reynolds number dependent as was the case on the pressure surface.

At $\alpha_1 = 48.5^o$ experimental results show a bubble length of $S^* \simeq 0.012$ and $S^* \simeq 0.008$ for $Re_c = 260,00$ and $Re_c = 400,000$ respectively. On the other hand MISES predicts bubble lengths of $S^* \simeq 0.012$ and $S^* \simeq 0.017$ for $Re_c = 260,000$ and $Re_c = 400,000$ respectively. The leading edge separation bubble should give rise to a larger increase in blade pressure loss at a lower Reynolds number in MISES' predictions compared to the experiment which shows a smaller increase in bubble size.

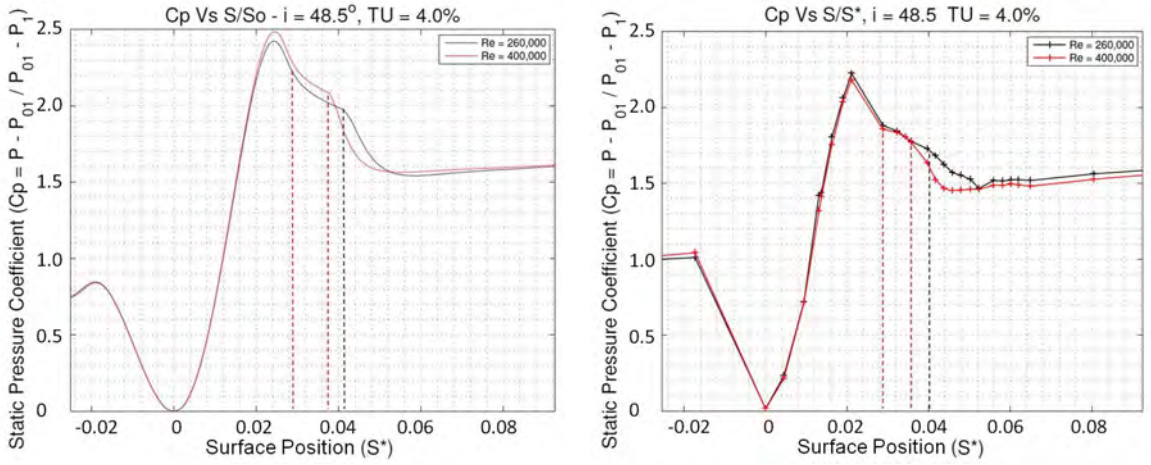

(a) MISES

(b) Experiment

Figure 6.8: Cp distributions from MISES predictions and experimental results at $\alpha_1 = 49.5^o$

Between $\alpha_1 = 45.8^o - 47.75^o$ experimental results show that blade pressure loss is higher with increased Reynolds number, which is the opposite trend to that predicted by MISES. It is believed that the extent of the blades turbulent wetted area is larger for $Re_c = 400,000$ compared to $Re_c = 260,000$.

At $\alpha_1 = 48.5^o$ the loss loops at both Reynolds numbers are seen to converge on a single value, which is to be expected as the boundary layers on both surfaces are seen to transition to a fully turbulent state very close to the leading edge stagnation point, before the leading edge spike. At such elevated inlet flow angles the blade pressure loss is seen to be increasing dramatically as a result of the formation and increase in size of a trailing edge separation.

6.3 Proportion of Individual Surface Loss Generation

The contribution of each surface to the total blade pressure loss is an important parameter to look at when identifying which surface has the most profound effect on blade performance.

Experiment results show that at $\alpha_1 = 42.6^o$ and $\alpha_1 = 48.5^o$ there is approximately a 55% : 45% split between the amount of loss generated by the suction surface and pressure surface respectively. Wheeler [98] reported MISES showing that approximately 70% is generated by the blades suction surface and only 30% by the pressure surface. These findings are considerably different from one another and may have led users of MISES to concentrate design efforts on the suction surface and not the pressure surface, particularly in the leading edge region where both surfaces have the potential to form leading edge velocity overspeeds

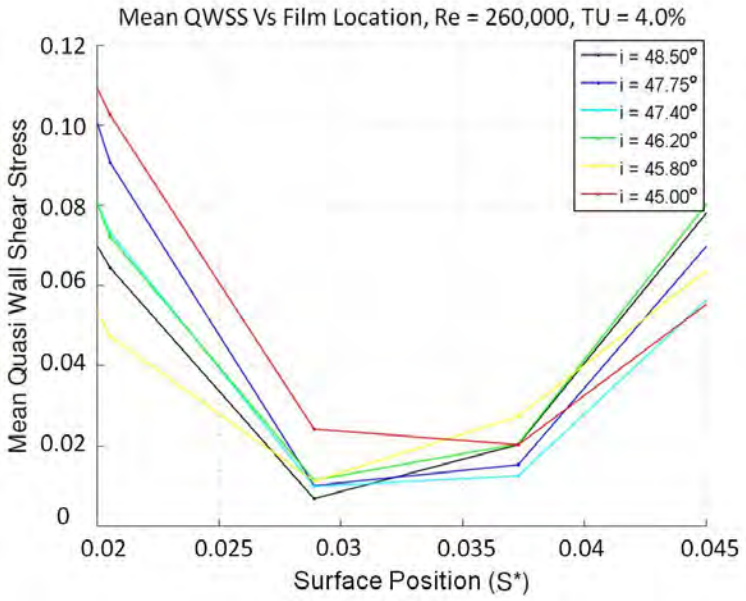

Figure 6.9: Time averaged quasi wall shear stress in region where leading edge separation bubbles are seen to form

resulting in the formation of a separation bubble and transition at the leading edge. Velocity overspeeds can be removed with appropriate leading edge designs [22].

6.4 Effect of periodic unsteadiness on blade pressure loss loops

There is a fundamental difference in the shape of the loss loop seen in Henderson's experimental work, those predicted by MISES and results obtained from the compressor cascade used in this thesis. The differences seen are believed to stem from the fact that Henderson's work was done in a 1.5 stage axial compressor where unsteady wake passing events were shown to have a significant impact on boundary layer transition, separation and development.

The characteristic difference in shape is seen near the stator blades design point ($\alpha_1 = 45^o$) where MISES and the experimental work in this thesis show that an increase in inlet flow angle leads to a leading edge separation bubble which, in turn, leads to a sharp increase in blade pressure loss. This is not seen in the experimental data obtained by Henderson as wake passing events interfere with the formation of the leading edge separation bubble and transition processes on the blade. The compressor at UTAS has a reduced frequency of $\omega_s = 1.88$ which results in an overlap of the one wake passing event with the calmed region following the previous wake. As a result the transition onset location will continuously

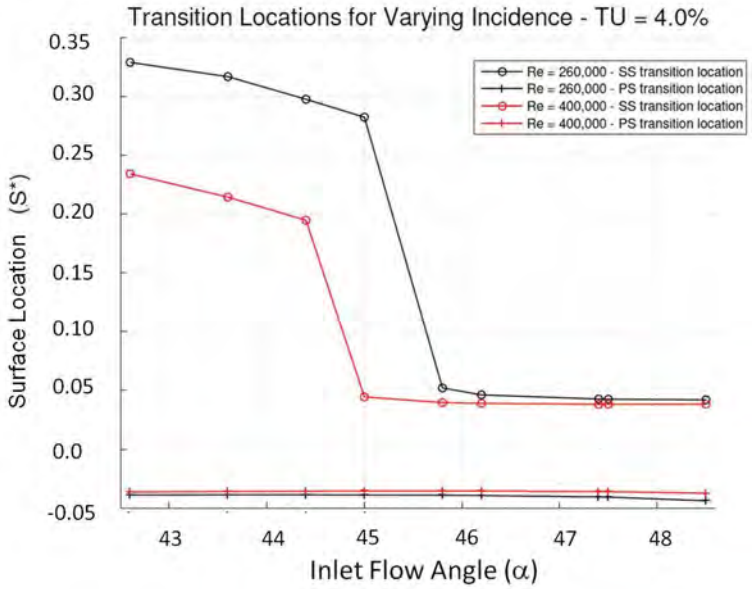

Figure 6.10: Block diagram of the MISES system

be moving and the leading edge separation will be seen to form between wake passing events and collapse as the wake passes over the leading edge. This then removes the chance of a discrete point forming where the initial transition location 'jumps' from a point near peak suction to the leading edge and as a result there is no sharp increase in loss as design incidence is passed.

6.5 Conclusions

This chapter shows that MISES makes a good attempt at predicting a number of very specific and complex flow phenomena such as the leading edge velocity over-speed, leading edge separation bubbles on the suction and pressure surfaces as well as trailing edge separations at high values of inlet flow angle - especially considering the minimal computational resources it requires.

Due to the previously mentioned lack of static pressure tapping resolution on the blade (Section 5.4) the experimental and computational Cp distributions will show some differences. The leading edge velocity over-speed is well represented by MISES and both data sets show the same trend in this region and around peak suction.

The Reynolds number dependency of the separation bubbles predicted by MISES displays the same trend as in the experimental results however the change in bubble size with in-

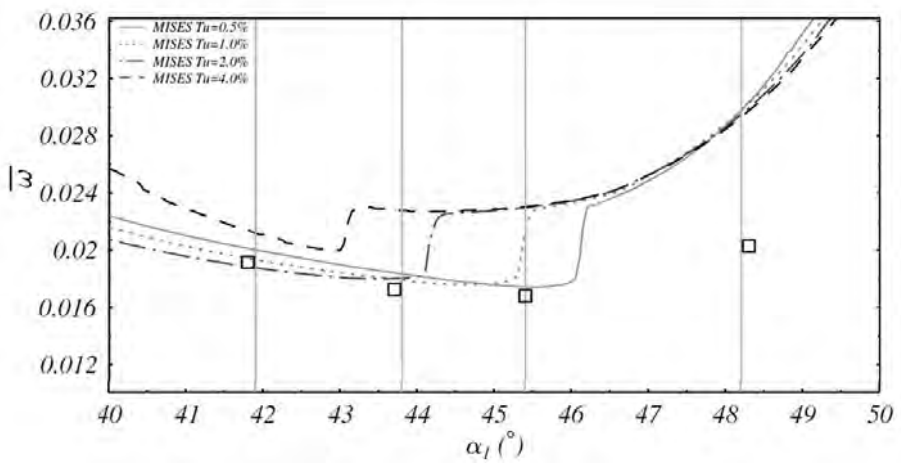

Figure 6.11: Loss loop plot from MISES and time averaged unsteady experimental data obtained by Henderson [30] showing the change in blade pressure loss with increasing inlet flow angle

creasing incidence is under-estimated with an almost constant bubble size predicted on both surfaces. The pressure surface bubble was seen to significantly decrease in length with an increase in inlet flow angle and the opposite trend was seen on the suction surface when a bubble formed at values of inlet flow angle above $\alpha_1 = 45^o$. This leads to an effective overestimate of bubble length at low Reynolds numbers by MISES leading to an increase in the proportion of blade pressure loss.

MISES is not capable of predicting boundary layer relaminarisation, which is clearly present on the suction surface leading to peak suction, particularly at low to moderate values of inlet flow angle and low Reynolds numbers. As a result MISES over predicts the turbulent wetted area on the blades surface when transition occurs in the leading edge region.

Overall MISES is a very useful tool to obtain a gauge on blade profile performance but its short falls must be taken into account. When increasing inlet flow angle from negative to positive incidence both experimental and predicted trends are very similar. It does not, however, predict the distribution of loss at some inlet flow angles over a range of Reynolds number accurately which may become problematic in future designs stages.

Chapter 7

Effects Of Changing The Stator Reduced Frequency Of A Compressor Cascade At Design Conditions

7.1 Introduction

Studies on high lift low pressure turbines have shown, by introducing periodic wake induced unsteadiness, a blade that performed poorly under steady flow conditions could produce up to 15% more lift and less loss than the datum steady flow test case. A large separation bubble formed downstream of peak suction in steady conditions, which was periodically suppressed by wake passing events, significantly reducing losses generated within the boundary layer [78, 11, 42].

Volino [92] studied the effect of changing the wake passing frequency with high and low free-stream turbulence conditions at two Reynolds numbers. At low wake passing frequencies the boundary separated between wakes as was observed under steady flow conditions. At an increased Reynolds number and freestream turbulence level, a lower reduced fre-

quency was required to largely suppress the separation. This supports previous studies that showed increasing Reynolds number and freestream turbulence level reduces the likelihood of a boundary layer separating and increases the likelihood of it reattaching once separated.

Howell [41] investigated the effect of varying reduced frequencies with an ultra high lift LP turbine blade profile in cascade. Results showed that as the reduced frequency and Reynolds number were increased a significant decrease in loss was seen. Five reduced frequencies were tested ranging from $\omega_s = 0 - 1,1$ over a range of Reynolds numbers from $Re_c = 70,000$ to $Re_c = 210,000$ and the profile loss was seen to decrease by up to a factor of approximately 2.5.

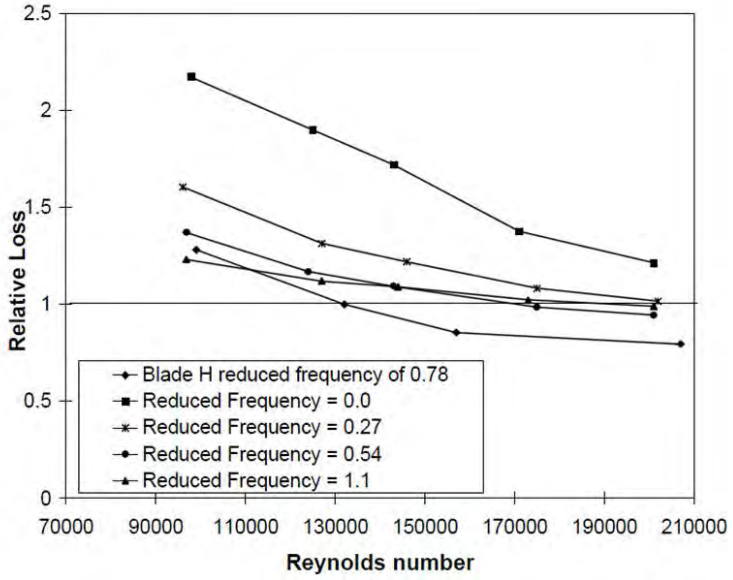

Figure 7.1: Effect of Reynolds number and reduced frequency on LP turbine blade profile loss [41]

The decrease in loss is linked with the size of a separation bubble that formed in the decelerating portion of the suction surface downstream of peak suction.

The effect of reduced frequency increase on loss was seen to decrease as the Reynolds number was increased because this leads to a decrease in the size of the separation bubble that re-formed in between wake passing events. As a wake event passed through the bubble which formed between wake passing events, the bubble collapsed and the resulting loss per unit area decreased. It was also shown that an optimum value of reduced frequency exists for a particular operating condition. Howell [41] showed that if this is exceeded the benefits gained from suppressing separated flow regions become outweighed by the increase in the proportion of the blade surface covered by wake generated turbulent flow (Figure 7.1). A

similar effect was seen when artificially generated turbulent spots were convected through a separated shear layer.

Varying the rotor wake passing frequency strongly influences boundary layer development and transition between wake passing events when one wake induced transitional strip overlaps the calmed region following the previous transitional strip. By removing a blade from the upstream rotor blade row Halstead *et al.* [27] showed that once the calmed region passed a laminar separation bubble formed inducing transition upstream of the transition location observed in the calmed zone.

A number of authors have shown that steady CFD predictions match well with unsteady experimental results in rotating compressors [30] and [22]. The difference in loss was expected to be due to the detrimental effect of the wake being balanced by the calmed region that follows the wake event over the blade surface and through the periodic suppression of separation bubbles at off design operating points - particularly in the leading edge region. In these experimental programs, the frequency of wake passing events at a given operating point was not changed. The current study aims to identify the effect of varying the stator blade's reduced frequency at a fixed flow coefficient and to identify how this change influences boundary layer development and blade pressure loss. In many numerical models transition is ignored and a fully turbulent boundary layer is defined from the blade leading edge resulting in an increased turbulent wetted area compared to the flow over a real blade. This increases rate of loss generation over portions of the blades suction surface that would be transitional in nature, resulting in an increase in blade pressure loss.

The pitchwise averaged inlet flow angle tested in this investigation is $\alpha_1 = 45.5^o$ (positive incidence $i = 0.5^o$) and based on results from Chapter 5, and from MISES predictions, a small separation bubble is expected to form at the leading edge of the suction surface under steady flow conditions. A separation bubble will also form on the pressure surface.

The introduction of unsteady wakes will influence the inlet flow angle to the compressor cascade. Figure 7.2 displays how a wake passing event alters the velocity triangle of the flow at the inlet of the blade row. The result is a periodic increase in inlet flow angle such that $\alpha_{1w} > \alpha_1$.

Wheeler [98] reported that wake passing events also lead to a local migration of the leading edge streamline and that this can lead to a local increase in incidence of up to 15^o (Figure 7.3). This local and periodic change in incidence is believed to make the separation bubble pulsate. The bubble initially grows as the wake approaches the leading edge where its potential field increases the inlet flow angle, the bubble is then suppressed as the wake passes over the leading edge region until it convected downstream where the bubble re-

forms to a similar size as that seen in a steady flow environment.

In the absence of a boundary layer separation the periodic passing of a wake increases the local time varying and time averaged incidence on to the blades in cascade. Wakes convect over the blades as a highly unsteady anisotropic turbulent strip [84] and as the wake encounters the blade's leading edge it is chopped, before circulation within a blade passages stretches and deforms it. Due to the velocity differential between the suction and pressure surfaces the wake segments move at different velocities on their respective surfaces.

Gostelow and Thomas [25] identified that the adverse pressure gradient imposed on a flat plate caused strong amplification of instabilities upstream of a separated flow region. These instabilities developed into turbulent spots inside the shear layer of a separation bubble, which eventually turned into a fully three-dimensional turbulent boundary layer.

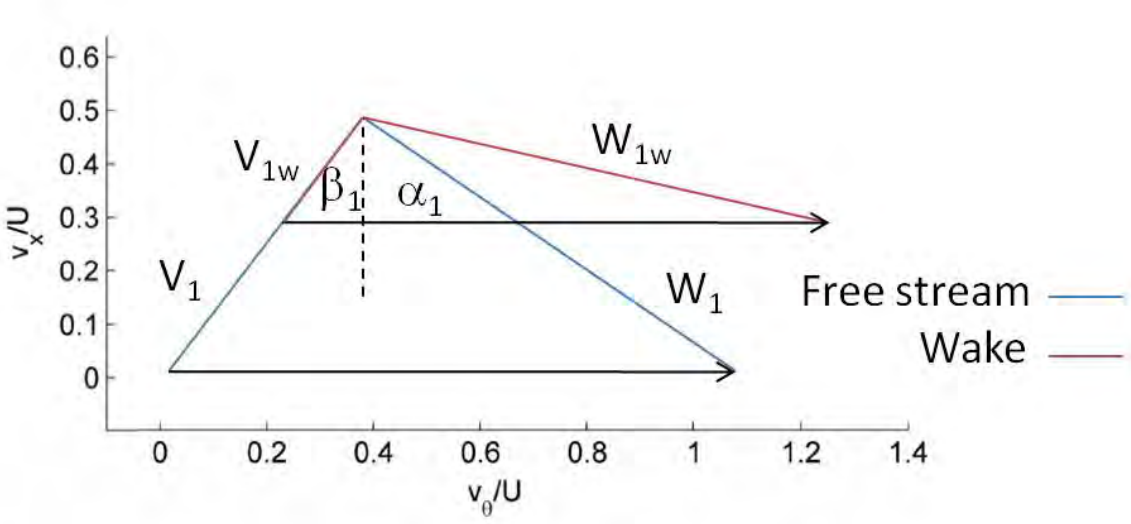

Figure 7.2: Effect of passing wakes on the inlet flow angle α_1 of a stator blade row

The ability of turbulent wake passing events to favorably influence the performance of turbomachinery blades is highly dependent on the size and location of separated flow regions. Away from the point of stall, compressors with blade geometries representative of that seen in real engines rarely see large separated flow regions under steady flow conditions, particularly near the design operating point, unlike highly loaded turbine blades. The largest reported on this blade occurred at the leading edge of the pressure surface at negative incidence and a low Reynolds number. As a result the likely gains in performance are expected to be lower that that seen in turbines without radical changes in blade profiles.

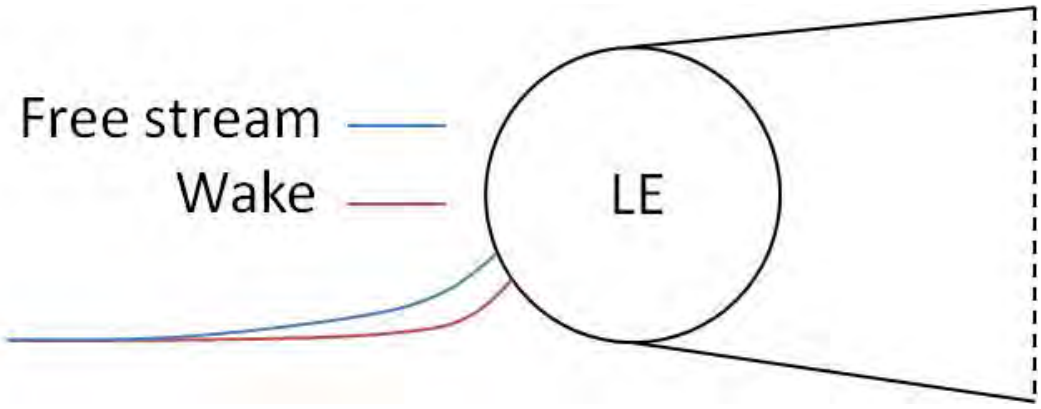

Figure 7.3: Effect of passing wakes on the leading edge stagnation streamline of a compressor stator blade row

7.2 Scope Of Investigation

Initial testing was intended to repeat the test conditions carried out by Henderson [30] in the research compressor at the University of Tasmania. As described in Section 3.2.3 three stator reduced frequencies were tested: $\omega_s = 0.47, 0.94$ and 1.88 at an inlet flow angle of $\alpha_1 = 45.5^o$, Reynolds number based on blade chord of $Re_c = 230,000$ and a freestream turbulent intensity of 4.0%. These values of reduced frequencies were chosen to cover a range centered around $\omega_s = 0.84$ - the value for a stator blade in an embedded stage of a large three-spool turbofan engine and was provided by Rolls Royce Pty. A value of $\omega_s = 1$ was identified as a target for compressor designers [40].

Figures 7.4(a) - 7.4(c) show the difference in wake passing period with an increase in stator reduced frequency. Lines are superimposed onto the plots to identify how long a particle would take to convect over the blade's surface at the freestream velocity. This gives a clear indication of how increasing reduced frequency increases the number of wake passing events present on the surface at any one time.

A range of measurements will be used to look at the blade's performance such as; time averaged surface static pressure measurements, inlet and exit 3-hole probe traverses and instantaneous, ensemble averaged and time averaged hot-film data for the calculation of turbulent intermittency and quasi wall shear stress.

Figures 7.5 and 7.6 show the distribution of inlet and exit flows through the cascade over the range of reduced frequencies tested showing a good level of periodicity.

The range of tests in the unsteady data set was limited by a number of uncontrollable

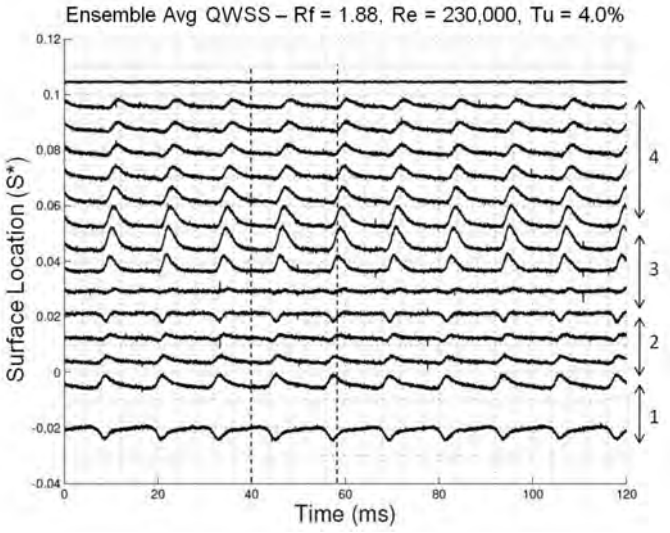

(a) $\omega_s = 1.88$

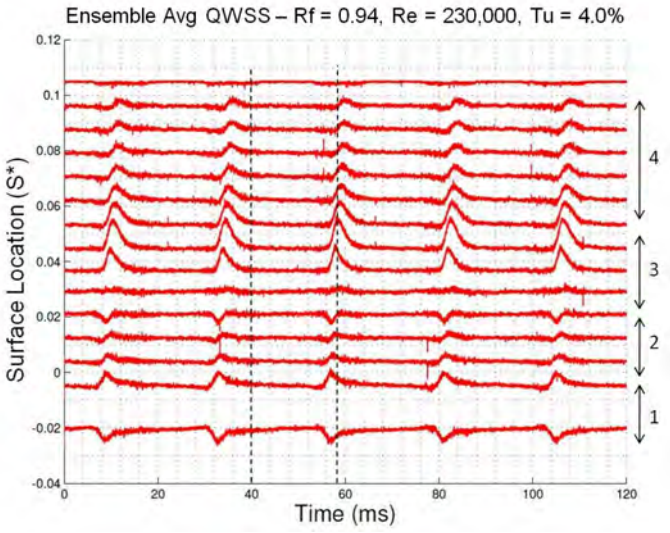

(b) $\omega_s = 0.94$

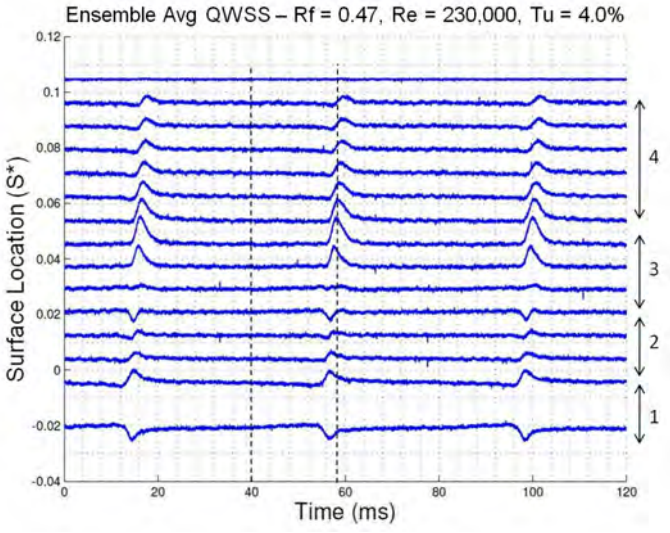

(c) $\omega_s = 0.47$

Figure 7.4: Ensemble averaged quasi wall shear stress traces for a stator reduced frequency of $\omega_s = 0.47$, 0.97 and 1.88

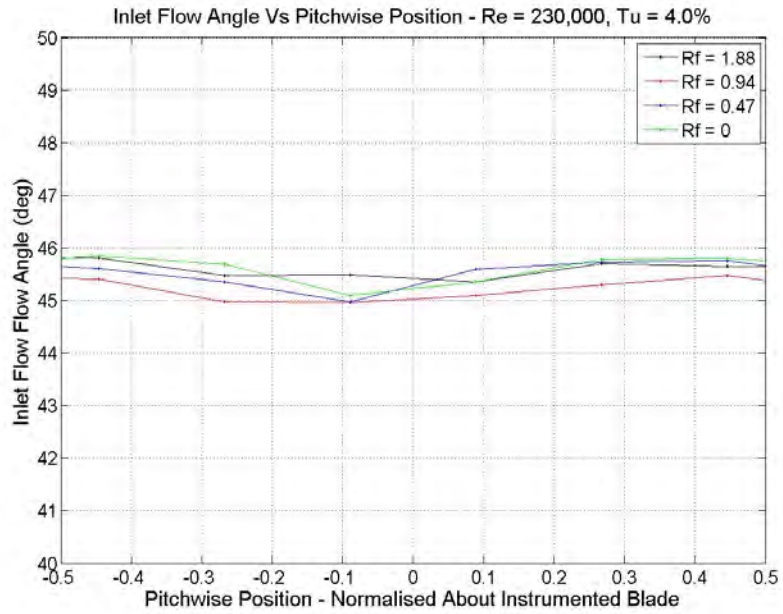

Figure 7.5: Distribution of inlet flow angle of the cascade with varying stator reduced frequency

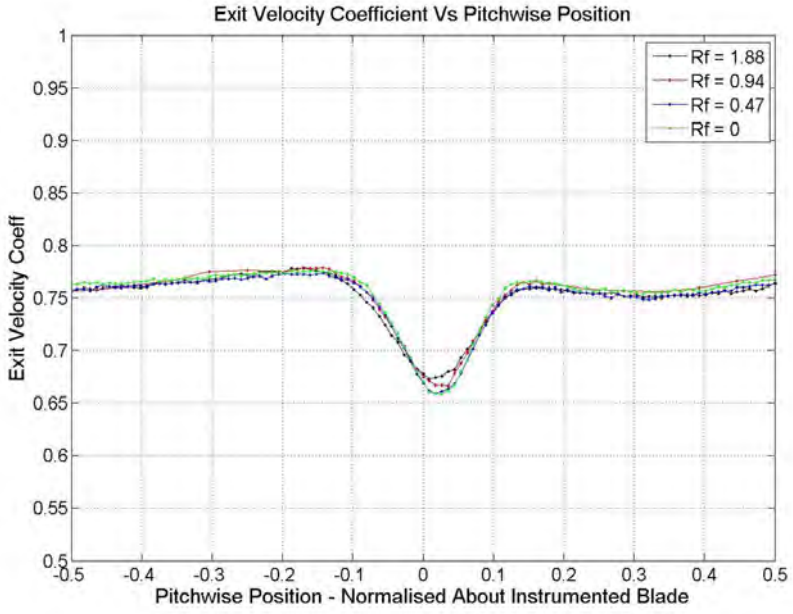

Figure 7.6: Distribution of exit velocity coefficient of the cascade with varying stator reduced frequency

factors. Strict time constraints were in place and as a result the unsteady experimental program was limited to testing at a single inlet flow angle.

7.3 Expected Steady Flow Performance at $\alpha_1 = 45.6^0$ and $Re_c = 230,000$

To create a baseline case, results from steady tests discussed in Chapter 5 are used to ensure consistency with results obtained when operating the cascade in an unsteady operating condition. In between wake passing events following the calmed zone region, trends in boundary layer development and blade pressure loss should return to values close to those observed under steady conditions, particularly at low reduced frequencies, where there is a large gap between the calmed region of one wake, and the wake induced turbulent strip generated by the following rotor blade or rotating bar [92].

Chapters 5 and 6 identified that at $\alpha_1 = 45.8^o$ and $Re_c = 260,000$ the suction surface boundary layer formed a small separation bubble in the decelerating portion of the velocity overspeed. Within the bubble, rapid transition occurred, increasing the turbulent intermittency to a value of $\gamma = 1$, which is indicative of a fully turbulent boundary layer. Downstream of the spike the newly turbulent boundary layer was relaminarised in the suction surface's favorable pressure gradient where the turbulent intermittency decreased to a value of approximately $\gamma = 0.5$. The favorable pressure gradient then relaxed prior to peak suction where final transition occurred and a fully turbulent boundary layer was then maintained to the trailing edge.

On the pressure surface, under the same conditions, the boundary layer separated at the leading edge and underwent transition within the separation bubble. As there is no significant favorable pressure gradient on the pressure surface, the boundary layer remained in a fully turbulent state until the trailing edge of the blade.

During unsteady testing, the Reynolds number was set at $Re_c = 230,000$ - lower than both steady test cases in Chapter 5. Decreasing the Reynolds number increases a boundary layer's likelihood of separation at a given inlet flow angle and a separation bubble will form at a lower value of incidence. In steady test cases an inlet flow angle of $\alpha_1 = 45.8^o$ was used, which compared to the unsteady test value of $\alpha_1 = 45.5^o$ should lead to an increased likelihood of a leading edge separation forming. Combining the differences in Reynolds number and inlet flow angle should lead to a very similar trend in the boundary layer development and loss generation. Comparing Figure 5.17 to Figure 7.14 confirms this and

at a reduced frequency of 0 there was a difference in blade pressure loss of $\triangle\overline{\omega} = 0.0001$ compared to the steady case with $Re_c = 260,000$ and $\alpha_1 = 45.8^o$.

A small separation bubble was thus expected to form at the leading edge at an inlet flow angle of $\alpha_1 = 45.5^o$ and $Re_c = 230,000$, triggering rapid transition of the boundary layer before the favorable pressure gradient of the suction surface relaminarised it from approximately $\gamma = 1 - 0.5$.

The formation of a separation bubble and leading edge transition is supported by results from MISES, which predicts that a leading edge separation bubble forms at the leading edge of both surfaces under both sets of steady conditions mentioned above. The separation bubble is slightly smaller for the $Re_c = 230,000$.

Based on findings from Chapter 5 boundary layer relaminarisation will be slightly more effective at $Re_c = 230,000$ compared to $Re_c = 260,000$.

Between wake passing events, after the calmed zone, the ensemble averaged distribution of intermittency is expected to resemble that of the equivalent steady flow case, which is confirmed in Figure 7.13.

7.4 Effect of Reduced Frequency on Leading Edge Velocity Spike

The leading edge velocity over-speed has a large influence over blade performance and loss generation (Section 5 and 2.7). Figure 7.7 shows that the suction surface spike height (point of maximum velocity in the spike) grows with an increase in stator reduced frequency. The opposite trend is seen on the pressure surface where the maximum value within the spike decreases with an increase in reduced frequency. The increase and decrease on the suction and pressure surfaces are small relative to the overall spike height.

Changes in time-averaged spike height are due to a combination of the local increase in time varying incidence at the leading edge (Figure 7.3) and an increase in the overall inlet flow angle to the cascade caused by a transfer of momentum to the inlet flow from the rotating bars as they moved in a downward direction parallel to the cascades leading edge plane. Both effects lead to an increase in incidence (Figure 7.2).

Figure 7.3 shows how the passing of a wake can increase the local time varying inlet flow angle of a blade row [98]. During this fluctuation the inlet flow angle will increase past the design point where, under steady conditions, a leading edge separation bubble would form based on observations in Chapter 5.

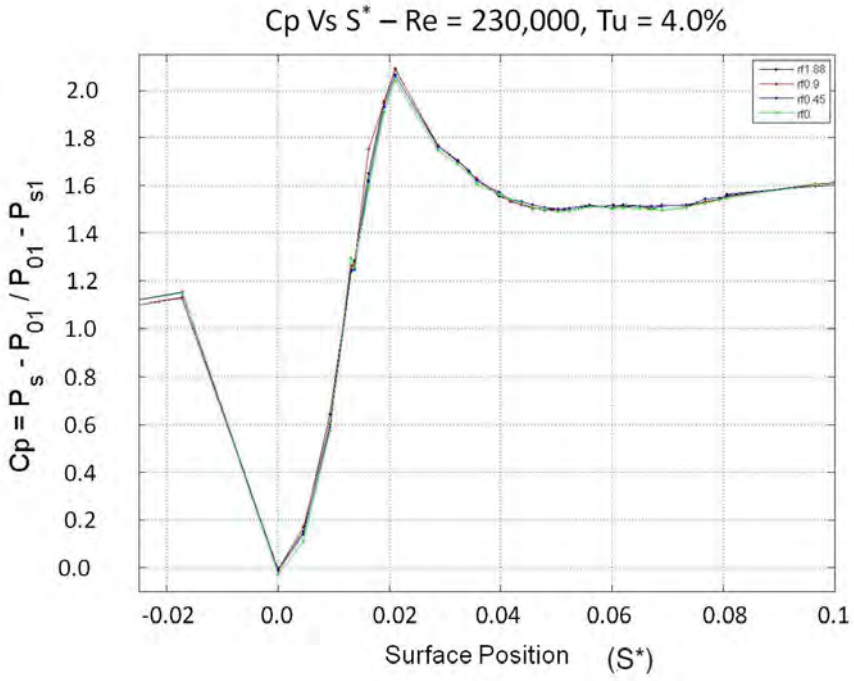

Figure 7.7: Time averaged effect of passing wakes on the leading edge velocity over-speed to the compressor cascade stator blade row

The overall shape of the static pressure distribution and thus blade loading is essentially independent of reduced frequency (Figure 7.8).

7.5 Leading Edge Boundary Layer Development

The influence of wake passing events on boundary layer development in compressors is critical as it periodically influences the location of transition, the formation/suppression of separations and the blade's turbulent wetted area.

Calculated values of turbulent intermittency and hot-film traces of quasi-wall shear stress (QWSS) were used to evaluate the state of the transitional boundary layer over the front portion of the blades suction surface. The intermittency routine developed by Solomon and Walker [83] and described in Section 4.6 was used in this investigation to determine the ensemble averaged transitional behavior of the cascade operating under unsteady conditions. The code bases its calculation on time records of voltage from the hot-film gauges, which are converted into a trace of quasi-wall shear stress using $(\tau_q = \left(\frac{E^2 - E_o^2}{E_0^2}\right)^3)$. Raw traces are also useful in providing confidence in the code through qualitative analysis and for identifying, by inspection, how the boundary layer develops over the blades surface.

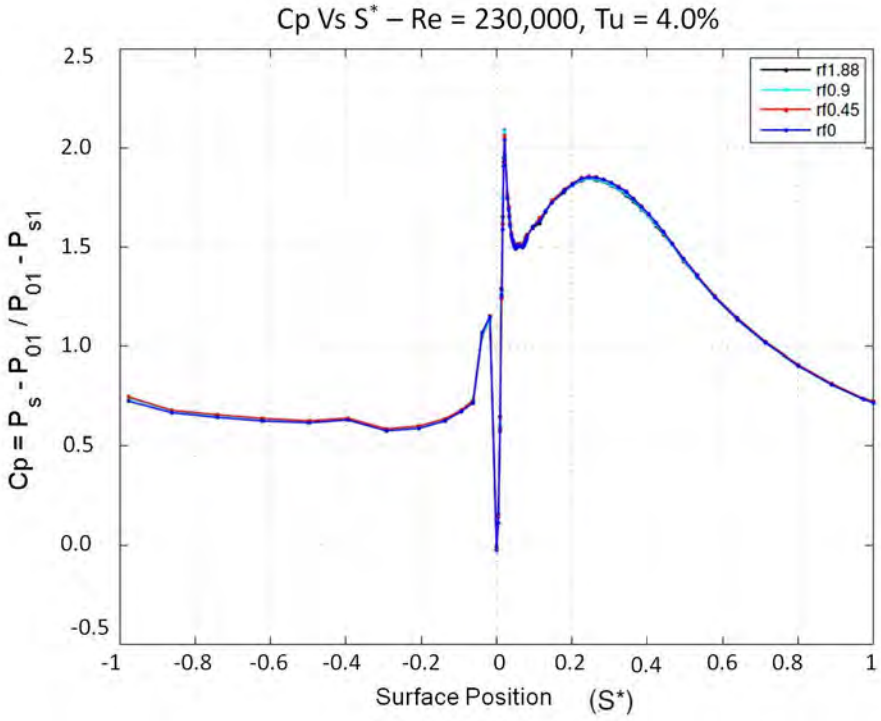

Figure 7.8: Time averaged Cp distribution over the range of stator reduced frequencies tested in the compressor cascade

It is important to view raw traces of quasi wall shear stress to evaluate the development of boundary layers over the blade surface. Raw and ensemble averaged traces are presented here to identify different trends as the boundary layer develops through the leading edge velocity spike and onto the suction surface. All quasi-wall shear stress traces are displayed as an AC component only. The AC coupling was achieved by removing the mean of each trace from the raw signal (Equation 7.1. Signals are spaced along the Y-axis based on either $S*$ or a constant factor of 5x$S*$ to avoid the overlapping of signals.

$$\tau_{qac} = \tau_q - \overline{\tau}_q \tag{7.1}$$

During the following discussion the relaminarisation of a boundary layer is defined to be a reduction in its turbulent intermittency and not the transformation of a fully turbulent boundary layer to a laminar one.

Plots of quasi-wall shear stress traces are divided into four areas highlighted on the secondary Y-axis. These correspond to: 1.) the initial portion of the pressure surface velocity overspeed, 2.) the strong favorable pressure gradient of the suction surface velocity overspeed, 3.) the extreme adverse pressure gradient of the suction surface velocity overspeed,

4.) favorable pressure gradient leading to peak suction on the suction surface. This has been done for ease of explanation in characteristically different regions of flow.

Comparing plots in Figure 7.4 with Figures 7.11(a)-7.11(c) and 7.12(a)-7.12(c) displays that each value of reduced frequency tested has a different number of wake passing events over a given period of time (t). The wake passing period decreases with an increase in reduced frequency. Referring to Figure 7.4 it is evident that following a wake passing event a calmed or region of relaxed flow exists before the ensemble average of the flow returns to its steady state value. This simplifies the actual time varying picture as can be seen in Figures 7.11(a)-7.11(c) and 7.12. Raw traces show a far less uniform distribution of quasi wall shear stress. Turbulent strips are still clearly evident as a steep increase in quasi wall shear followed by turbulent fluctuations.

Turbulent strips from wake passing events and turbulent bursts show a steep elevation in quasi-wall shear stress followed high frequency fluctuations. The quasi-wall shear stress then decreases gradually creating the calmed zone following the turbulent patch. Differences in the gradient of quasi-wall shear stress before and after a turbulent patch can clearly be seen in Figures 7.4 and 7.11(a)-7.11(c)

Figure 7.9 highlights come of the important characteristics of a wake passing event as it convects over the leading edge and early portion of the suction surface which will be discussed in detailed in the following passages.

.

The distributions of time averaged QWSS (Figure 7.10) shows that a boundary layer separation does not form continuously in the adverse pressure gradient of the leading edge spike on the suction surface. Figure 6.9 shows that under steady conditions the average value of QWSS dropped to near zero in the separated region - this trend is not present in Figure 7.10. Given that the boundary layer would separate under steady conditions the presence of wake induced turbulent strips periodically suppresses the formation of the separation bubble at the leading edge, increasing the time average value of QWSS in the separated flow region. This trend is expected based on literature previously discussed.

.

Increasing the reduced frequency changes not only the proportion of the blade's surface covered by wake induced turbulent strips at any given time, but also the calmed, laminar-like, region that follows each strip. The impact of this and its influence on boundary layer development is visible when comparing Figures 7.11(a)-7.11(c), which show raw traces of quasi-wall shear stress through the reattachment zone of the separation bubble near the end

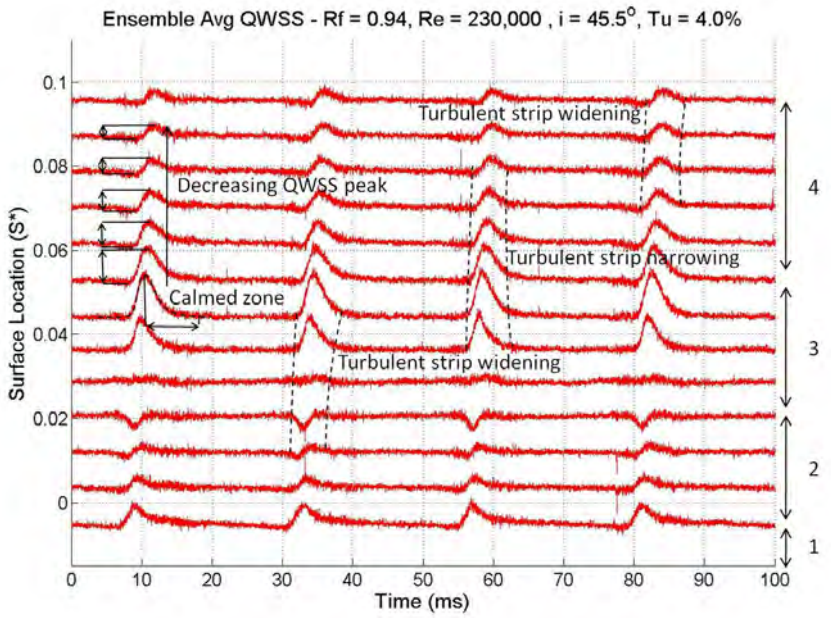

Figure 7.9: Plot of ensemble averaged QWSS with important wake characteristics highlighted

of the leading edge adverse pressure gradient and onto the very early portion of the suction surface. This region is where the most rapid amplification of turbulent fluctuations occur both inside and outside of wake passing events as shown in Figures 7.11(a)-7.11(c).

Upstream of this location in the extreme adverse pressure gradient of the spike, raw traces show a dramatic reduction in perturbations in quasi-wall shear stress between wake passing events indicative of stagnant flow, within a separated flow region, forming between wakes. A small increase in QWSS, indicative of a turbulent burst can still be seen in the trace as the wake passes through the separated region.

Dashed lines are overlaid on Figures 7.11(a)-7.11(c) and 7.12(a)-7.12(c) are approximate celerities of the wake centreline, which are to be used as a guide indicating the path of wake induced strips over the surface.

At a reduced frequency of $\omega_s = 1.88$ Figure 7.11(a) shows clearly visible wake induced turbulent strips, which have a significantly higher level of quasi-wall shear stress than the flow in between wakes. The turbulent bursts increase in amplitude and width as the wake convects over the surface through the adverse pressure gradient. Perturbations are also present between wakes, which appear to be puff-like turbulent events [31] and grow in a similar vein to the wake induced strips, however they are small in comparison.

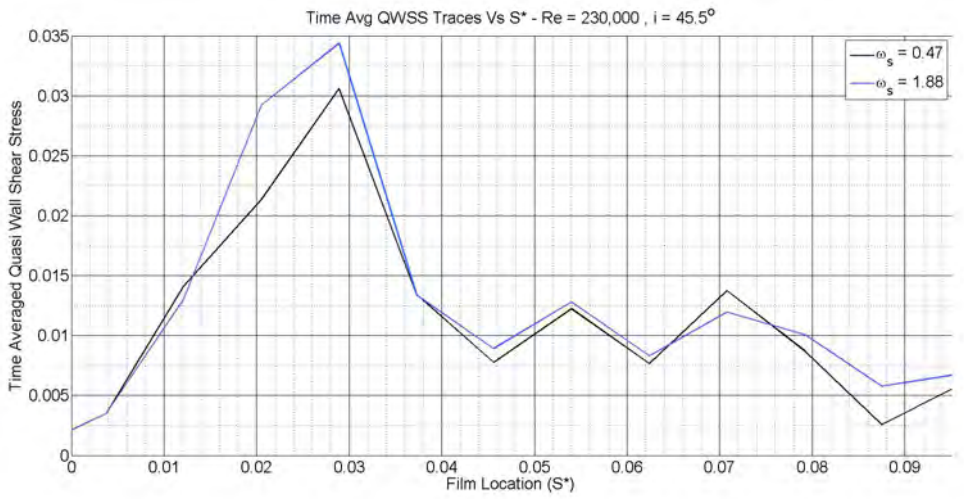

Figure 7.10: Distribution of time averaged quasi-wall shear stress over the range of reduced frequencies tested

As the stator reduced frequency is decreased to $\omega_s = 0.94$ and 0.47, Figures 7.11(b) and 7.11(c) show that by the end of the adverse pressure gradient in the leading edge overspeed, identifying wake passing events from turbulent bursts developing between them became increasingly difficult.

At a reduced frequency of $\omega_s = 0.94$ a very similar amplification in quasi-wall shear stress during a wake passing event was observed as at $\omega_s = 1.88$. In between wake passing events however, turbulent bursts are more prevalent and appear to be amplified more vigorously. By $5x S^* = 0.36$ in Figure 7.11(b) turbulent bursts developed away from wake passing events become comparable not only in appearance but also in size to wake induced turbulent strips.

At $\omega_s = 0.47$ wake induced turbulent strips are almost indistinguishable from turbulent bursts between wake events on the trace located at $5x S^* = 0.36$ (Figure 7.11(c)). The number of perturbations present near the separated flow region increases and each of these are heavily amplified in the adverse pressure gradient following. By the start of the favorable pressure gradient of the suction surface the boundary layer appears to be made up of a large number of turbulent events, most of which are similar in magnitude and appearance - including the wake induced turbulent strips. There is also evidence of adjacent turbulent bursts merging in a larger turbulent patch of flow.

Some typical cases are highlighted in Figure 7.11(c) where it is impossible, given a single trace, to identify wake induced turbulence from that developed between wake passing events.

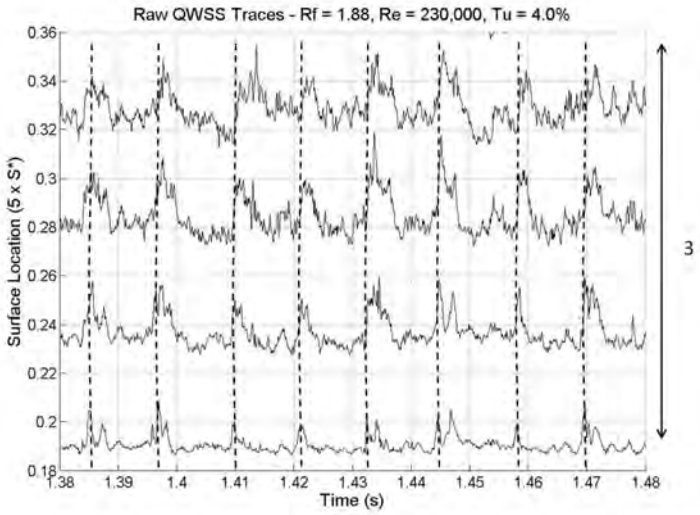

(a)

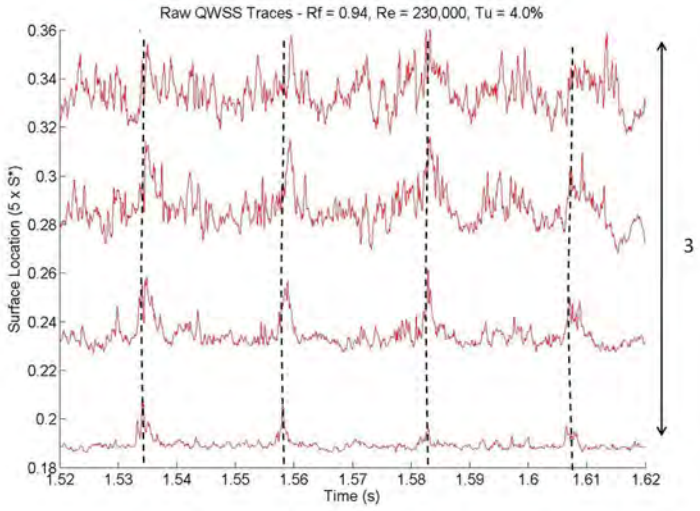

(b)

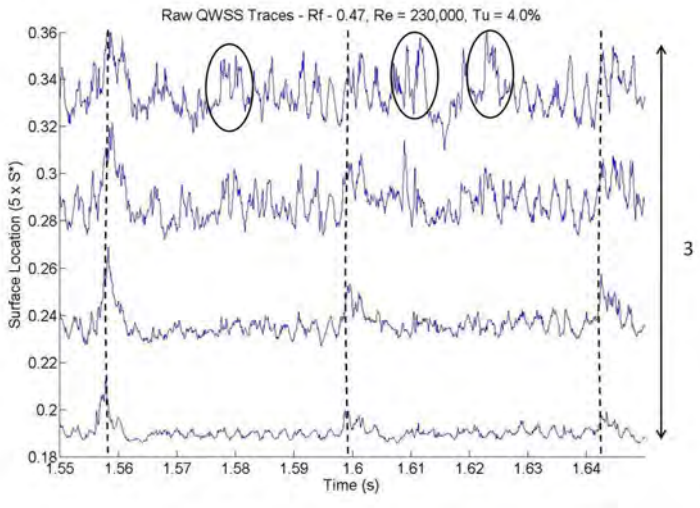

(c)

Figure 7.11: Close up of raw traces of quasi wall shear stress for a stator reduced frequency of $\omega_s = 0.47$, 0.97 and 1.88 in (a.), (b.) and (c.) respectively in the adverse pressure gradient of the leading edge spike (Section 3 - Figure 7.9)

This demonstrates that by reducing stator reduced frequency and increasing the wake passing period, the boundary layer in the leading edge spike and early portion of the suction surface is more susceptible to transition and the development of turbulent bursts in between wake passing events. This is a likely result of the decrease in the proportion of calmed flow between wake passing events. It also highlights how powerful the calmed region is at suppressing the development of turbulence within a boundary layer.

Further downstream the boundary layer accelerates (Section 4) towards peak suction in the favorable pressure gradient on the suction surface. This region has previously been shown to significantly relaminarise a turbulent boundary layer at a similar operating point in steady flow (Chapter 5) and a similar trend was observed during unsteady operation. Ensemble averaged plots of quasi-wall shear stress and intermittency in Figures 7.4 and 7.13 show this clearly and the damping of specific turbulent events can also be seen in Figures 7.12(a)-7.12(c).

Figure 7.13 displays the contour plot of ensemble averaged turbulent intermittency, which immediately demonstrates the transitional nature of the leading edge boundary layer under the influence of unsteady wake passing events. A strip of elevated turbulent intermittency ($\gamma = 1$) was formed in the decelerating portion of the spike in the region where a laminar separation bubble formed under steady flow conditions. This turbulent strip is followed by significant relaminarisation on the suction surface where γ reduced from a value close to unity to approximately 0.5 (Figure 7.13). This is consistent with predictions made in Section 7.3 and through comparisons with traces of quasi-wall shear stress provides confidence in the turbulent intermittency routine.

Wake passing events captured in each ensemble are consistent and spaced equally in time (Figure 7.4 and 7.13). A wake induced turbulent strip is visible from the leading edge to the end of the hot-film sensor array on both surfaces and have a higher level of intermittency than the surrounding flow.

In the two regions of accelerating flow on the suction surface (regions 2 and 4) between the stagnation point and the peak of the velocity spike, and downstream of the velocity spike leading to peak suction there is a narrowing of the wake induced turbulent strip. The opposite is observed in regions of decelerating flow (3) with the turbulent strips widening in this region [31]. The wake passing event is thinnest at the peak of the velocity overspeed following the extreme favorable pressure gradient and is widest at the end of the adverse pressure gradient of the velocity overspeed. These trends are also highlighted in Figure 7.9.

The favorable pressure gradient of the suction surfaces changes significantly between the end of the velocity overspeed and peak suction. Of particular note is the region between

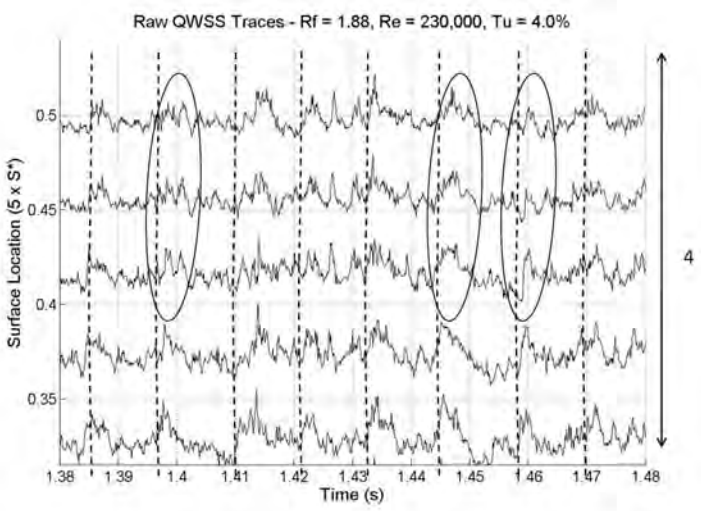

(a)

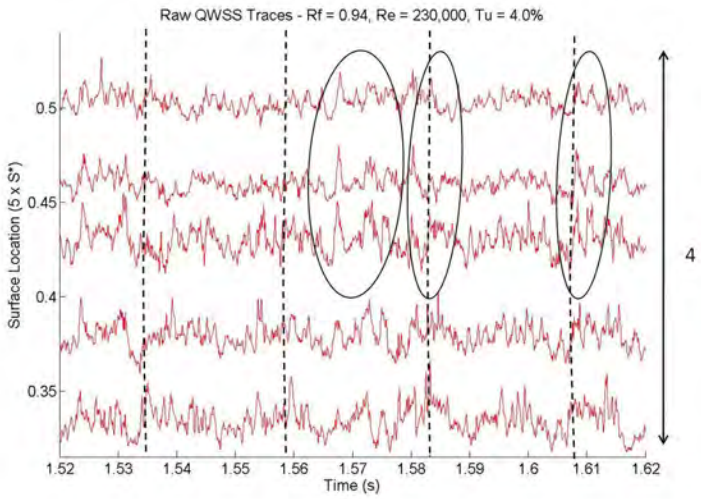

(b)

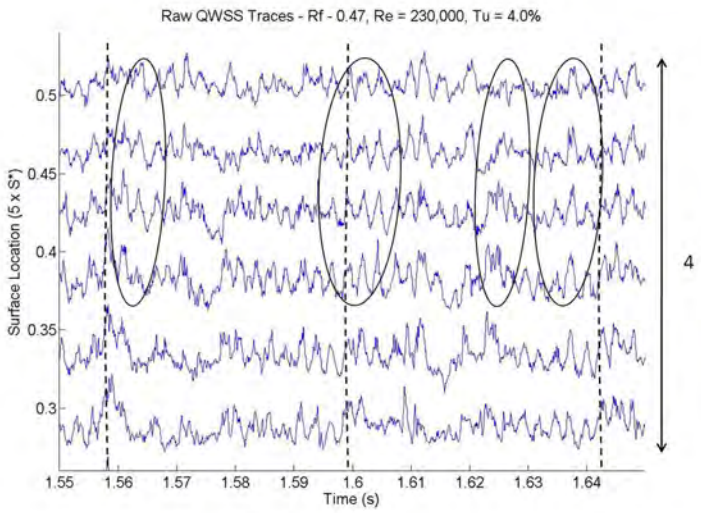

(c)

Figure 7.12: Close up of raw traces of quasi wall shear stress for a stator reduced frequency of $\omega_s = 0.47$, 0.97 and 1.88 in (a.), (b.) and (c.) respectively through the favorable pressure gradient on the suction surface leading to peak suction (Section 4 - Figure 7.9). Turbulent events damped by the favorable pressure gradient are highlighted

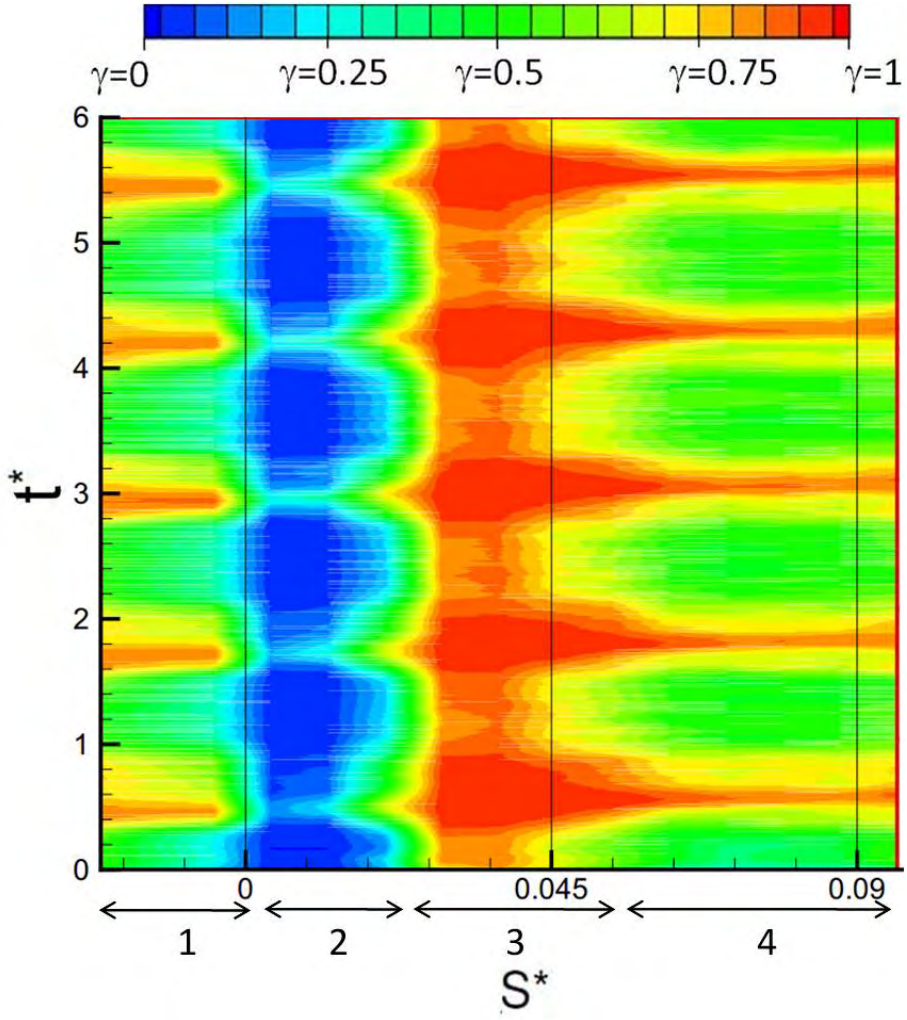

Figure 7.13: Ensemble average distribution of turbulent intermittency in the leading edge region at $\alpha_1 = 45.5^o$, $Re_c = 230,000$ and $Rf = 0.94$ in the compressor cascade

$S^* = 0.06 - 0.08$ where Figures 7.7 and 7.8 show a steep increase in pressure gradient. Downstream of $S^* = 0.08$ the pressure gradient relaxes, which results in not only a mild increase in intermittency but a widening of the wake induced turbulent strips. This relaxation is also shown in Figure 7.10 where a decrease in time average QWSS is observed. This is connected with an increase in boundary layer thickness in an accelerating boundary layer.

The intermittency level of the wake induced turbulent strip is also influenced by pressure gradients and follows the same trend as the flow between wake passing events. It is apparent from Figures 7.4, 7.13 and 7.11(a)-7.11(c) that pressure gradients have a greater influence over the relaminarisation of flow between wake passing events with a significantly greater reduction in intermittency observed even though, at the end of the velocity overspeed, both regions of flow have similar levels of intermittency. This ties in with the stabilising and

destabilising effect of favorable and adverse pressure gradients respectively, and suggests that a newly turbulent or advanced transitional boundary layer is more susceptible to relaminarisation compared to a well established turbulent strip such as that from a wake passing event.

The turbulent intermittency at particular blade surface locations varies with time in between wake passing events. Referring to Figure 7.13 at a surface location between $S^* = 0.05 - 0.06$, the plots of ensemble average intermittency show that following a wake passing event (wakes travel from top to bottom) there is a more gradual decrease in intermittency following the wake - evidence of a calmed region following each wake passing event as seen by Henderson and Walker [31], Gostelow and Thomas [25]. This supports previous discussions that focussed on traces of QWSS.

7.6 Effect of Stator Reduced Frequency on Blade Pressure Loss

Blade pressure loss is an important measure of blade performance especially when making comparisons between different machine operating points. Figure 7.14 shows how the nominal time average blade pressure loss varies with an increase in stator reduced frequency from $\omega_s = 0 - 1.88$ at a fixed flow coefficient of $\phi = 0.675$.

At a reduced frequency of 0 (steady flow case) the experimentally determined blade pressure loss is 0.001 or 0.5% higher than the closest test case ($\alpha_1 = 45.8^o$, $Re_c = 260,000$) described in Chapter 5.

Increasing the stator reduced frequency to $\omega_s = 0.4$ results in a slight increase in the experimentally determined blade pressure loss of 0.0002. In the closest steady test case from Chapter 5 an equivalent increase in loss would require an increase in inlet flow angle of approximately 0.47^o. Doubling the reduced frequency to $Rf = 0.94$ lead to a sharp rise in loss of 0.0005. The same value of loss under steady conditions was observed at an inlet flow angle of approximately $\alpha_1 = 47^o$ and $Re_c = 260,000$. Further increasing reduced frequency to $\omega_s = 1.88$ blade pressure loss continues to increase, however by a lesser amount of 0.0003 to a final value of 0.0233.

Increasing the stator reduced frequency from $Rf = 0 - 1.88$ brought about an overall increase in loss of 4% or $\triangle\omega = 0.001$ from the steady state baseline case.

Comparing this to the loss loop data from Chapter 5, it is the equivalent to a blade operating at an inlet flow angle of $\alpha_1 = 47.5^o$ and a Reynolds number of $Re_c = 260,000$. Under these

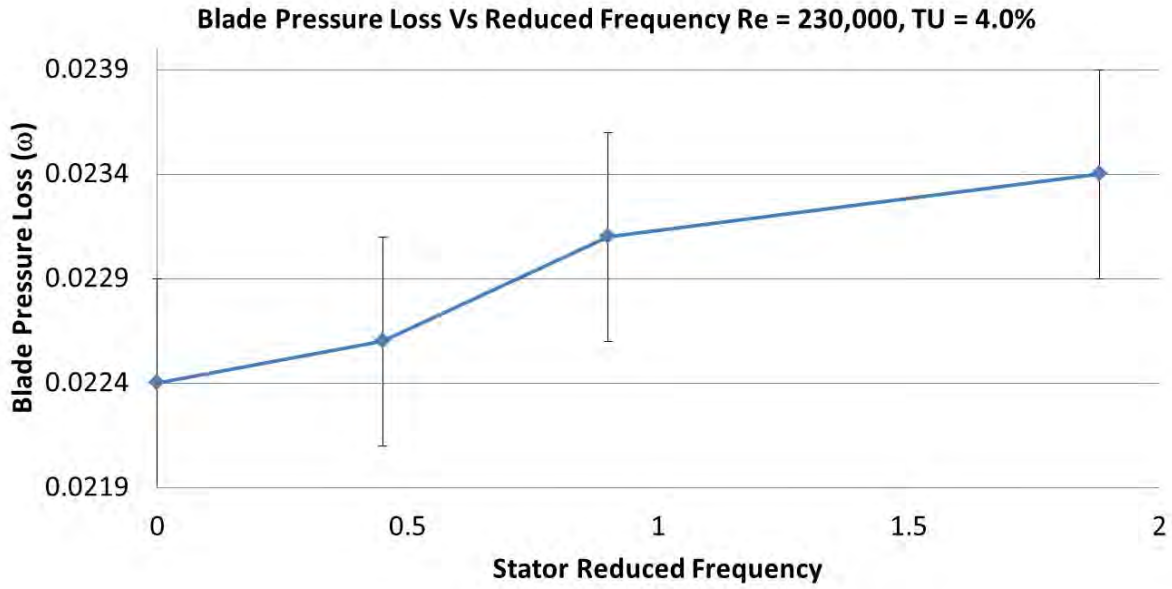

Figure 7.14: Effect of reduced frequency on blade pressure loss of a compressor stator blade row

conditions a separation bubble clearly formed on both blade surfaces initiating transition just downstream from the leading edge in the adverse pressure gradient of the spike. The pressure surface remained in a fully turbulent state to the trailing edge whilst the suction surface displayed a large turbulent patch after the leading edge spike before relaminarising to a value of approximately $\gamma = 0.65$ in the favorable pressure gradient leading to peak suction. As the favorable pressure gradient relaxed transition to fully turbulent flow occurred in the peak suction region. A trailing edge separation did not occur.

The overall loss loop shown in Figure 7.14 provides information about the overall performance of the blade only and the experimental uncertainty is large compared with the changes identified. Figure 7.15 helps identify how the overall blade pressure loss is distributed between the pressure and suction surfaces, which is important when identifying the main mechanisms behind loss generation under varying operating conditions - such as interpreting the influence an increase in the frequency of wake passing events has on the performance of the stator. The relative uncertainly in the surface specific loss generation is small.

From Figure 7.15, a definite trend is present on both surfaces. The influence of increasing the stator reduced frequency has an opposite effect on each surfaces of a CD stator with a

circular arc leading edge.

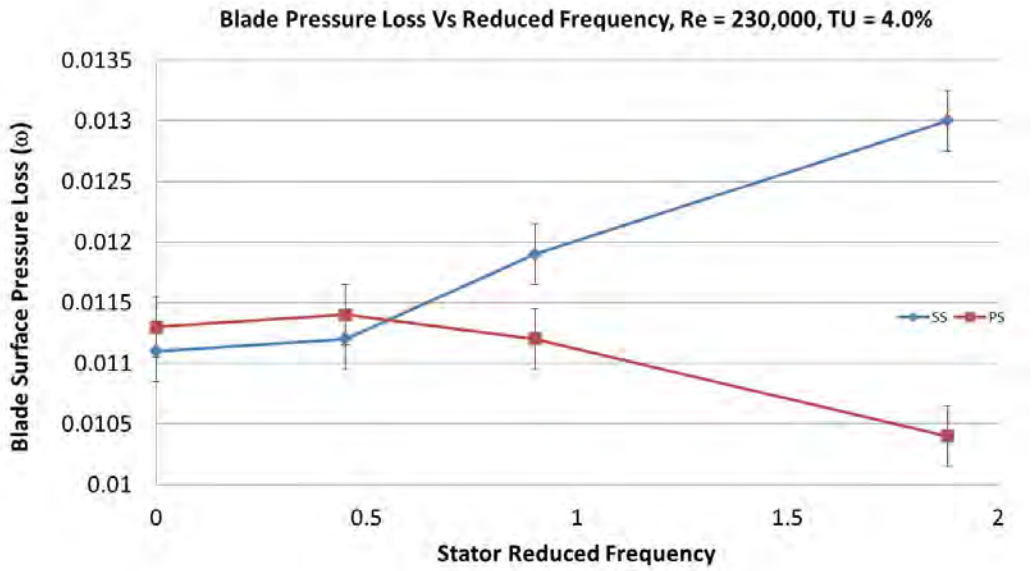

Figure 7.15: Breakdown of loss generated by the suction and pressure surfaces of the blade

7.6.1 Pressure Surface Loss

When moving from a steady to unsteady flow environment with a stator reduced frequency of $\omega_s = 0.44$ the loss generated by the pressure surface remains almost constant.

Downstream of the leading edge the pressure surface boundary layer is fully turbulent and remains in that state to the trailing edge.

Wakes travelling along the pressure surface appear as a positive jet, transporting fluid into the boundary layer which thickens it, increasing local loss generation. A calmed region follows the wake passing event as is convects over the surface which displays a similar velocity profile to a turbulent boundary layer, but with a loss production rate comparable to that of a laminar boundary layer (Section 2.4.1). It is possible that the benefits of the calmed region could, in a fully turbulent boundary layer, lead to a decrease in loss compared to the steady flow condition as there is no increase in turbulent wetted area caused by the presence of a wake.

Wake passing events and turbulent spots are known to suppress the formation of separation bubbles: a leading edge separation bubble was present under the current test conditions in

steady flow. The periodic suppression of the leading edge bubble reduced the local rate of loss generation compared to that under steady flow conditions.

As the reduced frequency is increased from $\omega_s = 0.44$ to 0.9 and 1.88 there is an almost linear decrease in blade pressure loss generated by the pressure surface. The increase in reduced frequency decreases the amount of time the leading edge separation bubble has to re-form in between being suppressed by wake passing events and thus decreases the ensemble average loss generation in this region.

Also as mentioned in Section 7.4 a slight increase in reduced frequency leads to an increase in time averaged inlet flow angle, which corresponds to a decrease in the pressure surface spike height and a reduction in the leading edge bubble length.

7.6.2 Suction Surface Loss

On the suction surface pressure loss follows an almost identical, but opposite trend to that seen on the pressure surface when introducing periodic unsteadiness at a stator reduced frequency of $\omega_s = 0.44$.

At a reduced frequency of $\omega_s = 0.44$ a wake induced turbulent strip is present on the surface 44% of the time resulting in the blade having no influence from a wake passing event for 66% of the time - during which the blade resumes a similar characteristic to that seen in steady operation.

On the suction surface the wake is seen as a negative jet and has a thickening effect on the boundary layer and boundary layer fluid is transported away from the surface.

A separation is expected to form, in between wake passing events, where the flow resumes a steady flow-like intermittency distribution 7.3. During a wake passing event the separation bubble is suppressed, as the wake convects through the leading edge region, resulting in a local reduction in leading edge momentum thickness - corresponding to a decrease in blade pressure loss (Section 2.7). The potential decrease in loss is offset as the turbulent wake leads to an increase in the time averaged turbulent wetted area on the suction surface. This increases the loss produced over the front half of the blade, which, between wake passing events was transitional and caused relaminarisation to occur in the favorable pressure gradient. The turbulent patch is followed by the same calmed region mentioned previously.

Increasing the reduced frequency increases the amount of time the blade is influenced by a wake passing event.

As ω_s is increased to 0.9 and 1.88 the loss produced by the suction surface increases in an almost linear fashion. At a reduced frequency of $\omega_s = 1.88$ the blade is in contact with 1.88 wakes at any one time. The increase in loss is as a result of the increase in turbulent wetted area on the blades surface caused by wake passing events that have no capacity to suppress separations on the surface and thus reduce blade loss.

If the inlet flow angle was increased such that under steady operation a leading edge separation bubble formed on the blade, causing transition to occur at the leading edge, then the influence of wakes could be beneficial and reduce the pressure loss on the suction surface as was seen previously to occur on the pressure surface. The same result could be achieved at large values of negative incidence where a separation bubble forms downstream of peak suction.

7.7 Conclusions

This investigation has demonstrated that at near design conditions increasing stator reduced frequency increases blade pressure loss. The pressure and suction surfaces react very differently to the change in reduced frequency.

On the suction surface, quasi-wall shear stress traces show an increase in turbulent activity between wake passing events with a decrease in reduced frequency. This is coupled with a reduction in wake induced turbulent wetted area due to an increase in wake passing period at a fixed machine operating point. The clear increase in blade pressure loss on the suction surface shown in Figure 7.15 suggests that an increase in the turbulent wetted area from wake induced turbulent strips has a more significant impact than the enhanced intermittency between wake events. Over the front portion of the blade steady flow is transitional and relaminarising in the favorable pressure gradient leading to peak suction. An increase in reduced frequency increases the overall turbulent wetted area of the blade - elevating blade pressure loss.

Increasing the stator reduced frequency past $\omega_s = 0.47$ increases the amount of loss generated by the suction surface whilst decreasing the loss generated on the pressure surface.

Wake-induced turbulent strips suppress the leading edge separation bubble present under steady flow conditions and between wake passing events following the calmed region behind the wake. However the influence of this is likely to be minimal as the separation bubble on the suction surface at $Re_c = 230,000$ and $\alpha_1 = 45.5^o$ under steady conditions is small. Figure 7.10 supports this and shows an average value of QWSS above that seen in

the separated flow regions in Chapter 5.

The pressure surface demonstrates a clear reduction in loss with an increased reduced frequency. Downstream of the leading edge separation bubble, which is much larger than than that seen on the suction surface, a fully turbulent boundary layer covers the blade's surface to the trailing edge. The increased periodic suppression of the leading edge separation bubble is expected to contribute to the decrease in pressure surface loss with an increase in reduced frequency. As the boundary layer is fully turbulent, a decrease in local loss production will be seen in the calmed zone following a wake passing event. The blade surface covered by the calmed zone increases with reduced frequency, however the blade's turbulent wetted area does not.

It is expected that trends seen at near design incidence would change considerably under off design conditions, particularly at positive incidence where a large separation bubble forms under steady conditions leading to a large increase in local loss generation. Under such conditions an increase in stator reduced frequency should reduce the increase in loss with reduced frequency and at large values of inlet flow angle could create a reversed trend similar to that seen on very high lift turbine blades.

Chapter 8

Turbulence Distortion and Amplification In The Leading Edge Region of An Axial Compressor Blade In Cascade

8.1 Introduction

Free stream turbulence can be characterised as small scale, time dependent, high-frequency, random velocity fluctuations superimposed on a time independent mean flow. Turbulence has a large effect on laminar-turbulent transition and the development of boundary layers in axial-flow compressors. Boundary layers on the leading edge of compressor blades are sensitive to changes in a machine's operating point and flow conditions, and have a significant impact on losses generated.

Computational fluid dynamics (CFD) has been a key tool in the aerodynamic design of compressor blading in gas turbine engines for decades and is being relied on more and

more in optimisation routines every day. Performance predictions during the design process are critically dependent on the simulated boundary layer development. Boundary layer physics such as transition, relaminarisation, separation and reattachment heavily impact performance and are rarely modeled at all.

Many of the key determining factors required in CFD can either be measured directly or modeled accurately using modern computational methods, except for free-stream and wake turbulence which is seldom known in many practical situations [14]. This leads the CFD user into making many, often crude, assumptions and the use of empirical turbulence models.

In the leading edge region of a compressor blade, the boundary layer is extremely thin, laminar, and highly receptive to free-stream turbulence, especially when laminar separation bubbles form. A number of detailed studies have shown the importance of the leading edge region and how sensitive it is to small changes in geometry and flow parameters, [31, 23].

Changes in levels of free-stream turbulence intensity have a significant impact on boundary layer development and thus on blade performance, which in turn can have a significant impact on engine performance [53, 95, 24, 88]. Free-stream turbulence also has a large affect on the mixing out of non-uniformities in enthalpy, entropy and temperature.

It is possible to modify low speed research facilities to better represent flow inside a multistage machine by installing upstream turbulence generating grids, fitting boundary layer trips to the hub and casing and by installing grids downstream of a stator row to replicate the potential flow field of a downstream stage.

Place *et al.* [65] showed that out of the previously mentioned changes elevating the free-stream turbulence by means of an upstream turbulence generating grid had the largest impact on performance leading to a 1.8% rise in stage efficiency.

Camp and Shin [6] conducted an experimental investigation into the turbulent flow field inside embedded stages of three different low-speed four stage compressors. They showed that the turbulence intensity at the inlet to stator varied from 3.6 - 7.0% and the turbulence length scale location varied from 3.6 - 7.1 % of mean blade chord. This work clearly shows that the environment inside the axial research compressor is highly unsteady and it is expected that these levels would further increase inside real engines.

The price of computing power is decreasing dramatically and the amount of computing power used early in the design process stages is ever increasing, which has lead to a vast

reduction in numerical errors. However CFD users are still subjected to large errors in their computations when incorrect models are selected within a particular solver.

Hobson [36, 37] showed, experimentally, that at medium to high incidence angles the free-stream turbulence intensity (Tu) increased by an order of magnitude just ahead of and in the leading edge region of a compressor cascade. This phenomena was attributed, not to streamwise diffusion but to the high levels of shear as the flow undergoes strong acceleration around the leading edge.

In regions of adverse pressure gradient Soranna *et al.* [84] showed, using PIV measurements, that the compressed streamwise component of velocity fluctuation is enhanced and the surface normal components, are stretched and suppressed. The opposite trend was seen in regions of accelerating flow, which is consistent with rapid distortion theory (RDT). It was also shown that in an area either side of peak suction where conditions are local non-equilibrium the wake turbulence was reduced by a rapid change in orientation of the compressive and extensive strains. This leads to the turbulence production rate becoming negative, which in turn leads to a decrease in turbulent kinetic energy.

The above findings clearly show that the turbulence field in any blade row is going to be highly anisotropic and non-homogeneous. Sarkar and Voke [71] indicated that the surface normal fluctuations are more effective than the streamwise fluctuations in initiating bypass transition and it is clear that if the performance of a blade is to be predicted accurately the above mentioned phenomena must be modeled correctly. However a number of turbulence models currently used in turbomachinery design processes assume isotropic and homogeneous (frozen) turbulence, which will not lead to physically accurate results in all scenarios.

This chapter investigates how three unmodified and widely accepted turbulence models predict the flow leading up to, and around, the leading edge of a compressor blade. The modelling is performed using ANSYS CFX and particular attention is focused on the prediction of the free-stream turbulence field. The turbulence models selected for this study are aimed to cover a range of scenarios from initial design calculations through to calculations aimed at investigating detailed flow phenomena. Currently a frozen turbulence assumption is used inside the MISES solver [17], which is used extensively in turbomachinery blade design and both the $k-\omega$ SST and RSM models available in ANSYS are used extensively by industry and academia.

This chapter begins with a brief description of the CFD and experimental set-ups and the turbulence models used. The results and discussion section presents a detailed comparison of the different test cases. Final conclusions are then drawn as to the applicability of dif-

ferent turbulence models to predict the turbulent flow field in the leading edge region of a compressor blade without tuning or modification of the model codes as would be the case for inexperienced CFD users.

8.2 Numerical Approach

The large scale, low speed, 2D compressor cascade in the Whittle Laboratory at the University of Cambridge was used in this investigation to provide experimental validation and comparison with the CFD results. Section 3.2 gives details of the compressor cascade. A CFD model was created and used in this work based on the cascade and Table 8.1 shows some of its key parameters.

Table 8.1: Compressor Cascade Details

Chord	[mm]	285
Cascade Span	[mm]	610
Cascade Pitch	[mm]	281
Reynolds Number (chord)		2.6×10^5
Inlet Flow Angle	[deg]	49

The model domain consisted of a single blade element with periodic boundary conditions above and below. The full span of the cascade was modeled (0.61m) with symmetry boundary conditions applied to each side plane. The inlet boundary was located a distance of 1.13c axially upstream from the leading edge and 1.13c downstream from the trailing edge. These lengths were based on the location of the turbulence grid upstream of the leading edge and this was then matched at the exit of the cascade.

The turbulence intensity and length scale at the inlet plane of the model, which was located the same distance upstream of the instrumented blades leading edge as the turbulence grid in the real cascade (Section 3.2.4) were chosen to be 8.2% and 0.016m respectively. These figures were based on calculations made to determine the decay of turbulence based on correlations from Roache [68] and the actual dimensions of the turbulence generating screen in the experimental rig. A simulated turbulence intensity of 4.5% was achieved at the inlet plane to the instrumented blade.

An O-mesh was chosen for the grid type due to its simplicity when applied to 2D geometries. O-meshes are also an essential requirement for accurate modelling of the near wall flow region. ANSYS ICEM was used to create the computational mesh, and this consisted

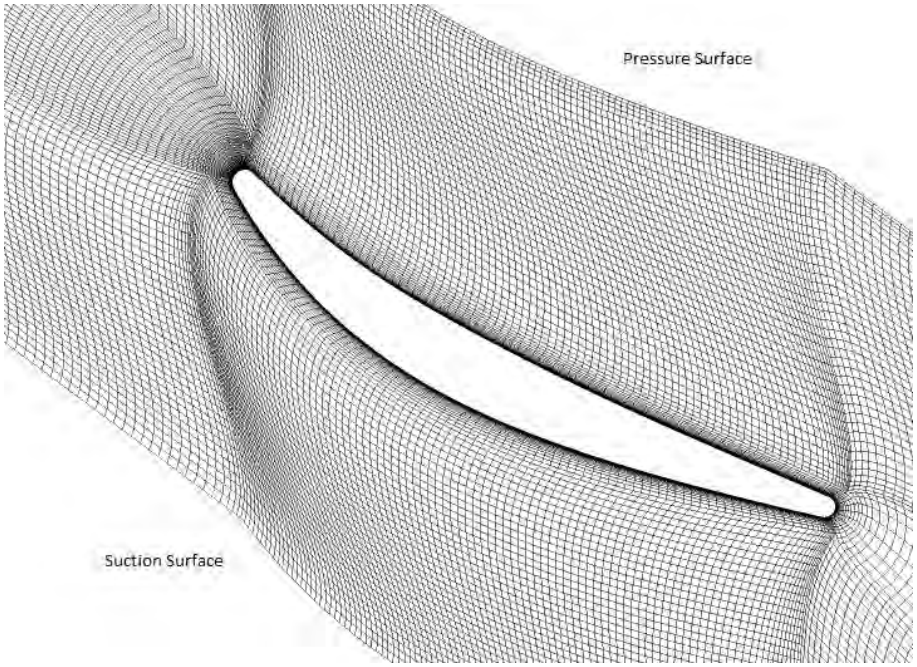

Figure 8.1: Computational mesh created in ANSYS ICEM with 1.3×10^6 elements

of 13×10^6 elements for the single passage (Figure 8.1). This is a very fine grid for a single passage simulation, however as free-stream turbulence was an important parameter, a fine grid was required throughout the three dimensional domain and not just in the boundary layer. A y^+ of less than 1 was maintained around the blades surface.

8.2.1 Reynolds-Averaged-Navier-Stokes (RANS) Modelling

Reynolds Averaged Navier Stokes based CFD significantly reduces computational requirements compared to LES or DNS, however it is at the expense of more detailed analysis of turbulent flow and excludes multiple length scales present in any turbulent flow field. Regardless of the specific RANS turbulence model only a single point in the wave number - energy spectrum can be computed creating a fundamentally non-physical foundation for the prediction of any turbulent flow field.

There are two main categories of RANS turbulence models: eddy viscosity models and Reynolds Stress Models (RSM). Models of both types use a set of equations to compute the Reynolds stresses. Both model types will be used in this investigation and the specific formulations are outlined in Sections 8.2.2 and 8.2.3. It is important to define the RANS equation and highlight where the Reynolds stress terms originate from.

The RANS equations are time averaged equations of motion for a fluid and are based on the

principal of Reynolds decomposition where the time-dependent velocity fluctuations (turbulence) are separated from the mean flow velocity and then time averaged. This decomposition creates a number of unknowns which are called the Reynolds Stresses. Reynolds stresses are functions of velocity fluctuations and require turbulence models which produce a closed system of equations.

It is then possible to describe a turbulent velocity as:

$$u = \overline{u}(x, y, z) + u'(x, y, z, t)$$

with

$$\overline{u'} = 0$$

.

For two or three dimensional flow the other components of velocity are defined in a similar fashion and the RANS equation in the x direction can be written as:

$$\rho\left[\frac{\partial}{\partial x}(\overline{u}^2) + \frac{\partial}{\partial y}(\overline{u}\overline{v}) + \frac{\partial}{\partial z}(\overline{u}\overline{w})\right] = -\frac{\partial \overline{p}}{\partial x} + \mu\left[\frac{\partial^2 \overline{x}}{\partial x^2} + \frac{\partial^2 \overline{x}}{\partial y^2} + \frac{\partial^2 \overline{x}}{\partial z^2}\right] - \left[\frac{\partial}{\partial x}(\rho\overline{u'u'}) + \frac{\partial}{\partial y}(\rho\overline{u'v'}) + \frac{\partial}{\partial z}(\rho\overline{u'w'})\right] \tag{8.1}$$

This is the traditional form of the equation and was chosen as the terms grouped in the last bracket are the derivatives of the Reynolds Stresses and are the source of turbulent disturbances in an otherwise steady flow equation.

A more appropriate and common rearrangement of Equation 8.1 may be:

$$\rho\left[\frac{\partial}{\partial x}(\overline{u}^2) + \frac{\partial}{\partial y}(\overline{u}\overline{v}) + \frac{\partial}{\partial z}(\overline{u}\overline{w})\right] = -\frac{\partial \overline{p}}{\partial x} + \left[\frac{\partial}{\partial x}\left(\mu\frac{\partial \overline{u}}{\partial \overline{x}} - \rho\overline{u'^2}\right) + \frac{\partial}{\partial y}\left(\mu\frac{\partial \overline{u}}{\partial \overline{y}} - \rho\overline{u'v'}\right) + \frac{\partial}{\partial z}\left(\mu\frac{\partial \overline{u}}{\partial \overline{z}} - \rho\overline{u'w'}\right)\right] \tag{8.2}$$

With this arrangement, terms involving time-dependent fluctuations or Reynolds Stresses take on a form that better represents their designation as pseudo stresses, since: $\mu\frac{\partial \overline{u}}{\partial \overline{x}}$ is the viscous normal stress in laminar flow and $-\rho\overline{u'^2}$ the normal stress due to turbulent fluctuations.

8.2.2 Reynolds Stress Model (RSM)

Reynolds Stress Models (RSM) discard the isotropic eddy viscosity approach and solve transport equations to directly compute the individual Reynolds stresses throughout a flow field. The Reynolds stress transport equation accounts for the anisotropy of the Reynolds stress tensor. It is often referred to as a Second Order Closure and is considered a high order and elaborate turbulence model used in detailed CFD studies and can be expressed as.

$$\frac{D\overline{u_i' u_j'}}{Dt} = P_{ij} + D_{ij} + R_{ij} - \epsilon_{ij} \tag{8.3}$$

The left hand side is the material derivative of the Reynolds stress component. The right hand side terms P_{ij}, D_{ij}, R_{ij} and ϵ_{ij} correspond to the production, diffusion, redistribution and dissipation terms, respectively.

RSM models are claimed to give superior performance than more simple two equation models in a number of situations such as in flows where streamline curvature or the curvature of solid bodies is important, flow affected by buoyancy, and flows near stagnation points and rotational flows. A number of RSM models are available and the SSG Reynolds Stress model developed by Speziale *et al.* [86] is considered to give superior accuracy compared to the LLR version developed by Launder *et al.* [48] in most flows, and this was used in this investigation.

From the exact form of P_{ij} the following kinetic energy production term can be derived.

$$P_{k,exact} = -\overline{u'u'}\frac{\partial U}{\partial x} - \overline{v'v'}\frac{\partial V}{\partial y} - \bar{u'v'}S \tag{8.4}$$

8.2.3 k-ω SST Model

A wide range of two equation turbulence models are often used in CFD analysis. The majority are based on solving convection-diffusion transport equations for k and ϵ (the rate of dissipation of kinetic energy) or k and ω (the frequency of turbulence $\omega = \frac{\epsilon}{k}$). In both cases k is the turbulent kinetic energy. The eddy viscosity is expressed as

$$\mu_t = \rho C_\mu \frac{k^2}{\epsilon} \tag{8.5}$$

or

$$\mu_t = \rho C_\mu \frac{k}{\omega} \tag{8.6}$$

for a $k-\epsilon$ or $k-\omega$ model respectively. The turbulent velocity is calculated as $u = k^{\frac{1}{2}}$ and the length scale is proportional to $\frac{k^{\frac{1}{2}}}{\omega}$.

The $k-\omega$ based Shear Stress Transport (SST) turbulence model is a blend of the $k-\epsilon$ and $k-\omega$ models [56]. The SST (Shear Stress Transport) model does not directly compute the transport of turbulent shear stresses as turbulent kinetic energy k and turbulent frequency ω are being convected in the flow. Bradshaw's assumption is used to account for their transport effects. The SST model uses of the $k-\omega$ formulation in the inner parts of the boundary layer and this makes the model directly useable all the way down to the wall through the viscous sub-layer. It then switches to a $k-\epsilon$ model in the free-stream and as a result avoids the common $k-\omega$ problem where the model is too sensitive to inlet free-stream turbulence properties. The $k-\omega$ SST model has been reported to behave well in non-equilibrium boundary layers compared with the popular $k-\epsilon$ and $k-\omega$ models and predicts boundary layer separation better than most other two equation models.

Bredberg [5] agues that turbulence affects the dissipation, diffusion and mixing processes in a similar way to viscosity and as a result it is reasonable to model Reynolds stresses in a way closely related to the viscous term.

$$D_v = \frac{\partial}{\partial x_j}\left[\nu\left(\frac{\partial U_i}{\partial x_j} + \frac{\partial U_j}{\partial x_i}\right)\right] \tag{8.7}$$

The Reynolds stress term produced by Reynolds-averaging is

$$D_R = \frac{\partial R_{ij}}{\partial x_j} = \frac{\partial}{\partial x_j}\left(-\overline{u_i' u_j'}\right) \tag{8.8}$$

which created the possibility to model for the Reynolds stress using

$$\overline{u_i' u_j'} = \alpha_{ijkl}(x, y, z, t)\left(\frac{\partial U_k}{\partial x_l} + \frac{\partial U_l}{\partial x_k}\right) \tag{8.9}$$

In Equation 8.2.3 α_{ijkl} is a fourth order tensor, which has the capability to contain spatial and temporal variations as well as anisotropic eddy viscosity. The directional component

is lost in the eddy viscosity model concept and as a result turbulence is predicted to be isotropic and results in

$$\overline{u_i' u_j'} = \nu_{ijkl}(x, y, z) \left(\frac{\partial U_i}{\partial x_j} + \frac{\partial U_j}{\partial x_i} \right) \tag{8.10}$$

The spatial variation is modeled using an algebraic relation and the temporal variation is in most cases dropped.

8.2.4 Solution Method

A second order accurate descritisation scheme was used and all solutions were converged to a RMS residual level of 10^{-6}; two orders of magnitude below the default level set in ANSYS.

8.3 Experimental Measurements

A series of experimental tests were performed in the leading edge region of the cascade to allow for direct comparison with CFD results. 2D Particle Image Velocimetry (PIV) was used in the suction surface leading edge region of the cascade's instrumented blade. The laser sheet was fired in the blade-blade plane at 50% span, whilst the camera was aimed along the blade in a spanwise direction. The PIV interrogation window measured 52×36.25mm and covered the first 7.5% of blade chord.

The instrumented blade was painted black to reduce surface reflections into the camera lens, however some were still present, which had an influence over the systems ability to capture the boundary layer and near wall region.

Section 3.2.4 discusses the turbulence generating grid designed to produce isotropic turbulence with a turbulent intensity in the plane of the leading edge of the instrumented blade of 4% with a turbulent length scale of 36mm - typical for a rig of this size and equivalent to that found in industrial machines [6]. This was confirmed using the PIV system in Figure 8.10 and a hot-wire probe. The isotropic nature of turbulence entering the cascade is demonstrated in Figure 8.17(b).

The PIV results give both instantaneous and time averaged information about the velocity flow field as well as key properties such as 2D turbulence intensity and Reynolds stresses.

Each time averaged image consisted of 960 image pairs, which was deemed to be sufficient in order to obtain reasonable statistics on the turbulent flow field. Figure 8.2 shows that the variation of *Tu* at different locations within the measurement window does not decrease obviously with an increase in the number of images used to average results. This suggests that the variability seen in the measurements is inherent in the flow field and is caused by its highly disordered and unsteady nature (Figure 8.5).

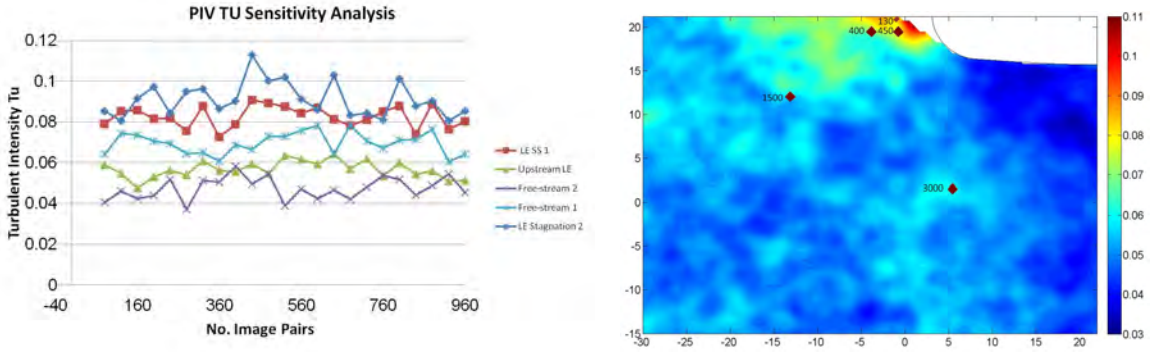

(a) Sensitivity of Tu to changes in the number of image pairs at various locations in the measurement window

(b) Locations where the sensitivity analysis was carried out in the contour plot of Tu

Figure 8.2: Sensitivity analysis of experimental PIV results

By over-seeding the flow with smoke, instantaneous images of the turbulent free-stream flow field could be taken using the PIV camera (Figures 8.5). This form of flow visualisation is extremely effective at providing a qualitative picture of the flow field. The images clearly demonstrate the enormous complexity of the flow field in the leading edge region of a compressor cascade with elevated free-stream turbulence. Photographs contained in Figure 8.5 were not taken as a series of consecutive images, but represent independent events.

Upstream and downstream of the blades three hole probe traverses were performed on the cascade to check flow periodicity and two dimensionality. These tests showed that the total pressure varied by less than 1.3% based on freestream velocity and that the inlet flow angle varied by less than 0.5^o over the pitch centered about the instrumented blade. Static pressure distributions were also used to confirm the inlet flow angle through comparison with CFD results. These measurements were used to set inflow conditions in the CFD analysis.

It should be noted that in all the experimental plots the x and y axes are aligned approximately parallel and normal respectively to the blade suction surface immediately downstream of the leading edge circle. Velocity component U is aligned parallel to the x axis and V to the y axis for reference. All plots focus on a field of view that is very small compared to the size of the complete blade passage and the field of view in the CFD results was matched as well could be achieved. Turbulent fluctuations are expressed as $\overline{|u'|}$ and $\overline{|v'|}$, which are

the time averaged absolute values of the fluctuating components of the mean velocity.

A customised colour map was created in CFX to match that available in MATLAB, where the PIV results were processed, however a perfect match was not possible so a direct colour by colour comparison cannot be made without taking into account the corresponding scales on each plot. Colour map ranges are consistent between experimental and computational plots and were mainly based around experimental results. This leads to clipping in the near wall region of some computation contour plots but this was done to allow for better comparison away from the blade surface.

8.4 Results and Discussion

8.4.1 Time Averaged Velocity Flow Field

As the flow approaches the leading edge stagnation zone it decelerates sharply before undergoing rapid acceleration as it is deflected around the circular arc of the blade's leading edge. Where the circular arc meets the main body of the suction surface a discontinuity in surface curvature is present, which causes a velocity over-speed or spike. Following this spike in velocity is a short region of extreme adverse pressure gradient, which can often cause the laminar boundary layer to separate from the blade's surface. Downstream of the leading edge spike the flow continues to accelerate gradually until the point of peak suction. This favorable pressure gradient assists in maintaining a stable and thin boundary layer. The PIV contour plot clearly shows the important features of the velocity distributions which are described in greater detail in Section 5

Comparison between trends in Figures 8.3 and 8.4 provides an initial validation of the PIV measurements, and shows that the velocity distribution is well predicted by the simplest of CFD models. Any of the models tested in this thesis could be used for the purpose of validating the experimental velocity distribution under conditions near the blade's design point where large separations are not present. Plots of velocity components (Figure 8.4) also validate that the components are aligned and have consistent signs.

Components of the velocity field in the leading edge region demonstrate in more detail how the flow is influenced by the blade row (Figures 8.4). The u component of velocity which aligns closely with the portion of the suction surface directly downstream of the leading edge and thus the blade's camber line in this region is heavily influenced by the blades presence compared to the v component of velocity. PIV results and RSM predictions agree

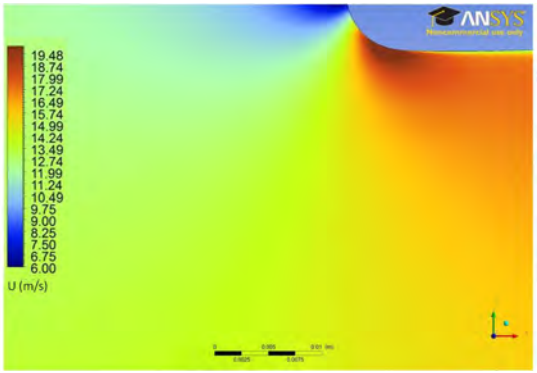

(a) Computed speed contour plot for the SSG-RSM model (m/s)

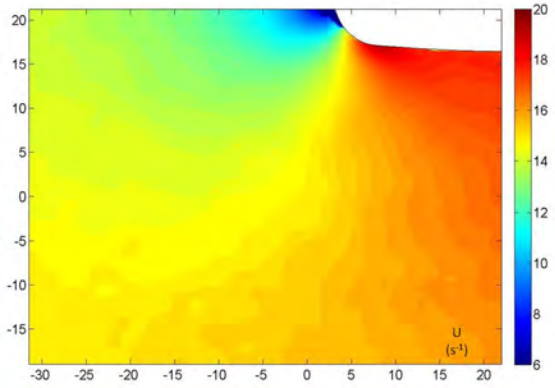

(b) Experimental PIV speed contour plot (m/s)

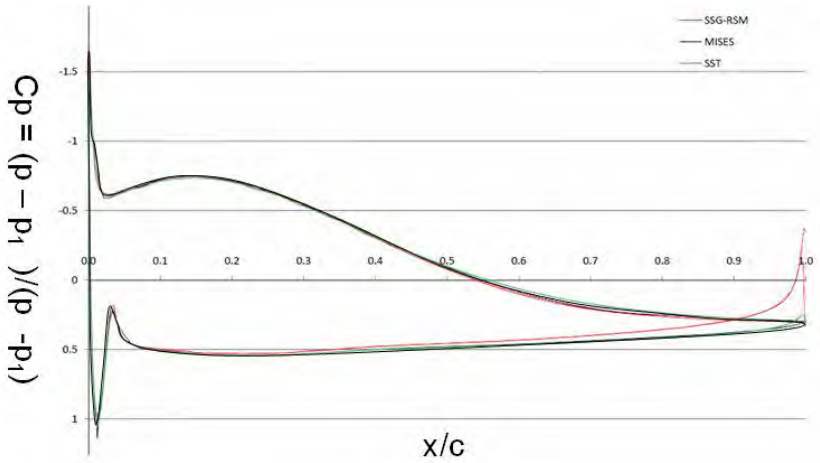

(c) Cp distribution of blade calculated using the computational models; Mises, k-ω SST and SSG-RSM

Figure 8.3: Experimental and computation predictions of velocity and static pressure used as an initial validation of PIV measurements

closely, displaying very similar trends as the flow is accelerated through the leading edge of the blade row.

8.4.2 Raw Instantaneous Turbulence Field

Flow visualisation is an excellent way of obtaining a physical appreciation of a flow field, especially when dealing with one that is highly turbulent and rapidly changing. The images contained herein display the immense complexity of the turbulent flow field in the leading edge of a compressor blade row with elevated inlet free stream turbulence under the simplest of conditions - in a linear cascade environment without periodic wake passing

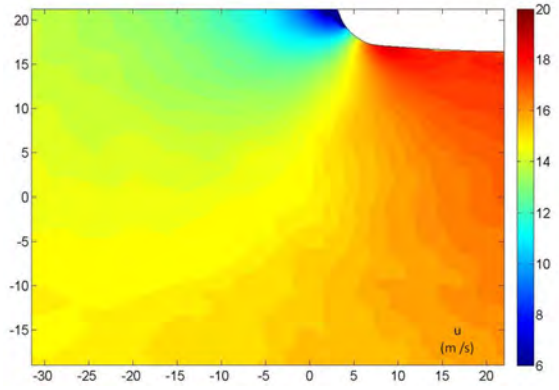

(a) Experimental contour plots of the u directional component of velocity (m/s)

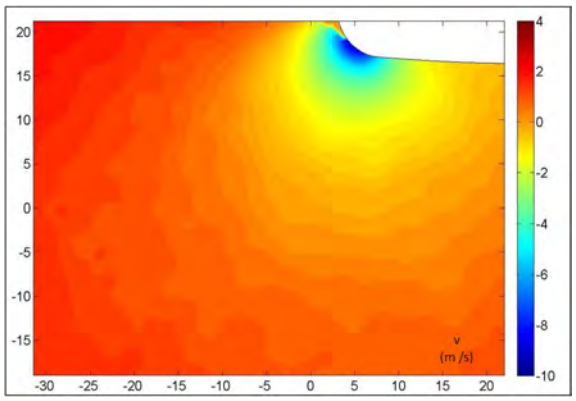

(b) Experimental contour plots of the v directional component of velocity (m/s)

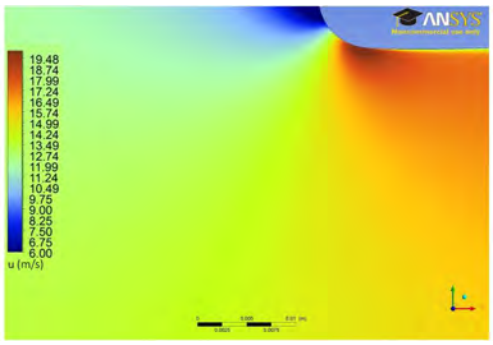

(c) RSM model contour plot predictions of the u directional component of velocity (m/s)

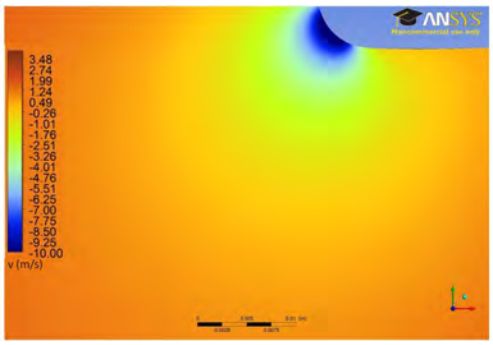

(d) RSM model contour plot predictions of the v directional component of velocity (m/s)

Figure 8.4: Experimental and CFD components of the time averaged velocity field (m/s)

events. This puts the seemingly impossible job turbulence modelers face into perspective when they face the task of designing codes to accurately model such flows.

Swirling and eddying flow is clearly visible by the distribution of smoke particles in Figures 8.5(a) - 8.5(h). The flow structures highlighted in the right hand column of the images in Figure 8.5 is to act as a visual aid only. From a general overview of the images there are a multitude of familiar 'eddy-like' flow structures covering a range of characteristic sizes: some are comparable in size to the leading edge diameter ($\varnothing = 10.6$mm), and some are many times smaller than this, but all appear smaller than the mean turbulent length scale, which was calculated to be 36mm based on results using a hot-wire probe and an autocorrelation technique. It is possible that large scale eddies are present but cannot be seen in the current field of view. This fits with the conventional way of visualising turbulence as a cascade of large eddies which break up into small eddies creating a flow of kinetic energy from large to small scales where it is then dissipated.

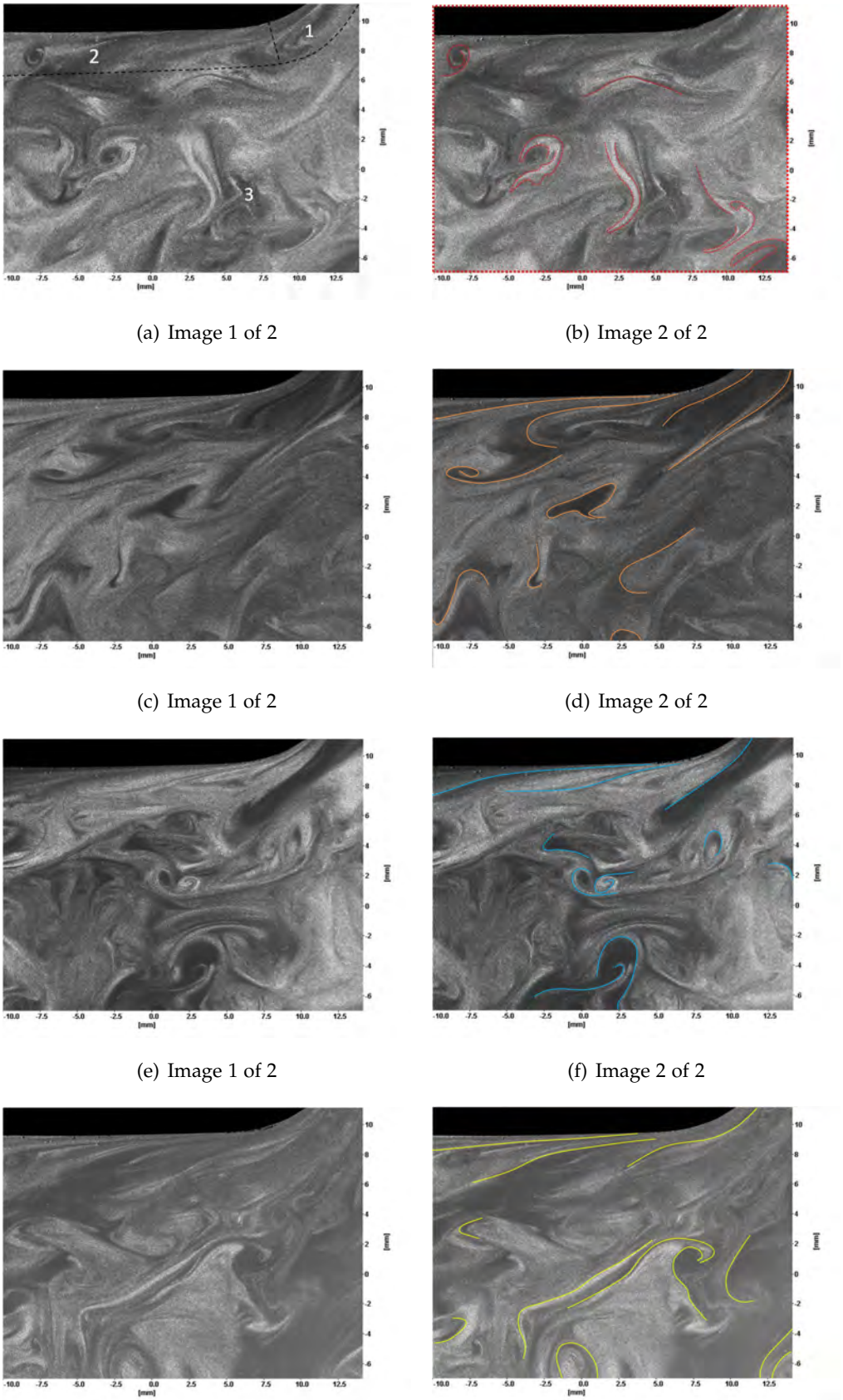

(a) Image 1 of 2

(b) Image 2 of 2

(c) Image 1 of 2

(d) Image 2 of 2

(e) Image 1 of 2

(f) Image 2 of 2

(g) Image 1 of 2

(h) Image 2 of 2

Figure 8.5: Instantaneous flow visualisation pictures of the leading edge turbulent flow field in the compressor cascade

The maximum boundary layer thickness (δ) in the leading edge region, based on the Blasius solution for a laminar boundary layer on a flat plate, is less than $\delta = 0.5mm$ for the range of test conditions used in this thesis. Many of the structures are orders of magnitude larger than δ, which suggests they have the potential to influence and create velocity perturbations deep within the boundary layer. Evidence of freestream perturbations penetrating the extremely thin laminar boundary layer between the leading edge stagnation point of the peak of the velocity spike can be seen in Figure 8.6. The traces contain typical high frequency turbulent like fluctuations which are interpreted as being in fully turbulent flow by the intermittency routine used in this project. With such small values of Re_θ in this region a fully turbulent boundary layer could not be sustained and the turbulent like high frequency perturbations were expected to be introduced from turbulence in the freestream flow. This is particularly important at the leading edge of a blade where boundary layers are highly receptive.

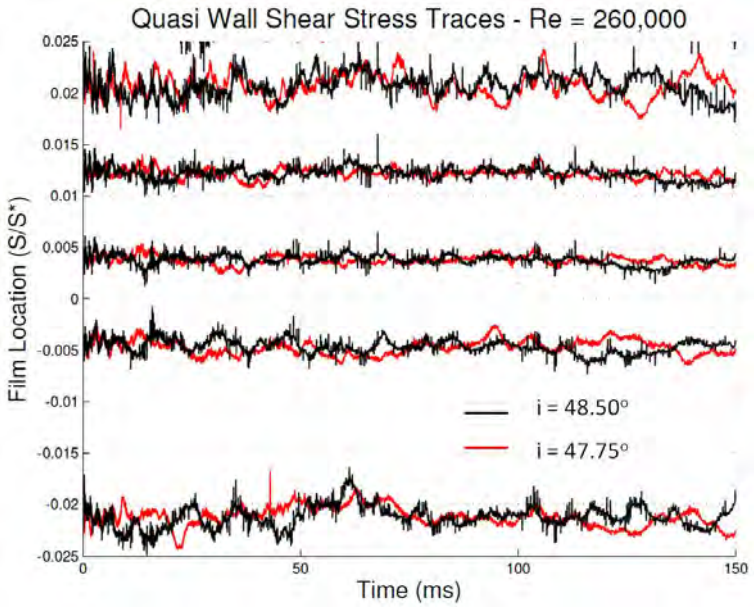

Figure 8.6: Raw traces of τ_w in the leading edge region

Turbulent like traces in this region occur only at high inlet flow angles where the leading edge spike imposes extreme pressure gradients and large shear strains. At lower values of incidence, pressure gradients and shear strains were high, however turbulent like traces were not visible and a typical laminar trace was produced as expected.

Based on the characteristic length of the turbulent flow field it is expected that larger structures are present, which cannot be seen in the current field of view. Large scale eddies, many times the size of the leading edge, could potentially play an important role by influencing the local inlet flow angle to the cascade in a similar way to a wake passing event

(Section 7).

The image pairs in Figure 8.5 have been split into three regions of interest: close to the leading edge circular arc, adjacent to the blade's suction surface downstream of the leading edge, and away from the blade in the bulk free-stream flow. These are shown in Figure 8.5(a) and are marked as region 1, 2 and 3 respectively.

In the region close to the leading edge of the blade, (1), the smoke particles have a smooth, ordered and elongated appearance compared to that of the bulk flow away from the blade. Stretching of structures present in the freestream upstream of the blade row is clearly occurring as the flow is accelerated and wrapped around the blades leading edge. The same stretched shapes occur close to the blade surface, in region (2), downstream of the leading edge where the flow is accelerated in the favorable pressure gradient of the suction surface leading to peak suction. In the bulk freestream flow (3), defined to start approximately 2mm away from the blade surface there is a change in the general appearance of the flow field. Structures no longer look ordered and smooth and the amount of stretching has dramatically reduced leading to a more stereotypical looking turbulent flow field.

Comparing the qualitative flow visualisation images and quantitative contour plots of $\frac{\overline{|u'|}}{\overline{|v'|}}$ (Figure 8.7) interesting trends can be identified. The regions marked in Figure 8.7 are in very similar locations to those discussed previously and shown in Figure 8.5(a). In regions 1 and 2 where the flow visualisation displays ordered and elongated structures Figure 8.7 shows elevated levels of turbulent anisotropy ($\frac{\overline{|u'|}}{\overline{|v'|}}$) compared to the bulk flow in region 3 which has a value closer to unity. As a result it is apparent that from inspection the highest levels of turbulent anisotropy are present in regions close to the blade surface where strong, rapidly changing pressure gradients are present.

8.4.3 Time Averaged Turbulent Flow Field

Time averaged experimental results assist in the investigation of important detailed trends in the turbulent freestream flow field which numerical codes need to predict accurately if boundary layer development and transition processes are to be modeled correctly. These include the variation of turbulence intensity Tu, amplification of Reynolds stresses and the development of turbulent anisotropy in the near wall region, all of which will influence the extremely thin laminar boundary layer in this region.

Figure **??** shows the predicted variation of turbulent intensity along a computed streamline taken from the inlet boundary of the model, around the blade's leading edge. The level of turbulent intensity decays substantially to a level of approximately 4.5%, as the flow

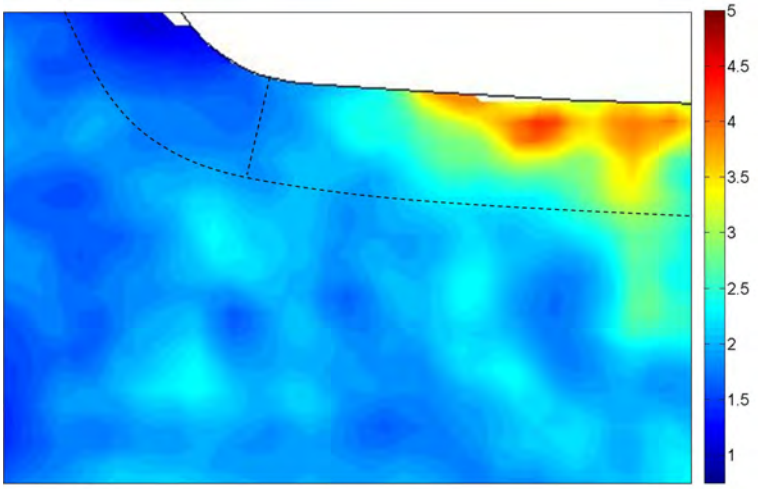

Figure 8.7: Time average PIV contour plot of $\overline{|u'|}/\overline{|v'|}$ covering the same region as the instantaneous raw images in Figure 8.5(a) - Figure 8.5(h)

moves through the inlet of the flow domain towards the leading edge plane of the blade row (Figure 8.3(c)). As the flow approaches the blades stagnation point, the turbulent intensity rises rapidly, which can be accounted for in two ways: firstly as the leading edge is approached the flow decelerates, decreasing the denominator of the Tu equation and; secondly as the flow enters the leading edge region, it is subjected to high levels of shear strain which can lead to an increase in the magnitude of the fluctuating component of the mean velocity thus increasing the Tu equations numerator. It is quite possible to have an increase in turbulence intensity in the presence of a decaying level of turbulent velocity fluctuations given sufficient deceleration of the mean flow velocity. As the flow moves around the leading edge it is accelerated giving rise to a decrease in turbulent intensity, however the level of turbulent fluctuations may be increasing in magnitude as elevated shear strain rate is associated with the rapid acceleration.

The SSG-RSM and $k-\omega$ SST models give good agreement in terms of turbulence intensity (Figures 8.9(a) and 8.9(b)). The PIV results have been used to validate the trends observed in both predicted plots (Figure 8.10).

The $k-\omega$ SST model predicts a larger amplification of Tu close to the leading edge and maintains a higher level over the early portion of the suction surface (Figure 8.8). Both models predict a freestream value of just over 4% in the blade passage away from the blade surface, showing very close agreement with that measured using a hot-wire probe - validating that both models accurately calculate the decay rate of turbulence in the inlet of the cascade.

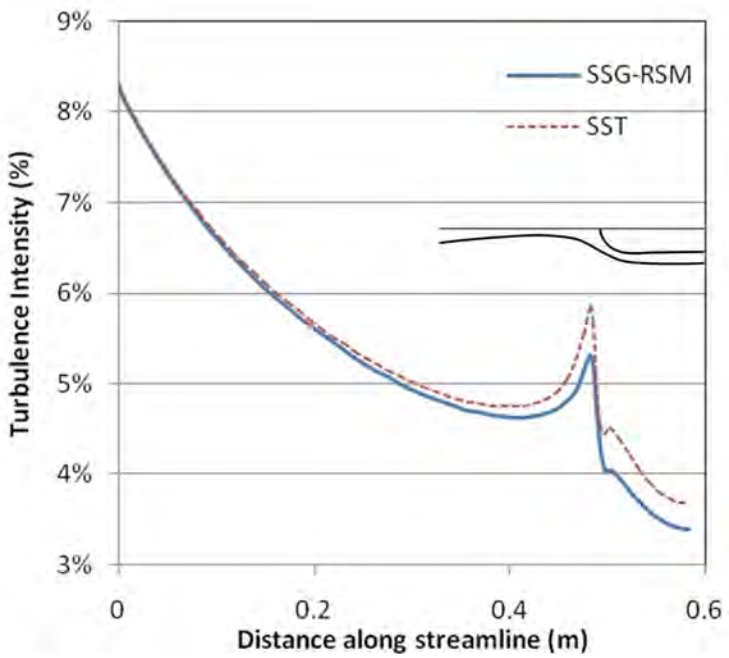

Figure 8.8: Distribution of Tu along a streamline in the leading edge region using the k-ω SST and RSM turbulence models

Both models predict almost identical overall trends in the decay and amplification of turbulence intensity, but differ visibly in two regions: near the stagnation point and in the near blade region downstream of the leading edge (Figures 8.9(a) and 8.9(b)).

In addition, immediately upstream of the stagnation region the SSG RSM model predicts a larger region of very high turbulence intensity compared to the $k-\omega$ SST model, with similar peak values between the two models. The gradient of increasing Tu is significantly greater in the SSG RSM model but the $k-\omega$ SST model shows an amplified level of Tu extending further upstream of the leading edge. In the suction surface boundary layer, downstream of the leading edge, the opposite trend is seen between the two turbulence models with the $k-\omega$ SST model indicating a more pronounced region of elevated turbulence intensity. The RSM model reaches the nominal value of Tu further upstream in the blade passage and displays a slightly higher value throughout the freestream region.

When computed predictions are compared with the time averaged PIV contour plot (Figure 8.10) it is immediately clear that all three plots share many of the same trends. Upstream of the leading edge as the blade is approached, the flow decelerates and Tu increases gradually until it reaches close proximity to the stagnation point where the rate of change of velocity increases rapidly and the level of shear strain rate also increases. In this region Tu rises rapidly and reaches a peak value adjacent to the surface at the stagnation point. This spike

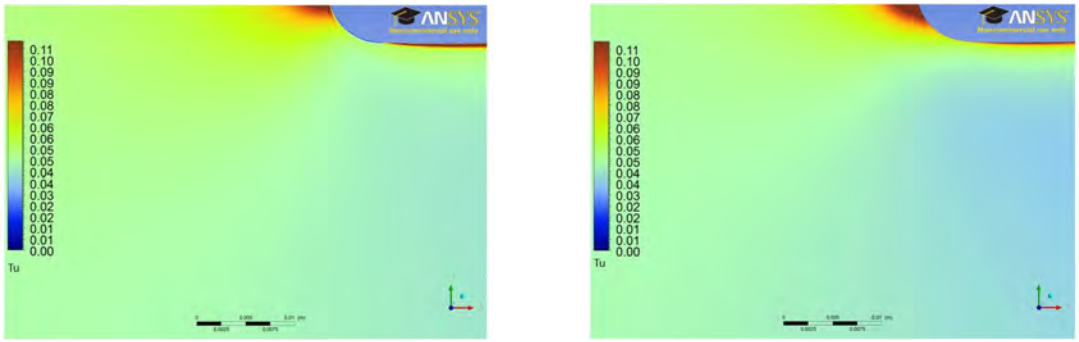

(a) k-ω SST turbulence model

(b) SSG RSM turbulence model

Figure 8.9: Time average contour plot of the average turbulence intensity, normalised by speed, in the leading edge region calculated in CFX

in Tu is localised and as the flow accelerates through the leading edge spike onto the suction surface, the value of Tu reduces to 4%, the nominal value of this investigation, which was maintained throughout the bulk freestream flow field within the blade passage.

The stagnation point was not captured in the PIV camera's field of view, and as a result the large spike in Tu in this region was not captured. Away from this region the levels of Tu align closely with those predicted using CFD.

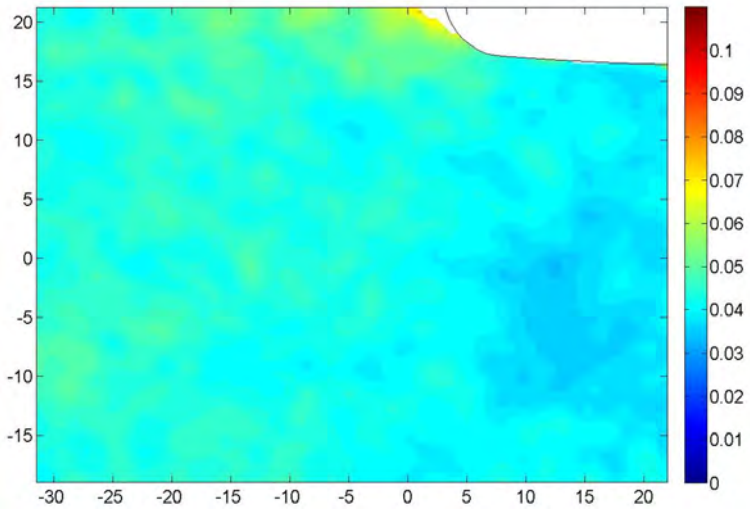

Figure 8.10: Time average PIV contour plot of the average turbulent intensity, normalised by flow speed, in the leading edge region.

To determine the origin of the increases in the overall turbulent intensity it is helpful to break down the overall turbulent intensity into its components defined as:

$$Tu_u = \frac{\sqrt{(u')^2}}{U}$$

and

$$Tu_v s = \frac{\sqrt{(v')^2}}{U}$$

.

This provides insight into how the individual fluctuating components are influenced by the blade row and introduces the concept of anisotropy (Figures 8.11 and 8.12). It must be noted that only the RSM model can evaluate the individual components of velocity fluctuations without modification and levels of Tu_u and Tu_v are based on a numerator of $\overline{|u'|}$ and $\overline{|v'|}$ respectively compared to the overall Tu, which uses the RMS of both $\overline{|u'|}$ and $\overline{|v'|}$ as the numerator.

Significant differences are present between predicted and experimental plots of Tu_u and Tu_v. Plots of time averaged velocity are extremely similar and as a result differences in the fluctuating component of velocity must be driving the dissimilarities.

It is still not possible to determine whether changes in turbulent intensity are due to changes in the fluctuating components of the mean velocity or from changes in the time averaged velocity field, however Figures 8.15 and 8.16 along with Figures 8.4 aid us in the interpretation of turbulent intensity. They display how the fluctuating components of the mean velocity field and the mean velocity field itself are increased or decreased as the flow moves around the leading edge.

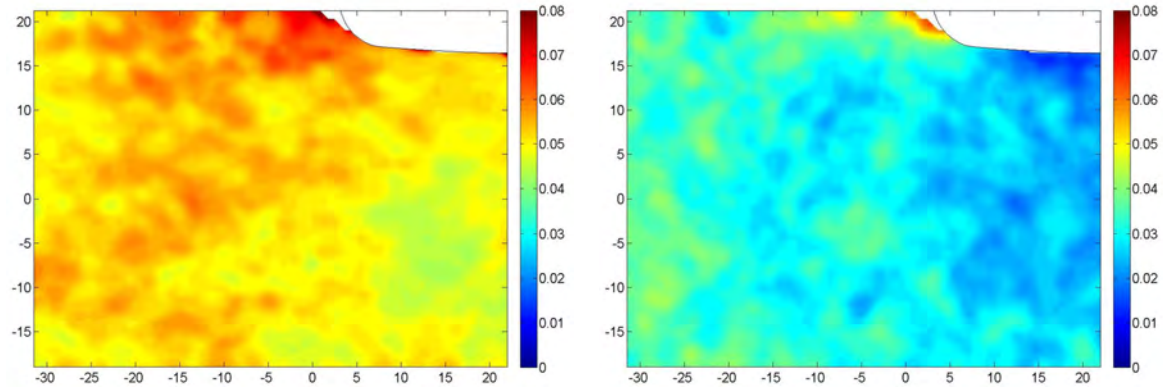

(a) Directional component of TU - u

(b) Direction component of TU - v

Figure 8.11: Experimental contour plots of the directional components of turbulent intensity

Comparisons made between plots of velocity highlight little notable difference between experimental and computational result with either model tested. As a result differences in the components of Tu must be originating from the amplification of the fluctuating component of the mean velocity by the blade row.

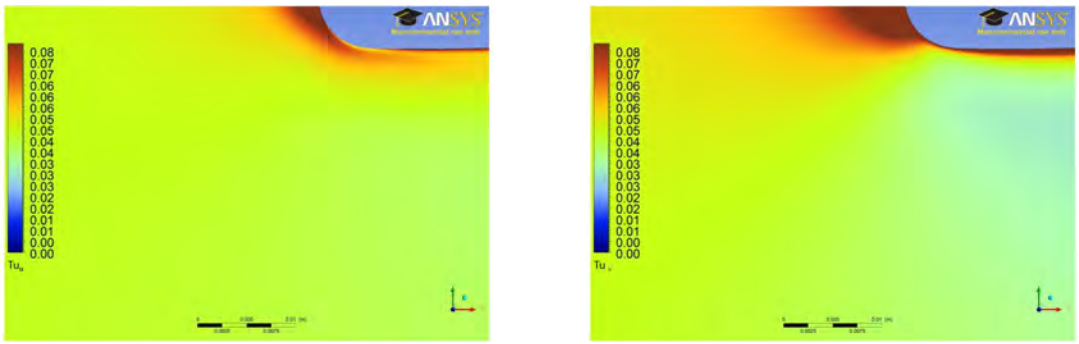

(a) Direction component of TU - u

(b) Direction component of TU - v

Figure 8.12: CFD predicted contour plots of the directional components of turbulent intensity using the RSM turbulence model

Energy is transferred between the mean flow to the fluctuating components and the contour plot of turbulent kinetic energy (Figure 8.13(c)) provides an indication of the amount of turbulent energy field across the field of view. Turbulent kinetic energy is mainly produced by fluid shear, friction and buoyancy, which is transferred down through the turbulent energy cascade and is eventually dissipated by viscous forces at the Kolmogorov scale.

The well known turbulence production term $\overline{(u_i u_j)}\frac{\partial U_i}{\partial U_j}$ appears in equations for the mean kinetic energy and mean fluctuating kinetic energy. However they have opposing signs, therefore the effect shear strain has on the kinetic energy of the mean is opposite to that which it has on the kinetic energy of the fluctuating component of the mean. When one increases the other decreases and vice versa. Comparing Figures 8.14(a) - Figure 8.14(c) it is evident that areas with the highest levels of shear strain and turbulent kinetic energy are closely related.

High strain rates around the leading edge (Figure 8.14) cause an increase in Reynolds stresses and anisotropic variations of turbulence properties. There is a strong correlation between high levels of shear and an increase in the values of $\overline{u'u'}$ and $\overline{v'v'}$ and $\overline{u'v'}$.

Figures 8.13(c), 8.13(a), and 8.13(b) indicate that the level of turbulent kinetic energy in the bulk flow is very similar across all test cases, which becomes amplified in the near blade region where high levels of shear strain are present. Comparing the surface location of the region of high shear and that of elevated turbulent kinetic energy indicates increases in TKE lag slightly behind the initial rise in shear strain.

In the freestream flow, the $k-\omega$ SST model predicts a slightly higher value of TKE, similar to the PIV results, and in the near wall region it displays a larger region of elevated TKE near the beginning of the suction surface.

The above findings tie in well with both experimental and predicted plots of shear strain with trends in both sets of plots being almost identical. High levels of negative shear are present as the flow accelerates from stagnation to the velocity overspeed, which is increased to zero at the peak of the spike, before becoming positive in the spike's adverse pressure gradient. The peak values of positive shear are slightly higher in the CFD predictions compared with the experiment, but the peak value locations are extremely similar. In the freestream region all plots asymptote to a shear strain of zero inside the blade passage.

Consistencies between the shear strain plots throughout the flow field and the turbulent kinetic energy plots in the freestream flow highlight that any differences produced are centered around the conversion of kinetic energy from the mean flow to its individual fluctuating components.

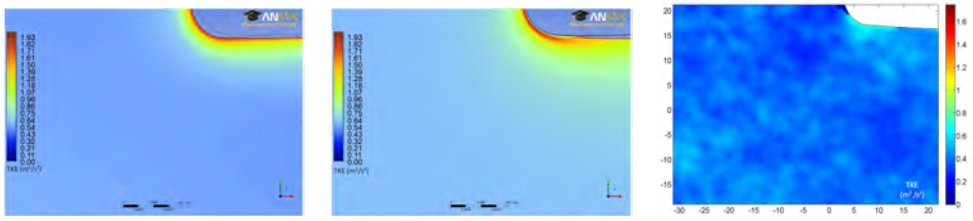

(a) RSM predicted contour plot of Turbulent Kinetic Energy

(b) $k-\omega$ SST predicted contour plot of Turbulent Kinetic Energy

(c) Experimental time average PIV contour plot of the shear strain

Figure 8.13: Details of the experimental and CFD predicted contour plots of turbulent kinetic energy in the leading edge region of the compressor cascade

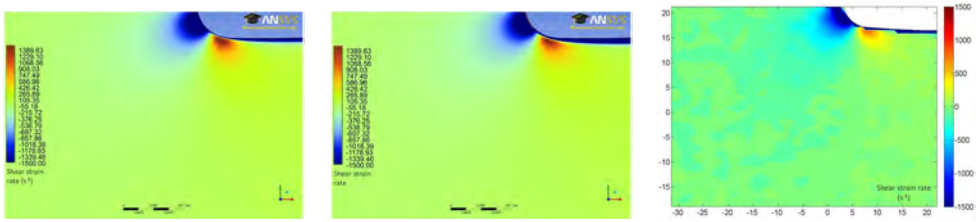

(a) RSM predicted contour plot of shear strain

(b) $k-\omega$ SST predicted contour plot of shear strain

(c) Experimental time average PIV contour plot of the shear strain

Figure 8.14: Details of the experimental and predicted contour plots of shear strain rate in the leading edge region of a compressor cascade

Comparing predicted and experimental values of the velocity components of the Reynolds stresses provide an insight in to how turbulent fluctuations are influenced by the blade row and indicate where differences in the *Tu* plots originate, given the similarities previously discussed between the plot of mean velocity.

Figure 8.15 shows that the Reynolds stress component $\overline{u'u'}$ is more heavily influenced by the blade row compared to $\overline{v'v'}$. The amplification of $\overline{u'u'}$ localised to the near wall region of the suction surface starting near the blend point between the leading edge and suction surface.

The RSM terms $\overline{u'u'}$ and $\overline{v'v'}$ show a consistent value close to 0.5 in the bulk flow away from the blade surface, which increases only in the presence of high shear strain in the near wall regions, particularly close to the leading edge. Between the stagnation point and the start of the velocity overspeed the flow accelerated predominantly in the v direction and $\overline{u'u'}$ is amplified more than $\overline{v'v'}$. Downstream of this point the flow is wrapped around the leading edge and is then accelerated primarily in the u direction. Through the velocity spike, the Reynolds stress component $\overline{v'v'}$ is most heavily amplified. Both of these trends support Rapid Distortion Theory [44] and produce anisotropy of the turbulent flow field. There is some overlap to this trend as no single component of velocity is accelerated or decelerated independently in this region.

Combining fluctuating components of velocity $\overline{|u'|}$ and $\overline{|v'|}$ leads to the Reynolds stress component $\overline{u'v'}$. Figures 8.15(a) and 8.16(a) both indicate a consistent average value of $\overline{u'v'}$ throughout the freestream flow. Close to the blades surface the RSM predicted a band of elevated $\overline{u'v'}$ around the surface with a peak value occurring at the same location as the velocity overspeed. PIV results shows a peak value lying in the same location as the RSM model, however the level is significantly smaller and this does not extend over the visible portion of the blade, but is more localised to the region of peak shear strain. This difference is exacerbated as the RSM takes into account and plots the boundary layer, which is not visible in the PIV results.

It is clear that the major difference between experimental and computational results are concentrated around the way in which individual component of velocity fluctuations are predicted in regions of high shear close to the blade surface particularly at the leading edge. Plots of overall turbulent intensity, turbulent kinetic energy, and $\overline{u'v'}$ show close agreement between computational and experimental results. These plots relate to the overall turbulent flow field rather than its individual components.

The $k-\omega$ SST turbulence model assumes isotropic eddy viscosity throughout the flow domain, and being a two equation model is known to have poor accuracy in regions of rapidly changing strain-rate. The RSM model, on the other hand, calculates the individual components of the time averaged velocity fluctuations and is expected to determine anisotropy more accurately within a complex turbulent flow field. Comparing these plots with Figure 8.17 indicates clear differences in how well the RSM model predicts the levels of anisotropy when compared to PIV results.

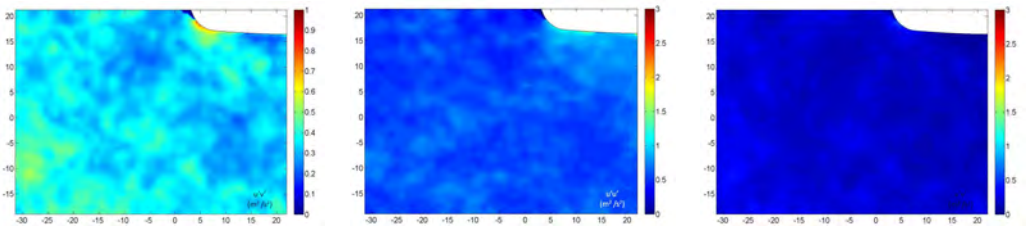

(a) Reynolds stress component $\overline{u'v'}$ (b) Reynolds stress component $\overline{u'u'}$ (c) Reynolds stress component $\overline{v'v'}$

Figure 8.15: Experimental contour plots of the Reynolds stress components $\overline{u'v'}$, $\overline{u'u'}$ and $\overline{v'v'}$

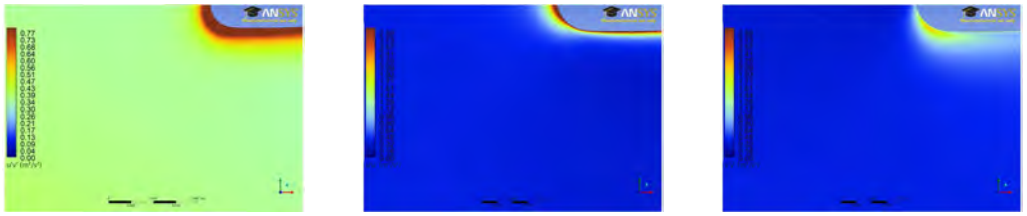

(a) Reynolds stress component $\overline{u'v'}$ (b) Reynolds stress component $\overline{u'u'}$ (c) Reynolds stress component $\overline{v'v'}$

Figure 8.16: Predicted contour plots of the Reynolds stress components $\overline{u'v'}$, $\overline{u'u'}$ and $\overline{v'v'}$ using the RSM turbulence model

Time averaged PIV data in Figure 8.17(b) show that the time averaged velocity fluctuations are anisotropic across the measurement window and that the level of anisotropy was enhanced in areas of high shear strain. The relative variation of the velocity fluctuations in the flow field appears to be dominated in areas of high shear strains (Figure 8.14(c)). A clear trend is present in Figure 8.17(a) where the fluctuating component normal to the direction of the mean flow acceleration is amplified and the component parallel to it is damped. This agrees with RDT but does not match the experimental results in Figure 8.17(b).

Figure 8.17(b) and 8.17(a) show isotropic turbulence ($\overline{|u'|}/\overline{|v'|} = 1$) entering the measurement window. As the flow enters the blade row the isotropic turbulence field becomes increasingly more anisotropic with proximity to the blade surface and regions of high shear strain.

The RSM model predicts a gradual increase in the magnitude of $\overline{|u'|}$ relative to $\overline{|v'|}$ as the stagnation point is approached. As the flow away from the surface accelerates around the leading edge the size of $\overline{|u'|}$ relative to v' reverses and along the suction surface of the blade $\overline{|v'|}$ is larger than $\overline{|u'|}$. In the near wall region and boundary layer region of the suction surface $\overline{|u'|}$ becomes larger than $\overline{|v'|}$.

Figure 8.17(b) shows that as the stagnation point is approached $\overline{|v'|}$ is larger than $\overline{|u'|}$. This is reversed as the flow moves around the leading edge and accelerates along the suction surface. In the near wall region of the suction surface $\overline{|u'|}$ is significantly large that $\overline{|v'|}$. When moving further into the blade passage $\overline{|u'|}$ still dominates however, there is a gradual decrease in the level of anisotropy.

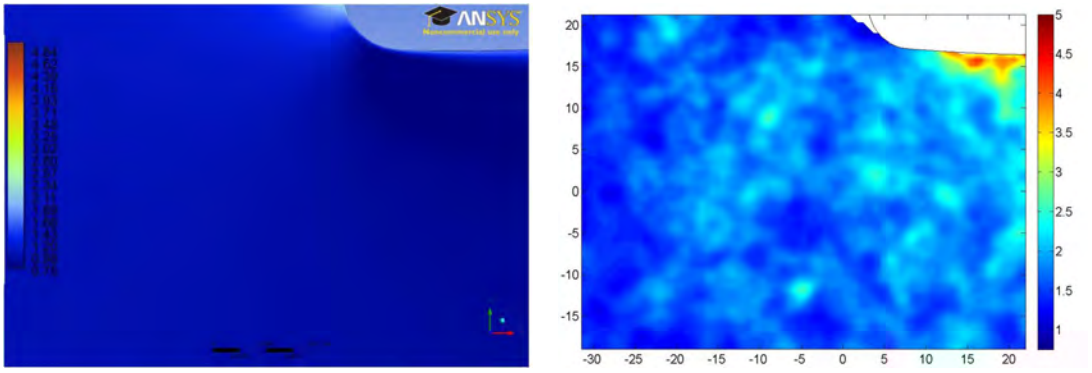

(a) Predicted $\overline{|u'|/|v'|}$ from the SSG-RSM model (b) Time average PIV contour plot of $\overline{|u'|/|v'|}$

Figure 8.17: Details of the experimental and predicted contour plots of turbulent anisotropy in the leading edge region of the compressor cascade

8.5 Conclusions

This chapter has shown that flow with free-stream turbulence travelling around the leading edge of a compressor blade is complex and random. While both $k-\omega$ SST and RSM models agree well with each other in their prediction of the turbulent intensity, including the sharp rise as the flow approaches the leading edge, they do not agree closely with the time averaged experimental results. In all cases models over-simplify the turbulent flow field smoothing over potentially important details.

The overall picture of turbulence in the measurement window viewed in terms of turbulent intensity and turbulent kinetic energy shows close agreement between both computational models and also with experimental results. These parameters contain both fluctuating components of the velocity field $\overline{|u'|}$ and $\overline{|v'|}$. It isn't until the turbulent flow field is split into its components that significant differences are exposed and the basic $k-\omega$ SST model can no longer be used. The overall level of turbulent intensity and kinetic energy of the turbulent fluctuations is consistent however the relative magnitudes of the fluctuating components within the flow field changed significantly depending on whether predicted or experimental results were observed.

The blade row introduces significant levels of anisotropy to the initially isotropic turbulent flow. The RSM model predicted a similar level of anisotropy as the experimental results, however the trends across the contour plots vary considerably with the opposite relative magnitudes of $\overline{|u'|}$ and $\overline{|v'|}$ predicted in the near wall region and blade passage. This highlights the need for caution when using turbulence models to predict turbulent flow in regions where there is the potential for significant amounts of energy transfer to and from the fluctuating components of velocity such as with rapidly changing pressure gradients and high levels of shear strain: even when the overall levels of turbulence are modelled accurately.

In the boundary layer and near wall region it is difficult to make comparisons between the computations and experimental results as this area of the flow field was not captured by the PIV due to the extremely thin nature of the boundary layer in this region and issues with laser surface reflections.

Recent studies [31, 99] have shown that the boundary layer at the leading edge is the principal receptivity site for transition processes on the suction surface of compressor blades and the results from this study further emphasise the need for accurate modelling of free-stream turbulence particularly when it has been indicated that the surface normal component of velocity fluctuations have a greater influence over boundary layer transition compared to the streamwise component [71].

It is possible to calibrate both turbulence models to improve their accuracy in particular test cases, however this investigation was purely aimed at highlighting the potential short falls of these models when used unmodified as would be the case with industrial users operating under time constraints and computational restrictions.

Chapter 9

Conclusion

Flow phenomena around the leading edge of a controlled diffusion compressor blade with a circular arc leading edge have been investigated under steady and unsteady conditions over a range of machine operating points. The boundary layer and freestream were investigated in the leading edge region using a range of experimental techniques.

9.1 Effect of Changing Incidence and Reynolds Number on CD Stator Blade Flow Characteristics in Steady Flow

Chapter 5 examined, in detail, the effect changing the Reynolds number and inlet flow angle had on flow around a CD stator blade with a circular arc leading edge in a cascade. The boundary layer development at the leading edge and early portion of the suction surface becomes increasingly Reynolds number dependent in the presence of a leading edge separation bubble. This dependency is reflected in the trends of blade pressure loss with an increase in inlet flow angle at both $Re_c = 260,000$ and $Re_c = 400,000$.

At negative incidence, blade pressure loss increased as the Reynolds number was decreased. In contrast at positive incidence the opposite trend was observed with blade pressure loss increasing with Reynolds number.

A separation bubble formed at the leading edge of the pressure surface under all test conditions. The bubble length was dependent on Reynolds number and incidence. A gradual decrease in bubble length was seen as the inlet flow angle was increased. Increasing the Reynolds number from $Re_c = 260,000$ to $Re_c = 400,000$ saw a decrease in bubble length which was more evident at negative incidence where the pressure surface bubble was largest. The suction surface of the blade displays a similar trend, however a bubble formed at values of positive incidence only ($\alpha_1 \geq 45^o$). Bubble length increased with inlet flow angle and displayed the same Reynolds number dependency as that seen on the pressure surface.

When a laminar separation bubble formed at the leading edge, it lead to rapid transition and the formation of a turbulent boundary layer upon reattachment. On the pressure surface this boundary layer remained turbulent downstream of the separation bubble's reattachment point to the trailing edge due to the lack of potentially stabilising pressure gradients. On the suction surface the favorable pressure gradient leading to peak suction, had a relaminarising effect on the newly developed, fully turbulent, boundary layer. The potential for relaminarisation is highest at negative incidence and low Reynolds numbers.

At negative incidence the blade experiences a lower level of pressure loss with an increased Reynolds number, whereas at positive incidence the opposite trend is observed. A sharp rise in loss occurred as the inlet flow angle of the cascade is increased past the blade's design point ($\alpha_1 = 45^0$). This is caused as the initial point of transition shifts forwards to the leading edge separation bubble ($S^* = 0.02 - 0.04$). When the inlet flow angle is increased to a point where the boundary layer separates at the trailing edge, near the blade's point of stall, the loss at both Reynolds numbers begin to converge. At this point a fully turbulent boundary

layer is present over the entire surface of the blade and relaminarisation is minimal.

Where high resolution static pressure tappings are present on the blade's suction surface, the Cp distribution predicted by MISES is very similar to that shown by experiment. The CD stator experiences an incidence dependent leading edge velocity over-speed on both suction and pressure surfaces. At low inlet flow angles, considered to be those below the design operating point and identified as negative incidence, a large velocity spike is seen on the pressure surface of the blade and at high inlet flow angles, considered to be those higher than the design operating point and identified as positive incidence, an overspeed is seen on the suction surface.

The observed Reynolds number dependency of the separation bubbles is also predicted by MISES which displays the same trend as seen in the experimental findings. Changes in bubble length with increasing incidence is however, underestimated by MISES, which predicts an almost constant bubble size on both surfaces. Experimental results show the pressure surface bubble significantly decreases in length with an increase in incidence. The opposite trend was observed on the suction surface when a leading edge bubble was present $\alpha_1 > 45^o$. This leads to an effective overestimate of bubble length at low Reynolds numbers by MISES, leading to an increase in blade pressure loss.

MISES is not capable of predicting boundary layer relaminarisation, which is present on the blade's suction surface leading to peak suction. As a result MISES is also unable to predict the increase in relaminarisation potential at low to moderate value of inlet flow angle and low Reynolds numbers. As a result MISES over predicts the turbulent wetted area on the blade's surface when transition occurs in the leading edge region.

These findings confirm that partial boundary layer relaminarisation is possible, with a sufficiently strong favorable pressure gradient over a significant surface length, and is most likely to occur at a low Reynolds number and negative incidence. Separation bubbles form at the leading edge of both surfaces, which initiate rapid transition, increasing the turbulent wetted area on the blade and local loss inside the bubble. It also demonstrates that MISES is a great tool to estimate blade profile performance but its limitations must be considered when used. When increasing inlet flow angle from negative to positive incidence, both experimental and predicted trends are very similar, however it does not predict the distribution of loss at some inlet flow angles over a range of Reynolds number accurately. This may become problematic in future designs stages.

9.2 Effects of Changing the Stator Reduced Frequency of a Compressor Cascade at Design Conditions

At a Reynolds number $Re_s = 230,000$ and inlet flow angle $\alpha_1 = 45.5^o$ (0.5^o positive incidence), increasing stator reduced frequency increases blade pressure loss. The pressure and suction surfaces react very differently to the change in reduced frequency. Breaking the blade pressure loss into suction and pressure surface components reveals each surface was influenced very differently by the increase in stator reduced frequency.

Increasing the stator reduced frequency past $\omega_s = 0.47$ increased the amount of loss generated by the suction surface whilst decreasing the amount generated on the pressure surface in an almost linear trend.

Wake induced turbulent strips suppress the leading edge separation bubble present under steady flow conditions and also in between wake passing events following the calmed region behind the wake. However the influence of this is likely to be minimal as the separation bubble on the suction surface at $Re_c = 230,000$ and $\alpha_1 = 45.5^o$ under steady conditions is small. Figure 7.10 supports this and show an average value of QWSS above that seen in the separated flow regions in Chapter 5.

The pressure surface demonstrates a clear and almost linear reduction in loss with an increased reduced frequency past $\omega_s = 0.47$. Downstream of the leading edge separation bubble, which is much larger than than that seen on the suction surface, a fully turbulent boundary layer covers the blade's surface to the trailing edge. The increased periodic suppression of the leading edge separation bubble is expected to contribute to the decrease in pressure surface loss, the effect of which increases with reduced frequency. As the boundary layer is fully turbulent, a decrease in local loss production will be seen in the calmed zone following each wake passing event. The blade surface area covered by the calmed zone increases with reduced frequency, however the blades turbulent wetted area does not and thus a reduction in blade pressure loss was achieved.

It is expected that trends seen at near design incidence would change considerably under off design conditions, particularly at positive incidence where a large separation bubble forms under steady conditions at the leading edge of the suction surface producing a large increase in local loss generation. A separation bubble could also form on the pressure surface at positive incidence as shown in Chapter 5. Under such conditions an increase in stator reduced frequency should reduce the increase in loss with reduced frequency and at large values of inlet flow angle could create a reversed trend similar to that seen on very high lift turbine blades.

9.3 Turbulence Distortion and Amplification In The Leading Edge Region of An Axial Compressor Blade In Cascade

Flow subjected to free-stream turbulence around the leading edge of a compressor blade is visibly extremely complex, unsteady and random. The compressor blade row introduces significant anisotropic variations in turbulence properties throughout the measurement window near the suction surface where very high levels of shear strain are present due to large pressure gradients.

Two turbulence models were used in RANS based numerical simulations: the $k-\omega$ SST and the RMS model which both agree with each other in their prediction of turbulent intensity, including the sharp rise as the flow approaches the leading edge. However they do not agree closely with the time averaged experimental results. In all cases where turbulence properties are investigated the computational models over-simplify the turbulent flow field smoothing over potentially important details. The rapidly changing strain rate decreases the ability of two-equation turbulence models to accurately predict detailed flow phenomena in this region.

Chapter 5 showed elevated levels of high frequency perturbations in the raw quasi wall shear stress traces of films located between the stagnation point and the peak of the velocity over-speed. The turbulent intermittency routine identifies these fluctuation with a turbulent boundary layer, which would be impossible to sustain in such a strong favorable pressure gradient and with such small values of Re_θ. This could be misleading if sufficient attention is paid to looking at the raw traces on which the intermittency routine bases its decisions on.

Identifying high frequency perturbations in the hot-film traces close to the leading edge indicates that the effects of the freestream turbulent flow field may be penetrating into the thin laminar boundary layer that forms in the stagnation region of the blade.

Recent studies [31, 99] have shown that the boundary layer at the leading edge is the principal receptivity site for transition processes on the suction surface of compressor blades and the results from this study further emphasise the need for accurate modeling of free-stream turbulence in this region of flow when freestream effects are being seen inside the boundary layer.

Chapter 10

Recommendations

This project has provided information and answers to a number of questions relating to the turbomachinery field surrounding the flow over and around the leading edge of a controlled diffusion compressor with a circular arc leading edge. Along with providing new information it has highlighted a number of areas that if further investigated would add to the work contained within this thesis. This section provides a guide towards research that could make a significant addition to the body of knowledge within this thesis, that is currently unavailable in the literature. It does not highlight the only areas that require future work but concentrates on those closely related to that contained within this thesis.

10.1 Measurements Within Leading Edge Separation Bubbles

Following on from the steady flow measurements of leading edge separation bubbles made in this thesis it is recommended that an investigation is undertaken to look at the unsteady nature of these bubbles and how this varies with changes in flow conditions. A combination of Laser Doppler Velocimetry (LDV) and single element hot-wires could be used. LDV would be preferable as reverse flow can be captured, however this may be at the expense of measurement resolution within the boundary layer.

Of particular interest is the transition process that occurs within the separated flow region and following on from this how the boundary layer reattaches in a region with rapidly changing and extreme pressure gradients.

10.2 Developing Transition Length and Relaminarisation Capability Within MISES

For a simple and very fast running model, MISES does an excellent job at predicting the flow around, and loss generated by, an airfoil in cascade. Under steady operation it has one clear shortfall identified by this project - it is incapable of predicting the phenomena of relaminarisation and the potential for a large portion of a blade's surface to be covered with a transitional boundary layer.

Adding this functionality would improve MISES' ability to predict blade pressure loss and boundary layer development at a range of flow conditions found in real engines and would be applicable to both compressors and turbines.

10.3 Comparison between steady experimental findings and advanced turbulence modeling techniques with transition models

An extension of the study carried out in Chapters 5 and 6 should be performed using commercial CFD software packages such as ANSYS CFX. Comparison should be made between the experimental findings of Chapter 5 and computation predictions using advanced turbulence modelling techniques with and without transition models.

A turbulent boundary layer is often assumed to form at the leading edge of a compressor blade and remain in this state to the trailing edge. Chapter 5 has shown that is is not necessarily the case and considerable portions of a compressor blade's surface can be covered in a laminar or transitional boundary layer.

The aim of this research should be to highlight potential shortfalls in current commercial CFD packages with respect to transition modeling and loss predictions. Findings from this work could be used to aid in the development of a transition modeling option in MISES.

10.4 The Effect of Stator Reduced Frequency on Blade Performance Over A Range of Inlet Flow Angles and Reynolds Numbers

The formation and size of separation bubbles are Reynolds number and incidence dependent. Wake passing events have been shown to heavily influence the development of separation bubbles and boundary layers, particularly in the leading edge region of compressor blades with circular arc leading edges. Tests during this investigation showed that at close to design incidence the blade pressure loss varied significantly with an increase in stator reduced frequency. Further tests should be conducted at positive and negative incidence, where a large separation bubble forms at the blade's leading edge on the suction surface and pressure surface respectively.

10.5 High Resolution Leading Edge Freestream Turbulence Measurements

It is recommended that the complexities of freestream turbulence in the leading edge region of compressor blades identified in Chapter 7 be further investigated using measurement techniques with a high frequency response such as with hot-wire probes. If an X-probe was used the directional time resolve unsteady nature of the turbulent flow field could be determined. Measurements could be made from within the boundary layer into the freestream around the leading edge.

Ideally this would be carried out during steady and unsteady operation to observe if wake events are influenced in a different manner to the freestream flow with background turbulence.

Bibliography

[1] **Abu-Ghannam B J and Shaw R** (**1980**) Natural transition of boundary layers - the effects of turbulence, pressure gradient, and flow history. *Journal of Mechanical Engineering Science*, **22**(5), pp. 213.

[2] **Arena A V and Mueller T J** (**1980**) Laminar separation, transition, and turbulent reattachment near the leading edge of airfoils. *AIAA Journal*, **18**(7), pp. 747.

[3] **Bindon J P** (**1987**) Pressure distributions in tip clearance region of an unshrouded axial turbine as affecting the problem tip burnout. *ASME Turbo Expo*.

[4] **Bradshaw P** (**1972**) The understanding and prediction of turbulent flow. *Aeronautical Journal*, pp. 403–418.

[5] **Bredberg J** (**2001**) On two-equation eddy-viscosity models. Technical report, Chalmers University of Technology - Department of Thermo and Fluid Dynamics.

[6] **Camp T R and Shin H W** (**1995**) Turbulence intensity and length scale measurements in multistage compressors. *Journal of Turbomachinery*, **117**, pp. 38 .

[7] **Collis D C and Williams M J** (**1959**) Two-dimensional convection from heated wires. *Journal of Fluid Mechanics*, **6**, pp. 357.

[8] **Comte-Bellot G and Corrsin S** (**1966**) The use of a contraction to improve the isotropy of grid generated turbulence. *Journal of Fluid Mechanics*, **25**, pp. 657 .

[9] **Cumpsty N A** (**1989**) *Compressor Aerodynamics*. Longnam Scientific and Technical.

[10] **Cumpsty N A, Dong Y and Li Y S** (**1995**) Compressor blade boundary layers in the presence of wakes. *ASME Paper 95-GT-443*.

[11] **Curtis E M, Hodson H P, Banieghbal M R, Denton J D and Howell R J** (**1996**) Development of blade profiles for low pressure turbine applications. *ASME Paper 96-GT-358*.

[12] **Dawes W N and Molinari M** (**2006**) Review of evolution of compressor design process and future perspectives. *ProQuest Science Journal*, **220**, pp. 761.

[13] **Denton J D** (**1993**) Loss mechanisms in turbomachines. *Journal of Turbomachinery*, **115**, pp. 621 .

[14] **Denton J D** (**2010**) Some limitations of turbomachinery CFD. *ASME Paper GT2010-22540*.

[15] **Dong Y and Cumpsty N A** (**1990**) Compressor blade boundary layers: Part 2 - Measurements with incident wakes. *Journal of Turbomachinery*, **112**, pp. 231.

[16] **D'Ovidio A, Harkins J A and Gostelow J P** (**2001**) Turbulent spots in strong adverse pressure gradients. Part 2 - Spot propagation and spreading rates. *ASME Paper 2001-GT-406*.

[17] **Drela M and Youngren H** (**1998**) A User's Guise to MISES 2.53.

[18] **Elazar Y and Shreeve R P** (**1990**) Viscous flow in a controlled diffusion compressor cascade with increasing incidence. *Journal Of Turbomachinery*, **112**, pp. 256.

[19] **Escudler M P, Abdel-Hameed A, Johnson M W and Sutcliffe C J** (**1998**) Laminarisation and re-transition of a turbulent boundary layer subjected to favourable pressure grandient. *Experiments in Fluids*, **25**, pp. 491 .

[20] **Gallimore S J** (**2008**) *Axial compressor design*. Cambridge Turbomachinery Course 2008. Cambridge University Whittle Laboratory.

[21] **Gibson W H** (**1970**) *Flow research on blading*. Elsevier Science Ltd.

[22] **Goodhand M N and Miller R J** (**2009**) Compressor blade leading edge spikes: a new performance criterion. *ASME Paper GT2009-59205*, pp. 1 – 10. ASME Turbo Expo.

[23] **Goodhand M N and Miller R J** (**2010**) The impact of real geometries on three-dimensional separations in compressors. *ASME Paper GT2010-22246*.

[24] **Gostelow J P, Blunden A R and Walker G J** (**1994**) Effects of free stream turbulence and adverse pressure gradient on boundary layer transition. *Journal Of Turbomachinery*, **116**, pp. 392.

[25] **Gostelow J P and Thomas R L** (**2005**) Response of a laminar separation bubble to an impinging wake. *Journal Of Turbomachinery*, **127**, pp. 35.

[26] **Halstead D E, Wisler D C, Okiishi T H, Hodson H P, Walker G J, Shin H W** *et al.* (**1997**) Boundary layer development in axial flow compressors and turbines 1. *Journal Of Turbomachinery*, **119**, pp. 114.

[27] **Halstead D E, Wisler D C, Okiishi T H, Walker G J, Hodson H P and Shin H W** (**1997**) Boundary layer development in axial flow compressors and turbines 4. *Journal Of Turbomachinery*, **119**, pp. 128.

[28] **Hazaeika B K and Hirsch C** (**1997**) Transition cver C4 Leading edge and measurement of intermittency factor using PDF of hot-wire signal. *Journal Of Turbomachinery*, **119**, pp. 412.

[29] **He L** (**2008**) *Unsteady flow and aero-mechanics*. Cambridge Turbomachinery Course 2008. Cambridge university whittle laboratory edition.

[30] **Henderson A D** (**2006**) *Unsteady flow and transition phenomena in an axial flow compressor*. Ph.D. thesis, University of Tasmania, University of Tasmania, Regent Street, Sandy Bay, Tasmania, 7005.

[31] **Henderson A D and Walker G J** (**2010**) Observations of transition phenomena on a controlled diffusion compressor stator with a circular arc leading edge. *Journal of Turbomachinery*, **132**, pp. 1 .

[32] **Henderson A D, Walker G J and Hughes J D** (**2008**) Unsteady transition phenomena at a compressor blade leading edge. *Journal Of Turbomachinery*, **130**, pp. 1.

[33] **Hilgenfeld L and Pfitzner M** (**2004**) Unsteady boundary layer development due to wake passing effects on a highly loaded linear compressor cascade. *Journal Of Turbomachinery*, **126**, pp. 493.

[34] **Hobson G V, Hansen D J, Schnorenberg D G and Grove D V** (**2001**) Effect of Reynolds number on separation bubbles on compressor blades in cascade. *AIAA Journal of Propulsion and Power*, **17**, pp. 154.

[35] **Hobson G V, Hansen D J, Scnorenberg D G and Grove D V** (**2001**) Effects of Reynolds number on separation bubbles on compressor blades in cascade. *Journal Of Propulsion and Power*, **17**, pp. 154.

[36] **Hobson G V and Shreeve R P** (**1993**) Inlet turbulence distortion and viscous flow development in a controlled - diffusion compressor as very high incidence. *Journal Of Propulsion and Power*, **9**, pp. 397 .

[37] **Hobson G V, Wakefield B E and Roberts W B** (**1999**) Turbulence amplification with incidence at the leading edge of a compressor cascade. *Journal of Rotating Machines*, **2**, pp. 89 .

[38] **Hobson G V and Weber S** (**2000**) Prediction of a laminar separation bubble over a controlled - diffusion compressor blade.

[39] **Hodson H P, Huntsman I and Steele A B** (**1994**) An investigation of boundary layer developments in a multi-stage LP turbine. *Journal of Turbomachinery*, **116**, pp. 375.

[40] **Howard M** (**2010**) Private communication.

[41] **Howell R J** (**1999**) *Wake-separation bubble interaction in low Reynolds number turbomachinery*. Ph.D. thesis, Whittle Laboratory, Cambridge University.

[42] **Howell R J, Ramesh O N, Hodson H P and Schulte V** (**2000**) High life and aft loaded profiles for low pressure turbines. *ASME 2000-GT-261*.

[43] **Hughes J D and Walker G J** (**2001**) Natural transition phenomena on an axial compressor blade. *Journal Of Turbomachinery*, **123**, pp. 392.

[44] **Hunt J and Kevlahan N** (**1993**) Rapid distrotion theory and the structure of turbulence. *New approaches and concepts in turbulence*.

[45] **Kendall J M** (**1991**) Studies on laminar boundary-layer receptivity to freestream turbulence near a leading edge. *Boundary Layer Stability and Transition to Turbulence*, **114**, pp. 23.

[46] **Klebanoff P S** (**1971**) Contributions on the mechanics of boundary-layer transition. Technical report, Bulletin of the American Physical Society.

[47] **Knapp C F and Roache P J** (**1968**) A combined visual and hot-wire anemometer investigation of boundary-layer transition. *AIAA Journal*, **6**(9), pp. 29.

[48] **Launder B, Reese G and Rodi W** (**1975**) Progress in the developments of reynolds-stress turbulence closure. *Journal of Fluid Mechanics*, **68**, pp. 537 .

[49] **Lieblein S** (**1965**) Experimental flow in 2D cascades. Technical Report SP 36, NACA.

[50] **Lieblein S and Roudebush W H** (**1956**) Theoretical loss relations for low-speed two-dimensional cascade. Technical Report TN 3662, NACA.

[51] **Lui Y, Zaki T A and Durbin P A** (**2008**) Boundary-layer transition by interaction of discrete and continuous modes. *Journal of Fluid Mechanics*, **604**, pp. 199.

[52] **Mailach R and Vogeler K** (**2004**) Aerodynamic blade row interaction in an axial compressor - part 1: unsteady boundary layer development. *Journal Of Turbomachinery*, **126**, pp. 35.

[53] **Mayle R** (**1991**) The role of laminar - turbulent transition in gas turbine engines. *Journal Of Turbomachinery*, **113**, pp. 509.

[54] **Mayle R** (**1992**) Unsteady multimode transition in gas turbine engines.

[55] **Mayle R E and Schulz A** (**1997**) The path to predicting bypass transition. *Journal Of Turbomachinery*, **119**, pp. 405.

[56] **Menter F R** (**1994**) Two-equation eddy-viscosity turbulence models for engineering applications. *AIAA Journal*, **32**, pp. 1598.

[57] **Morkovin M V** (**1968**) On the man faces of transition. *Symposium on Viscous Drag Reduction*.

[58] **Narasimha R and Shreenivasan K R** (**1979**) Relaminarisation of fluid flows. *Advances In Applied Mechanics*, **19**, pp. 221.

[59] **Orth U** (**1993**) Unsteady boundary layer transition in flow periodically disturbed by wakes. *Journal Of Turbomachinery*, **115**, pp. 707.

[60] **Ottavy X, Vilmin S, Hodson H P and Galimore S** (**2004**) The effects of wake-passing unsteadiness over a highly loaded compressor-like flat plate. *Journal Of Turbomachinery*, **126**, pp. 14.

[61] **Parker R and Watson J F** (**1972**) Interaction effects between blade rows in turbomachines. *Proceesing of the Institute of Mechanical Engineers*, **186**, pp. 331.

[62] **Paxson D E and Mayle R** (**1991**) Laminar boundary layer interaction with an unsteady passing wake. *Journal Of Turbomachinery*, **113**, pp. 419.

[63] **Perkins S C T and Henderson A D** (**2012**) Separation and relaminarisation at the circular arc leading edge of a controlled diffusion compressor stator. *Proceeding of ASME Turbo Expo 2012, GT2012-69384*.

[64] **Perkins S C T, Henderson A D, Walker G J and Sargison J E** (**2010**) Preduction of free-stream turbulence variation at the leading edge of an axial compresor blade. *Australian Fluid Mechanics Conference*.

[65] **Place J M M, Howard M A and Cumpsty N A** (**1996**) Simulating the multi-stage environment for single-stage compressor experiments. *Journal of Turbomachinery*, **33**, pp. 706.

[66] **Preston J H** (**1957**) The minimum Reynolds number for a turbulent boundry layer and the selection of a transition device. *Journal of Fluid Mechanics*, **3**, pp. 373.

[67] **Rhoden H G** (**1952**) Effects of Reynolds number on the flow of air through a cascade af compressor blades. Report 2919, Aeronautifcal Research Council R and M.

[68] **Roache P J** (**1987**) The Generation of nearly isotropic turbulence by means of grids. *Journal of Heat and Fluid Flow*, **8**, pp. 82 .

[69] **Roberts W B** (**1995**) Advanced turbofan blade refurbishment technique. *Journal of Turbomachinery*, **117**, pp. 666 .

[70] **Sanger N L and Shreeve R P** (**1986**) Comparison of Calculated Experimental Cascade Performance for Controlled-Diffusion Compressor Stator Blading. *Journal of Turbomachinery*, **108**, pp. 42 .

[71] **Sarkar S and Voke P R** (**2006**) Large - Eddy Simluation of Unsteady Surface Pressure Over a Low - Pressure Turbine Blade due to Interaction of Passing Wakes and Inflexional Boundary Layer. *Journal of Turbomachinery*, **128**, pp. 221 .

[72] **Savill A M** (**2002**) By-pass transition using conventional closures. *Closure Strategies for Turbulent and Transitional Flows*, pp. 493 – 521. Cambrdige University Press.

[73] **Savill A M** (**2002**) New stratergies in modelling by-pass transition. *Closure Stratergies for Turbulent and Transitional Flows*. Cambrdige University Press.

[74] **Schaubauer and Klebanoff P S** (**1956**) Contributions on the Mechanics of Boundary Layer Transition. *NACA, Report 1289*.

[75] **Schlichting H** (**1979**) *Boundary Layer Theory*. Series In Mechanics Engineering. McGraw and Hill, 6th edition.

[76] **Schlichting H and Das A** (**1969**) On the influence of turbulence level on the aerodynamic losses of axial turbomachines.

[77] **Schobeiri M T, Read K and Lewalle J** (**2003**) Effect of unsteady wake passing frequency on boundary layer transition, experimental investigation, and wavelet analysis. *Journal of Fluids Engineering*, **125**, pp. 251.

[78] **Schulte V and Hodson H P** (**1994**) Wake-separation bubble interaction in low pressure turbines. *AIAA/SAE/ASME/ASEE 30th Joint Propulsion Conference*, **30**.

[79] **Schulte V and Hodson H P** (**1996**) Unsteady wake-induced boundary layer transition in low pressure turbines. *Journal of Turbomachinery*, **120**, pp. 28.

[80] **Smith A M O** (**1956**) Transition, Pressure Gradient and Stability Theory.

[81] **Solomon W J** (**1996**) *Unsteady Boundary Layer Transition On Axial Compressor Blades*. Ph.D. thesis, University of Tasmania.

[82] **Solomon W J and Walker G J** (**1995**) Observations of wake-induced transition on an axial compressor blade. *ASME Turbo Expo*.

[83] **Solomon W J and Walker G J** (**2000**) Indcidence effects on wake-indiced transition on an axial compressor blade. *AIAA Journal of Propulsion and Power*, **16**, pp. 397.

[84] **Soranna F, Chow Y, Uzol O and Katz J** (**2006**) The Effect of Inlet Guide Vanes Wake Impingement on the Flow Structure and Turbulence Around a Rotor Blade. *Journal of Turbomachinery*, **128**, pp. 82 .

[85] **Speidel L** (**1957**) Influence on the laminar boundary layer by periodic disturbance of the flow. *Z Flugwiss Weetraumsforsch*, **5**, pp. 270.

[86] **Speziale C, Sarkar S and Gatski T** (**1991**) Modelling the pressure-strain correlation of turbulence: an invariant dynamical systems approach. *Journal of Fluid Mechanics*, **277**, pp. 245.

[87] **Stieger R D, Hollis D and Hodson H P** (**2004**) Unsteady surface pressures due to wake-induced transition in a laminar separation bubble on a low-pressure turbine cascade. *Journal Of Turbomachinery*, **126**, pp. 544.

[88] **Tain L and Cumpsty N A** (**2000**) Compressor blade leading edges in subsonic compressible flow. *ProQuest Science Journal*, **214**, pp. 221.

[89] **Tani I** (**1964**) Low speed flows involving separation bubble. *Progress in Aero. Sci.*.

[90] **Thomas R L and Gostelow J P** (**2005**) The pervasive effect of the calmed region. *ASME Paper GT2005-69125*.

[91] **Thwaites B** (**1949**) Approximate calculation of the laminar bounday layer. *Aeronautical Quarterly*, **1**, p. 245.

[92] **Volino R J** (**2010**) Effect of unsteady wakes on boundary layer separation on a very high lift low pressure turbine airfoil. *Proceedings of ASME Turbo Expo 2010*.

[93] **Walker G J** (**1968**) The prediction of boundary layer development on axial flow turbomachine blades. *Conference on Hydraulics and Fluid Mechanics*, pp. 97–104.

[94] **Walker G J** (**1972**) *An investigation of the boundary layer behavior on the blading of a single stage axial-flow compressor.*. Ph.D. thesis, University of Tasmania.

[95] **Walker G J** (**1993**) The role of laminar - turbulent transition in gas turbine engines: a discussion. *Journal Of Turbomachinery*, **115**, pp. 207.

[96] **Walker G J, Hughes J D, Kohler I and Solomon W J** (**1998**) The Influence of wake-wake interactions on loss fluctuations of a downstream axial compressor blade row. *Journal of Turbomachinery*, **120**, pp. 695.

[97] **Walraevens R E and Cumpsty N A** (**1995**) Leading edge separation bubbles on turbomachinery blades. *Journal Of Turbomachinery*, **117**, pp. 115.

[98] **Wheeler A P S** (**2007**) *The effect of unsteady flows on compressor performance*. Ph.D. thesis, Whittle Laboratory, University of Cambridge.

[99] **Wheeler A P S, Miller R J and Hodson H P** (**2007**) The effects of wake induced structures on compressor boundary layers. *Journal Of Turbomachinery*, **129**, pp. 705.

[100] **Wheeler A P S, Sofia A and Miller R J** (**2007**) The effect of leading-edge geometry on wake interactions in compressors.

[101] **White F M** (**1974**) *Viscous fluid flow*. Series In Mechanics Engineering. McGraw and Hill.

[102] **Wisler D C** (**1985**) Loss reduction in axial-flow compressors through low speed model testing. *Journal of Turbomachinery*, **107**, pp. 354.

[103] **Wisler D C, Halstead D E and Beacher B F** (**1999**) Improving compressor and turbine performance through cost-effective low-speed testing. *ISOBE*, pp. 99–7073.

[104] **Wu X and Durbin P A** (**2000**) Boundary layer transition induced by periodic wakes. *Journal of Turbomachinery*, **122**, pp. 442 .

[105] **Zaki T A and Durbin P A** (**2005**) Mode interaction and bypass route to transition. *Journal of Fluid Mechanics*, **531**, pp. 85.

[106] **Zhong S, Chong T P and Hodson H P** (**2003**) A comparison of streading angles of turbulent wedges in velocity and thermal boundary layers. *Journal of Fluid Mechanics*, **125**, pp. 267.

[107] **Zohar Y and Ho C M** (**1996**) Dissipation scale and control of turbulence in a plane mixing layer. *Journal of Fluid Mechanics*, **320**, pp. 139.